Fibre-optic borehole observations and numerical modelling of complex ice-sheet thermodynamics

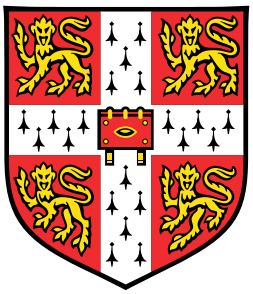

Robert Jonathan Law

Scott Polar Research Institute
Fitzwilliam College, University of Cambridge

This thesis is submitted for the degree of
Doctor of Philosophy

June 2022

Declaration

I hereby declare that except where specific reference is made to the work of others, the contents of this thesis are original and have not been submitted in whole or in part for consideration for any other degree or qualification in this, or any other university. This thesis is my own work and contains nothing which is the outcome of work done in collaboration with others, except as specified in the text and Acknowledgements. This thesis does not exceed the length limits prescribed by the Degree Committee for the Faculty of Earth Sciences and Geography.

Robert Jonathan Law
June 2022

Fibre-optic borehole observations and numerical modelling of complex ice-sheet thermodynamic

Abstract

Robert Jonathan Law

Predictions of ice-sheet mass loss, and therefore predictions of global sea level rise, depend sensitively upon how ice-sheet motion is incorporated into numerical models. Using field observations and numerical modelling, this thesis demonstrates that two frequently overlooked processes are central to describing borehole observations of fast ice-sheet motion — intermediate-scale (<25 m, $\lesssim$2 km) interaction of ice motion with *realistic* or *real* bed topography, and modulation of these ice-motion patterns through a basal layer of temperate ice (much softer ice at the pressure-melting point). I first present a fibre-optic data set from a 1,043 m deep borehole drilled to the base of the fast-moving (>500 m a^{-1}) marine-terminating Sermeq Kujalleq (Store Glacier) at the western margin of the Greenland Ice Sheet. This reveals hitherto unappreciated complexity in the processes behind fast ice-sheet motion. I observe substantial but isolated strain heating $\sim$ 220 m beneath the surface within stiffer interglacial-phase ice where previously none was expected. Ice deformation within glacial-phase ice below 889 m is further observed to be strongly heterogeneous, with a possible high-strain interface demarcating the Last Glacial-Interglacial Transition. I also find a 73-m-thick temperate basal layer, notably thicker than the <10-m-thick temperate layer just 8.9 km away, unexplained by existing theory, and interpreted to be important for the glacier's fast motion.

To disentangle this observed complexity, I then model three isolated 3D domains from the Greenland Ice Sheet's western margin — two from Sermeq Kujalleq and one from the land-terminating Isunnguata Sermia, all centred above a central borehole observation. By incorporating high-resolution *realistic* geostatistically simulated topography, I demonstrate that a layer of basal temperate ice with spatially highly variable thickness forms naturally in both marine- and land-terminating settings, alongside ice-motion patterns which are far more complex than previously considered. I show that temperate ice is expected to be vertically extensive in deep troughs, but to thin over bedrock highs. I further show that basal-slip rates are interconnected with this variability, reaching >90% or <5% of surface velocity dependent on setting. Last, I apply the assembled model to *real* high-resolution bed topography data produced by radio-echo sounding at Thwaites Glacier, Antarctica. This reveals a distinct pattern of ice motion controlled by rough topographic highs where

basal slip rates are highly variable, and the landscape is predominantly erosive, with broader topographic basins where basal slip is high and uniform, and the landscape is predominantly depositional. This work further suggests the existence of basal temperate ice layer beneath Thwaites Glacier, at least at the rougher topographic highs. Overall, this thesis advances understanding of how ice sheets move, which may ultimately lead to improved parameterisations of ice-sheet motion for predictive models.

Acknowledgements

Completing this thesis has been quite a journey, beset by more than one wrong turn, thickets of overgrowth, and fallen walls. It has often been solitary, deepened by a global pandemic, but almost all of the highest rises were crested, and deepest depressions traversed, with company. First, thanks mum for exposing me to the mountains and mountain lore that probably germinated some early love of landscapes, cold places, and thinking about our place amongst them. Thanks also for always and gently encouraging me on my way — I would not have even got to the starting point without your support.

Thanks, Poul, for supporting my deviations far from the beaten track, for the guidance when the way ahead was fog-strewn, and for pushing me to the outer limits of my capabilities. It has not always been easy, but I have you to thank for the scientist I have become.

Thanks also to the other members of the RESPONDER team: Bryn for steadfast resolve and a wealth of glaciological insight; Sam Doyle for showing how fieldwork should be done; Tom honestly just for being there and for the strangely uplifting influence of knowing that at least I wasn't eating Cup a Soup day in day out from the same unwashed mug; Samuel Cook[1] for cynicism, Derbyshire walks, and getting me established with Elmer/Ice; and TJ for calm intellectual sparring and advice. Impasses were passed with support from astute collaborators: Marianne for mathematical and numerical guidance; Olivier for Elmer/Ice wizardry; Cedric for lab testing (and also Maison Clement); and Mickey and Nick for pulling away the ice to reveal the landscapes hidden beneath.

I am indebted to the fellow travellers who rambled along the way. Craig for daydreams, distractions, and deliberation; Josh and MA for making Red Cottage home; TMB for five years of conversation; James for Free Press pints and endless fascination; Fred for a place to stay in rainy Macclesfield; Claire's world; and Peter for acknowledging we cannot acknowledge. Ason, Jake, Omar, Holly, Spanish Carlos, Brazilian Carlos, Øyvind, Marc, Tobias, Yorkshire Alex, Lincolnshire Alex, Lena, Jonathan, Elyem, Des: thanks for making the climbing trips, not-climbing trips, and time spent in Cam so worthwhile. Thanks too to those at SPRI who made it such an incredible and supportive environment to work in. B Dell, Karla, the attic dwellers (Bob [my favourite CoE pagan] and Peter), Iain, Amelia, Frazer, Sasha, Neil, Ian, and Ilona to name but a few. Thanks to Fitzwilliam College for extensive funding and support. Last, thanks to you for picking up and putting up with this bedizened old manuscript.

[1] My apology is sincere for any missing adjectival hyphens.

No surface is allowed to be bare,

& nothing to stand still. A man[2] could forever study a pebble

& at last see dilations & expansions of the hills—

to pull the most slender stalk, is to jostle the stars,

& between the bearded grass

& man "looking in the vegetable glass

of Nature," is a network of roots & suckers

fine as hairs.

I threw a stone upon a pond

& it bounded the surface, its circles interlacing

& radiating out to the most ephermeral edge.

Flint & Mica, Lichened Limestone, Shale & Sarcens, Sandstone, Soil.

I saw the wind moving on a meadow

& the meadows moving under wind—

lifting, settling & accumulating.

Flint & Mica, Lichened Limestone,

Shale & Sarcens, Sandstone, Soil.

What the Earth Told Me — Ronald Johnson

2 ⚍

Table of contents

Notation

Greek Symbols

β	Basal traction parameter
$\boldsymbol{\tau}$	Deviatoric stress tensor (MPa)
$\boldsymbol{g}$	Gravitational acceleration vector (m a^{-2})
$\boldsymbol{G}_b$	Geothermal heat flux (J m^{-2} a^{-1})
$\boldsymbol{n}_b$	Basal normal vector
$\boldsymbol{q}$	Energy flux (J m^{-2} a^{-1})
$\boldsymbol{u}$	Vector of ice velocity (m a^{-1})
$\Delta\alpha$	Differential attenuation
$\dot{\boldsymbol{\epsilon}}$	Strain rate tensor (a^{-1})
$\dot{\epsilon}$	Compressive strain rate (a^{-1})
$\dot{\epsilon}_e$	Effective strain rate (a^{-1})
$\dot{\epsilon}_{ij}$	Strain rate tensor components (a^{-1})
Γ	Modelled variogram
γ	Clausius-Clapeyron constant (K MPa^{-1})
$\hat{\Gamma}$	Empirical variogram
κ	Enthalpy diffusivity (kg m^{-1} s^{-1})
κ_c	Enthalpy diffusivity for cold ice (kg m^{-1} s^{-1})
κ_t	Enthalpy diffusivity for temperate ice (kg m^{-1} s^{-1})
$\Leftarrow$	Reverse DTS measurement direction
ν	Fitting values for ice surface in chapter 5
ω	Water content (%)
ω_{lim}	Water content upper limit for rheological calculations (%)
ω_{max}	Maximum water content (%)

Π Thickness of overlying ice column (m)

ρ Density (kg m^{-3})

ρ_i Density of ice (kg m^{-3})

ρ_w Density of water (kg m^{-3})

$\Rightarrow$ Forward DTS measurement direction

σ Compressive stress (MPa)

τ_b Basal traction (MPa)

τ_d Driving stress

τ_e Effective stress (MPa)

θ Ice surface and bed slope in chapter 3, orientation of gravity vector in chapter 4 and 5 (°)

φ Material constant in flow equation 2.1 (MPa^{-3} a^{-1})

ξ Glaciostatic pressure (MPa)

ζ sensitivity of (anti-)Stokes scattering to temperature

A Creep parameter in Glen's flow 'law' (MPa^{-3} a^{-1})

A_s Parameter in equation 4.6

A_1 and A_2 Rate factors (MPa a^{-1})

A_{max} Maximum rate factor (MPa a^{-1})

C Dimensionless function of alignment and sensitivity of the optical system in chapter 3 and dimensionless morphology parameter in chapters 2 and 4

C_a and C_b Enthalpy heat capacity constants (J kg^{-1} K^{-1})

c_i Heat capacity of ice (J kg^{-1} K^{-1})

C_p Constant in plastic deformation relationship

C_S Friction parameter in basal traction relationship of Gagliardini et al. (2007)

D Normalised depth

d Depth (m)

D_v Vertically integrated water drainage volume (m^{-3} a^{-1})

E_a, E_b, and E_c Enthalpy quadratic curve parameters

F Dimensionless parameter used to set O

F_b Frictional basal heating (J m^{-2} a^{-1})

g Gravitational acceleration (m s^{-2})

g_i Gravitational acceleration vector components (m a^{-2})

H Specific enthalpy of ice (J kg^{-1})

h Lag distance in variogram calculation

H_s Phase change specific enthalpy of ice (J kg^{-1})

H_{loads} Specific enthalpy loads

$H_{weights}$ Specific enthalpy weights

k Thermal conductivity of ice (W m^{-1} K^{-1})

L Latent heat capacity of ice (J kg^{-1})

M_b Basal mass balance (kg m^{-2} a^{-1})

N Number of point pairs in empirical variogram calculation

n Exponent in Glen's flow 'law'

N_e Effective subglacial pressure (MPa)

n_i Normal vector component

O Dimensionless proportionality parameter relating N_e to driving stress

p Pressure (MPa)

p_i Ice overburden pressure (MPa)

P_S Stokes power

P_{aS} Anti-Stokes power

p_{tr} Triple point pressure of ice (MPa)

Q Energy released per unit length of borehole during drilling (W m^{-2})

q Constant in Weertman-type basal traction relationship

Q_a Advective energy sink (W m^{-1})

Q_b Basal energy changes related to basal hydrological storage and transport (J m^{-2} a^{-1})

Q_s Strain heating (J m^{-3} a^{-1})

Q_1 and Q_2 Activation energies (J mol^{-1})

R Gas constant (J mol^{-1} K^{-1})

s Time duration (s)

T Temperature (k)

t Time (s in chapter 3 or a in chapters 4 and 5)

T_0 Reference temperature specific enthalpy (K)

T_h Homologous temperature (K)

T_m Melting point of ice (K)

T_{eq} Undisturbed ice temperature (K)

T_{lim} Limit temperature (K)

T_{tr} Triplepoint temperature of ice (K)

u Deformation velocity (m s^{-1})

u_b Basal velocity (m a^{-1})

u_i Ice velocity vector components (m a^{-1})

v_s Surface velocity (m a^{-1})

W_1, W_2, and W_3 Water viscosity factors (MPa a^{-1})

x_a Location in variogram calculation

z Depth (m) (chapter 3) or z coordinate axis (chapters 4 and 5)

Z_s and Z_b Position of the ice surface and base (m)

BH19a Borehole 2019 a (abandoned)

BH19b Borehole 2019 b (geophone string)

BH19c Borehole 2019 c (DTS and DAS installation, thermistor string, and basal piezometer)

BH19d Borehole 2019 d (seismic sparker)

BH19e Borehole 2019 e (thermistor string and basal piezometer)

BH19f Borehole 2019 f (abandoned)

BH19g Borehole 2019 g (basal pressure transducer)

IS2015 Study site on Isunnguata Sermia from Maier et al. (2019)

Lake 028 Lake near R30 ∼28 km from glacier terminus

R29 RESPONDER 2018 camp location ∼29 km inland from glacier terminus

R30 RESPONDER 2019 camp location ∼30 km inland from glacier terminus

S1 through S5 Borehole sites at Isunnguata Sermia from Harrington et al. (2015)

S30 SAFIRE 2014 camp location ∼30 km inland from glacer terminus

Sermeq Kujalleq Greenlandic name used here for Store Glacier as it is often called in the literature. Literal translation is Glacier Southern.

Sermeq Kujalleq in Kangia in Kangia suffixed to avoid confusion with Sermeq Kujalleq (Store Glacier). Often called Jakobshavn Isbræ in the literature.

Acronyms

AIS Antarctic Ice Sheet

APC Angle polished connector

AR6 Sixth Assessment Report

CReSIS Center for Remote Sensing of Ice Sheets

CTS Cold-temperate transition surface

DAS Distributed acoustic sensing

DEM Digital Elevation Model

DEM Digital elevation model

DSS Distributed strain sensing

DTS Distributed temperature sensing

EAIS East Antarctic Ice Sheet

GrIS Greenland Ice Sheet

InSAR Interferometric synthetic-aperture radar

IP68 Ingress protection 68, withstands dust, dirt, and submersion up to 1.5 m for 30 min

IPCC Intergovernmental Panel on Climate Change

ISMIP6 Ice Sheet Model Intercomparison Project 6

MEaSUREs Making Earth System Data Records for Use in Research Environments

MSGL Mega-scale glacial lineation

NEEM North Greenland Eemian Ice Drilling

OM3 Optical multi mode fibre optic (bandwidth 2000 MHz km)

OS2 Loose tube optical single mode fibre optic

PT1000 Platinum resistance thermometer with a resistance of 1000 Ω at 0°C

RESPONDER Resolving Subglacial Properties, hydrological networks and dynamic evolution of ice flow on the Greenland Ice Sheet

SAFIRE Subglacial Access and Fast Ice Research Experiment

WAIS West Antarctic Ice Sheet

WISSARD Whillans Ice Stream Subglacial Access Research Drilling

Chapter 1

Introduction

1.1 Motivation and narrative

For most of the last few centuries Earth's two ice sheets, the Greenland(ic) Ice Sheet (GrIS) and Antarctic Ice Sheet (AIS), were either entirely unknown or were considered to be far away geologic curiosities slipping off into the high latitudes (not, of course, for the Greenlandic). Over the last few decades this perspective has inverted, with ice-sheet response to climatic forcing becoming a central aspect of the unfolding climate catastrophe. The GrIS and AIS are now shrinking at an accelerating rate (Fig. 1.1, The IMBIE Team, 2019; Mouginot et al., 2019; The IMBIE Team, 2021) with incommensurate understanding of mass loss processes substantially contributing to uncertainty in global sea level rise predictions over the 21st century and beyond (Aschwanden et al., 2012). Such uncertainty arises from an intricate and often overlapping set of processes: surface algal blooms, firn aquifers, and subglacial hydrology to name but a few. Addressing these problems and working towards a commensurate scientific understanding of ice-sheet systems and thermodynamics[1] is of crucial importance for the tens of millions of people living within coastal communities facing rising seas and catastrophic flooding (Kulp and Strauss, 2019), for policy makers across the political spectrum, for climate activists, and for concerned citizens for whom the Earth's ice sheets are an influential barometer of anthropogenically forced climate change.

A unifying feature of this ice-sheet prediction puzzle is ice motion, which transports vast quantities of frozen precipitation from the cold ice-sheet interior to its melting and fracturing margins. For the purposes of ice-sheet modelling and the interpretation of field observations, such ice-sheet motion is separated into two processes: (1) internal ice deformation, or the macroscopic manifestation of microscopic creep processes within and between ice crystals, and (2) basal slip, where the glacier either slides directly over a rigid base in the presence of a water-filled cavity system (e.g. Helanow et al., 2021) or deforms a thin horizon of underlying wet sediment (e.g. Zoet et al., 2021). Paramaterisations, or constitutive relationships, for these two processes form the dynamic core of the process-based ice-sheet models used to predict the future trajectory of ice sheets and their contribution to sea level rise. However, there is significant debate surrounding the appropriate form and parameters for such relationships (e.g. Tsai et al., 2015; Bons et al., 2018; Stearns and Van

[1] The relation between temperature, other forms of energy (such as gravitational potential), and work (i.e ice displacement).

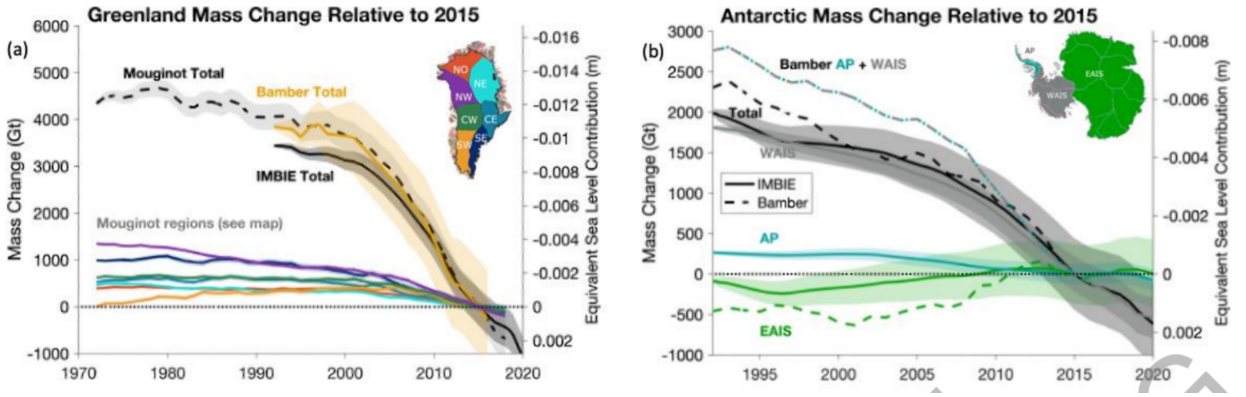

Fig. 1.1 . Mass changes and equivalent sea level contribution for (a) the GrIS and (colour-coded) the major GrIS drainage basins shown in the inset figure with data from Bamber et al. (2018) and Mouginot et al. (2019) and (b) the AIS and (colour-coded) West Antarctic Ice Sheet, East Antarctic Ice Sheet, and Antarctic Peninsula with data from (Bamber et al., 2018). Figure from from IPCC AR6, Fig. 9.16 (Fox-Kemper et al., 2021).

Der Veen, 2018; Joughin et al., 2019; Millstein et al., 2022) which can significantly influence model output (e.g. Ritz et al., 1996; Bindschadler et al., 2013; Brondex et al., 2017; Bons et al., 2018; Zeitz et al., 2020; Cheng et al., 2021). It is therefore of clear importance that we have a thorough understanding of ice-motion mechanics and how ice motion is influenced by intrinsic ice properties (temperature, water content, and impurity content), extrinsic forcing (ice sheet surface, margin, and basal geometries), and the complex hydrological and sedimentary interactions occurring between the ice sheet and its base. Addressing the continued paucity of understanding surrounding these processes was the leading motivation for the work presented in this thesis.

However, advancing understanding of processes is often predicated on advancing observations of the processes in question. For ice sheets, it is often borehole observations that offer the least ambiguous way of measuring ice motion beneath the surface. At ice-sheet divides, where horizontal deformation rates are extremely low, continuous logging apparatus can be slowly lowered into mechanically drilled boreholes enabling continuous measurements (e.g. Clow et al., 1996). However, the much faster (>100 m a^{-1}) margins of the GrIS require a different approach as much higher internal deformation rates would quickly destroy equipment used inland. Here, hot-water borehole drilling (e.g. Hubbard et al., 1995) provides very temporary access (unless the glacier is fully temperate) to the subsurface, and a short window within which senors may be lowered into the ice. Typically, discrete sensors spaced along an electrical cable are used (e.g. Lüthi and Funk, 2001; Harrington et al., 2015; Miles et al., 2018). These measurements have enabled decades of crucial advances in understanding, but their discrete nature means that ice properties and behaviour between sensors have been the subject of continued speculation (e.g. Doyle et al., 2018).

The introduction of ruggedised remotely-deployable fibre-optic distributed temperature sensing (DTS) systems offered a potential solution. DTS functions by using back-scattered light to obtain temperature measurements at very high spatial resolution (<1 m) in a distributed manner over the entire length of an optical fibre housed in protective cabling, effectively eliminating the inter-sensor uncertainty that can cloud discrete measurements. DTS had been increasingly widely applied to environmental-sensing problems (such as groundwater, Selker et al., 2006, or evapotranspiration, Schilperoort et al., 2018) as technology and remote capabilities improved, but had only previously been applied to two glacial settings, both in Antarctica where ice-deformation rates were low (Tyler et al., 2013; Fisher et al., 2015). From inception, a central motivation of this thesis was then to (1) determine the feasibility of DTS in rapidly deforming ice, (2) provide a clear methodology for future installations, and (3) constrain ice behaviour and temperature between discrete sensors. Of these, (1) and (2) were important methodologically while (3) had the potential to reveal exciting and previously hidden details of ice-sheet thermodynamics. This work is detailed in chapter 3.

Next, while field observations often provide extremely useful insights into ice-sheet processes directly, process understanding can be further advanced by integrating field data and numerical modelling (e.g. Ryser et al., 2014a). Such modelling was central to the proposed PhD project, but the focus evolved following the results detailed in chapter 3. These results revealed a thick and spatially variable layer of temperate ice (softer ice at the pressure-dependent melting point co-existing with some percentage of water) at the base of Sermeq Kujalleq (also known as Store Glacier), a fast-moving marine-terminating outlet glacier roughly halfway up the west coast of Greenland, just north of the Nuussuaq Peninsula (Fig. 3.2). This temperate layer variation was a significant departure from the then pervasive hypothesis that the temperate layer should evolve smoothly and uniformly towards the margins of the GrIS, reasonably based on existing sparsely spaced borehole observations (Harrington et al., 2015). Fibre-optic results from chapter 4 additionally added to a series of papers showing variable ice deformation towards the margins of the GrIS that had largely eluded explanation under existing theories and modelling approaches (e.g. Doyle et al., 2018; Lüthi et al., 2002; Maier et al., 2019; Ryser et al., 2014a, see chapter 2 for further information).

Disentangling the complexity in GrIS borehole records — for curiosities sake and to assess its importance in ice-sheet motion — then became the main motivation of my work. This focused on overlooked 'intermediate-scale' (>25 m, $\lesssim$2 km) ice-motion processes, bridging a gap between improving understanding of ice motion at small (e.g. Zoet and Iverson, 2020; Helanow et al., 2021) and large scales (e.g. Aschwanden et al., 2016; McCormack et al., 2022). Previous studies provided an initial framework for this work. Ryser

et al. (2014a) and Maier et al. (2019) developed 2D periodic finite-element models with free-surface evolution for variable basal traction and sinusoidal bedforms respectively. Helanow et al. (2021) constructed a 3D periodic model for fully temperate ice motion over drone-acquired high resolution digital elevation models (DEMs) of recently deglaciated terrains, and MacKie et al. (2021) provided a methodology to geostatistically simulate realistic DEMs for presently glaciated areas where only sparsely located radar flight lines were available. Last, Gilbert et al. (2014) developed an enthalpy approach for Elmer/Ice which could accurately account for thermomechanical coupling within temperate ice. The combination of these studies allowed me to produce the model detailed in chapter 4 and use it to explore the complex ice motion of the GrIS as recorded in borehole records.

Last, Thwaites Glacier in West Antarctica is of considerable importance for future and existing mass loss from the AIS, with the potential to raise global sea level by >3 m over the coming centuries following retreat beyond a threshold thought to depend sensitively upon bathymetry and subglacial topography (e.g. Parizek et al., 2013; DeConto and Pollard, 2016; Scambos et al., 2017). Recent studies of Thwaites Glacier motion are significantly improving our understanding of ice-motion and landscape formation there (e.g. Holschuh et al., 2020; Alley et al., 2021; McCormack et al., 2022), but intermediate-scale ice-bed interaction processes remain largely obscured, a situation exacerbated by an absence of borehole studies. High-resolution swath radar data of the Thwaites Glacier bed (Holschuh et al., 2020), in combination with the model I assembled in chapter 4, offered an effective way to improve our understanding of this important glacier and investigate (1) the influence of subglacial water pressure and temperate ice rheology on ice-motion patterns, (2) the difference on ice-motion patterns between *real* and *realistic* topography, and (3) subglacial landscape formation. The results from this work are presented in chapter 5.

In summary, this thesis was primarily motivated by a need to advance understanding of ice-sheet motion. Achieving this objective required methodological advances in both borehole observation techniques and numerical modelling.

1.2 Aims

This thesis has three central aims:

1. To demonstrate the applicability and usefulness of DTS in fast-moving glacier settings, and to use DTS to uncover the behaviour and ice properties of the marine-terminating Sermeq Kujalleq, Greenland.

2. To develop a model capable of investigating ice-motion processes and temperate ice formation in isolated ice-sheet domains using statistically realistic topography. To then apply this to demonstrate the important role realistic topography and a basal temperate ice layer play in ice-sheet motion.

3. To further apply the assembled model to investigate basal-motion processes and landscape formation beneath Thwaites Glacier, Antarctica.

1.3 Work presented

There are five chapters beyond this introduction:

Chapter 2 situates the research presented within existing literature on observations and predictions of mass loss from ice sheets, ice deformation and basal slip observations and theories, and fibre-optic sensing techniques.

Chapter 3 details results from distributed fibre-optic sensing of Sermeq Kujalleq, Greenland. This work is published in Science Advances as Law et al. (2021).

Chapter 4 covers the development of a model for isolated glacier domains that includes temperate ice rheology and statistically realistic topography and its application to three sites on the western margin of the GrIS, including two from Sermeq Kujalleq. This work is in review in Science Advances with an EarthArXiv preprint as Law et al. (2022).

Chapter 5 extends the model developed in chapter 4 to Thwaites Glacier, Antarctica, over high-resolution swath radar data to further investigate basal-motion processes alongside landscape development.

Chapter 6 synthesises the advances made in the preceding chapters, discusses how complexity can be incorporated into an understanding of ice-sheet motion, and details future research possibilities.

Chapter 2

Background

2.1 Ice sheet mass loss

2.1.1 Observations

Before the satellite era (1992-present, Bamber et al., 2018) the mass balance behavior of the GrIS and AIS was equivocal, even as disquiet surrounding the effects of anthropogenic greenhouse gas emissions steadily mounted (Pales and Keeling, 1965; Hansen et al., 1981; Arrhenius, 1896). Serious concerns[1] had been raised that the WAIS (the West AIS, west of the Transantarcitc Mountains) was effectively a fossil of the Last Glacial Period (Mercer, 1968) and was vulnerable to collapse over a period of centuries under a global temperature increase of only a few degrees (Alley, 1990) due to sections being grounded deep below sea level (Fig. 2.1). However, ice-sheet sectors grounded mostly above sea level (which includes almost all of the GrIS) had been considered to have a response time to climatic change of up to thousands of years (Alley and Whillans, 1984). 30 years of overlapping satellite and airborne (MacGregor et al., 2021) measurements show that the latter hypothesis is incorrect, and that ice-sheets are susceptible to large (and negative) decadal shifts in mass balance irrespective of grounding elevation, even if heightened concern around marine-grounded ice-sheets remains (Fig. 1.1, Mouginot et al., 2019; The IMBIE Team, 2021). This behaviour is of clear societal importance: if the GrIS and AIS disappeared entirely, they would contribute around 7 m and 57 m to global sea level rise equivalent respectively (Fretwell et al., 2013; Mouginot et al., 2019) and there is evidence that their partial demise during the Last Interglacial Period contributed 5.5-9.0 m to global sea level when mean global temperature was only 1-2°C warmer than present (Dutton and Lambeck, 2012; Sutter et al., 2016). However, to fully appreciate the impact of mass loss from ice sheets we need to consider their rate of mass loss over timescales relevant to communities and policy makers, which is not always proportional to the ice-sheet's sea level rise equivalent.

Looking specifically at the GrIS, increases in negative surface mass balance (i.e. surface melt) and dynamic losses (i.e. marine-terminating glacier calving) contribute roughly evenly to increases in annual mass loss, which significantly increased from a state of near balance in the 1980s and 1990s to a maximum of 345±66 Gt a^{-1} (errors to 1 standard

[1] now largely confirmed, Garbe et al., 2020.

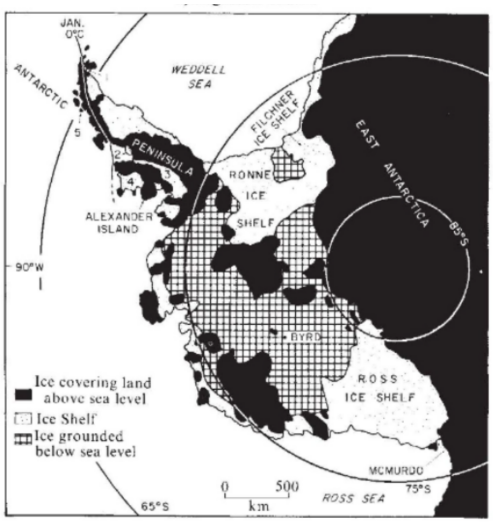

Fig. 2.1 . West Antarctica with ice shelves, and ice grounded above or below sea level demarcated. 0°C isotherm from 1962. From Mercer (1978).

deviation unless otherwise stated) in 2012 (Van Den Broeke et al., 2016; The IMBIE Team, 2019). Cumulatively, the GrIS was responsible for roughly a fifth of total sea level rise between 1992 and 2018 (10.8±0.9 mm, Fig. 2.2, Cazenave et al., 2018, The IMBIE Team, 2019). However, such bulk figures belie high inter-annual and regional variability — a consequence of high variation in the atmospheric and oceanic conditions that are the main drivers of GrIS mass balance variations[2]. For example, a cooler atmosphere and increased precipitation associated with a shift of the North Atlantic Oscillation reduced overall mass loss between 2013 and 2018 while increasing the rate of surface melt in southwest Greenland (Bevis et al., 2019), and the acceleration of just four glaciers was responsible for half of the increase in dynamic losses in the 2000s (Enderlin et al., 2014) while dynamic losses are now more evenly distributed across the GrIS's numerous marine-terminating glaciers (Mouginot et al., 2019).

In Antarctica, surface melting is limited to ice-sheet margins (Trusel et al., 2013) and ice shelves (particularly on the Antarctic Peninsula, Siegert et al., 2019, but now extending to even East Antarctica, Fricker et al., 2021) where it can negatively influence ice-shelf stability (Lai et al., 2020) but does not directly contribute to sea level rise. Instead, the vast majority of AIS contribution to sea level rise comes from mass flux over ice shelf grounding lines, with a sea level contribution of 7.6±3.9 mm between 1992 and 2017 (The IMBIE Team, 2019). Mass is then ultimately lost from the ice sheet via ice-shelf basal melting (∼55%) and ice-shelf calving (∼45%), with disproportionately large losses from smaller ice-shelves which more commonly have incursions of warm ocean water beneath them (Rignot et al., 2013). As with the GrIS, there is high inter-annual variability, though with

[2]Excepting millennial-scale binge-purge behaviour of very large paleo-ice sheets during ice ages thought to be internally forced (Alley and MacAyeal, 1994).

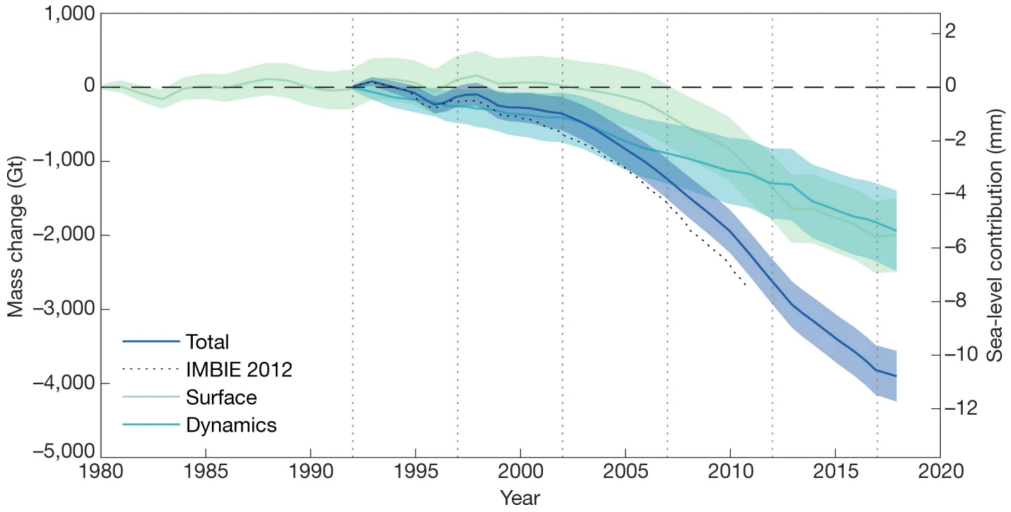

Fig. 2.2 . Mass change and sea level rise equivalent for the GrIS showing contributions from surface mass balance and dynamic losses. The change in surface mass balance is determined from three regional climate models relative to their mean over 1980-1990 and the change in dynamic loss is calculated as the difference between the change in total and surface mass (The IMBIE Team, 2019). Vertical dashed lines are 5 year periods from the beginning of the IMBIE satellite record in 1992

a notably increased spread in measurement confidence between different regions. While contiguous, the WAIS, EAIS (the AIS east of the Transantarctic Mountains), and Antarctic Peninsula show distinct variation. Mass loss from the Amundsen Sea Embayment in West Antarctica (home to Thwaites Glacier, chapter 5) increased threefold to 159 $\pm$26 Gt a^{-1} from 1992 to 2017, driven by reductions in the thickness and extent of ice shelves (The IMBIE Team, 2019), while mass loss from the entirety of East Antarctica is lower, partly a result of increased snowfall (with possible mass gain over the two decades from 1990, Shepherd et al., 2012; The IMBIE Team, 2019) with a much greater ratio of uncertainty to mass loss (Martin-Español et al., 2017). Mass loss from the Antarctic Peninsula is significant (42$\pm$5 Gt a^{-1}), with an increase in discharge brought about in large part by the collapse of large ice-shelves (Rignot et al., 2004), but was less than a third of the contribution from the WAIS in the decade preceding 2017 (Rignot et al., 2019).

2.1.2 Predictions

The studies outlined above show that the key drivers of past and present ice-sheet change can often be disentangled given sufficient high-quality observational data — even if in some instances disagreement arises (e.g. Rott et al., 2020; Tuckett et al., 2020). However, predictions into the future are generally fraught with difficultly and hard-to-quantify uncertainty. First, accurately constraining the stress resisting ice motion at the grounded base of the ice-sheet is extremely challenging (e.g. Stearns and Van Der Veen, 2018; Minchew et al., 2019; Riel et al., 2021) and complicated by a subglacial hydrology system that is

difficult to observe and likely has high spatial and temporal variation (e.g. Engelhardt et al., 1990; Vaughan and Arthern, 2007; Doyle et al., 2021), alongside high expected spatial variation in the properties of subglacial material (e.g. Harper et al., 2017). Uncertainty in the topography beneath ice sheets also plays an important (Aschwanden et al., 2016) but relatively unexplored (MacKie et al., 2021) role. Second, calving fronts and ice shelves are the locus of a multitude of complex processes that are near-impossible to incorporate into a universal calving 'law' (Benn et al., 2007) or basal-melt parameterisation, with uncertainty arising from (amongst other factors) ice damage (e.g. Berg and Bassis, 2022), the influence of subglacial plumes (e.g. Cook et al., 2021a), and atmosphere-ocean variability (e.g. Christie et al., 2018). Last, the complex non-linear rheology of ice, which is further sensitive to impurity content and anisotropic fabric development (Cuffey and Paterson, 2010), makes it challenging to focus on one ice-dynamic process in isolation, and is, in addition, difficult to constrain in and of itself. Addressing these challenges is the focus of much glaciological research, including this thesis, with the outcome hopefully enabling more accurate understanding and model-representation of ice-sheet dynamics.

In Greenland, surface mass balance and dynamic losses, both individually highly complex processes, have important nonlinear interactions. Dynamic thinning increases melting by lowering the ice-sheet surface into a warmer atmosphere, with some evidence that the western GrIS is critically close to a tipping point triggered by this feedback (Boers and Rypdal, 2021), and surface melt can influence the basal traction and hence motion of the ice sheet through a complex surface, englacial, and subglacial hydrological system (Flowers, 2018). The former interaction is relatively simple to include in ice-sheet models (though subject to much uncertainty in atmospheric warming pathways). The latter, while the subject of numerous localised modelling and regional observation studies, remains severely challenging (Chu, 2014; Goelzer et al., 2017). In addition, coupling the model to regional climate models (e.g. Robinson et al., 2012), initialising the model so that its internal thermal and age structure is consistent (e.g. Adalgeirsdóttir et al., 2014; Born and Robinson, 2021), and accurately constraining bed topography (e.g. Morlighem et al., 2017), amongst other challenges, continue to present difficulties.

Once an ice sheet model is fully assembled, predictions of mass loss still vary, dependent upon methodology, emission scenario, and global climate model projection. The *medium confidence*[3] process-based Intergovernmental Panel on Climate Change (IPCC) Sixth Assessment Report (AR6) estimate for the highest emission pathway (SSP5-8.5) for the GrIS for the end of the century encapsulates several other studies but has considerable spread and remains at the more conservative end of estimates (0.13 m central estimate, with 17$^{\text{th}}$ and 83$^{\text{rd}}$ percentile values of 0.09 and 0.18 m, Fox-Kemper et al., 2021). Aschwanden et al.

[3]See Mastrandrea et al. (2010) for a description of IPCC terminology.

(2019) and Hofer et al. (2020) for example suggest expected losses of up to 0.33 m by 2100 (Aschwanden et al., 2019; Hofer et al., 2020) with 0.5-2.5 m of mass loss modelled to be locked in by the time the GrIS reaches equilibrium under current climatic forcing (which could be centuries, Gregory et al., 2020). Structured expert judgement, where calibrated expert responses are used within a formal framework, may help categorise lower-likelihood, higher-impact outcomes (Werner et al., 2017). Bamber et al. (2019) use this to suggest that under 2°C of warming, 0.57 m of sea level rise by 2100 is within the 95th percentile of probabilities. Last, whether dynamic mass loss or surface mass balance will provide the greatest contribution to future mass loss remains an open question (Aschwanden et al., 2019; Choi et al., 2021). However, each process will still be responsible for large absolute values of mass loss over the 21st century and beyond, making both important areas for future research.

In Antarctica, concern and uncertainty regarding marine-based sections of the ice sheet (particularly West Antarctica, but also extending to East Antarctica Jones et al., 2015) continues to be generally greater than for land-based sections. This is because of two processes with unique importance for the Antarctic continent. First, marine ice sheet instability, where a reverse bed slope means that ice thickness at the grounding line increases as the glacier retreats. As ice thickness at the grounding line is an important control on ice flux over the grounding line, this can lead to rapid and unstable retreat in a positive feedback loop (Schoof, 2007; Bamber et al., 2009). Some modelling suggests marine ice sheet instability is already underway and will continue to progress at Pine Island (Favier et al., 2014) and Thwaites (Joughin et al., 2014) glaciers in West Antarctica, and projection uncertainty is amplified when marine ice sheet instability is included in ice-sheet models (Robel et al., 2019). While consideration of full 3D geometries and ice-shelf buttressing suggests the situation is not quite as severe as once considered (Pegler, 2018), marine ice-sheet instability is still cause for serious concern. Second, marine ice-cliff instability, where coastal ice cliffs greater in height than a critical threshold rapidly collapse following ice-shelf disintegration as they are no longer strong enough to sustain themselves, has been confirmed from paleo-landscape evidence for Pine Island Glacier (Wise et al., 2017). A growing body of literature suggests that marine ice-cliff instability also has a highly uncertain influence on future sea level rise predictions (Edwards et al., 2019; Crawford et al., 2021). At present, it is very difficult to incorporate marine ice-cliff instability processes into standard large-scale continuum mechanic modeling frameworks.

The distinct marine nature of large parts of Antarctica (in addition to the general modelling challenges present for the GrIS) mean mass loss predictions for the AIS are generally considered even more uncertain than predictions for the GrIS (Ritz et al., 2015; DeConto and Pollard, 2016; Le Bars et al., 2017). While the central estimate for sea level contribution

under the highest emission scenario and standard modelling procedure reported by the IPCC is similar to the GrIS (0.12 m) the spread is much larger (17^{th} and 83^{rd} percentile values of 0.03 and 0.34 m) with *low confidence* that marine ice-cliff instability will substantially shift this (0.34 m central estimate, with 17^{th} and 83^{rd} percentile values of 0.19 and 0.53 m, Fox-Kemper et al., 2021).The same structured expert judgement excercise used for the GrIS suggests a 95^{th} percentile mass loss of 1.39 m by 2100 (Bamber et al., 2019). Additionally, there is greater confidence that under 2°C of warming the WAIS is expected to largely disintegrate, along with retreat of much of the EAIS, resulting in around 2.6 m of sea level rise once equilibrium is eventually met (Garbe et al., 2020). When combined with thermosteric expansion of a warming ocean, the 'deep uncertainty' in ice-sheet processes understanding outlined here and by the most recent IPCC summary for policy makers (Masson-Delmotte et al., 2021) means a total 2 m of sea level rise by 2100, and 5 m by 2150 cannot be ruled out under a low-likelihood high-impact scenario. The global ramifications of such rapid and substantial sea level rise would clearly be catastrophic. Improving our understanding of the slow (and sometimes fast) conveyance of frozen freshwater through these systems offers a route towards reducing one aspect of this uncertainty, even if addressing the spectre of this mass loss is then a matter of global cooperation.

2.2 Ice-sheet motion and thermodynamics

2.2.1 History

'The question then occurs, is the viscosity real or apparent?' — **John Tyndall** (on glaciers, in 1857)

The earliest glaciological studies were to confirm that glaciers are, in fact, moving (rather than having boulders and debris move over them, Hugi, 1842, Clarke, 1987). Almost immediately after this had been established, disagreements regarding the nature of this motion arose, along lines that remain surprisingly contemporary. While Forbes (1842) proposed the entirely viscous flow of ice (Fig. 2.3) following early theodolite measurements, Agassiz (1840) argued instead for glacier motion almost entirely through sliding at the bed with ice deformation only occurring to account for variations in glacier-bed geometry. In a not particularly surprising turn for science in the 19^{th} century, this debate was actually quite acrimonious and drawn out — due in large part to a lack of experimental and observational measurements. Forbes and Agassiz, once close contemporaries, ceased correspondence entirely, though their disagreements were at least partly responsible for further investigation

into ice motion[4]. The first laboratory measurements of ice deformation processes were conducted by Reusch (1864) and measurements of ice velocity (and velocity variation) became increasingly common in Europe and America. In time these velocity measurements began to be used to estimate ice rheological properties and were also used to determine the emergent and submergent components of surface velocity and hence estimate the age stratification of glaciers (Reid, 1896).

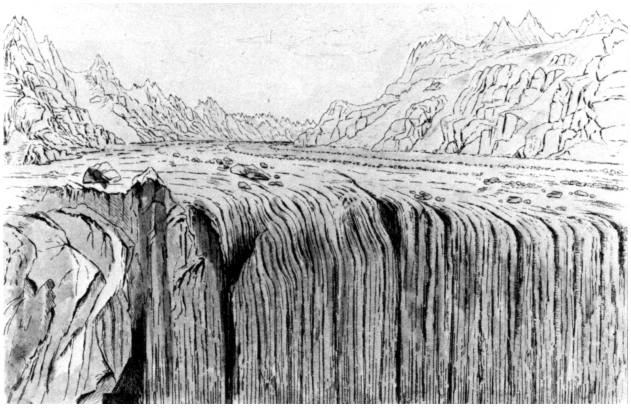

Fig. 2.3 . Illustration of glacial bands at Unteraar Glacier, Switzerland by James David Forbes (Forbes, 1842).

More involved and complex field studies began in the 20th century, encouraged by increasing public interest in polar regions and exploration. In a trans-continental endeavour, Chamberlin (1928) installed clockwork devices to measure slip in glaciers across North America and the European Alps, recording distinct slippages and concluding that viscous liquid flow should therefore be eliminated from understanding of glacier motion. This was followed in the 1930s by theories suggesting glacier velocity actually increased with depth, i.e. extrusion flow, with both theories in clear contradiction of our present understanding of how glaciers move (Clarke, 1987). After two decades, this continued disagreement motivated the first direct borehole observations of glacier deformation (Perutz, 1950; Gerrard et al., 1952) providing us with the now classic view of ice deformation rates having a sweeping and monotonic increase towards the bed (Fig. 2.4). Still, in a microcosm of modern glaciology, mathematical modelling helped close the debate, showing that if extrusion flow were occurring in the GrIS, the flow velocity would exceed one-quarter of the speed of light within 100 years (Nye, 1952a).

The central methodologies of modern glaciology — fieldwork, laboratory testing, and numerical modelling — are well represented in the above debate and bring us to perhaps the most influential series of glaciological developments that can still be contained within a 'history' section. In a short paper, Glen (1952) compressed a small block of polycrystaline ice at -1.5°C to show convincingly that in the equation

[4]Depending on your reading of deterministic history.

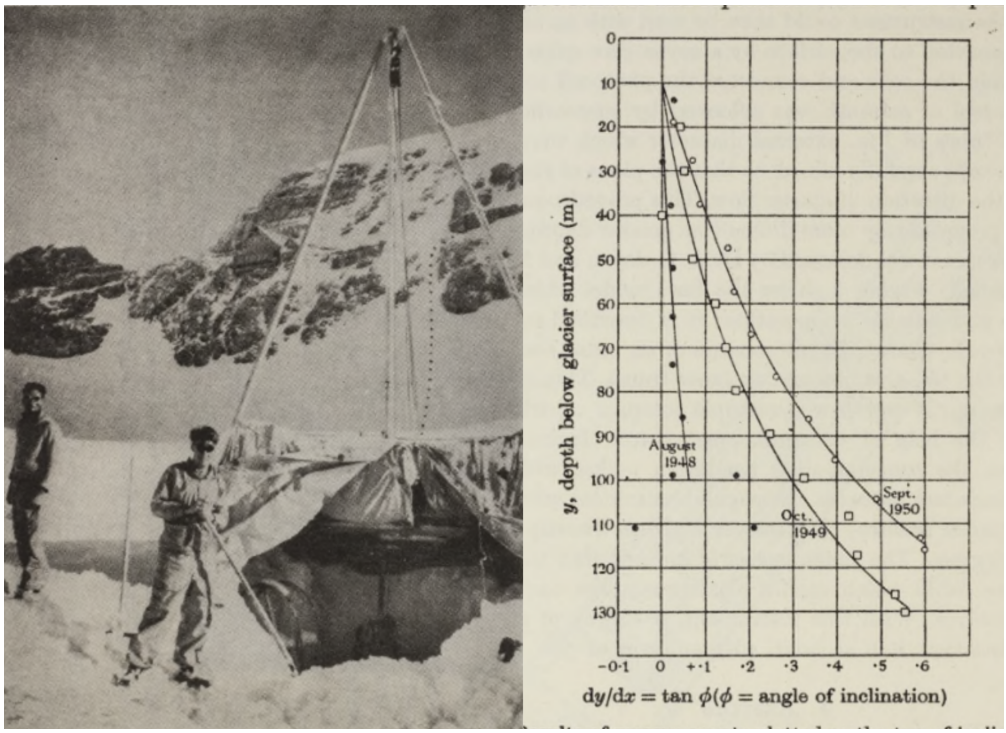

Fig. 2.4 . Left. Boring instrumentation from Gerrard et al. (1952) close to Jungfraujoch Hotel and Research Station. The dotted line marks the gully through which the cable was laid. Right. Results of borehole measurements plotted as the tan of inclination against depth (Gerrard et al., 1952).

$$\dot{\epsilon} = \varphi \sigma^n \tag{2.1}$$

where $\dot{\epsilon}$ is compressive strain rate (a^{-1}), φ is a material constant, and σ is compressive stress (bars), n does not equal 1 (and is equal to around 3). In other words, that ice is not a linear-viscous fluid. This has significant implications, as the non-linear aspect of ice flow brings about considerable complications in analytical and numerical modelling. The mathematical implications of Glen's experiments were then explored by Nye (1952b) and advanced in Nye (1953) to bring together Glen's laboratory experiments with the borehole data of Gerrard et al. (1952). This resulted in a so-called flow 'law'[5] in full 3D tensorial glory (eq. 3.6), extended to the variable temperature-dependent rheology of ice in Glen (1955). This relationship is still the clear default for calculating ice deformation in contemporary glaciology.

[5]Despite its frequent usage in the literature, I avoid the term 'law' in favour of 'relationship' or similar, in appreciation of the messy and imprecise nature of environmental science, leaving 'laws' to more foundational features of our universe.

2.2.2 Temperate ice

Temperate ice is a crucial component of much of the research presented in this thesis. Physically, temperate ice has a specific enthalpy, H (J kg^{-1}), that is equal to or in excess of the estimated phase change enthalpy of ice, $H_s(p) = c_i(T_m(p) - T_0)$, where c_i is a constant heat capacity (J kg^{-1} K^{-1}) and T_0 is a reference temperature usually chosen as well below modelled/observed temperatures so that H_s remains positive (Aschwanden et al., 2012). $T_m(p)$ is the pressure-dependent melting point, typically calculated as $T_m = T_{tr} - \gamma(p_i - p_{tr})$ where T_{tr} is the triple point temperature, γ is the Clausius-Clapeyron constant, p_i is the ice overburden (hydrostatic) pressure, and p_{tr} is the triple point pressure. The precise definition is more complex — the above formulation assumes c_i and υ remain constant in time and space when υ at least is known to vary enough to change T_m by >0.1°C at 1 km depth (Lliboutry, 1971; Harrison, 1972; Doyle et al., 2018) and variation in solute concentration may alter the melting point at small (<1 m) scales (Lliboutry, 1976). Additionally, the above definition means that ice can technically have a water content of 0% and still be considered temperate in the very narrow case that $H = H_s$, though the more broadly adopted definition that temperate ice has some percentage of liquid water co-existing with the solid phase is not materially different (e.g. Adams et al., 2021).

There are several different configurations of temperate ice in glaciers. The glacier may be wholly temperate, as is the case for many valley glaciers (e.g. Fountain and Walder, 1998) and all of Iceland's glaciers and ice caps (Björnsson and Pálsson, 2020). Alternatively, in a polythermal glacier, temperate and cold ice are both present, with two common structures (Fig. 2.5). In a Scandinavian type, water percolation within firn and transfer and storage of latent heat means most ice is temperate when formed, with a zone of cold bare ice in the ablation zone where latent heat is not stored within firn throughout winter. In a Canadian type, the majority of the glacier is cold and strain heating results in a temperate layer developing near the bed, some distance downflow from the valley head or ice divide. These definitions were developed for glaciers and ice caps, but the idea can be extended to ice sheets. There is abundant observational evidence from borehole records (e.g. Ryser et al., 2014b; Harrington et al., 2015; Doyle et al., 2018) and iceberg composition (Lüthi et al., 2003) that the GrIS has a Canadian type structure, while at present all evidence for the Canadian structure of the AIS is based on models, rather than observations (Meyer and Minchew, 2018; Haseloff et al., 2019), though there is clear evidence for pervasive thawed-bed conditions in Antarctica (Llubes et al., 2006; Joughin et al., 2009). In Greenland, the temperate layer is *typically* (see chapter 4 for a thorough discussion) thought to drape uniformly across the ice sheet bed and increase in thickness slowly towards the margin. In Antarctica, existing theories posit that isolated temperate zones exist towards the base of ice-stream shear margins (e.g. Haseloff et al., 2019). Note that this classification framework

neglects the surface-bed hydrological connections across the margins of the GrIS which must locally be at least at the pressure-dependent melting point, though enveloped by cold ice, and the existence of ponded meltwater atop the GrIS margins and some AIS ice shelves.

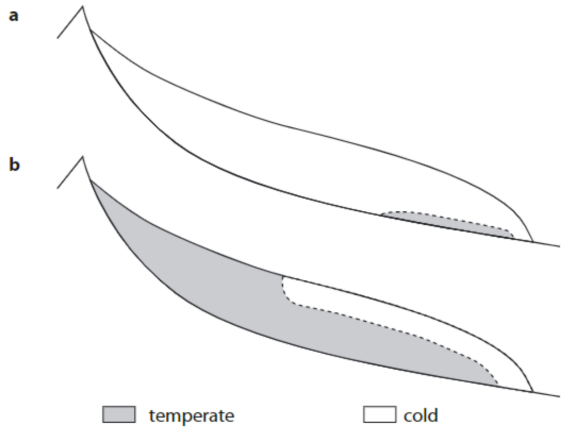

Fig. 2.5 . Schematic view of (a) Canadian type and (b) Scandinavian type polythermal glaciers. The dashed line is the cold-temperate transition surface. From Aschwanden et al. (2012).

Temperate ice is much softer than cold ice. Limited experimental evidence suggests that strain rates in ice increase 5 to 10 times as the melting point is approached (Morgan, 1991) and a further 5 to 8 times as water content increases up to to 0.8% (Duval, 1977; Krabbendam, 2016). Adams et al. (2021) separately suggests effective viscosity is independent of water content beyond 0.6% water content, at least for secondary creep. Additionally, field and laboratory experiments, including analysis of bulk stress and strain rates from the fully temperate Glacier de Tsanfleuron, Switzerland suggests that n in Eq. 2.1 is probably closer to 1 (Marshall et al., 2002; Colbeck and Evans, 1973; Chandler et al., 2008; Adams et al., 2021), which would mean that temperate ice is actually better represented as a linear-viscous Newtonian fluid[6]. The consensus view of the influence temperate ice has on the rate factor, A, in Glen's flow relationship (Duval, 1977; Cuffey and Paterson, 2010), as utilized in most modelling studies, is shown in Fig. 4.3A with an upper limit applied at a water content of 0.6%.

The distinct rheological behavior of temperate ice is a result of water along grain boundaries influencing a range of deformation mechanisms. First, in diffusion creep, where crystallographic vacancies (missing atoms, essentially) diffuse through a crystal lattice, a liquid phase can markedly increase the efficiency of a given diffusion pathway (Goldsby and Kohlstedt, 2001). Second, water along grain boundaries also decreases the surface area of grain-to-grain contacts thereby increasing grain-to-grain contact stresses and enhancing dislocation creep, where dislocations (irregularities in the crystal structure)

[6]Whether this can account for early disagreements on the rheology of ice is not clear.

move through a crystal lattice (Duval, 1977). Third, dynamic recrystallisation and grain growth is much faster in temperate ice and tends to form crystals with a more favourable orientation for dislocation creep (Duval et al., 1983). Fourth, grain boundary melting, where highly stressed grain boundaries melt and transport water to lesser stressed grain boundaries where it refreezes, probably also increases strain rates in temperate ice (Wilson, 1986). In addition to the above references, see Cuffey and Paterson (2010) and, in particular, Krabbendam (2016) for further information on these processes. Last, the anistropy and anistropic evolution of temperate ice is unclear, but is thought to be slightly lower than for cold ice under similar conditions (Llorens et al., 2020). The individual importance of these processes and their interrelations, remains unclear, though for the glacier modelling applications discussed in this thesis it is the bulk continuum-scale ($\gtrsim$10 cm) behaviour that is important, with micro-scale processes necessarily omitted.

The nature of water movement within temperate ice also remains contentious and poorly constrained. This water movement is important as it directly influences rheology by controlling the distribution of water (and hence the rate factor), alongside production of water in-situ by strain-heating and local variation in the phase change enthalpy. Measured water contents in temperate glacier ice are typically low. Ice cores from two temperate French Alpine glaciers indicated water contents generally not in excess of 3%, with an average value of 0.7% (Vallon et al., 1976; Lliboutry and Duval, 1985) and in situ measurements of the temperate Engabreen in Norway gave water values of around 1% and not more than 2.5% (Cohen, 1998). Radar and seismic studies of valley glaciers give similar values (Pettersson et al., 2004). As models of temperate ice (including the one in chapter 4 if no upper limit is enforced) can produce much higher water content percentages (8% in Haseloff et al., 2019) this strongly suggests the permeability of temperate ice is linked non-linearly to its water content — reducing or eliminating the occurrence of high values of water content observed in the field. Under assumptions of Darcian flow, Fowler and Iverson (2022) obtain permeability in the range 10^{-12} to 10^{-15} m^{-2} using a laboratory permeater. Schoof and Hewitt (2016) and (Hewitt and Schoof, 2017) use the permeability at the upper end of this range but develop a model where water flux is further dependent on water content and the compacting pressure of the ice (i.e. not strictly Darcian flow). However, further complexity is likely present in nature, with the existence of air bubbles in some veins, dust (Lliboutry, 1971), and the possibility of bulk water transport in larger fracturing events (Harper et al., 2010; Harrington et al., 2015; Zhang et al., 2022), making a water-transport relationship that can be applied across a wide range of settings with appropriate properties a long-term research goal, rather than a reality at present.

Another important aspect of temperate ice in polythermal settings is its transition to cold ice (the cold-temperate transition surface, or CTS), described here with specific reference to

Scandinavian type polythermal glaciers. Originally, this was treated in numerical/analytical applications using a jump condition that treats the cold and temperate section of the glacier as individual bodies and determines the position of the boundary that separates them (Greve, 1997). However, more recent models (including those in this thesis) tend to use an enthalpy approach, where the CTS is a level set of the specific enthalpy variable — meaning the surface is not explicitly represented and that there are no a priori restrictions on the CTS shape (Aschwanden et al., 2012). An enthalpy approach further means that the temperature and the water content of ice can be treated using one variable (specific enthalpy, J kg^{-1}), rather than a more complicated separation of the two. Processes responsible for the formation and erosion of the temperate layer, and for the spatial variation of the CTS are covered in detail in the discussions of chapters 4 and 5 but are briefly restated here. From a Eulerian reference frame, deformation heating above the CTS will eventually result in temperate ice (and hence upwards movement of the CTS) if it exceeds negative conductive and advective heat fluxes. Deformation heating below the CTS will not form new temperate ice, but will instead contribute to the melting of ice that is already temperate and possibly its eventual removal dependent upon the drainage scheme. Transfer of latent heat as water across the CTS through ice-grain interfaces or basal crevassing to form new temperate ice has also been proposed (Harrington et al., 2015; Krabbendam, 2016). Any basal heat source (such as frictional and geothermal heat) will lead to basal melting and will reduce the overall thickness of a basal temperate layer.

Models of polythermal glaciers, in particular those featuring thermomechanical coupling, are relatively limited. Aschwanden et al. (2012) apply the enthalpy formulation they develop to the Parallel Ice Sheet Model across the whole of the GrIS, finding that the enthalpy formulation reduces the basal temperate layer thickness as the now softer (dependent on water content) temperate ice focuses deformation heat below the CTS. Gilbert et al. (2014) use this formulation to develop an enthalpy solver for Elmer/Ice finite element modelling software, which is used in chapters 4 and 5. Their model is applied to Col du Dôme Glacier, France, where the implemented strain heating, surface meltwater percolation in firn, and refreezing help reproduce borehole temperature measurements (Gilbert et al., 2014) and to Rikha Samba Glacier, Nepal, where water percolation through crevasses helps to explain radar observations of temperate ice (Gilbert et al., 2020). Usage of specific enthalpy as the state variable is becoming more widespread (e.g. MacGregor et al., 2016; Aschwanden et al., 2019) but is still not pervasive, with most models in the most recent ice sheet model inter-comparison project (ISMIP6) using temperature as the state variable, often without thermomechanical coupling (Goelzer et al., 2018; Seroussi et al., 2020).

Looking at smaller scales, process based studies indicate the importance of temperate ice on AIS ice stream shear margin evolution and strength (Suckale et al., 2014; Meyer et al., 2018; Minchew et al., 2018; Haseloff et al., 2019; Hunter et al., 2021). Here, softer temperate ice accommodates greater deformation (generating water and reducing ice viscosity in a positive feedback limited by conductive and advective heat losses and water drainage) and also provides an important source of water to the subglacial hydrological system. In contrast to growing interest in Antarctica, studies on temperate ice in Greenland are extremely limited. Lüthi et al. (2002) and Harrington et al. (2015) construct separate 2D flow line models of temperate ice development for land- and marine-terminating settings respectively. Lüthi et al. (2002) obtain reasonable agreement between modeled and observed temperate layer thickness, although the borehole they drill into the ∼2.5 km deep central trough of Sermeq Kujalleq in Kangia (often called Jakobshavn Isbræ in the literature) does not reach the temperate layer (which they expect to be over 300 m thick), leaving considerable measurement-side uncertainty. Harrington et al. (2015) simulate a notably thinner temperate layer in their model than they observe in boreholes spaced along a 34 km transect of Isunnguata Sermia. They suggest the larger temperate layer thickness they observe can be accounted for by basal crevassing and water transport which is omitted in their numerical model. Consideration of pervasive water-filled surface crevasses (e.g. Chudley et al., 2021; Hubbard et al., 2021) in the GrIS ablation zone *not* producing large thicknesses of surface-adjacent temperate ice probably suggests the basal-crevassing hypothesis can not fully account for the mismatch between models and observations. Zhang et al. (2022) provide an initial 2D exploration of heat transfer from basal hydrofracture, but do not incorporate temperate ice. All of these studies use smoothly-varying basal topography, which may reduce deformation heating above the CTS — the full implications of which are comprehensively explored in chapter 4. Last, while not numerical, Krabbendam (2016) provide an excellent conceptual framework of temperate ice processes in Greenland (alongside a review) and use this to argue for the importance of temperate ice in facilitating ice streaming motion over hard bedrock in northeast Greenland. Alongside observations from chapter 3, Krabbendam (2016) provided the initial impetus to expand upon the 2D models of Lüthi et al. (2002) and Harrington et al. (2015) and investigate a wider range of processes responsible for temperate layer evolution.

2.2.3 Observations: boreholes

Satellite and airborne measurements of ice sheet surface phenomena have improved significantly over the last few decades. The geometry, evolution, and water content of individual crevasses can be tracked across the entire GrIS (Chudley et al., 2021), AIS ice shelf thickness can be monitored over decades (Paolo et al., 2015), and high-resolution velocity maps are

available at weekly or even daily intervals (Kääb et al., 2016). In the near future it may even be possible to use airborne radar to gather englacial temperature profiles at coarse resolution (Schroeder et al., 2016). Surface geophysics can further be used to give an indication of subglacial properties (e.g. Hofstede et al., 2018; Muto et al., 2019a; Young et al., 2022), vertical ice strain rates (Young et al., 2019), ice fabric (Young et al., 2021), and the vertical extent of subglacial aquifers (Gustafson et al., 2022) amongst many other applications. The information obtained from these studies is crucial in glaciological methodologies ranging from calibrating machine-learning surface melt models (Hu et al., 2021) to estimating n in ice-shelf settings (Millstein et al., 2022). Nonetheless, direct borehole studies still provide the least ambiguous recordings of ice properties and remain the only way to directly obtain the partitioning of surface velocity into internal deformation and basal slip. Such information is crucial in assessing the realism of theories of ice motion. Disagreements will continue regarding the relative importance of (a) scale and (b) accuracy and precision, which are common (but not universal) trade offs in glaciological observations. However, the extremely high utility of information from borehole studies, even if sparsely located, means they have a legacy of continuously advancing and refining our understanding of ice sheet thermodynamics.

Ice-sheet borehole studies can be divided into (1) those primarily concerned with ice cores as paleoclimate records, which are typically located at very slow flowing ice divides (e.g. Dahl-Jensen et al., 1998; Wolff et al., 2010), (2) those that study the thermal structure and melt rates of AIS ice shelves (e.g. Engelhardt and Determann, 1987; Tyler et al., 2013), and (3) those seeking to understand ice motion – which are typically located towards ice sheet margins. Only ice-sheet marginal boreholes are covered here in great detail, with studies from the GrIS presented in Table 2.1 for easy comparison. Studies relevant to Thwaites Glacier are covered separately in chapter 5. Ice-sheet marginal boreholes are drilled using hot water pumped through an insulated hose at a rate of about 50 l min^{-1}, proceeding vertically downwards at a rate of about 1-2 m min^{-1} meaning a 1000 m borehole takes in the region of 24 hours to drill. In cold ice, a window of a few hours is then available for instrument installation, though it is encouraged that this is done as quickly as possible. Early boreholes were often drilled with a hose over a shoulder, but setups used in ice-sheet settings today are more advanced, featuring drill towers and motorised spools (e.g. Doyle et al., 2018).

Location	Measurement(s)	Characteristics	Modelling	Date	Reference
Sermeq Kujalleq [Store Glacier] S30 (70.52°N, 49.92°W). Boreholes drilled within 75 m of one another.	Deformation, temperature, and subglacial water pressure.	**Marine terminating**. ~600 m ice thickness, 4-7 km a-1 surface velocity. Basal slip ratio of 0.63-0.71, temperate layer thickness up to 8 m. Variable deformation above bed.	No.	2014	Doyle et al., 2018
Sermeq Kujalleq [Store Glacier] R29 (70.56°N, 50.01°W).	Temperature.	**Marine terminating**. ~950 m ice thickness, 700 m a-1 surface velocity. Warmer near-surface (<200 m depth) temperature than produced in model. ~15 m temperate zone.	Yes. Large scale model output to show mismatch between modelled and observed temperature related to water freezing in crevasses.	2018	Hubbard et al., 2021
Sermeq Kujalleq in Kangia [Jakobshavn Isbræ] A, B, C (69.17-69.20°N, 48.76-48.77°W, ice stream sites), and D (69.24°N, 48.69°W, ~2 km north of ice stream).	Deformation, temperature, conductivity, and subglacial water pressure.	**Marine terminating**. Variable ice thickness, ~600 m a-1 surface velocity at site D (ice sheet) up to ~1 km a-1 at ice stream centre drill sites and ~7 km a-1 at glacier terminus. Only sites A and D reach the bed, though the centerline (E, B) is extremely deep (2.5 km). Basal slip ratio calculated as 0.57-0.63 at site D and expected to be <0.6 at site E. 31 m temperate layer at site D, expected to be >300 m at sites E and B. Basal slip. Variable deformation in glacial-phase and temperate ice.	Yes in parts II and III. 2D flowline model over very smooth bed topography. Convergent flow not captured by 2D approach but determined to be important for estimated temperate layer thickness variation.	1989 and 1995	Iken et al., 1993; Luthi et al., 2002; Funk et al., 1994
FOXX (69.45°N, 49.89°W) and GULL (69.45°N, 49.72°W) sites 30 km and 20 km down a flowline from Swiss Camp respecitvely, both sites are **~30 km north of Sermeq Kujalleq in Kangia** [Jakobshavn Isbræ].	Deformation, temperature, conductivity, and subglacial water pressure.	**Land terminating**. ~600 (FOXX) and 700 m (GULL) ice thickness, ~100 m a-1 surface velocity. Basal slip ratios of 0.73 (FOXX) and 0.44 (GULL), increasing up to 0.9 in summer. Temperate layer thickness decreases down flow from ~40 to ~20 m. Variable deformation in glacial-phase and temperate ice. Sites on topographic highs.	Yes. 2D with free surface and periodic boundary conditions and no thermomechanical coupling. Flat bed and time varying basal traction to relate stress transfer and basal water pressure with surface velocity and deformation measurements.	2012	Ryser et al., 2014a, b
Isunnguata Sermia at 5 sites (S1-S5) along a flowline extending to glacier margin beginning at S5 (67.20°N, 49.29°W).	Temperature.	**Land terminating**. ~100 m a-1 surface velocity. Temperate ice layer increases from 20 m at S5 to fully temperate at S1, 300 m from the margin though with some variation in temperate layer thickness relative to total ice thickness. Sites mostly on topographic highs.	Yes. 2D flowline model with smooth bed topography that does not reproduce the large observed temperate layer thickness. Harrington et al. ascribe this to difference to basal crevassing.	2010-2012	Harrington et al., 2015
Isunnguata Sermia at site here called IS2015 (67.18°N, 49.57°W). 9 boreholes drilled within 500 m of one another.	Deformation, temperature, and subglacial water pressure.	**Land terminating**. ~640 m ice thickness, ~100 m a-1 surface velocity. Basal slip ratio of 0.003 to 0.094, thin to absent temperate layer. Located on a topographic high.	Yes. 2D with free surface and periodic boundary conditions and no thermomechanical coupling. Low amplitude (~5 m) sinusoidal bedrock perturbations used to reproduce deformation observations.	2014 and 2015	Wright et al., 2016; Hills et al., 2017; Maier et al., 2019, 2021
Kangerluarsuup Sermia [Bowdoin Glacier] 3 boreholes within 200 m of one another ~3 km from glacier calving front (77.68°N, 68.56°W).	Temperature.	**Marine Terminating**. ~180 m ice thickness, ~400 m a-1 surface velocity. Temperate layer thin to absent.	Yes. Simple analytical equations to determine strain contribution to heating.	2014-2017	Seguinot et al., 2020

Table 2.1 . Key GrIS margin borehole studies.

The typical borehole temperature profile ∼40 km inland from the GrIS margin is concave, with the coldest temperatures (down to below -20°C) found towards the middle of the ice column. This is the shape apparent in many of the temperature profiles detailed in Table 2.1 (Lüthi et al., 2002; Ryser et al., 2014b; Harrington et al., 2015; Doyle et al., 2018; Hubbard et al., 2021) with the concave shape more accentuated in marine-terminating glaciers. Borehole records closer to (thinner) marine and land margins are warmer overall, loosing the definition of the central cold section and typically have a greater proportion of temperate ice, with cold ice warming gradually and monotonically towards the glacier bed (Harrington et al., 2015; Seguinot et al., 2020). Temperature profiles from ice-divide sites inland also increase monotonically towards the ice-sheet bed, though surface temperatures may be as low as -30°C (Dahl-Jensen et al., 1998). A comprehensive review of GrIS borehole temperature records is provided by Løkkegaard et al. (2022, *in review*).

Thermodynamic description of borehole temperature profile evolution

The development in temperature profiles outlined above can be well approximated in a 2D flowline model (Dahl-Jensen, 1989). Geothermal heat flux and strain heating increase the temperature of basal ice until the pressure melting point is reached (which occurs up flow of all of the studies in Table 2.1). Horizontal advection brings cold ice from the centre of the ice sheet to the margins forming the cold centre of the profile, while strain heating heavily concentrated towards the lower section of the ice column warms basal ice, explaining the more accentuated temperature profile in marine-terminating settings, where the advective component is greater. Reduced ice thickness (and hence diffusion timescale) and high surface and basal energy inputs eventually warm the profile to the point where the cold central section is no longer apparent. Given sufficient strain heating and latent heat input towards the base, a temperate ice layer may develop. Deviations away from this standard model indicate greater complexity not captured under the simple assumptions of Dahl-Jensen (1989), and can reveal important information about ice-sheet thermodynamic processes. Chapter 3 provides a new high-resolution temperature profile and discusses these processes in depth.

Basal velocity ratio variation

While the temperature profile evolution of the GrIS is not especially problematic to explain (with a few exceptions, e.g. Doyle et al., 2018), borehole studies from the GrIS (Table 2.1) indicate a high degree of complexity in ice sheet motion which is more difficult to thoroughly account for. Basal velocity ratios for land-terminating glaciers vary from a

low of 0.44 (GULL site on the Swiss Camp flowline during winter) to a high of 0.997 (site from Maier et al., 2019, hereafter IS2015). There are fewer observations from marine-terminating sites but these show a spread of below 0.6 at Sermeq Kujalleq in Kangia (without a defined lower limit, Lüthi et al., 2002, also known as Jakobshavn Isbræ) to 0.71 at Sermeq Kujalleq (Doyle et al., 2018). Given the available evidence, speculating about basal velocity ratios elsewhere would suggest high variability, though a paucity of data makes quantitative assessments difficult. Part of this variability may be controlled by local variation in basal conditions (topographic and basal traction), or by catchment-scale force balance considerations. For example, the highest basal velocity ratios (at IS2015) are found on a topographic rise (Maier et al., 2019), whilst the lowest ratios (at GULL) are in a local topographic depression (Ryser et al., 2014b). The lower basal velocity ratio at a marine-terminating site (based on a partial-depth profile) is also located within a deep topographic channel (Lüthi et al., 2002). Further observations are required to properly comment on catchment-scale factors. Numerical modeling in chapter 4 examines some of these points in more detail.

Pre-Holocene ice

Pre-Holocene ice[7], occupying roughly the lowermost 15% of the ice column, is a further ubiquitous feature of GrIS borehole observations (e.g. Lüthi et al., 2002; Ryser et al., 2014b) and is is also well recorded across the GrIS from radar data (Karlsson et al., 2013; Macgregor et al., 2015). This ice is substantially softer than Holocene ice, with strain rates that may be 2.5 times higher than interglacial-phase ice under simple shear in laboratory experiments (Paterson, 1991). While in temperate ice softening results from liquid water influencing grain-scale deformation processes, in glacial-phase ice softening is a result of wind-blown impurities from a drier, dustier, ice-age. These impurities impede grain-boundary migration and grain growth thereby preventing large interlocking ice grains, while also enhancing the development of a strong single-maximum ice fabric (Paterson, 1991). This results in pre-Holocene ice being even more anisotropic than Holocene ice where impurity content is much lower, and leads multiple studies to conclude that an anisotropic flow relationship is required to fully describe the behaviour of pre-Holocene ice (Budd and Jacka, 1989; Paterson, 1991; Wang and Warner, 1999; Gagliardini et al., 2009). High variability in vertically-oriented deformation rates within pre-Holocene ice is also a common feature of borehole records (Lüthi et al., 2002; Ryser et al., 2014b) and is further expected based on grain-scale measurements (Kuiper et al., 2020b; Kuiper et al., 2020a). Further, the transition between pre-Holocene and Holocene ice (the Last Glacial-

[7]Often called Wisconsin ice in ice-dynamic borehole literature after the most recent North American glaciation.

Interglacial Transition) may be a high-strain interface with discrete slip events (Lüthi et al., 2003). It is possible that high deformation rates keep grain size small here (e.g. Kuiper et al., 2020a), weakening the pre-Holocene ice at the Last Glacial-Interglacial Transition more than ice within the body of the pre-Holocene ice and perpetuating the fluttering deformation behaviour observed by Lüthi et al. (2003) where the orientation of tilt sensors inferred to be close to the Last Glacial-Interglacial Transition changes rapidly within an hour. Last, as most observations of temperate ice are from below 85% of ice thickness, most temperate ice across the GrIS is also pre-Holocene ice. To my knowledge, there are no physically based studies investigating physical processes in such ice, which has both a high impurity content and a melt fraction. Gilbert et al. (2016) do however implement pre-Holocene ice rheology in an Elmer/Ice model to study the stability and characteristics of the Barnes Ice Cap, Baffin Island, Canada. As temperate pre-Holocene ice may carry a large percentage of overall internal ice deformation it is an important subject for future research. See chapter 3 for further measurements and discussion of temperate ice.

Temperate ice

Last, the flowline profiles from Harrington et al. (2015), Wright et al. (2016), and Hills et al. (2017) suggest the thickness of the basal temperate layer (in absolute terms and relative to the total ice thickness) increases gradually towards the margin with the trend of this observation, but not the magnitude, supported by 2D flowline modelling over a smooth bed (outlined in section 2.2.2). However, profiles only 1 km south this flowline suggest a very thin or absent temperate layer (Maier et al., 2019). Additionally, Ryser et al. (2014b) record a relative temperate layer thickness decrease between GULL and FOXX sites and Seguinot et al. (2020) do not observe a temperate basal layer under their measurement resolution at all, despite the sites' proximity to the marine terminus of Kangerluarsuup Sermia, north Greenland. This heterogeneity indicates hitherto unappreciated processes are influencing the distribution of temperate layer thickness across the GrIS. Observations in chapter 3 and modelling in chapter 4 further addresses these issues.

2.2.4 Observations: glacier bed

Geophysical studies of the glacier bed help to constrain the position and nature of this crucial model input. In very isolated regions, intensive geophysical studies give an indication of subglacial properties such as properties and continuity of the subglacial till or crystalline bedrock (e.g. Kulessa et al., 2017; Hofstede et al., 2018; Muto et al., 2019a; Booth et al., 2020) and even till porosity (Blankenship et al., 1986). Direct borehole access

can enable extraction of subglacial sediment (Tulaczyk et al., 2000). These studies are important for providing a detailed view of ice-bed processes at a local scale, which can in turn inform our view of how ice sheets work in totality. However, full ice-sheet models used in sea-level-rise predictions require products across the entire bed, which are presently only available for bed topography (Fretwell et al., 2013; Morlighem et al., 2017). These are obtained through a variety of interpolation and mass conservation techniques using sparse ice-thickness radar data, gravity modelling, and some limited seismic data sets. In fast-moving areas, a mass-conservation approach (Morlighem et al., 2011) removes the mass-flux divergence caused by earlier kriging interpolation approaches (e.g. Seroussi et al., 2011). However, an unavoidable result of this methodology is that the produced bed topography is much smoother than high-resolution topography of deglaciated areas, with a continued mismatch between the bed topography product and the flight lines used to produce it (MacKie et al., 2021). This is generally noted, but difficult to act upon — whole ice-sheet models would not be able to run at resolutions much higher than presently available BedMachine (Greenland) or BedMap (Antarctica) topography.

Uncertainty in bed topography is of significant importance in ice-sheet modelling because bed topography is clearly demonstrated to exert a major control on glacier flow at larger scales (Aschwanden et al., 2016), though its importance at smaller scales is still relatively under-explored. There are three possible ways to circumvent this problem and investigate the smaller-scale influence of bed topography on ice motion: (1) use geostatistical methods to generate realistic bed topography that conforms to sparse radar measurements and reproduces the roughness along radar lines where broader bed topography measurements are not available (MacKie and Schroeder, 2020), (2) use high-resolution bed topography data from ice sheets for a limited area (presently only available for the AIS, Smith et al., 2007; King et al., 2009; Bingham et al., 2017; Holschuh et al., 2020) and, (3) use widely available surface topography from deglaciated terrains, though subsequent sedimentary processes may have filled in overdeepenings (Krabbendam and Bradwell, 2014). This smaller-scale understanding can then help inform paramaterisations useful at larger scales. Chapter 4 takes approach (1) where high-resolution bed topography data is not available and chapter 5 takes approach (2). Approach (3) is an interesting avenue for further research.

2.2.5 Constitutive relationships for ice deformation and basal traction

Despite the complexity of underlying processes and an enormous breadth and depth of studies, (differences in) constitutive relationships for basal traction and ice deformation

can be represented in a handful of line graphs (Figs. 2.6, 4.3A). This variation and disagreement is important — the selection of the form of the relationship, and of its parameters, significantly influences the output of predictive ice-sheet models (Gillet-Chaulet et al., 2012; Parizek et al., 2013; Bons et al., 2018; Kyrke-Smith et al., 2018; Brondex et al., 2019).

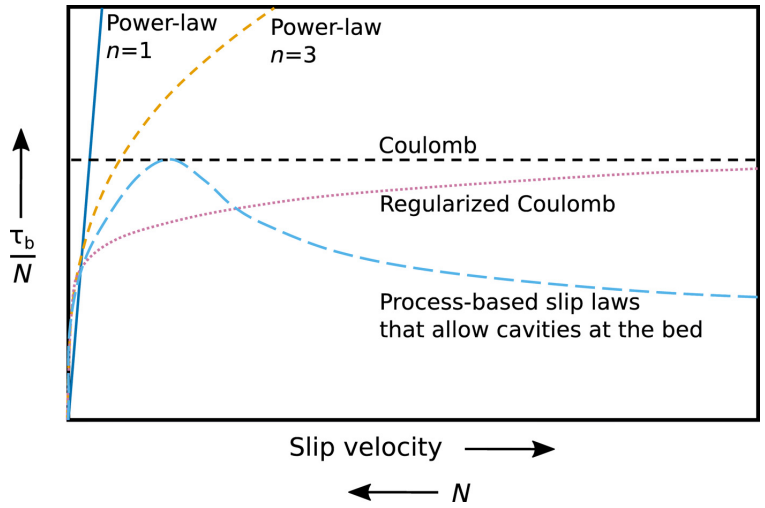

Fig. 2.6 . Basal traction relationships from Helanow et al. (2021) where N here is effective pressure (N_e in the text).

The representation of ice deformation in ice-sheet models is more uniform than the representation of basal traction, with only limited suggestions that the form of Glen's flow relationship (Eq. 2.1) is inappropriate (e.g. Goldsby and Kohlstedt, 2001; Graham et al., 2018). Further, Glen's flow relationship is typically used with a standard set of parameters (Cuffey and Paterson, 2010) in inversions for basal-traction parameters, rather than vice versa (though some recent work does begin to asses the importance of rheological uncertainty in basal-traction inversions, Babaniyi et al., 2021). Nonetheless, the values of n and φ in Eq. 2.1 are repeatedly questioned. n values ranging from one to five are obtained from observations of ice flow (Hutter, 1983; Cuffey and Kavanaugh, 2011; Gillet-Chaulet et al., 2011; Millstein et al., 2022) and, given the complex mechanisms behind ice deformation, it is likely that n has different values in different settings. These differences have important influence on modeled patterns of ice motion and ice-sheet thermodynamics. Bons et al. (2018) suggest an n value of 4 (rather than 3) is appropriate for the northern GrIS where driving stress exceeds 0.04 MPa, which leads to a substantial shift in the area of the ice sheet bed that is expected to be thawed — from ~50% to ~10%. Separately, Zeitz et al. (2020) use an idealized 1D geometry to suggest that varying flow parameters (n directly and φ indirectly) within a range constrained by observations can result in a doubling of dynamic mass loss within a century of a realistic warming perturbation. Pre-Holocene ice rheology will also influence φ and possibly n (e.g. Thorsteinsson et al., 1999; Lüthi et al., 2002) but is currently not incorporated into ice-sheet models.

Turning to basal traction, regardless of the processes hypothesised, modelled, or observed, there are four main forms proposed theoretically and used in models (Fig. 2.6). First, Weertman, Weertman-type, or power law of the form

$$\tau_b = \left(\frac{u_b}{\beta}\right)^{\frac{1}{q}} \tag{2.2}$$

where τ_b is basal traction, q is a positive constant, β is a spatially varying parameter, and u_b is the velocity magnitude at the ice base. Here, basal traction continues to increase unbounded as basal velocity increases. Second, rate-weakening Coulomb of the form

$$\tau_b = \frac{C_S u_b^m}{\left(1 + \frac{C_S}{C_{max} N_e}^{\frac{1}{m}} u_b\right)^m} \tag{2.3}$$

(Gagliardini et al., 2007) where C_S is a friction parameter, N_e is effective pressure, and C_{max} is a positive value set by the maximum value of τ_b / N_e and bounded by the local maximum bed-slope (Iken's bound, Gagliardini et al., 2007, Brondex et al., 2017, and discussion below for further information). Here, basal-traction reaches a maximum before decreasing with increasing velocity (i.e. rate-weakening behaviour). Third, regularised-Coulomb sliding of the form

$$\tau_b = C N_e \left(\frac{u_b^{-n+1}}{u_b + A_s C^n N_e^n}\right)^{\frac{1}{n}} u_b \tag{2.4}$$

(Helanow et al., 2021) where C is a spatially varying parameter that must be less than the maximum up-slope gradient of the bed. Here, basal traction initially increases steeply before gradually approaching a maximum value. Last, entirely plastic basal slip of the form

$$\tau_b = C_p N_e \tag{2.5}$$

where C_p is a parameter that can be spatially varying meaning basal traction has a fixed value at a given N_e and C_p. There are alternative formulations for these relationships that result in minor differences (e.g. Zoet and Iverson, 2020, which is covered in section 6.2.2).

The theories behind these formulations fall into the categories 'hard bed' or 'soft bed'. Hard bed sliding theory began with Weertman (1957) assuming that a film of water a few microns thick exists at all points between the ice and the underlying bedrock with a 'tombstone' geometry, meaning the base itself is essentially frictionless and that all resistance to ice motion comes from the normal force exerted by bedrock obstacles. Nye (1969) and Nye (1970) expanded this to determine ice motion over beds comprised of uniform sinusoids and a wavy surface constructed considering the Fourier components of real surface topography respectively. These hard bed theories invoke regelation creep and enhanced creep. In regelation creep greater pressure on the stoss side of an obstacle decreases the local melting point and prompts melting, with water transferred to the lee side where pressure is lower, the local melting point is greater, and refreezing occurs. The importance of regelation dramatically diminishes for obstacle sizes >4 cm (Weertman, 1964). In enhanced creep, larger obstacles (tested up to 10 m in the original papers) increase longitudinal stress and prompt increased plastic deformation. A Weertman-type formulation is still commonly applied in ice sheet models (Goelzer et al., 2017; Babaniyi et al., 2021), though the theoretical underpinnings of a subglacial sheet of water of uniform thickness and pressure is generally considered not to hold (Fowler, 2010b).

Work assuming a continuous film of water at the glacier-bed interface continued (e.g. Nye, 1969; Kamb, 1970; Gudmundsson, 1997), though with growing acceptance of the importance of subglacial water pressure and cavities forming on the lee side of bedrock perturbations (Lliboutry, 1968; Walder and Hallet, 1979), meaning a hard-bed sliding relationship must account for both N_e and u_b. Iken (1981) developed subglacial cavitation theory further, showing that for periodic 2D bumps there must be an upper bound on the basal traction given as $\tau_b/N \leq \tan(m_{max})$ where m_{max} is the maximum up-slope angle between the bed and mean flow direction, which (Schoof, 2005) showed also applies to arbitrary 2D geometries (i.e. 'Iken's bound'). Basal-traction relationships obtained from numerical, analytical, or observational consideration of these 2D periodic obstacles suggests that once basal traction has matched Iken's bound, a further increase in u_b or decrease in N_e will result in decreasing, or rate-weakening basal traction (Lliboutry, 1968; Fowler, 1987; Schoof, 2005; Gagliardini et al., 2007; Zoet and Iverson, 2015). This is a result of continued cavity growth with increasing basal velocity, leading to diminishing ice-bed contact area close to bump crests.

The rate-weakening Coulomb relationship outlined above presents notable instabilities if applied to ice-sheet models, which therefore tend to neglect a rate-weakening Coulomb relationship on heuristic grounds (Helanow et al., 2020). That sensible results are not obtained under a rate-weakening Coulomb relationship suggested that deeper complexity, which can not be accounted for under an ideal 2D formulation, is occurring. To expand cavitation theories to more realistic settings, Helanow et al. (2020) and Helanow et al. (2021) model cavity formation in 3D over idealized and realistic beds respectively. This 3D geometry effectively eliminates — or makes insignificant — rate-weakening drag, largely as the realistic nature of the bed provides alternative pathways for subglacial water to exit a specific cavity. The outcome of this 3D consideration is a regularised-Coulomb relationship with no rate weakening.

Looking at 'soft' or sedimentary beds, deformation of the sediment itself becomes important, with experiments indicating plastic sediment deformation beyond a yield stress, which is controlled by the effective stress and sediment material properties (Boulton and Hindmarsh, 1987; Kamb, 1991; Iverson, 2010). However, how underlying sediment interacted with overlying ice remained unclear until recent laboratory experiments where ice at the melting point was placed over sediment at high pressure (Zoet and Iverson, 2020). These experiments indicated a threshold basal velocity where basal slip transitions from viscous deformation and regelating of ice around static particles at the bed surface (with rate-strengthening slip), to obstacle ploughing at a yield strength determined by the till's material properties. Zoet and Iverson (2020), in conjunction with 3D cavity experiments (Helanow et al., 2021), therefore suggests that a regularised-Coulomb may be applicable to both hard and soft bed settings (Minchew and Joughin, 2020). This provides a clear physical justification for the use of a regularised-Coulomb basal-traction relationship in ice-sheet models across a variety of settings (e.g. Bougamont et al., 2011; Pattyn, 2017; Riel et al., 2021).

However, these developments do not close the debate surrounding basal slip (see also section 6.2.2). Using a 28 year record from Argentière Glacier in the French Alps and Elmer/Ice modelling, Gimbert et al. (2021) suggest that long-term changes in year-averaged sliding velocities still follow a Weertman-type relationship and scale with bed shear stress, as opposed to a more complex pressure-dependent relationship, and that basal effective pressure is primarily set by bed shear stress — rather than by water input and subglacial drainage system specifics as is commonly thought (e.g. Rada and Schoof, 2018). Gimbert et al. (2021) propose that this may be due to the influence of bed shear stress on cavity geometry, stating that their relationship may therefore not hold where ocean-induced buoyancy can control subglacial water pressure (such as the margins of the GrIS, Stearns and Van Der Veen, 2018). In addition, Maier et al. (2021) suggest a Weertman-type

relationship is still applicable across large parts of the GrIS at large scales (>6 km). This indicates at least a degree of mismatch between the small-scale slip relationships of Zoet and Iverson (2020) and Helanow et al. (2021) and large-scale relationships, particularly in predominantly hard-bedded settings (Gimbert et al., 2021; Maier et al., 2021). Last, Tsai et al. (2021) propose a model for basal slip that incorporates the effect of transient and spatially varying subglacial water pressure. They find that this produces a similar basal traction relationship to that proposed by Budd et al. (1979), which heuristically incorporates water pressure into a Weertman-type relationship and has characteristics between Weertman-type and regularised-Coulomb sliding. Tsai et al. (2021) find their model to be effective at describing diurnal surface velocity fluctuations at a land-terminating sector of the GrIS near Kangerlussuaq.

2.2.6 Inversion procedures

In addition to basal topography, ice-sheet models require a field of basal-traction parameters (A_s, β, C, C_s, or C_p in Eqs. 2.2-2.5). This basal traction field is usually obtained using an inversion procedure to minimize a cost function that measures the mismatch between observed and modeled surface velocity or position (e.g. Gillet-Chaulet et al., 2012; Goelzer et al., 2017; Derkacheva et al., 2021). Such inversion procedures are capable of resolving variations in basal-traction parameters at resolutions lower than about one ice-thickness, meaning smaller-scale variability is not represented in inversion output. In addition, while most basal-traction relationships are explicitly posed for skin drag, resistance at the ice-sheet bed due to bed material properties, it is expected that inversions also account for some amount of form drag, the resistance to flow from the interaction of ice with basal topography. However, the importance, nature, and quantification of form drag, and the point where it is considered distinct from internal ice deformation, remains poorly constrained (e.g. Kyrke-Smith et al., 2018). Further, basal-traction parameters should theoretically show only minor temporal variability and therefore be transferable between models. However, variation in the choice of basal-traction relationship and inversion methodology makes such comparison challenging. Barnes et al. (2021) show the difference between three different inversion/model implementations of Weertman-type sliding results in a 13-32% variation in mass loss over 40 years from the Amundsen Sea Embayment, Antarctica. They suggest that implementing increased transferability of basal-traction parameter fields and standardising methodology may be useful for future ice-sheet model intercomparison projects. These studies indicate there is still substantial scope to improve our understanding of basal-traction processes and how this understanding is implemented in predictive ice-sheet models.

2.2.7 Modelling approaches

Analytical models gave early insights into glacier behaviour and still prove very useful today, though often with a computational hand at some point (e.g. Mantelli and Schoof, 2019; Schoof and Hewitt, 2016). However, predictive ice sheet models incorporating variable bed topography and ice-ocean boundary conditions require numerical solutions, made increasingly accessible as computing power has increased over the last few decades. Three main modelling approaches exist for ice sheets:

Shallow ice approximation. Here longitudinal, transverse, and vertical stress gradients are neglected, essentially assuming the driving stress is balanced by the basal traction at all points. This formulation neglects basal slip and is generally effective for interior portions of ice sheets but can be less realistic towards ice-sheet margins. It is computationally inexpensive (Pattyn, 2018).

Shallow shelf approximation. Here basal traction is assumed to be zero while internal ice deformation is taken to be negligible meaning all motion comes from basal slip. This formulation was developed for ice shelves but is also sometimes applied to AIS ice streams where traction is assumed to be very low. A hybrid coupling of shallow shelf and shallow ice approximations can be used where the shallow shelf approximation is effectively a sliding relationship (Bueler and Brown, 2009). This is also computationally inexpensive but becomes more expensive when combined with the shallow ice approximation.

Full Stokes. This solves the full Stokes equations (section 4.6.1) governing ice flow and considers the full stress tensor. It is is computationally expensive but provides the most realistic numerical representation of ice motion (Kirchner et al., 2016).

A variety of these approaches are implemented in present-day ice-sheet model applications (Goelzer et al., 2018; Seroussi et al., 2020).

2.3 Previous studies at Sermeq Kujalleq

Sermeq Kujalleq has been subject to two major field campaigns. The Natural Environment Research Council funded SAFIRE (Subglacial Access and Fast Ice Research Experiment) project running from 2013-2017 and the European Research Council funded RESPONDER

(Resolving subglacial properties, hydrological networks and dynamic evolution of ice flow on the Greenland Ice Sheet) project running from 2016-2022.

The SAFIRE project involved GPS, radar, and seismic surveys, with borehole drilling focused at site S30 (Fig. 3.2) over two field seasons. This project resulted in a series of papers on the physical conditions of fast glacier flow (1. Doyle et al., 2018, 2. Hofstede et al., 2018, 3. Young et al., 2019) as well as additional methods development (Young et al., 2018), radar measurements of subglacial melting (Young et al., 2022), numerical modelling (Todd et al., 2018), and work produced with collaborators at the university of Stanford (Kendrick et al., 2018).

The larger RESPONDER project involved three main summer field campaigns (2017, 2018, and 2019), two further spring field campaigns (2018 and 2019) as well as a further clean up trip when covid restrictions began to ease in summer 2021. Initial work was focused on uncrewed drone radar surveys of the calving front (Chudley et al., 2019; Cook et al., 2021b) with concurrent modelling of calving processes and their interaction with the subglacial drainage system (Cook et al., 2021a, 2020b) before further borehole, drone, radar and seismic work at or near site R29 (Fig. 3.2, Chudley et al., 2019; Booth et al., 2020; Hubbard et al., 2021; Law et al., 2021; Peters et al., 2021; Prior-Jones et al., 2021). A full report on borehole instrumentation is Doyle (2020).

2.4 Fibre optic sensing

This section is an abridged and adapted version of a section from my first year report.

In most environmental applications fibre optic sensing makes intrinsic use of an optical fibre as the sensor itself. This has several advantages over conventional sensing systems involving discrete sensing units connected by electrical cable: the signal is immune from electromagnetic interference; the sensor can have a very small diameter ($<$1 cm); signal noise is much lower over long ($>$1 km) distances; inter-instrument uncertainty is effectively eradicated; and measurements can be obtained with very high ($\sim$0.65 m) resolution along the entire cable. Fibre optics manufacturers focus on the purity of fibre optic materials in order to reduce scattering and absorption - energy losses that are known as attenuation (Fig. 2.7). However, it is the intensity, wavelength, and phase of this scattered light that is used in fibre optic sensing to gather information on environmental variables, with each potentially sensitive to the measurand, allowing a wide range of environmental variables to be measured even when their relationship to an optical beam may not at first be obvious

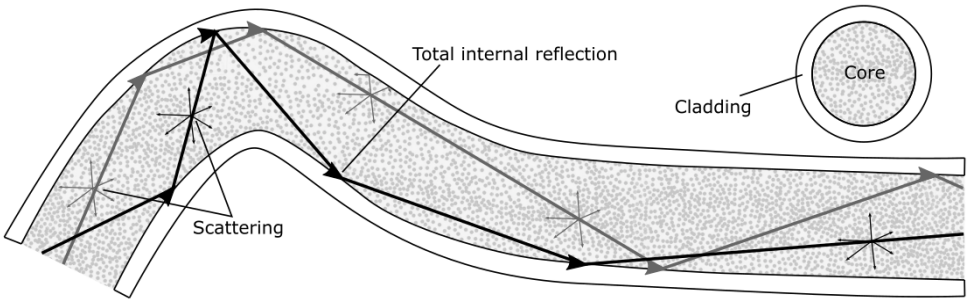

Fig. 2.7 . Schematic representation of fibre optic structure, total internal reflection and scattering. Fibre optics work by passing light through a core with a higher refractive index surrounded by cladding of lower refractive index. In commercially available fibres this results in a critical incident angle (where total internal reflection occurs) of $\sim 66°$.

(for example dissolved oxygen content, Bagshaw et al., 2011, or flow sensing, Peng et al., 2004).

Fibre-optic technology has a surprisingly long history. Alexander Graham Bell patented the first 'Photophone' in 1880 (Mims III, 1982) before glass fibres for the transmission of images were developed for medical purposes in the 1920s and used in 1930 (Hecht, 1999). Imaging from bundles of fibres without aberrations (optical losses) was shown in two separate 1954 Nature papers (Hopkins and Kapany, 1954; Van Heel, 1954) and, by 1960 more reliable cladding required for total internal reflection over longer distances was under development. This was followed shortly after by the invention of the laser and a burgeoning global communications system (Hayes, 2010), with signal losses in silica fibres being reduced from 10 dB km^{-1} in 1966 to 0.4 dB km^{-1} in 1988 (losses are now around 0.15 dB km^{-1}) when the first transatlantic cable was installed with a capacity of 565 Mb s^{-1} (Hecht, 1999).

2.4.1 DTS

DTS was the first sensing application to utilize the developed communication technology, which was quickly applied in the petro-chemical industry to monitor borehole leaks, fluid flow with temperature as a proxy, and thermal conductivity (Dakin et al., 1986; Großwig et al., 1996; Hurtig et al., 1997). Hydrology studies, again using temperature as a proxy, made use of this nascent sensing technology to observe high resolution changes in flow through time (Selker et al., 2006; Lowry et al., 2007), before its more widespread use in geoscience applications.

Most DTS sensing systems utilize Raman scattering of the input light. Raman scattering, discovered by Sir Raman in 1930, occurs when incident photons interact with particles

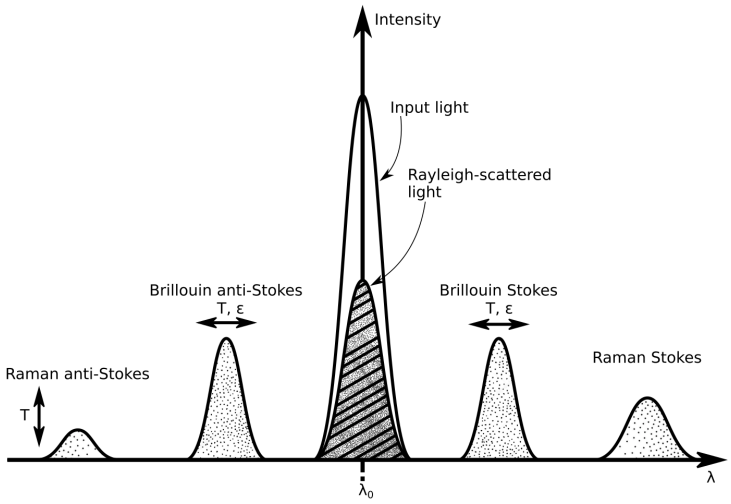

Fig. 2.8 . Signal wavelength and intensity, schematically showing relationship between incident light, Raleigh scattering, Brillouin scattering, and Raman scattering, where T is temperature, λ_o is transmission wavelength, and ϵ is strain. Raman anti-Stokes intensity varies depending on fibre temperature, Brillouin (anti-)Stokes varies depending on fibre temperature and strain. Adapted from Ng and Lalam (2017).

(atoms, molecules, or crystalline lattices) in such a way that the photon either gains or loses energy, shifting the frequency of returning photons dependent upon the vibrational and/or rotational properties of the scattering particle (The Nobel Prize, 2019). This behaviour is inelastic, in contrast to elastic Rayleigh scattering (which makes the sky blue) where there is no transfer of energy between the photons and particles. If a particle is excited to a higher vibrational mode by the incident photon, returning photons are diminished by the value of the vibrational transition energy. Alternatively, if the particle the photon interacts with has elevated vibrational excitation then the scattered photons frequency will exceed the incident frequency, as the photons gain the vibrational energy lost by the particle. When observed through spectral analysis this results in a Stokes line, where the return frequency is lower, and an anti-Stokes line where the return frequency is greater (Fig. 2.8). The anti-Stokes line is typically a few times less intense than the Stokes line. The wavelength of the laser used is around 1500 nm (NKT, 2019), within the infrared range, which explains why the vibrational energy of the medium is perturbed and measured, rather than electron levels (visible light), ionisation (ultra-violet), or rotational energy (microwave) (Krohn et al., 2014).

Raman scattering is used in physics and chemistry to gain information about a molecules moment of inertia and hence structure. In fibre optic sensing, this is simplified as the material in question is always a silica lattice (SiO_2) with very limited impurities. Because the anti-Stokes component shows a strong temperature dependence, whereas the Stokes component does not, a relationship can be derived relating the return signal to temperature at any point along the cable. As this relationship is dependent on the proportion of Stokes

to anti-Stokes backscatter, not the absolute value, it can be extended to great lengths, so long as a coherent signal is still detectable by the interrogator. Temperature as a function of length is centered on the simple equation

$$T(z) = \frac{\zeta}{ln\frac{P_S}{P_{aS}} + C - \Delta\alpha Z} \tag{2.6}$$

where ζ is the energy shift in photons between incident and scattered Raman photons, P_s and P_{aS} are the intensities of the Stokes and anti-Stokes backscatter respectively, C is a dimensionless parameter to account for the properties of the source laser and the DTS instrument, $\Delta\alpha$ is the differential attenaution coefficient for the anti-Stokes and Stokes photons within the fibre, and z is the location in the fibre where the scattering occurs (Hausner et al., 2011; Tyler et al., 2013). A more sophisticated approach, detailed in Chapter 3, was used for data from Sermeq Kujalleq in order to constrain measurement uncertainty.

Brillouin scattering (Fig. 2.8) is also related to the vibrational properties of the matter the photons interact with. However, while Raman scattering is dependent upon interactions between neighbouring atoms, Brillouin scattering is caused by larger scale vibrations (technically, phonons, Muanenda et al., 2019). The result of this is that the Brillouin scattering signal is additionally sensitive to the strain of material, making it useful in structural applications of temperature measurement where strain is negligible but extremely challenging for glaciology applications where strain rates are high. Combined with DTS based on Raman scattering however, Brillouin scattering can be a highly effective way of measuring strain (see section 2.4.2).

Processes uncovered by DTS include Freifeld et al. (2008) monitoring thermal conductivity in permafrost boreholes, Moffett et al. (2008) looking at tidal estuary behaviour, Roth et al. (2010) measuring sensible heat loss from stream surfaces, and Keller et al. (2011) using fibre optics tethered to a weather balloon to study the atmospheric boundary layer. However, only two projects use DTS to investigate glacier processes. The first, detailed in Tyler et al. (2013) and Stern et al. (2013) uses 300 m and 700 m lengths of optical fibre to investigate the incursion of warm water currents beneath the McMurdo Ice Shelf and the effect of this on basal ice shelf melt rates over a 6 month period. Stern et al. (2013) use this record, in conjunction with numerical modeling to better understand the influence of marine currents and bathymetry on basal melt rates.

In the second glacier application of DTS, Fisher et al. (2015) look at geothermal heat flux beneath Subglacial Lake Whillans, and heat flux from the lake into the overlying

ice. They deployed a cable down the WISSARD (Whillans Ice Stream Subglacial Access Research Drilling) borehole, which was at least 0.5 m in diameter (Tulaczyk et al., 2014). Two measurements were obtained, one directly after installation, where the temperature profile was clearly totally perturbed by the thermal disturbance of drilling, and one the following year. The latter temperature profile showed good agreement with a simple 1D advection-conduction model as would be expected due to low internal deformation within the ice stream and no water movement and refreezing processes. Two thermal anomalies remained within the profile even after a year, due to large sub-surface drilling reservoirs. Both of these glaciology applications are in relatively low strain environments, simplifying their longer-term operation.

2.4.2 DAS and DSS

Two further fibre-optic sensing technologies are discussed briefly. Distributed strain sensing (DSS) which was a part of the initial project proposal but ultimately not implemented — though it remains an interesting area for future glaciological work — and distributed acoustic sensing (DAS) which was not a part of the initial project but was implemented by Adam Booth of Leeds University in collaboration with Silixa Ltd using the same cable installed at Sermeq Kujalleq for DTS and a Silixa iDAS (Booth et al., 2020). DAS results also have the potential to be used for DSS (Jousset et al., 2018).

Three DSS techniques are covered. First, Brillouin scattering (the photonics of which are briefly outlined above). As Brillouin scattering also varies with temperature, an independent measurement of temperature is required in order to isolate strain. For an ice-sheet application, this means a Brillouin interrogator must be coupled to a Raman interrogator. This increases the experiment cost and means any failure in the Raman sensing set up would also have catastrophic ramifications for Brillouin sensing. For these reasons it was decided to forego this technique for the 2019 field season, however, as the Brillouin setup is likely to fail before the Raman setup, future work involving Brillouin scattering may prove worthwhile (chapter 6).

Second, Fibre Bragg gratings — millimeter scale increases to an optical fibre's refractive index inscribed using high power ultra-violet light. Each fibre Bragg grating reflects light (the Bragg wavelength) within a tight spectral range which changes with temperature and strain (Paschotta, 2008b), making fibre Bragg grating cables quasi- rather than truly distributed. The spectral range of each fibre Bragg grating is differentiated within a $\sim$0.5 - 1 m length of cable allowing the interrogator to differentiate between them, but fibre Bragg grating ranges are reused beyond this (Paschotta, 2008b). Fibre Bragg grating temperature

sensing typically offers far greater spatial resolution than Raman scattering (down to 5 mm), though temperature resolution is decreased ($\sim 0.7^{o}$C). These features mean fibre Bragg gratings are most commonly used in applications such as aerospace and the steel industry where temperature differences are larger and spatial resolution is a priority (Campanella et al., 2018). As the Bragg wavelength is also dependent on temperature and strain it is unsuitable in isolation in glaciological applications and a separate temperature measurement must be obtained for strain sensing to be accurate. Strain measurements using fibre Bragg grating were excluded due to the far greater costs associated with fibre Bragg grating cables and as the lifetime of the cables in the ice sheet may have prevented meaningful time series from being obtained. Again, and as for Brillouin scattering, fibre Bragg gratings may prove useful in future work (chapter 6).

However, fibre Bragg gratings in more flexible and deformable *polymer* fibre optics present capabilities highly applicable to a glacial setting. This is because polymer fibre optics can greatly exceed the elongation at failure of conventional silica fibre optics (up to 100% compared to $\sim$1%) (Yuan et al., 2011). The Youngs modulus and the threshold of qausi-elastic behaviour is important in some polymer fibre optic applications (Webb, 2015), such as aeroplane wings, but inconsequential in an ice sheet setting where strain will not be reversed and the strength of the fibre will not influence ice shear. However, polymer fibre optics typically have much higher attenuation compared to silica fibre ($\sim$1 dB/m compared to $\sim$1 dB/km, Webb, 2015) meaning the return signal may be much weaker and making longer distances infeasible. A commercially available work-around is to use a Sensuron RTS125+ (www.sensuron.com/rts125/) which can achieve a total sensing length of 104 m, sufficient for the high-strain lowermost section of the glacier and potentially underlying glacial sediment which has so far evaded high resolution measurements. A polymer termination could be coupled with a silica fibre optic upper section, however the high (>£60,000) cost was deemed to push this approach beyond an acceptable risk-reward limit.

Third, optical frequency domain reflectometry using polymer optical fibre (Liehr et al., 2008; Liehr et al., 2009; Liehr et al., 2010; Liehr et al., 2018; Liehr, 2018). Here each optical fibre has a unique loss signature, which is permanent and does not change as the fibre undergoes strain. An algorithm can then be used to track the shifts in attenuation peaks and achieve a displacement resolution of $\sim$2 cm. This technique is extremely promising, especially as it can be used with perfluorinated polymer fibre optic. However, at present this methodology remains tied to very controlled settings and tests in extreme ice-sheet settings are presently out of reach. Similar to fire Bragg gratings, this technology may be practicable in the near future and would likely prove cheaper as inscription of fibre Bragg gratings is not required.

Last, DAS has seen marked uptake over the last few years in the oil and gas industry where dynamic processes need to be monitored, such as pipelines and sub-surface seismic profiling (Muanenda, 2018). DAS uses Rayleigh reflections which have been tested with known acoustic sources, though the detailed process for this inversion still remains unpublished (Parker et al., 2014). Environmental applications that have used DAS are limited but have yielded impressive results. Ajo-Franklin et al. (2019) used DAS technology to gather a 7 month record from existing telecoms infrastructure in California, resolving basin-scale hydrological variations and seismicity with vastly improved spatial resolution. Jousset et al. (2018) used existing telecoms infrastructure and a Silixa iDAS on the Reykjanes peninsula, Iceland to identify normal faults and volcanic dykes in exceptional detail. The high spatial resolution (10 m) and broad band response (0.01 Hz to 50 kHz) available through DAS make it an exciting frontier in environmental sensing.

2.5 Subglacial landscape formation

The subglacial landscape of an ice sheet exerts a first-order control on the ice sheet's geometry, the nature of the ice sheet's motion, and the ice sheet's vulnerability to a changing climate. Steep and rough mountains comprised predominantly of Precambrian crystalline rocks fringe a large part of Greenland's coast, presenting an obvious obstacle to ice motion (Dawes, 2009), while a predominantly above present-day sea level interior makes the GrIS largely immune to marine ice sheet instability. Conversely, in West Antarctica active tectonic extension between the Transantarctic Mountains and the Amundsen Coast results in along-flow basins beneath the Siple Coast ice streams draining the WAIS which provide little, if any, topographic obstacles to ice motion. The nature of this region – sufficiently shallow ($\sim$1 km below present day sea level) to easily contain ice during glacial periods yet sufficiently deep that the presence of this ice is unstable in interglacials (Hay et al., 2014) further presents a very real and human problem over the coming decades to centuries (section 2.1.2).

Ice-sheets furthermore interact with the subglacial landscape to form the ground over which they flow in complicated and non-linear ways at distances from metres, to tens of kilometres, to whole continents; prompting studies of subglacial landscape formation across this scale continuum (e.g. Hallet, 1996; Harbor et al., 1988; MacGregor et al., 2000; Coulon et al., 2021). Looking first at processes of erosion, the simplest relationship is one where erosion scales with the velocity of overriding ice which has good experimental support at sub-metre scales (Hansen and Zoet, 2022) and support from modelling studies of U-shaped valley formation at kilometre scales (MacGregor et al., 2000). The leading theory

for processes behind this roughly linear erosion relationship is abrasion from entrained debris, meaning the quantity, weight, and roughness of debris are key controls on erosion alongside sliding speed (Hallet, 1981). The difficulty in predicting every factor except for basal velocity (with even this difficult, see chapter 4) means a simple and approximate single parameter is normally used in modelling studies (e.g. MacGregor et al., 2000; Jamieson et al., 2010). Quarrying related to subglacial water flow and temporal variations in this (Hallet, 1996), or the more recently quantified and adjacent subglacial ripping (Krabbendam et al., 2022) are also proposed and supported by abundant field evidence, but are harder to implement in numerical models of subglacial erosion. Good estimates exist for the total quantity of eroded material from ice-sheets (Dowdeswell et al., 2010) and suggest faster moving outlet glaciers are responsible for the majority of material exported from beneath the GrIS (Overeem et al., 2017). Nonetheless, modelling studies tackling erosion and landscape formation are limited and largely restricted to scales of multiple kilometres or continents (e.g. Jamieson et al., 2010). Processes of erosion alongside results of ice motion over rough topography at sub-kilometre scales, and their bearing on erosion are discussed further in chapter 5.

Glaciers also function as the worlds largest non tectonic transporters and depositors of material (Dowdeswell et al., 2010) – carrying sediment derived from surrounding mountains supra- and englacially, and sediment derived from their substrate through the subglacial hydrological system and entrained in basal ice. This results in a wide array of glacial landforms: terminal moraines that are shaped and moulded as the glacier ploughs sediment at its snout which can reach over 100 m in height and tens of km in length (Evans et al., 2005); and a family of subglacial landforms inferred to form beneath actively deforming ice including drumlins, eskers, and mega-scale glacial lineations (MSGLs) (Benn and Evans, 2010). Of these (and more besides), MSGLs are particularly relevant for the research presented in this thesis, and are hypothesised to form beneath regions of fast ($\gtrsim 1$ km a^{-1}) ice motion, with radar observations of inferred MSGLs beneath active ice-streams at Thwaites Glacier (Holschuh et al., 2020), and Rutford Ice Stream (Schlegel et al., 2022). MSGLs were only recognised following the advent of satellite imagery (Clark, 1993) and have since been the subject of of numerous formation theories including deformation by ice (e.g. Ó Cofaigh et al., 2013b), steady subglacial water flow (e.g. Fowler, 2010a), and catastrophic subglacial floods (e.g. Shaw et al., 2008). Further discussion covering formation theories, extended in light of novel modelling results, is presented in chapter 5.

Finally, with a density roughly one third of rock comprising the Earth's crust, overlying ice will subtly depress the earth over which is lies through isostatic adjustment, with subsequent readjustment following ice removal. This has particular importance at larger temporal and spatial scales. For example, uplifting land at the grounding line of an ice

sheet following ice removal may stabilize the boundary of that ice sheet by lowering local sea level over at centennial, or even decadal timescales (e.g. Whitehouse et al., 2019. Overall, improving understanding of subglacial landscape formation also gives us a deeper understanding of the solid earth, and the glacial-motion mechanisms that give rise to such beguiling features.

Chapter 3

Results I: Thermodynamics of a fast-moving Greenlandic outlet glacier revealed by fiber-optic distributed temperature sensing

3.1 Preface

The results of this chapter were published as '*Thermodynamics of a fast-moving Greenlandic outlet glacier revealed by fibre-optic distributed temperature sensing*' in Science Advances in May 2021 (Law et al., 2021). After notes on the background and author contributions, the paper is presented as published, with minor alterations in order to conform with thesis formatting requirements and minor notation changes for consistency across chapters. The text itself is not modified. It should be noted that this means the American spelling is retained as published in this chapter (and as submitted in chapter 4), despite the thesis as a whole using English spelling.

3.1.1 Setting

The original motivation for this work was a paucity of field observations (and in particular borehole records), and therefore a lack of observation-based understanding, of fast-moving outlet glaciers in Greenland. Prior to the RESPONDER project of which this installation was a part, the only investigations of fast moving GrIS glaciers were Jakobshavn Glacier in 1988-1999 and 1995, Sermeq Kujalleq in 2014 and 2016 as part of the SAFIRE project, and Kangerluarsuup Sermia (Bowdoin Glacier) in 2014 (Iken et al., 1993; Lüthi et al., 2002; Doyle et al., 2018; Seguinot et al., 2020). All of these studies significantly advanced understanding of the thermodynamics of marine-terminating glaciers, but also demonstrated a complexity in ice-motion that required further investigation. In particular, the discrete sensing systems used in these studies means down-borehole profiles omitted detail between individual sensors. For example, numerous interpretations are possible for the temperature measurements presented in Doyle et al. (2018) but the simplest linear

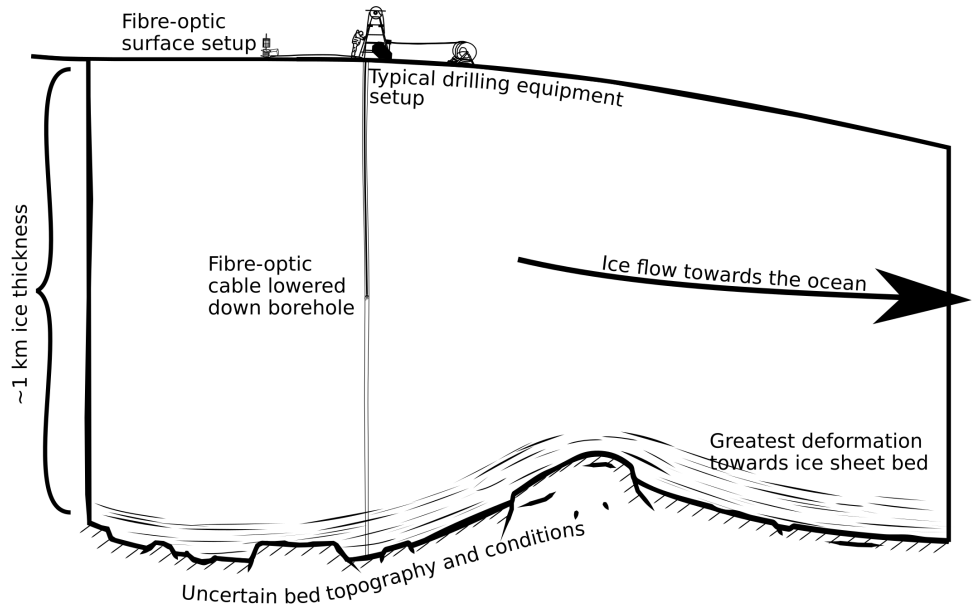

Fig. 3.1 . Schematic representation of borehole setup showing hot-water drill and uncertain bed topography.

interpolation between points is typically used. Prior to the work presented here, the detail that may lie between discrete sensors remained essentially the subject of speculation.

Speculation about results was persistent in this project too, throughout the entire preparation period from October 2018 to July 2019 and until daily data collections of equilibrating temperature data from the successfully installed DTS system slowly revealed a profile with interesting and unexpected features. These features include isolated strain heating within interglacial phase ice at relatively shallow (208-242 m) depth, strongly heterogeneous ice deformation in glacial-phase ice below the Last Glacial-Interglacial Transition at 889 m depth, and a 73-m-thick layer of temperate ice at the base of the glacier. These observations were benevolently facilitated by a cable that failed after 6 weeks, far exceeding worst-case estimate of only 10 days and providing a temperature record within 0.2^{o}C of the predicted equilibrium temperature at all points. Given the success of this experiment, and the accompanying DAS study utilizing the same cable (Booth et al., 2020), it is likely that fibre-optic sensing will enable a step-change in the quality of borehole records it is possible to obtain from fast ice-sheet settings. While the work in this chapter was an integral part of the funded PhD project, what came after was more open to blue-sky thinking, the direction of which was expected to be heavily influenced by the DTS results. Fortunately, the features present in the DTS record offered several good starting points. Ultimately I decided to investigate the unexpectedly thick temperate layer at the borehole location, and its variation across the Sermeq Kujalleq catchment. This lead on to modelling work presented in chapter 4.

3.1.2 Contributions

Poul Christoffersen developed the earliest iteration of the experiment design, obtained funding for the project from the European Research Council Horizon 2020 Program, led the fieldwork campaign, and supervised the project. I realised the execution of the experiment (including selection and procurement of the fibre-optic cabling and DTS unit and construction of the field-capable DTS system with solar-power setup and fibre-optic connections), processed and analysed the collected data, and conducted additional strain experiments at the Civil Engineering Building, University of Cambridge. Bryn Hubbard and Samuel Doyle led the borehole drilling work. Bas des Tombe and Bart Schilperoort advised on the use of the dtscalibration Python package. Cedric Kechavarzi assisted with experiments at the Civil Engineering Building, Univeristy of Cambridge. Poul Cristoffersen, Bryn Hubbard, Samuel Doyle, Thomas Chudley, Charlotte Schoonman, and Adam Booth assisted with data collection in the field. I wrote the first version of the manuscript which then received input from all listed co-authors. A shortened version of this author contribution statement is available in the published work and included later in the chapter.

3.2 Abstract

Measurements of ice temperature provide crucial constraints on ice viscosity and the thermodynamic processes occurring within a glacier. However, such measurements are presently limited by a small number of relatively coarse-spatial-resolution borehole records, especially for ice sheets. Here, we advance our understanding of glacier thermodynamics with an exceptionally high-vertical-resolution (0.65 m), distributed-fiber-optic temperature-sensing profile from a 1043-m borehole drilled to the base of Sermeq Kujalleq (Store Glacier), Greenland. We report substantial but isolated strain heating within interglacial-phase ice at 208 to 242 m depth together with strongly heterogeneous ice deformation in glacial-phase ice below 889 m. We also observe a high-strain interface between glacial- and interglacial-phase ice and a 73-m-thick temperate basal layer, interpreted as locally formed and important for the glacier's fast motion. These findings demonstrate notable spatial heterogeneity, both vertically and at the catchment scale, in the conditions facilitating the fast motion of marine-terminating glaciers in Greenland.

3.3 Introduction

Mass loss from the Greenland Ice Sheet (GrIS) has increased sixfold since the 1980s and is now the single largest cryospheric contributor to global sea-level rise (Mouginot et al., 2019; The IMBIE Team, 2019). Around half of this mass loss is from surface meltwater runoff, while the other half is driven by discharge of ice into the ocean (Van Den Broeke et al., 2016). Surface melting and runoff can be observed by satellites and in situ methods in a relatively direct manner, facilitating validation of surface process models and a more straightforward exchange between modeling and empirical observations (e.g. Cook et al., 2020a). In contrast, ice dynamics, which are largely controlled by englacial ice properties and basal conditions, present substantial observational challenges and are therefore less well constrained in models, making such processes one of the largest sources of uncertainty in global sea-level projections (Goelzer et al., 2017; Aschwanden et al., 2019).

A crucial but scarce source of information comes from boreholes, which provide unambiguous records of subsurface ice properties, such as temperature profiles, deformation rates, and the conditions at the bed that influence basal motion. These records are especially relevant for Greenland's marine-terminating glaciers, which flow rapidly ($\geq$200 m a^{-1}) through englacial deformation and basal motion (Doyle et al., 2018). Such glaciers drain most of the ice sheet (Rignot and Mouginot, 2012; Mouginot et al., 2019), yet they are rarely the subject of borehole investigations due to logistical challenges including pervasive crevassing and high strain rates that damage installed equipment (e.g. Iken et al., 1993; Doyle et al., 2018; Seguinot et al., 2020). As a consequence, GrIS models often rely on physical constraints from theoretical considerations or from studies conducted on smaller and more accessible glaciers elsewhere, which may not be representative of larger or faster ice masses (e.g. Bougamont et al., 2014; de Fleurian et al., 2014).

Here, we report results from the first use of fiber-optic distributed temperature sensing (DTS) on the GrIS, installed in a 1043-m-deep borehole drilled to the base of the fast-moving Sermeq Kujalleq (Store Glacier in the literature and used hereafter), which has one of the largest glacial catchments in Greenland (34,000 km^2, Rignot et al., 2008). The installed fiber was sampled every 0.25 m, providing an englacial borehole temperature record with a vertical resolution (0.65 m; see Materials and Methods for further information) two orders of magnitude higher than in previous comparable borehole studies using discrete sensor setups. With this highly resolved temperature record, we report on the thermodynamics of Holocene ice [formed since 11.7 thousand years (ka) in the current interglacial period], pre-Holocene ice (formed before 11.7 ka in the most recent glacial period and prior), and the Last Glacial-Interglacial Transition that separates the two sections. We also report on the transition from cold ice (with no liquid phase) to basal temperate ice (in equilibrium with

a liquid phase at the ice-water phase transition temperature), all in unprecedented detail. These results indicate a heterogeneity in deformation between and within different ice sections that emphasizes a need for a multilayered approach to ice rheology and represent an important improvement in our observation-based understanding of ice deformation in fast-moving sectors of the GrIS.

3.4 Results

We installed a DTS system on 5 July 2019 in a 1043-m hot-water drilled borehole located at site R30 on Store Glacier (70.57°N, 50.09°W; Fig. 3.2), where surface ice motion is ~600 m a^{-1}. Borehole BH19c was drilled at the center of Lake 028, which had drained rapidly 2 months before drilling (Chudley et al., 2019), leaving a large fracture and active moulin with continued inflow by supraglacial melt water (Fig. 3.2). The DTS system, which consisted of a Silixa XT-DTS, armored cable housing fiber optics, and thermistors for calibration purposes, works by measuring the temperature-sensitive components of Raman backscatter (Stokes and anti-Stokes wavelengths) and travel time, when a laser pulse is transmitted through the optical fiber (Materials and Methods).

Our DTS measurements span from 5 July to eventual cable failure at 889 m depth at 21:30 UTC on 13 August (see Materials and Methods for sampling time information). Although our observations are limited to this 40-day period, the temperature profile for measurements averaged over the last 4 days before cable failure is within 0.2°C of equilibrium ice temperatures calculated from theoretical cooling curves at all points above 925 m (Materials and Methods). Below, we describe our observed vertical temperature profile (Fig. 3.3) in three distinct sections: first, cold ice with smooth temperature gradient variations interrupted by isolated perturbations; second, cold ice characterized by a shallower temperature gradient, more frequent temperature gradient variations, and substantial heterogeneous cable deformation; and third, temperate basal ice.

First, the temperature decreases progressively from -1.2°C at the surface to a minimum of -21.1°C at 580 m depth, where the temperature gradient switches from negative to positive downward, reaching a maximum sustained (varying smoothly over >20 m) value of 0.13°C m^{-1} at 865 m. This concave profile is a characteristic feature of fast-moving GrIS outlet glaciers (Dahl-Jensen, 1989), where advecting ice from the cold, high-elevation interior has not yet been warmed by heat diffusion from the warmer surface air temperature at lower elevations, basal geothermal heat flux, and strain heating concentrated toward the bed (Cuffey and Paterson, 2010). This section terminates at the location of cable failure (889

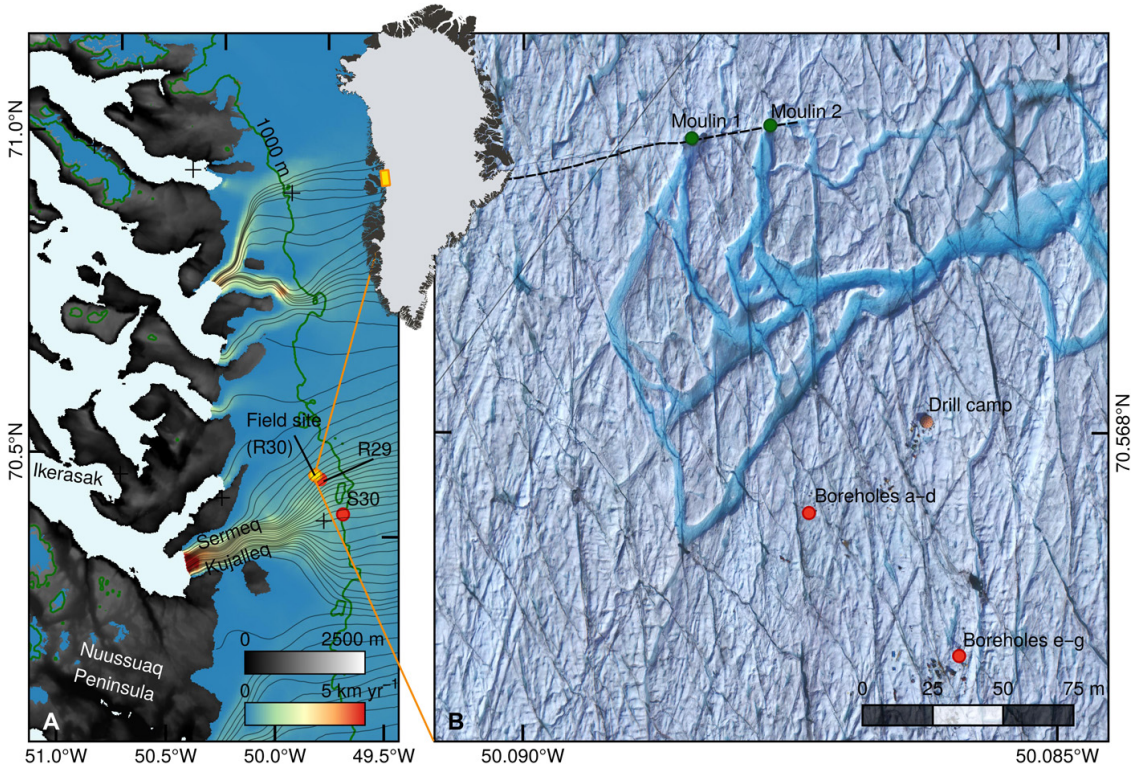

Fig. 3.2 . Map showing Store Glacier in West Greenland.(A) Map showing flow of the GrIS and glaciers flowing into Uummannaq Fjord. Black lines show direction of ice flow (originating 80 km inland at 2-km spacing). Surface velocity (color scale) is 2018 annual velocity from MEaSUREs data (Joughin et al., 2010; Joughin et al., 2015). Off-ice surface elevation (gray scale) and 1000-m ice-sheet surface elevation contour (green line) are from ArcticDEM v3 (Porter et al., 2018). Yellow box in Greenland inset shows study location. (B) Aerial image of site R30 showing location of boreholes BH19a-d (including BH19c where the DTS system was installed) and BH19e-g (red dots). Moulins (green dots) are fed by supraglacial streams. Black dashed line traces fracture that caused supraglacial lake drainage and moulin formation before boreholes were drilled. Image acquired by drone on 21 July 2019 (Chudley et al., 2019).

m), where the temperature is -5.3°C following a slight decrease in temperature gradient to 0.11°C m^{-1}. Herein, we observe (i) a local minimum in temperature of -6.9°C at 8 m depth, followed by a local maximum of -6.7°C at 16 m depth; (ii) two localized gradient increases and reversals at 100 to 111 m and 208 to 242 m (hereafter Anomaly-208); (iii) a sharp (4 m) and temporary 60% dip in temperature gradient of 0.07°C m^{-1} at 837 m, below which is a minor (10%) increase in temperature gradient of 0.1°C m^{-1}. Anomaly-208 is the largest of these anomalies (0.25°C) and is clearly distinguishable throughout the entire time series (Fig. 3.4), indicating that it is a stable feature over the length of observation.

The top of the second section is defined by a step change in temperature gradient from 0.13°C m^{-1} to 0.07°C m^{-1} (53%) at 889 m (Fig. 3.3, A and B), below which the temperature continues to increase gradually downward, although with more fluctuations compared to the section above. We observe a notable temperature anomaly with magnitude 0.25°C at 912 m, associated with a temperature gradient fluctuation of magnitude 0.15°C m^{-1}

over 5 m, as well as numerous temperature fluctuations between 889 and 935 m with a maximum amplitude of 0.1°C m^{-1} over distances as short as 0.6 m. Because this length scale approaches the DTS spatial resolution, we cannot rule out the possibility that the latter, smaller temperature perturbations, which occur after 8 August, stem from notable localized (<1 m) cable deformation (see Materials and Methods and figs. 3.7 and 3.8 for further details). Below 935 to 959 m, the temperature gradient oscillations reduce to the same magnitude observed in the uppermost section and the temperature gradient gradually settles below 959 m to a consistently low negative value (-0.002°C m^{-1}) at 982 m. We use this gradual transition in gradient over 23 m to define a cold-temperate transition

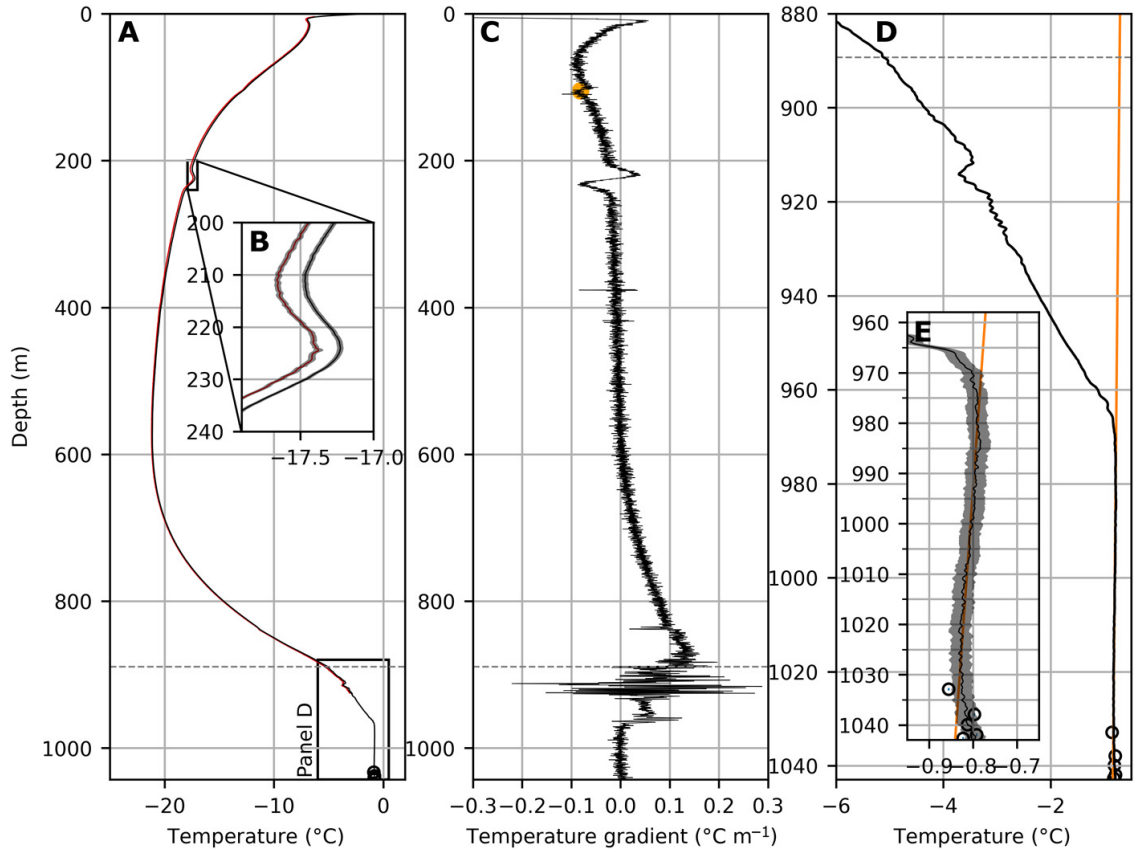

Fig. 3.3 . Vertical ice temperature profiles.(A) Full temperature record from DTS measurements averaged over the 96 hours prior to the last recorded measurement before cable failure at 21:30 UTC on 13 August. The combined sampling time was 3.8 hours, with 10 min of active recording every 4 hours over this period. Solid black line is recorded temperature, with 95% confidence interval shown in light gray shading. Red line is the equilibrium temperature estimated from observations and theoretical freezing curves, with dark gray shading showing root mean square error. Horizontal gray dashed line (at 889 m depth) is the point of cable failure on 13 August and the inferred location of the Last Glacial-Interglacial Transition. (B) Close-up of Anomaly-208 with same axis units. (C) Temperature gradient, with orange circle highlighting a temperature gradient anomaly at 100 to 111 m. (D) Close-up showing temperatures in the bottom part of the borehole below 880 m. Orange line is the pressure-dependent melting point assuming a linear Clausius-Clapeyron slope of 9.14 × 10-8 K Pa^{-1}. Black circles are thermistor data. The highest thermistor at 1033 m is interpreted to be an outlier. (E) Inset shows temperatures in the lowermost 100 m.

zone (959 to 982 m) as opposed to the cold-temperate transition surface used in previous theoretical studies (e.g. Hutter, 1982).

Third, while we define the cold-temperate transition zone as a zone extending to 982 m depth, we observe temperatures within the boundaries of the expected pressure and solute-dependent ice-water phase transition temperature from 970 m downward (fig. 3.9). Hence, we define 970 m as the top of the basal temperate zone giving it a thickness of 73 m, noting that the upper 12 m also forms part of the cold-temperate transition zone. Within this lowermost section, we also observe spatiotemporal temperature changes (Figs. 3.3E and 3.4C), indicating that processes influencing the ice-water phase transition temperature are operating at a time scale of days to weeks. These subtle variations are especially notable within the lowermost 20 m of the ice column. The temperature at 1040 m drops 0.04°C to -0.85°C from installation on 5 to 14 July, increasing gradually to -0.83°C over the remainder

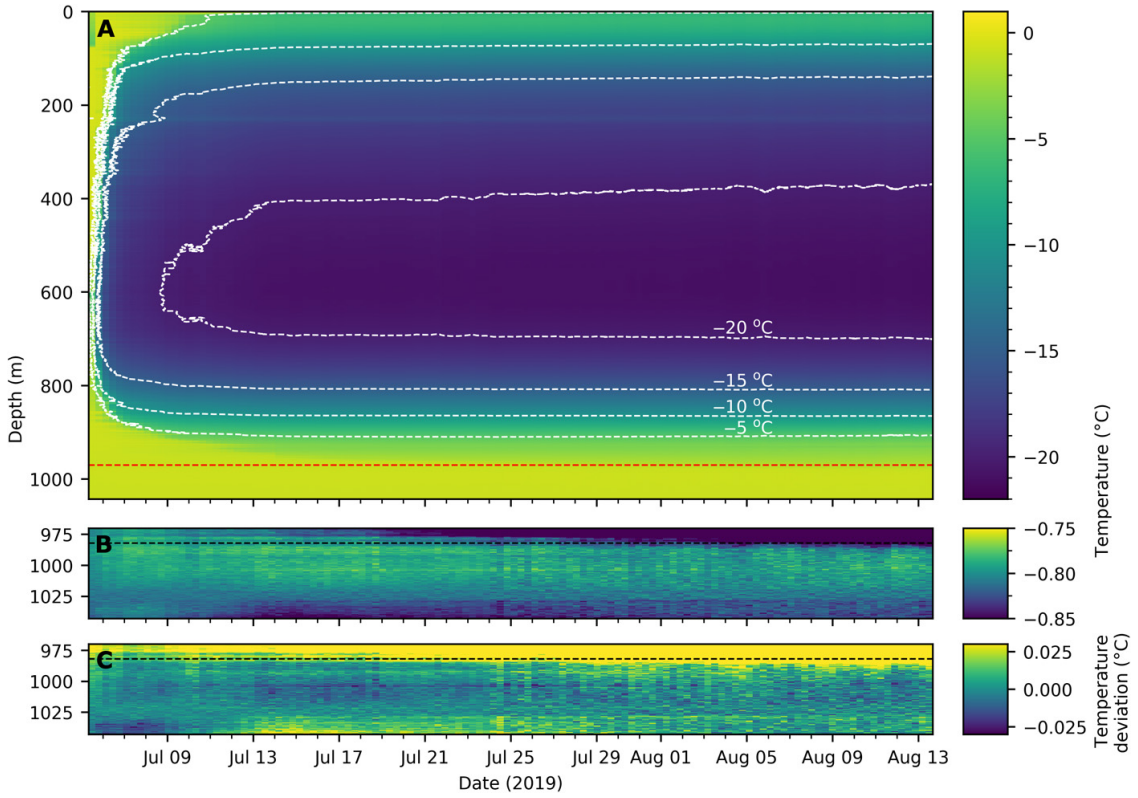

Fig. 3.4 . Ice temperature variations during the measurement period.(A) Full temperature record from 5 July to 13 August. The red dashed line is the boundary of close-ups shown in (B) and (C). White dashed lines are temperature contours with 5°C spacing. (B) Close-up showing the temperate zone below 970 m. (C) Difference between temperature measurements shown in (B) and theoretical ice-water phase transition temperatures calculated with the Clausius-Clapeyron slope shown in Fig. 2 (9.14×10^{-8} K Pa^{-1}). The bottom of the cold-temperate transition zone at the end of the measurement period (982 m) is shown as a dashed black line throughout in (B) and (C). The time series was created by averaging DTS measurements over 8-hour periods regardless of active DTS sampling time, giving 8 hours of active sampling time between 5 and 21 July, 96 min between 21 and 23 July, and 20 min beyond 23 July (with 1 in 24 outputs from a 10-min sampling period; see Materials and Methods for further information).

of the record. While our recorded basal temperate zone thickness decreases significantly as the borehole refreezes in the days after installation (Fig. 3.4), this adjustment becomes gradually slower and ceases altogether on 10 August when our measurements stabilize. We take the stabilized record after 10 August (Fig. 3.3) to represent the true basal temperate zone thickness of 73 m.

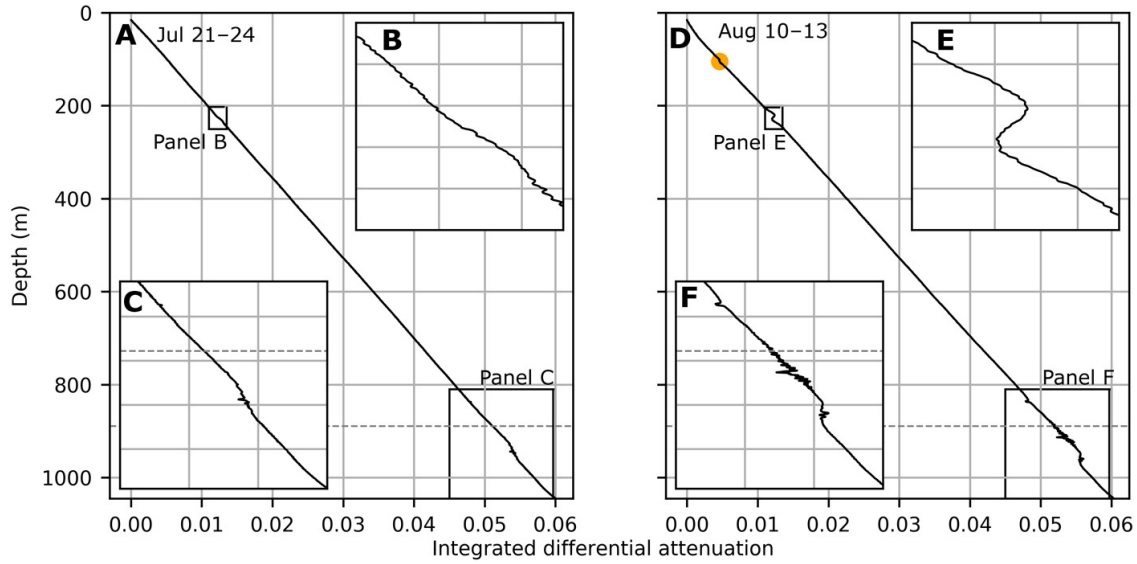

Fig. 3.5 . Integrated differential attenuation along the borehole averaged over two time periods.(A and D) Averaged integrated differential attenuation profiles recorded between 21 and 24 July (10.5 hours total sampling time) and the 96 hours before cable failure at 21:30 UTC on 13 August (3.8 hours total sampling time), respectively. Close-ups are shown in (B), (C), (E), and (F). The orange circle in (D) shows a slight perturbation that matches the location of the temperature anomaly also identified by an orange circle in Fig. 3.3C.

The raw DTS data also give a qualitative indication of cable deformation. Integrated differential attenuation (Fig. 3.5) quantifies the difference in cumulative signal attenuation between the Stokes and anti-Stokes wavelengths along the fiber and is used in calibration to correct for optical perturbations that may arise from fiber deformation through bending or extension (Tyler et al., 2013, Materials and Methods). Laboratory strain gauge testing, using the same cable as deployed in the field, showed that an integrated differential attenuation signal is first clearly visible at a strain of 1.00% and increases in magnitude up to a maximum tested strain value of 1.85% (figs. 3.14 to 3.11). We see a growing integrated differential attenuation signature of deformation throughout the measurement period in the exact location of Anomaly-208 (Fig. 3.5, B and E). We also see substantial variations between 889 and 935 m that vary on a meter scale (Fig. 3.5, C and F), suggesting more heterogeneous deformation than over Anomaly-208 where integrated differential attenuation varies smoothly. Below the cold-temperate transition zone, integrated differential attenuation remains as smooth as in the central section of the profile, suggesting that the cable has undergone less deformation there than in the region directly above.

3.5 Discussion

The Store Glacier temperature profile at R30 (Fig. 3.3A) is broadly consistent with theoretical estimates of ice temperature governed by advection—which in glaciers such as Store brings cold ice from high elevations to warmer settings at lower elevations—and vertically directed diffusion (Dahl-Jensen, 1989). The advective component explains why ice temperature at 580 m depth is at -21.1°C, even though near-surface ice is much warmer given a mean annual temperature of -9°C (7). Variations in ice temperatures within ∼10 to 15 m of the surface are tied to seasonal air temperature cycles (Cuffey and Paterson, 2010). Temperatures higher than the mean annual air temperature below this depth can be explained by latent heat of fusion released when water freezes in firn pores and within crevasses in the ablation area (Lüthi et al., 2015), which can extend to depths of several hundred meters (Hubbard et al., 2020). Below 580 m, the temperature increases toward the basal zone, a result of geothermal heat flux and strain dissipation heating concentrated near the bed (e.g. Doyle et al., 2018). Where the bed is wet across large regions of the GrIS's margins (MacGregor et al., 2016), and basal ice is therefore pinned at the phase transition temperature, frictional heat from basal sliding and sediment deformation and viscous dissipation of subglacial water also supply energy (Mankoff and Tulaczyk, 2017), with freeze-on of temperate ice occurring if the pressure-dependent melting point drops rapidly (Dow et al., 2018). Under such conditions, a basal temperate zone consisting of ice at the phase transition temperature may ultimately develop if strain heating exceeds the conductive heat flux away from the cold-temperate transition zone (e.g. Hutter, 1982; Krabbendam, 2016) or if liquid water in veins or fractures freezes and releases latent heat within the ice (Krabbendam, 2016). While our observations are consistent with previous records of these processes at other sites using discrete sensors, typically spaced tens of meters apart or more (Lüthi et al., 2002; Ryser et al., 2014b; Harrington et al., 2015), our continuous DTS measurements enable us to resolve both previously identified and presently undocumented thermodynamic processes in unsurpassed detail.

We separate the ice profile at R30 into three major and distinct sections, inferring (i) cold Holocene ice (0 to 889 m) characterized by smooth temperature changes and featuring the steepest sustained gradient, indicative of low and uniform deformation with isolated strain bands; (ii) cold pre-Holocene ice (889 to 970 m) characterized by a transition to a shallower, nonuniform temperature gradient and substantial variations in integrated differential attenuation, indicative of strongly heterogeneous deformation throughout; and (iii) temperate but still pre-Holocene ice (970 to 1043 m) with subtle departures from a linear Clausius-Clapeyron slope and with relatively low cable deformation. These sections and their implications are discussed in turn below.

3.5.1 Localized temperature anomalies in the upper Holocene ice

Although Anomaly-208 is unique in resolution, local temperature anomalies that could feasibly be fitted with a shape similar to Anomaly-208 have been detected in previous borehole-based studies, albeit at a lower resolution (Iken et al., 1993; Lüthi et al., 2002; Harrington et al., 2015; Doyle et al., 2018). This suggests that anomalies such as the one described here may be widespread. We consider it unlikely that Anomaly-208 is a result of the thermal influence from drilling given (i) drilling rates were fast ($\sim$1.2 m min^{-1}) and designed to produce a borehole with a uniform diameter of approximately 12 cm using a specialized model (fig. 3.12) through solid ice with no firn present, (ii) borehole drilling rates for proximal boreholes also varied smoothly over this depth range (fig. 3.12), and (iii) additional heat input in this depth range during drilling would increase the borehole diameter and lengthen the time until borehole freezing, which was not observed (Fig. 3.4).

Anomaly-208 may then hypothetically be a result of a latent heat source, historic deposition of snow at elevated temperatures, or enhanced deformation. A latent heat source from freezing of a nearby water-filled crevasse would, however, lead to a thermal influence over a much greater vertical extent than we observed, as recorded at the terminus of Bowdoin Glacier further north (Seguinot et al., 2020), and would not lead to the sustained cable deformation we report (Fig. 3.5, B and E). In addition, water freezing in crevasses or conduits cannot explain the heat sink above the anomaly, which is required to maintain its shape on multiyear time scale (Fig. 3.6). Deposition of snow at elevated temperatures in a past climatic event can also be ruled out as this would produce a far more diffuse profile (Dahl-Jensen et al., 1998). We therefore hypothesize that strain heating can explain the temperature anomaly, with additional evidence provided by the integrated differential attenuation recorded in the optical fiber at exactly the same depth (Fig. 3.5, B and E). The integrated differential attenuation record shows that the cable froze in with no measurable deformation, but increasing strain was placed on the cable at the exact location of Anomaly-208 over the duration of the measurement period.

In a simple vertical one-dimensional (1D) heat diffusion model, Anomaly-208 rapidly ($\sim$1 year) loses much of its shape and magnitude if there are no heat inputs or sinks (Fig. 3.6) but is maintained when a square-wave heat input of 30.8 mW m^{-2} is added between 222 and 227.5 m together with a heat sink of 10.8 mW m^{-2} between 208 and 216 m (Materials and Methods). This energy input and sink can be used to estimate the associated deformation rate. If ice is assumed to deform in simple shear, we obtain a deformation velocity integrated over the shear band thickness of 14 m a^{-1} (see Materials and Methods for calculation and creep parameter uncertainty). When the heat sink is assumed to be the result of an advective flux with constant velocity through depth, we obtain a deformation

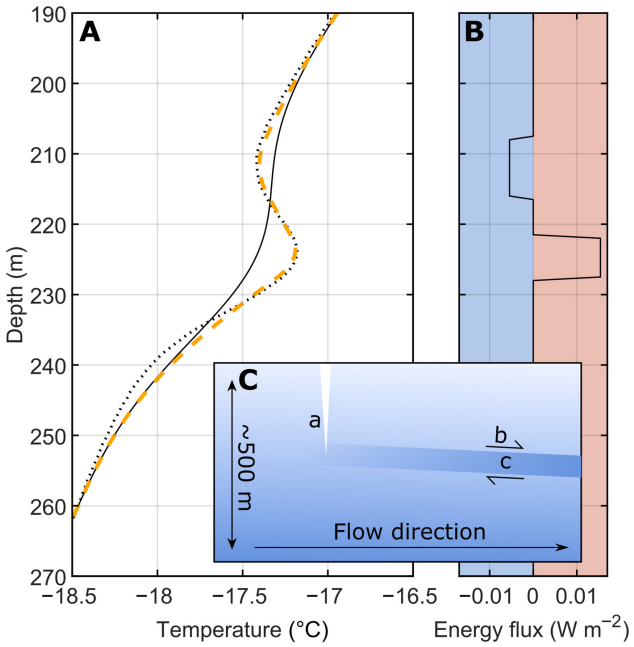

Fig. 3.6 . Temperature anomaly reproduced in a simple strain band model.(A) Ice temperature distribution of Anomaly-208, with dotted black line showing the final observed temperature profile. Solid black line is a theoretical temperature profile after 400 days of vertical diffusion and no horizontal advection. Dashed yellow line is temperature profile obtained with a strain band model with square-wave heat source and sink as shown in (B). (B) Energy flux input and sink used in the model. (C) Schematic representation of strain band (darkening blue band) with (a) possible deep fracture, (b) advecting cold ice, and (c) concentrated deformation.

velocity of 8 m a^{-1} (Materials and Methods). Although, once installed, the borehole cable moves with the ice (a Lagrangian reference frame), the influence of ice advection and deformation that occurred prior to installation (a Eulerian reference frame) is recorded by the installed cable, as the magnitude of subsequent changes relative to the inherited signal is small. The advective flux described here is assumed to be composed of incoming cold ice that has not yet been thermally affected by localized strain heating, similar to the interpretation of Hills et al. (2017), who argued that a negative change in ice temperature in a setting where vertically directed heat diffusion and strain heating would be expected to increase temperature must result from advection. This requirement for an advective heat sink implies that heat production and Anomaly-208 are spatially localized features. A deformation rate of 8 to 14 m a^{-1} accounts for roughly 2% of surface velocity (600 m a^{-1} at R30), or 7% of internal ice deformation if internal deformation and basal motion are partitioned similarly to previous borehole observations at site S30, located 8.9 km away (Fig. 3.2, Doyle et al., 2018).

Enhanced deformation could result from stress perturbations, local rheology changes, or both. Volcanic ash would reduce viscosity, in the same manner that wind-blown dust softens glacial ice (Paterson, 1991), and volcanic events are well recorded in GrIS ice cores (Sigl et al., 2015) over the radio stratigraphy age estimate for Anomaly-208 (0 to 3 ka,

Macgregor et al., 2015). However, the relative smoothness of Anomaly-208 over a depth range of 30 m, which contrasts with temperature and integrated differential attenuation perturbations within pre-Holocene ice (discussed below), suggests that it is not caused by one or a series of discrete thin horizons. As crevasses prevent non-orthogonal stress transfer (Colgan et al., 2016) and water-filled crevasses were observed to a maximum depth of 265 m in a borehole drilled 1 km away at site R29 (Fig. 3.2, Hubbard et al., 2021), we instead hypothesize that Anomaly-208 is a result of increased deviatoric stress below the depth of maximum crevasse propagation or a result of longitudinal and lateral stress transfer from spatially varying bed conditions (e.g. Ryser et al., 2014a). With similar integrated differential attenuation signatures tied to other temperature anomalies at 100 to 110 and 837 m depth, we further hypothesize that strain heating can occur within Holocene ice as well as within pre-Holocene ice in which variable deformation is more commonly observed (e.g. Lüthi et al., 2002; Ryser et al., 2014b; Doyle et al., 2018).

3.5.2 Enhanced deformation in pre-Holocene ice

Pre-Holocene ice is typically identified geophysically by lower reflectivity in radio-echo sounding data (Karlsson et al., 2013) or an anisotropic reflection in active seismic data (Hofstede et al., 2018). Pre-Holocene ice has a higher dust and impurity content than Holocene ice, impeding grain growth such that crystals remain smaller in the former. It also has a strongly anisotropic rheology (Herron et al., 1985), with a near-vertical c-axis orientation that develops from bed-parallel shear (Kuiper et al., 2020a), meaning the strain rate of this ice is sensitive to the orientation of the applied stress field. Consequently, deformation rates are typically 2.5 to 5 times greater in pre-Holocene ice than in Holocene ice under similar temperature and stress conditions (Dahl-Jensen and Gundestrup, 1987; Paterson, 1991; Kuiper et al., 2020a). The inferred transition from Holocene to pre-Holocene ice (i.e., the Last Glacial-Interglacial Transition) at 889 m depth (85% of the ice thickness) matches the transition from isotropic to anisotropic ice recorded at ∼880 m depth in the same borehole using distributed acoustic sensing with 10-m spatial resolution (Booth et al., 2020). The inferred Last Glacial-Interglacial Transition also agrees well with the depth inferred previously from seismic studies of this transition at site S30 on Store Glacier (84%, Hofstede et al., 2018), and it falls within the estimated range for the Last Glacial-Interglacial Transition in a wider regional study (82 to 85%, Karlsson et al., 2013). While pre-Holocene ice properties are well studied, we are the first to report the thermal and physical manifestation of these properties, and those of the Last Glacial-Interglacial Transition, on a glacier in a marine-terminating drainage basin.

The drop in temperature gradient (53%) across the Last Glacial-Interglacial Transition is consistent with increased strain heating through the pre-Holocene ice, while the larger-scale variations (>5 m) in temperature gradient (e.g., 915 m depth) are consistent with enhanced strain heating similar to that associated with Anomaly-208, discussed above. If these variations are a result of deformational folds (Bons et al., 2016), these folds would need to occur on a small scale (5 m). The highly heterogeneous integrated differential attenuation response (Fig. 3.5) further suggests that enhanced strain may occur at a submeter scale, consistent with deformation trends determined from ice core records at the North Greenland Eemian Ice Drilling (NEEM) site for pre-Holocene ice at premelting temperatures (>-10°C, Kuiper et al., 2020a). The location of cable failure falls exactly at this step change in temperature gradient, suggesting that the Last Glacial-Interglacial Transition is a high-strain interface. This is expected as the less viscous Holocene ice would be more capable of transferring stress, as hypothesized at the ice stream margin of Jakobshavn Isbræ (Lüthi et al., 2003), in slower flowing ice 30 km further north of Jakobshavn Isbræ due to changes in the subglacial hydrological system at the end of the melt season (Ryser et al., 2014a) and in much smaller valley glaciers (e.g. Willis et al., 2003). Our results indicate that this behavior also occurs at Store Glacier.

Heterogeneous ice deformation and fabric in pre-Holocene ice are extensively studied at ice core sites at interior locations near ice divides, where ice flow is slow (e.g. Dahl-Jensen and Gundestrup, 1987; Kuiper et al., 2020a). Our results, specifically the integrated differential attenuation, indicate that meter- or submeter-scale deformation heterogeneity in pre-Holocene ice may also be important for the fast motion of marine-terminating glaciers such as Store. This is important as this variability is not well represented in the widely applied Nye-Glen isotropic flow law (Nye, 1953; Glen, 1955) and as pre-Holocene ice is generally interpreted to be responsible for most of the ice deformation occurring in fast-moving outlet glaciers (e.g. Ryser et al., 2014b; Doyle et al., 2018). The reason that such heterogeneous ice deformation has not previously been observed on glaciers such as Store may stem from strain being estimated by discrete sensors in cabled borehole studies, which may not have sufficiently high spatial resolution to fully capture the spatial heterogeneity (e.g. Doyle et al., 2018; Lüthi et al., 2002), with the exception of Ryser et al. (2014b) who captured this heterogeneous behavior within the limits of 40-m sensor spacing. The more limited spatial resolution in discrete inclinometer studies compared to DTS may mean that strain-banding location has been missed or overlooked in previous studies, possibly leading to an overestimation of basal motion.

The cold-temperate transition zone itself is often described as a discrete, isothermal surface in ice-sheet models (e.g. Hutter, 1982) and inferred as such between discrete temperature sensors (e.g. Lüthi et al., 2002; Doyle et al., 2018). However, we observe its

presence as a change in temperature gradient over 23 m, which supports Lliboutry (1976) and Lliboutry (1993) who proposed a "fuzzier" or diffuse transition due to changes in pressure in veins and lenses and a dependence of melting temperature on the scale of ice crystals. While 23 m (959 to 982 m) falls below the resolution of most models, a "fuzzy" cold-temperate transition zone, as observed here, may have important implications for hypothesized processes that shift the cold-temperate transition zone position, such as water movement through the ice matrix (Krabbendam, 2016) or basal crevassing (Harper et al., 2010).

3.5.3 Temperate ice beneath the cold-temperate transition zone

The basal temperate ice recorded at R30 is substantially thicker than that at site S30, located only 8.9 km away (Fig. 3.2, Doyle et al., 2018), where thermistors close to the bed constrain temperate ice thickness to at most a few meters. Furthermore, boreholes drilled only 1 km away at site R29 in 2018, where ice thickness is 950 m, limit the basal temperate zone to a maximum of 14 m there (Hubbard et al., 2021). This shows that the vertical extent of temperate ice can vary greatly over distances as short as one ice thickness. Investigations of Jakobshavn Isbræ (Iken et al., 1993; Funk et al., 1994; Lüthi et al., 2002; Lüthi et al., 2009) also reveal a markedly varying temperate zone thickness, with as much as 300 m or ∼10% of the total ice thickness inferred as basal temperate ice near the center of the ice stream, although the borehole at that location did not reach the bed. However, Funk et al. (1994) interpret this to arise from convergent flow into a bedrock trough that is 1.5 km below sea level, whereas our study region exhibits lower convergence (Fig. 3.2) and bedrock topography amplitude is <500 m (fig. 3.13). This distinction between Jakobshavn Isbræ and Store Glacier implies that basal temperate zone thickness may be attributable not only to convergent flow into a bedrock trough but also to spatially varying basal conditions.

Because diffusive heat flux is directed away from the cold-temperate transition zone in both vertical directions (precluding conductive transfer of basal heat inputs into cold ice above the cold-temperate transition zone), a continuous heat source is needed to maintain it. Potential heat sources are advective heat flux, strain heating, and latent heat of freezing from movement of water through grain boundaries or fractures (Krabbendam, 2016). Basal melting from geothermal heat flux, high viscous heat dissipation from turbulent melt water (Mankoff and Tulaczyk, 2017), and sliding across high-traction sticky spots may also reduce the thickness of the temperate zone. The variability in the thickness of the temperate zone ice we record in this sector of Store Glacier (∼5 to 73 m) therefore indicates that the conditions responsible for temperate zone thickness are similarly variable over distances of ∼1 to 10 ice thicknesses. We hypothesize that the greater temperate ice

thickness at R30 compared to R29 may be a result of local variations in strain heating as the ice passes through a bedrock saddle (fig. 3.7) or encounters variations in subglacial sediment properties and drainage conditions. Booth et al. (2020) show that borehole R30 at Store Glacier is likely to be underlain by consolidated sediment, the shear strength of which may vary depending on porosity and water supplied in subglacial drainage pathways (Clarke, 2005), and Hofstede et al. (2018) report notable differences in the availability of water at the ice-sediment interface beneath Store Glacier across distances of only a few kilometers. Alternatively, latent heat may be supplied to the cold-temperate transition zone via basal crevassing by surface water from the drainage of the overlying lake and subsequent moulin development (Chudley et al., 2019). As temperate ice exhibits strain rates 5 to 10 times greater than cold ice under equivalent stress (Duval, 1977; Krabbendam, 2016), this may have substantial ramifications for ice flow modeling in terms of both deformation profiles and basal conditions. Our findings and previous studies at Jakobshavn Isbræ (Iken et al., 1993; Funk et al., 1994; Lüthi et al., 2002) demonstrate a clear need to advance our understanding of temperate zone processes in fast-moving glaciers.

The temperate basal zone does not have a constant temperature gradient predicted by a spatiotemporally constant Clausius-Clapeyron value, water content, mean stress, and solute concentration (Fig. 3.3E). Drawing on original studies on alpine glaciers (e.g. Lliboutry, 1971; Harrison, 1972), we conclude that the temperature of temperate ice in Store Glacier varies over time scales of days and weeks. However, the temperate ice we observe is of "Canadian" type (Greve and Blatter, 2009), where water content is derived from the melting of basal ice and possible inclusion of subglacial water, rather than primarily the metamorphosis of wet firn into ice observed at valley glaciers such as Blue Glacier, Alaska (Harrison, 1972). Calculations of the influence of Clausius-Clapeyron value, shear stress, and solute concentration on temperate ice temperature (fig. 3.9, Cuffey and Paterson, 2010) show that the first two, and to a lesser degree, solute concentration, can explain the variation we observe. The variation may also result from incomplete return to the phase transition temperature following rapid decompression (Goodman et al., 1979). While it is challenging to effectively isolate the primary cause of these variations, our high-resolution temperature record helps to constrain the parameter space of water, heat, and solute transport mechanisms within basal temperate ice (fig. 3.9), which may influence the cold-temperate transition zone and exert a direct control on ice deformation rates.

Last, we do not record a substantial integrated differential attenuation response within the basal temperate zone, which is consistent with low deformation rates within basal temperate ice in previous borehole studies (Lüthi et al., 2002; Ryser et al., 2014b; Maier et al., 2019). This reduced deformation may be a result of the larger crystal fabric associated with temperate ice inhibiting grain boundary sliding and hence limiting deformation (Peltier

et al., 2000) or alternatively be a result of concentrated high deformation rates over the cold-temperate transition zone in the same manner as over the Last Glacial-Interglacial Transition. The integrated differential attenuation response at the top of the cold-temperate transition zone (fig. 3.7) supports the latter interpretation, which is further supported by previous work showing a marked reduction in ice viscosity at temperatures close to, but below, the pressure-dependent melting point due to premelting effects (e.g. Dash et al., 2006; Kuiper et al., 2020a).

3.5.4 New insights from DTS

Our results demonstrate the transformative potential of high-resolution DTS in the field of glacier thermodynamics. We have shown that substantial heat can be generated by previously unrecorded localized strain within Holocene ice, which is otherwise characterized by a smooth variation in temperature gradient. We record fundamental differences in the temperature profiles of Holocene and pre-Holocene ice, demarcated by a step change in temperature gradient and a potential high strain interface at the Last Glacial-Interglacial Transition. The underlying pre-Holocene ice is characterized by temperature anomalies and substantial integrated differential attenuation variations, suggesting strongly heterogeneous ice deformation. We identify a diffuse 23-m transition from cold pre-Holocene ice to a basal temperate zone, with less cable deformation within the temperate ice than in overlying cold ice, suggesting that deformation may be concentrated in the cold-temperate transition zone as well as the Last Glacial-Interglacial Transition. Measurements at our study site show a basal temperate zone thickness of 73 m, considerably thicker than previous measurements of <14 m at a site just 1 km distant (Hubbard et al., 2021). As temperate ice has a viscosity 5 to 10 times lower than cold ice)Duval, 1977; Krabbendam, 2016), ice deformation may therefore vary greatly over distances as short as one ice thickness. These findings demonstrate that ice deformation and temperature, both vertically in borehole profiles and spatially within catchments, exhibit greater heterogeneity than previously considered.

3.6 Materials and methods

3.6.1 Drilling and installation

Fiber-optic cables were installed in borehole BH19c, at site R30 within the drained lake L028, drilled on 4 to 5 July 2019 using the system of Doyle et al. (2018) with an additional heater pressure unit to deliver a total of 60 liters min^{-1} at a surface temperature of roughly 80°C and a 1350-m hose. To reduce the thermal disturbance to background ice temperature and thus the time for the refrozen borehole to reach equilibrium and the overall drilling time, the model of Greenler et al. (2014) was used to calculate optimum drilling speeds for a borehole diameter of 12 cm at a time 4 hours after installation using the ice temperature profile for S30 (Fig. 3.2, Doyle et al., 2018). An average drill speed of 1.2 m min^{-1}, modulated to account for colder ice in the center of the profile, was used from 0 to 1020 m, decreasing to 0.5 m min^{-1} for the final 10 m due to loading and unloading behavior in the drilling system. This contrasts with previous boreholes on Store Glacier (Doyle et al., 2018), which were drilled with a more constant speed, resulting in a variable borehole diameter that was in some places larger than necessary, and which therefore extended the time for borehole freezing. While faster speeds were theoretically possible with the supplied heat input, the narrow aperture of the drill nozzle meant that this was not mechanically feasible. Drilling ceased when the borehole rapidly drained. Fig. 3.12 shows the modeled borehole diameter for each of the three boreholes drilled to the bed in 2019.

The fiber-optic cable was attached to a thermistor-piezometer cable weighted with a 2-kg chain 280 mm above the piezometer diaphragm; this assembly was lowered to 1043 m below the ice surface, whereupon pressure readings stopped increasing, and then raised 50 mm above the inferred bed location. We used a Solifos BRUsens fiber-optic sensing cable containing two single-mode fibers [OS2, for separate distributed acoustic sensing covered by Booth et al. (2020) alongside four multimode (OM3) bend-insensitive fibers for DTS in a duplex arrangement. A stainless steel basal turnaround with an outside diameter of 15 mm and internal fiber loop of 5 mm diameter was used. The cable diameter was 4.8 mm, with fibers enclosed in a gel-filled stainless steel capillary tube further protected by stainless steel wires and a polyamide outer sheath. The hydrostatic pressure resistance of the cable was 30 MPa, with a specified installed tensile stress resistance of 3 kN. Our own tensile tests show that cable failure at 21°C actually occurs in excess of 5 kN (fig. 3.10).

3.6.2 DTS system and calibration

A Silixa XT-DTS with a 0.25-m sampling resolution and ∼0.65-m manufacturer-stated spatial resolution was configured to take measurements from the two multimode (OM3) fiber loops in sequence, connected by a basal turnaround assemblage. The manufacturer-stated spatial resolution refers to the distance over which 80% of a ∼30°C step change in temperature can be observed along the fiber (Silixa, 2018, see Tyler et al., 2009 for further details). The DTS unit was powered via a low-voltage disconnect by two 116-Ah deep-cycle lead acid batteries connected to three 45-W solar panels and contained in a large Pelican case. The batteries were topped up by a generator during field operations. To remove the need for fusion splicing in the field, E2000/APC pigtail connectors were preattached using IP68 conduits leading from a small Pelican case containing the fiber-optic splices. The measurement averaging time was originally set at 2 min with near continuous operation from 5 to 21 July whereupon it was set to 10 min with a rest time of 40 min, with the rest time increased to 4 hours on 23 July to reduce power consumption for unattended operation.

We used the open source Python "dtscalibration" package (des Tombe et al., 2020) to calculate a temperature time series, T (K), with uncertainty bounds at time t (s) and depth z (m), which builds on the standard DTS equation

$$T(z,t) = \frac{\zeta}{ln\frac{P_S(z,t)}{P_{aS}(z,t)} + C(t) + \int_0^z \Delta\alpha(z')dz'} \tag{3.1}$$

where P_S and P_{aS} are the Stokes and anti-Stokes power and ζ is the sensitivity of (anti-)Stokes scattering to temperature which is dependent on fiber material and does not vary in time. C is a dimensionless function of the alignment and sensitivity of the optical system, connectors, and splices that can vary with interrogator temperature and movement. The integral term is the integrated differential attenuation, where $\Delta\alpha(z')$ (m^{-1}) is equal to the attenuation of the Stokes wavelength minus the attenuation of the anti-Stokes wavelength and is nonzero as attenuation is related to wavelength. Strain, sharp bends, fiber microbending, and splices are known to affect differential attenuation (Tyler et al., 2009; van de Giesen et al., 2012; Tyler et al., 2013). To calculate the integrated value of this term at each point, a double-ended calibration must be used, where the DTS shoots laser pulses first in a forward direction and then in a reverse with the reasonable assumption that temperatures are equal in the forward and reverse directions (the basal turnaround assemblage marks the halfway point). The correction from integrated differential attenuation may not be perfect for highly localized, high-magnitude, cable deformation occurring

on the scale of the DTS spatial resolution (0.65 m). This may explain the very fine scale changes of <0.1°C between 889 and 935 m that occur after 8 August (Fig. 3.3D and figs. 3.7 and 3.8); these could result from heterogeneous and high-magnitude cable deformation leading to minor over- or undercompensation in the calibration procedure.

We further used the dtscalibration package to align and correct for asymmetric losses (greater attenuation in one direction than the other) in the turnaround splice, thought to be caused by differential modal spreads in (anti-)Stokes wavelength following a splice within 50 mm of a 5-mm bend radius turnaround. The dtscalibration package uses a Monte Carlo simulation to approximate the probability density function and confidence intervals of the estimated temperature and its variation with depth and time. A full description of the dtscalibration package can be found within des Tombe et al. (2020) and accompanying GitHub documentation. The spatial temperature change within the absolute 95% confidence intervals produced with this method (Fig. 3.3, A to E) has an instrument stated precision of <0.01°C under our calibration procedure (Silixa, 2018); that is to say, we have very high confidence in the observed temperature changes with depth with the possible exclusion of the <0.1°C changes discussed above but that the entire profile can shift within the absolute confidence intervals. The DTS calculates distance using the refractive index of the cable and gives a total depth of 1062 m; all depth values were therefore scaled by a factor of 0.9821.

If ζ is assumed constant as in van de Giesen et al. (2012), then only one reference section is required for calibration purposes. We use a ζ value of 476.53 K, obtained in a separate laboratory-based calibration procedure using the same DTS unit and cabling as used in the field and two precalibrated (class A, $\pm$ 0.15 + 0.002xT °C) PT100s placed into well-mixed polystyrene-insulated water baths with 25-m fiber sections at 0°C and ambient room temperature (18°C, left to settle overnight). Two hours of measurements were taken, but only the 20 min showing the lowest Stokes wavelength variance were used in the calibration. We additionally maintained an ice bath during field operations measured by the same thermistors described above. However, insufficient water mixing and a high resultant temperature variation ($\pm$0.4°C) led us to use a section of the temperate zone between 100 and 1010 m in place of the ice bath for field calibration of C and integrated differential attenuation, as the temperate zone exhibited far lower temperature variability (fig. 3.15). The ice bath was ultimately dismantled for unattended operation due to concern about high winds. The temperate zone temperature was calculated as

$$T_m = T_{tr} - \gamma(p_i - p_{tr}) \tag{3.2}$$

where T_m (K) is the depth-dependent melting point of ice, T_{tr} (K) is the triple point temperature of ice, γ is the Clausius-Clapeyron constant (K Pa-1), and p_{tr} (Pa) is the triple point pressure of ice. The local (hydrostatic) pressure, p_i (Pa), for a parallel-sided slab of ice is calculated as

$$p_i = \rho g \Pi \cos(\theta) \tag{3.3}$$

where ρ is the ice density taken as 910 kg m^{-3}, g is the gravitational acceleration (m s^{-2}), Π is the height of overlying ice (m), and θ is the ice surface and bed slope (taken as 0.96° using a linear regression along flow line using ArcticDEM surface elevation data over 10 ice thicknesses). A Clausius-Clapeyron constant of 9.14×10^{-8} K Pa^{-1} was used to provide the best fit possible for the thermistors over the last 4 days of the record and assumed constant for the full measurement period. This method has the limitation of needing to assume a constant temperature within the temperate zone but is used here for simplicity and in the absence of a more reliable method of calculating the exact temperature. A separate cable with digital temperature sensors was installed in the borehole; however, this deployment failed. Our recommendation for future studies is to use the cold central section and a temperate zone, if present, for calibration. The section between 1000 and 1010 m, rather than the basal section next to the thermistors, is used as (i) different heat capacities and thermal conductivities mean that the two sensing systems equilibrate at different rates, which has a large impact especially for the first few days, and (ii) no fit could be obtained incorporating all thermistors. As manufacturer-stated thermistor uncertainty is very low, this probably arises from a small thermistor calibration error. (iii) Initial calibration (not incorporated into the final record) using the ice bath as a reference section suggests that this section of the temperate zone exhibits the least temporal temperature variation, and (iv) this approach allows more noticeable temperature changes at the top and base of the temperate zone to be measured. A comparison of thermistor and DTS recorded temperature in temperate ice can be found in the Supplementary Materials (fig. 3.15).

3.6.3 Equilibrium ice temperature

The undisturbed ice temperature (T_{eq} in K) and root mean square error were estimated following (Humphrey, 1991; Ryser et al., 2014a) as

$$T_{eq} = T(t) - \left(\frac{Q}{4\pi k(t-s)} \right) \tag{3.4}$$

where Q (W m^{-2}) is the heat energy released per unit length of the borehole during drilling, k= 2.1 W m^{-1} K^{-1} is the thermal conductivity of ice, s is the delay in seconds until the onset of asymptotic cooling, and $T(t)$ is the temperature in Kelvin at time t in seconds. Following Ryser et al. (2014b), the parameters Q, s, and T_0 were determined by fitting Eq. 3.4 to temperature at the given depth during asymptotic cooling using the SciPy optimize.curve_fit nonlinear least squares fit function. This method produced errors at lower temperature change rates where the final observed temperature is closer to 0°C and was not used beyond 930 m depth. Borehole diameter modeling following Greenler et al. (2014) for a target diameter of 12 cm ensured that latent heat energy input was as low as possible. The final observed temperature (13 August, 6 weeks following installation) is within 0.2°C of the predicted equilibrium ice temperature at all points above 930 m (Fig. 3.3, A and B). A further 40 days would be required for the fitted exponential cooling curve to fall within 0.05°C of the predicted equilibrium temperature.

3.6.4 Strain from differential attenuation

Integrated differential attenuation was also used separately to the dtscalibration package as a measure of strain. This was calculated following van de Giesen et al. (2012) as

$$\int_{z}^{z+\Delta z} \Delta\alpha(z')dz' = \frac{\ln\left(\frac{P_s(z+\Delta z)}{P_{aS}(z+\Delta z)}\right)_{\Rightarrow} - \ln\left(\frac{P_s(z)}{P_{aS}(z)}\right)_{\Rightarrow} + \ln\left(\frac{P_s(z)}{P_{aS}(z}\right)_{\Leftarrow} \ln\left(\frac{P_s(z+\Delta z)}{P_{aS}(z+\Delta z)}\right)_{\Leftarrow}}{2} \tag{3.5}$$

where $\Rightarrow$ and $\Leftarrow$ indicate forward and reverse measurement directions, respectively, and Δz is the sampling resolution. As Raman scattering has not previously been used as a measure of strain, we conducted laboratory testing using a Testometric X350-10 stress and strain gauge in a temperature-controlled (21 ± 0.5°C) room. A 2-m section of cable of the same specification as used in the field was strained by 1.85% (ductile deformation began at 0.65%) at a maximum force of 5.8 kN. A 10-min measurement averaging time was used at each strain increment. This produced a similar disturbance to that seen in Fig. 2 (fig. 3.14).

3.6.5 Anomaly-208 heat transfer and deformation

We used a simple 1D heat diffusion model adapted from Law et al. (2020) to investigate temperature evolution in the region of Anomaly-208 with a vertical resolution of 0.5 m under (i) no heat inputs or sinks and (ii) heat inputs and sinks prescribed manually as square waves to maintain the anomaly at a steady state. The energy input and sink required to sustain the anomaly can be used to estimate the deformation rate. Strain heating, Q_s, is expressed as $Q_s = \mathrm{tr}(\boldsymbol{\tau}\dot{\boldsymbol{\epsilon}})$, where $\boldsymbol{\tau}$ is the deviatoric stress tensor and $\dot{\boldsymbol{\epsilon}}$ is the strain rate tensor (Seguinot et al., 2020; Cuffey and Paterson, 2010). Stress and strain are related via

$$\dot{\boldsymbol{\epsilon}} = A\tau_e^{n-1}\boldsymbol{\tau} \tag{3.6}$$

(Glen, 1955; Nye, 1953), where τ_e is the effective stress and $\tau_e^2 = \frac{1}{2}\mathrm{tr}\,(\boldsymbol{\tau}^2)$, and A is the creep parameter, which we take as 7.7 10^{-25} s^{-1} Pa^{-3} following aggregate values in Cuffey and Paterson (2010) (table 3.3) with the range 6.7 10^{-25} to 8.7 10^{-25} s^{-1} Pa^{-3}, used to test parameter sensitivity and the flow exponent n ≈ 3. Following Seguinot et al. (2020), effective strain rate (dimensionless), $\dot{\epsilon}_e^2 = \frac{1}{2}\mathrm{tr}\left(\dot{\boldsymbol{\epsilon}}^2\right)$, is related directly to energy dissipation as

$$\dot{\epsilon}_e = \left(\frac{1}{2}Q_s A^{\frac{1}{n}}\right)^{\frac{1}{1+\frac{1}{n}}}. \tag{3.7}$$

We follow the assumption of Seguinot et al. (2020) that deformation occurs within a 2D cross section with vertical, z, and horizontal along-flow, x, dimensions (with y perpendicular to flow), yielding effective strain in Cartesian components, $\dot{\epsilon}_e^2 = \frac{1}{2}\left(\dot{\epsilon}_{xx}^2 + \dot{\epsilon}_{zz}^2\right) + \dot{\epsilon}_{zx}^2$, and giving stress units of N m^{-2} and strain heating units of W m^{-2}. Assuming incompressibility, $\nabla \cdot \dot{\boldsymbol{\epsilon}} = \dot{\epsilon}_{xx} + \dot{\epsilon}_{zz} = 0$, gives effective strain as a function of longitudinal and shear components, $\dot{\epsilon}_e^2 = \dot{\epsilon}_{xx}^2 + \dot{\epsilon}_{zx}^2$. We neglect the longitudinal component as we are not in a zone of rapid ice thinning, but note that the effect of a longitudinal component would be to reduce the simple shear component and relate effective strain to deformation velocity, u (m s^{-1}), as (Hooke, 2005, equation 2.6a)

$$\dot{\epsilon}_e \approx \frac{1}{2}\frac{\partial u}{\partial z}. \tag{3.8}$$

Finally, assuming a constant deformation velocity with depth and combining Eqs. 3.7 and 3.8 gives

$$u \approx 2\Delta z \left(\frac{1}{2} \frac{\partial u}{\partial z} \right) \tag{3.9}$$

where Δz = 5.5 m is the height over which deformation is occurring. This gives a deformation velocity of 14.2 m a^{-1} with limits 13.7 to 14.7 m a^{-1} for creep parameters 6.7 × 10^{-25} and 8.7 s^{-1} Pa^{-3}, respectively.

We further constrain deformation velocity by assuming that the heat sink is a result of an advective flux prior to cable installation with constant velocity through depth within a z x plane to give (e.g. Caissie and Luce, 2017)

$$u = \frac{Q_a}{\rho C \Delta T} \tag{3.10}$$

where Q_a is our advective energy sink (W m^{-2}). Here, the depth over which advection occurs does not need to be considered. We take the specific heat capacity of ice at -17°C as 1.972 kJ kg^{-1} K^{-1}. Taking a value of ΔT of 0.2 K, the difference between the peak and trough of the anomaly gives a velocity of 8.2 m a^{-1}.

3.7 Acknowledgments

We thank A. Andreasen and Uummannaq Polar Institute for hospitality. We are grateful to S. Tyler and CTEMPs Instrument Facility for technical guidance; L. Greenler for providing code for modeling borehole diameter; M. MacKie, S. Peters, M. Prior-Jones, and E. Dawson for assistance in the field; and N. de Battista for help with strain gauge testing. We thank A. Aschwanden and two other anonymous reviewers for comments. **Funding:** This research was funded by the European Research Council as part of the RESPONDER project under the European Union's Horizon 2020 research and innovation program (grant 683043). R.L. and T.R.C. were supported by Natural Environment Research Council Doctoral Training Partnership studentships (grant NE/L002507/1). B.H. was supported by a HEFCW/Aberystwyth University Capital Equipment Grant. **Author contributions:** R.L. and P.C. designed the DTS experiment. P.C. led the field operations. B.H. and S.H.D. led the drilling work. R.L., P.C., B.H., S.H.D., T.R.C., C.M.S., and A.B. collected data in the field.

R.L. analyzed the DTS data with support from B.d.T. and B.S. C.K. advised in laboratory experiments for integrated differential attenuation. R.L. wrote the manuscript with help from all coauthors. **Competing interests:** The authors declare that they have no competing interests. **Data and materials availability:** All data needed to evaluate the conclusions in the paper are present in the paper, the Supplementary Materials, and the Apollo repository (available at https://doi.org/10.17863/CAM.65812).

3.8 Supplementary Material

3.8.1 Temperate zone temperature variation

We examine the variation in temperate zone temperature to four parameters: water content, solute concentration, air content, and pressure (Harrison, 1972). Eq. 3.2 in the main text is expanded, and P_0 = 611.73 Pa is small and omitted to give (Cuffey and Paterson, 2010; Lliboutry, 1976)

$$T_m = T_0 - \gamma P_i - \frac{AS}{W} \tag{3.11}$$

where A = 1.86 K kg mol^{-1} is a constant (Lliboutry, 1976), S is salt concentration in mol kg^{-1}, and W is water fraction. Defining $\Delta T_m = T_{m_1} - T_{m_2}$ gives the following relationships when the variables not preceded by Δ are fixed:

$$\Delta T_m = -\Delta\gamma P_i, \tag{3.12}$$

$$\Delta T_m = \frac{-A\Delta S}{W}. \tag{3.13}$$

The pressure-dependent melting point of ice is often discussed in terms of hydrostatic stress, $\tau_{hyd} = \frac{1}{3}\text{tr}(\boldsymbol{\tau})$. We follow Harrison (1972) and use the first principle stress, σ_1, (defined as the largest eigenvalue of the stress tensor) as P_i in Eq. 3.2 (main text) to account for deviatoric stress components. In this way $\sigma_1 = \rho g(\cos(\theta) + \sin(\theta)) + \tau_{xz}$ if $\tau_{xy} = \tau_{yz} = 0$ (plane strain) and $\sigma_{xx} = \sigma_{yy} = \sigma_{zz} = \rho g h \cos(\theta)$. We note that if part of the cable is within a cavity, σ_1 will still account for a hydrostatic pressure increase, and if $\tau_{xz} = \tau_{xy} = \tau_{yz} = 0$, σ_1 will be equal to the largest confining stress. From here, defining $T_m = T_0 - \lambda\sigma_1$, $T_{m_1} = T_0 - \lambda\sigma_{zz}$, $T_{m_2} = T_0 - \lambda(\sigma_{zz} + |\tau_{xz}|)$, and $\Delta T = T_{m_2} - T_{m_1} = \lambda|\tau_{xz}|$ gives

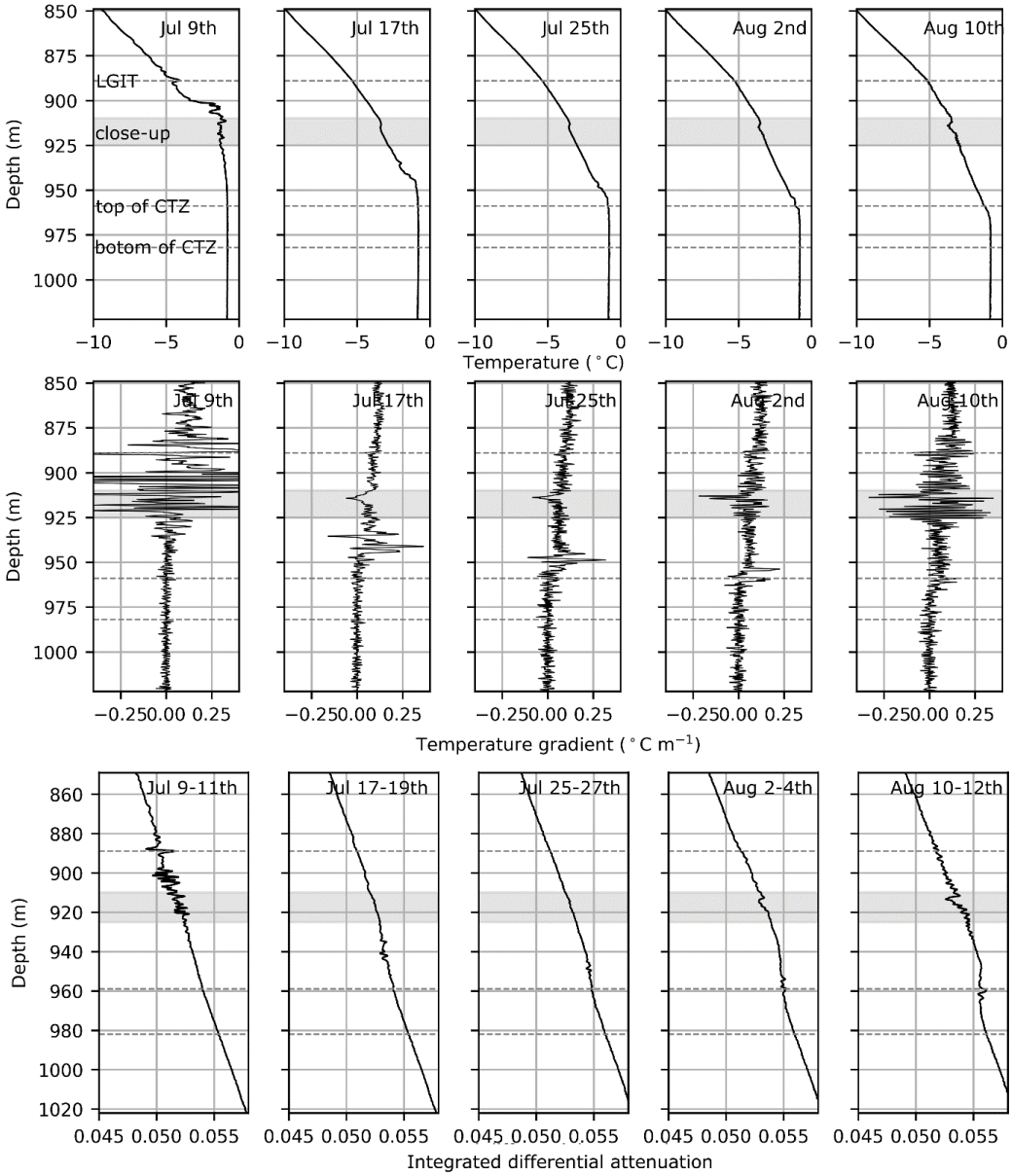

Fig. 3.7 . Close ups between 850 and 1020 m of temperature, temperature gradient, and integrated differential attenuation. Top left panel indicates the significance of horizontal dashed lines and shaded area. The close-up between 910 and 925 m can be found in Fig. 3.8. The top two rows of measurements are obtained from one 10-minute sampling interval, the bottom row is an average of all measurements over a 2 day period.

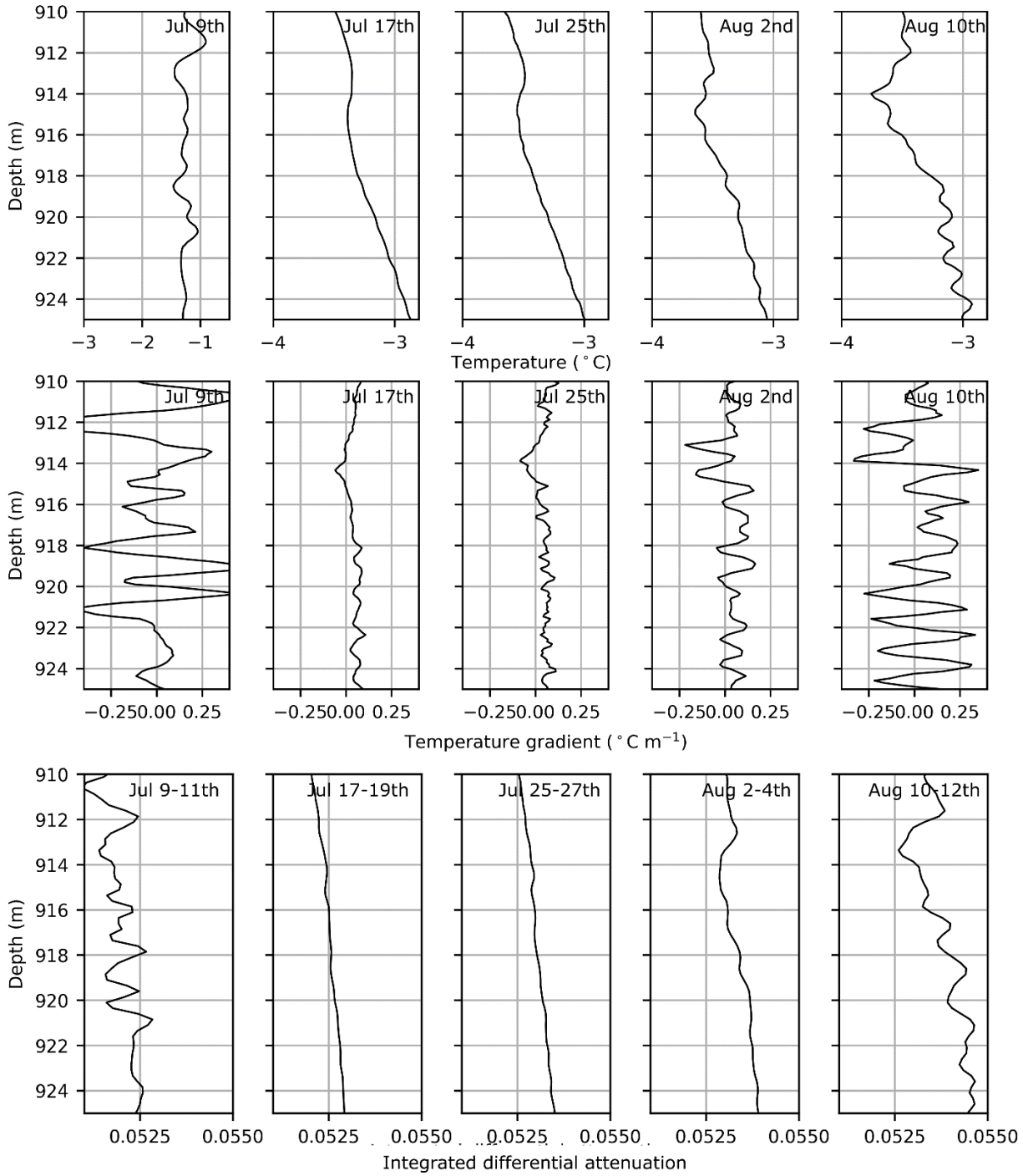

Fig. 3.8 . Close ups between 910 and 925 m of temperature, temperature gradient, and integrated differential attenuation. Calculated as Fig. 3.7 but different x- and y-axis scales.

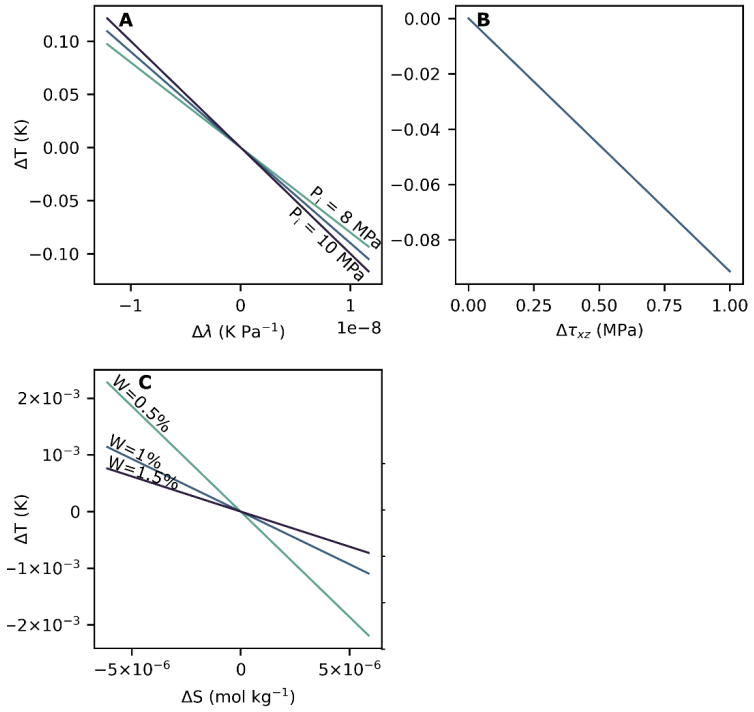

Fig. 3.9 . Parameter influence on temperature. Temperature change ΔT, in response to a change in A: Clausius-Clapeyron value, $\Delta\lambda$, B: deviatoric stress measure (or pressure increase if rheology is controlled by fluid-phase), $\Delta\tau_{xz}$, C: solute concentration, ΔS.

$$|\tau_{xz}| = \frac{\Delta T}{\lambda}. \tag{3.14}$$

We then set λ= 9.14 × 10^{-8} K Pa^{-1} as above to calculate the required τ_{xz} to bring about the temperature variation. If we modify Eq. 3.11 to determine the dependence of ΔT on ΔW, the result is asymptotic and gives unreasonable values when $W_1 + \Delta W \to 0$ where W_1 is an initial water content value. For this reason, we have omitted this relationship but note its possible importance in further temperate zone studies.

3.8.2 Strain from differential attenuation

In support of the discussion, we propose that variation in differential attenuation can be taken as a novel qualitative measure of significant strain. This follows from (i) laboratory tests under controlled conditions for strains of $\geq$1% showing a similar signal to the one we observe in the borehole profile, and (ii) the fact that the differential attenuation signal develops over time in areas of suspected strain, demonstrating that it is not a function of temperature change within the profile. The observed signal may be explained by exten-

sional strain reducing the cross-sectional area of the fibre and increasing the attenuation of the Stokes wavelength which has a greater mode area (Paschotta, 2008a). However, more in depth testing and theoretical work would be required to thoroughly understand the photonic basis.

We note that this relationship will be complicated by the cable being overstuffed by 1% and being loose buffered which allows free movement of the fibre within the cable. This may explain the lack of an integrated differential attenuation signature within the majority of Holocene ice whereas the possible large localized horizontal movement at Anomaly-208 could create a bend in the cable and loose tube, increasing friction and reducing the freedom of the optical fibres thereby putting them under strain during elongation of the cable. A similar effect may also have influenced the lab tests, where the tensile rig used requires coiling the cable on capstan clamps multiple times around a tight bend radius (∼50 mm) to isolate the section under examination. Alternatively, the low ice temperature, particularly at Anomaly-208 may have affected the viscosity of the gel contained within the fibre.

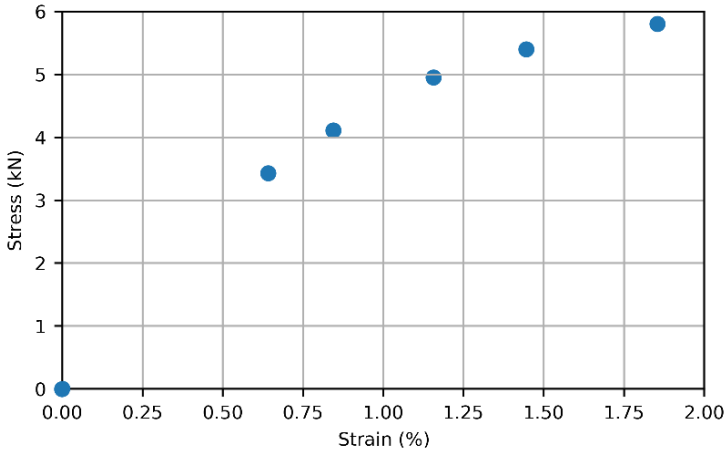

Fig. 3.10 . Stress-strain trend for cable during lab testing. This test was not run until failure.

3.8.3 DTS-thermistor comparison

We hypothesise that the discrepancy observed in early July (fig. 3.15) is a result of the greater heat capacity of the thermistor units, and our usage of a fixed calibration temperature within the temperate zone. The ±0.05 °C value for thermistors is as stated by the manufacturer, with calibration in a distilled-water-ice bath in a laboratory using the fully constructed thermistor strings. Additional sources of measurement uncertainty that are harder to quantify are not included, these include: datalogger, half-bridge circuit, and long cable effects such as voltage drop and stray capacitance. This shows that absolute

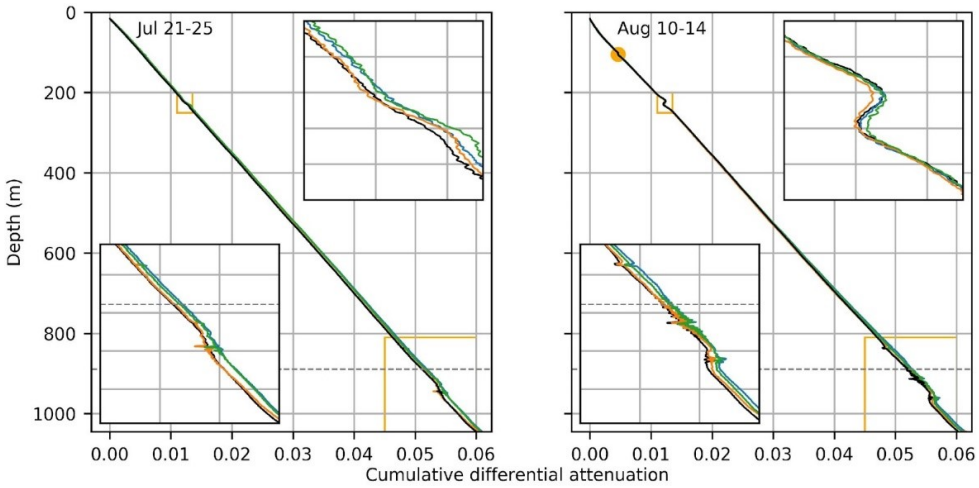

Fig. 3.11 . Borehole integrated differential attenuation for 4 fibres. As for Fig. 3.3 E-H in the main text but showing integrated attenuation for each available fibre section. Black is channel 1 down, blue is channel 1 up, orange is channel 3 down, green is channel 3 up. The variation is likely a result of the gel within the fibre allowing some internal movement. This shows that the trend is replicated across fibres within the cable.

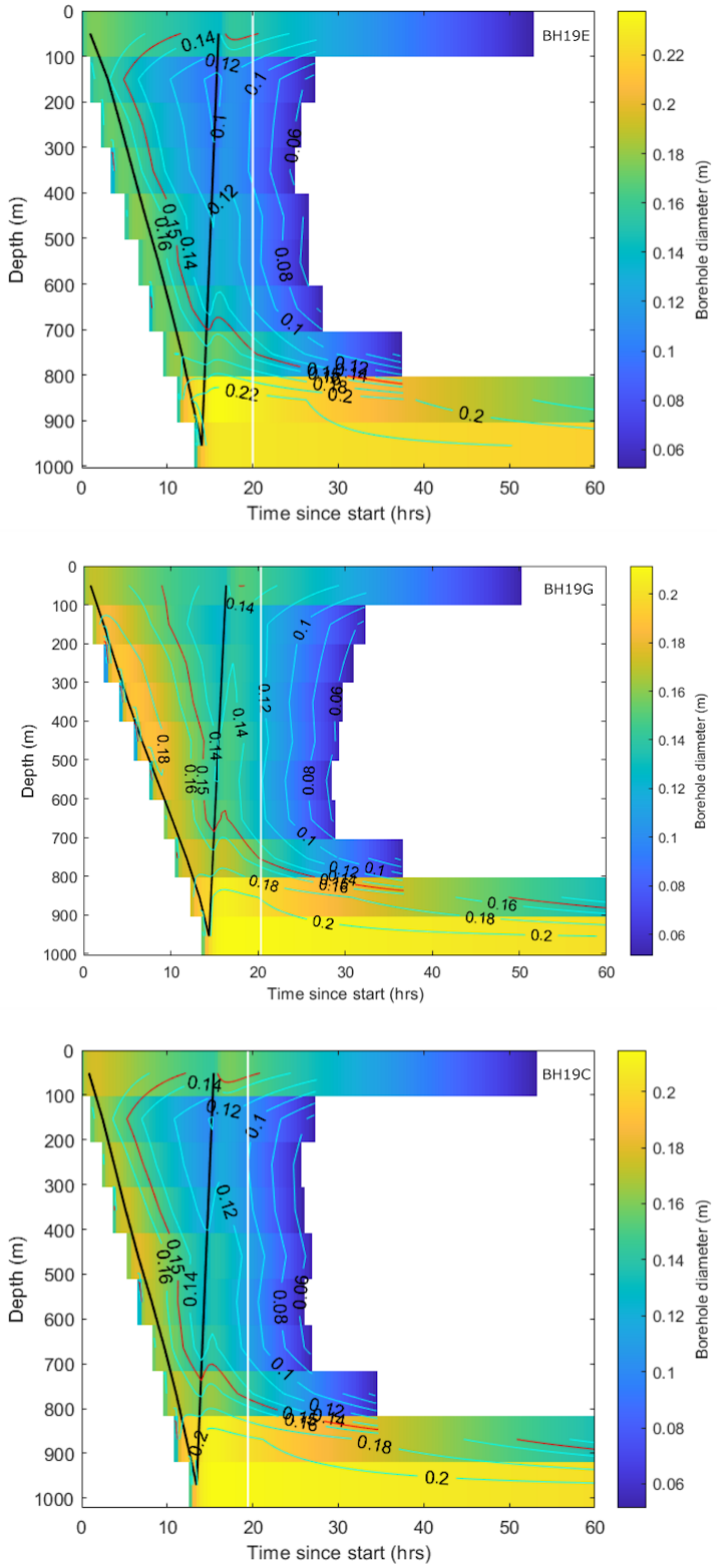

Fig. 3.12 . Modelled borehole diameters. Modelled using observed temperature in BH19C, recorded drill rates, and the model of Greenler et al. (2014). Contours are 2 cm diameter spacing, the black line shows the progress of the drill head, and the red line highlights the diameter of 15 cm.

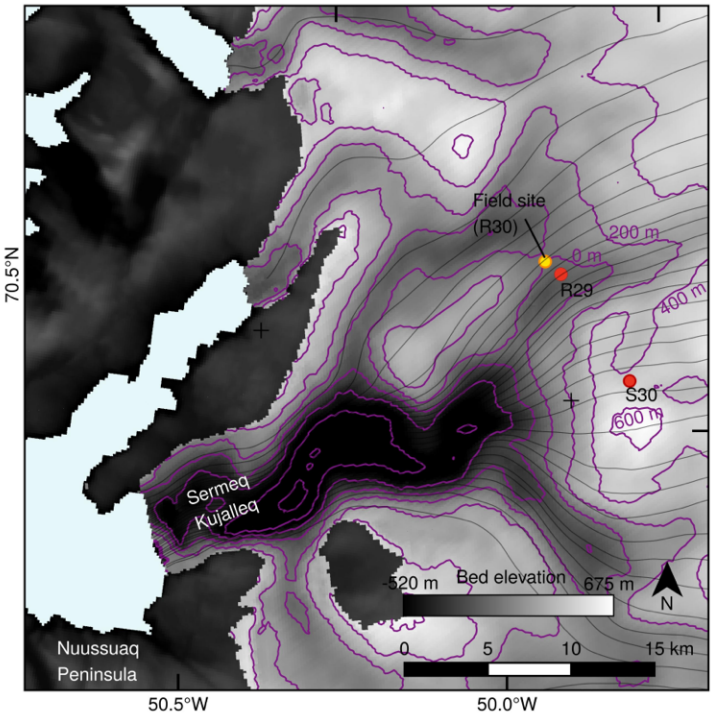

Fig. 3.13 . Bedrock topography around R30, Store Glacier. 200 m bed topography contours in purple (BedMachine v3, Morlighem et al., 2017). Ocean in light blue. Terrestrial topography in dark-grey to black.

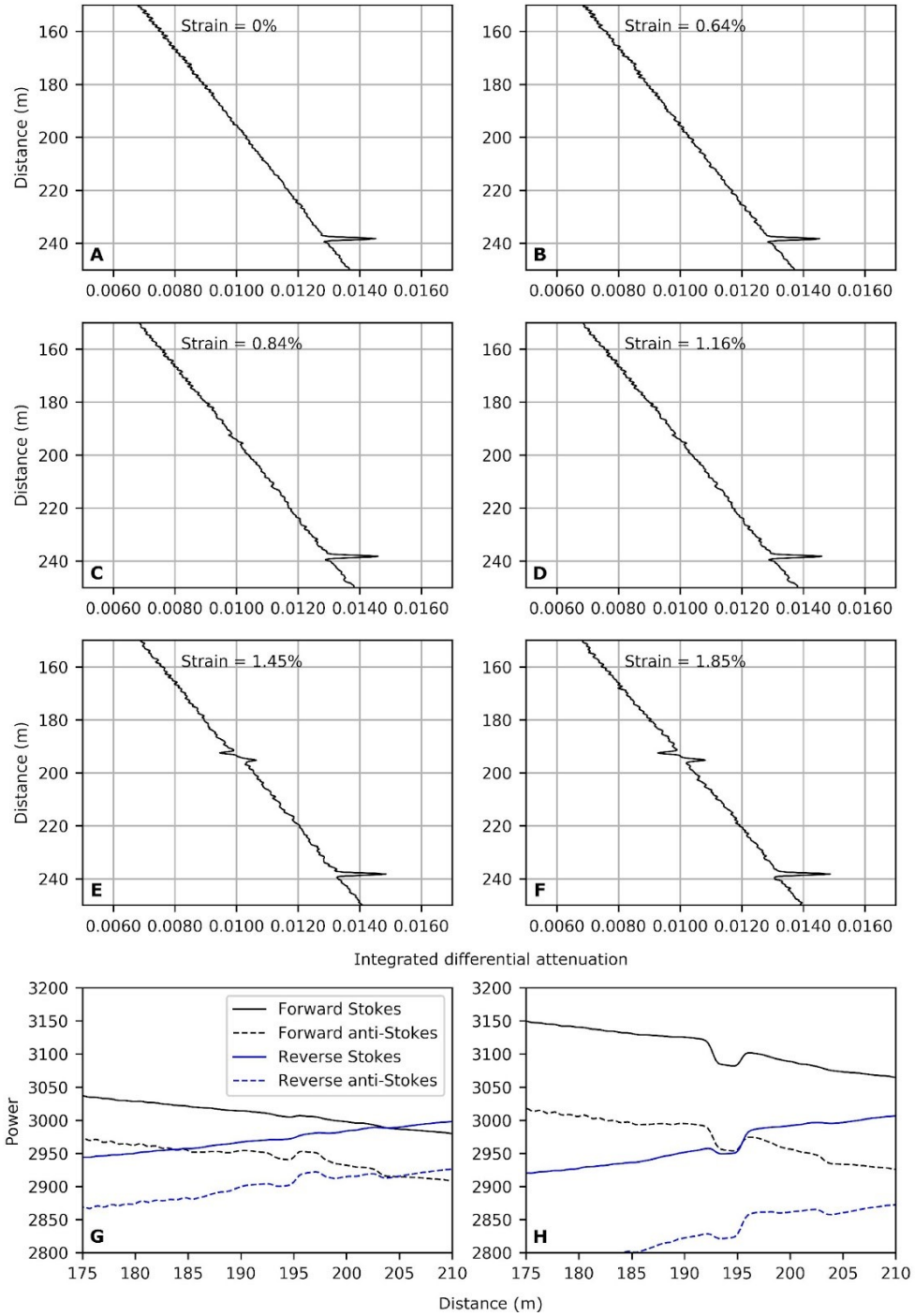

Fig. 3.14 . Lab testing of integrated differential attenuation. A-F: Integrated differential attenuation at varying levels of strain during lab testing with the Testometric X350-10 tensile testing machine at a controlled temperature of 21 $\pm$ 0.5°C and a ten-minute measurement averaging time. Strained location is 193-195 m which was determined prior to extension using a hot air gun to locate the cable sections. The splice and bend is at 239 m and also prompts an integrated differential attenuation response which is likely down to different modal spreads in (anti-)Stokes wavelengths as they pass around a tight bend following minor splice dispersion. G: (anti-)Stokes data at 0% strain. H: (anti-)Stokes data at 1.85% strain where the x axes is distance.

uncertainty in DTS measurements is roughly equivalent to thermistor uncertainty. However, when thermistors are used to calibrate a DTS record, the additional uncertainty this presents should also be taken into account. The time series was created by averaging DTS measurements over 8-hour periods, regardless of the total time the DTS had been actively recording. Therefore, 8 hours of sampling time for temperature profile outputs between 5-21 July, 96 minutes for temperature profile outputs between 21-23 July, and 20 minutes beyond 23 July (with 1 in 24 outputs being derived from a 10 minute sampling period). See Materials and Methods for sampling intervals. This shows the decrease in DTS accuracy that comes with decreasing averaging time for unattended operation with lower power usage, though note that Fig. 3.3A-E use an extended averaging period of 4 days.

The gradual decrease in temperature of the thermistor record can be explained by gradual borehole freezing of temperate ice as the borehole has lower solute concentration and thus higher pressure-dependent melting point than surrounding temperate ice with increased solute concentration in the liquid phase (Harrison, 1972). The opposing trends in panel C may be a result of the cable and thermistor being in different sections of the borehole (as theorized in Doyle et al., 2018). For example, if one area of the borehole is freezing another will gain the latent heat, and both areas (one warmer than the other) should equilibrate in different directions. There will also be a small degree of instrument self-heating in the thermistors (Ryser et al., 2013).

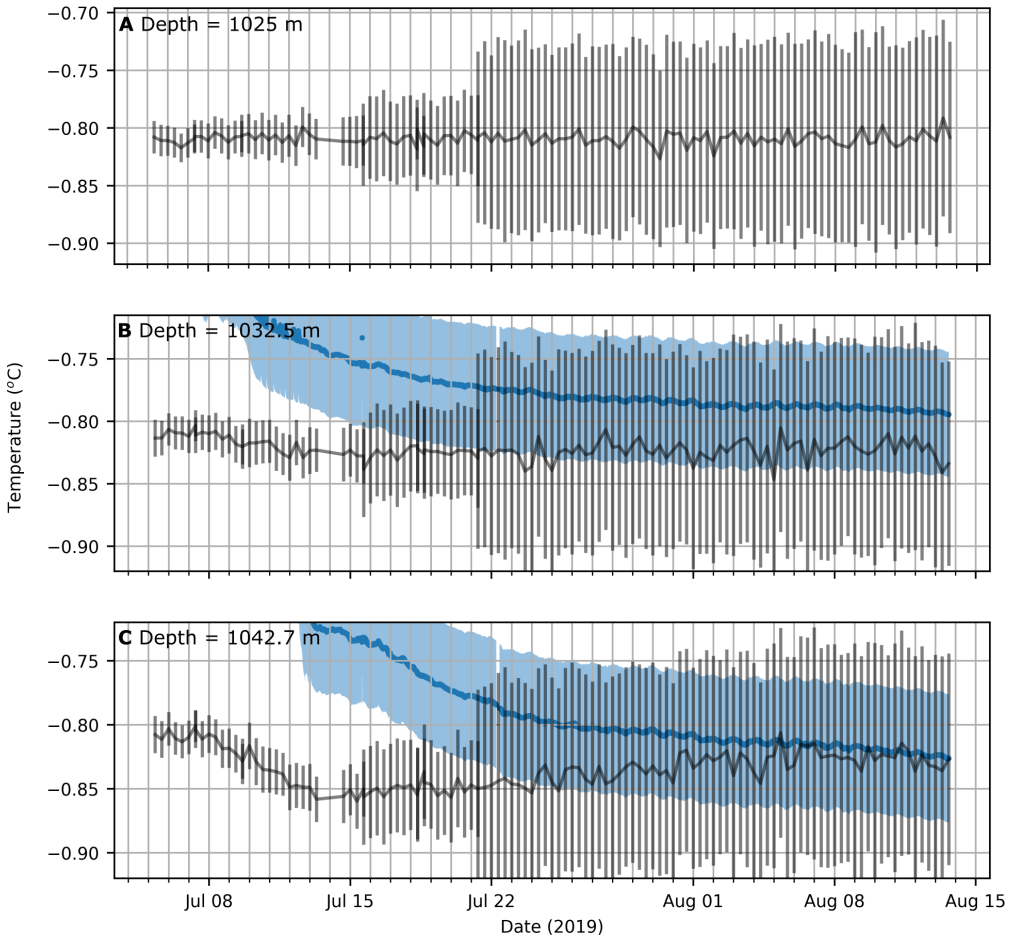

Fig. 3.15 . DTS-thermistor comparison. DTS temperature time series (black, with 95% confidence intervals for absolute uncertainty) at three locations within the temperate zone with comparison to two thermistors (blue, with shaded error boundary of ±0.05 °C).

Chapter 4

Results II: Complex motion of Greenland Ice Sheet outlet glaciers with basal temperate ice

4.1 Preface

The results of this chapter were submitted as '*Complex motion of Greenland Ice Sheet outlet glaciers with basal temperate ice*' to Science Advances on 10 May and are now under review. A preprint of the manuscript, which has not undergone peer review, is available on EarthArXiv (Law et al., 2022). After notes on the background and author contributions, the paper is presented as submitted, with minor alterations in order to conform with thesis formatting requirements and minor notation changes for consistency across chapters. This chapter makes reference to repository data — the intention is to upload this following acceptance for publication in a journal to avoid repeated repository uploads.

4.1.1 Setting

This study arose directly from the results of chapter 3 and was initially solely focused on variation in temperate layer thickness across Sermeq Kujalleq, beginning at the very start of the Covid-19 pandemic. I initially attempted to understand the variation in temperate layer thickness using a 1D vertically-oriented finite-difference model. However, after a couple of months it became apparent that the horizontal advection component of this problem was simply too complex and I switched focus to 3D modelling in Elmer/Ice.

I began to look at simple sinusoidal obstacles, which could already partly account for temperate layer thickness variability, but wanted to apply my model to more realistic settings to see if this could reconcile borehole observations from the GrIS. So, with help from Mickey MacKie, I then ran the model over a flat bed, with roughness prescribed based on variograms constructed using flight line data from the whole of the GrIS. Here things began to get really interesting, and it seemed that highly variable basal slip was an important part of the story. However, to test more local variability in ice motion and

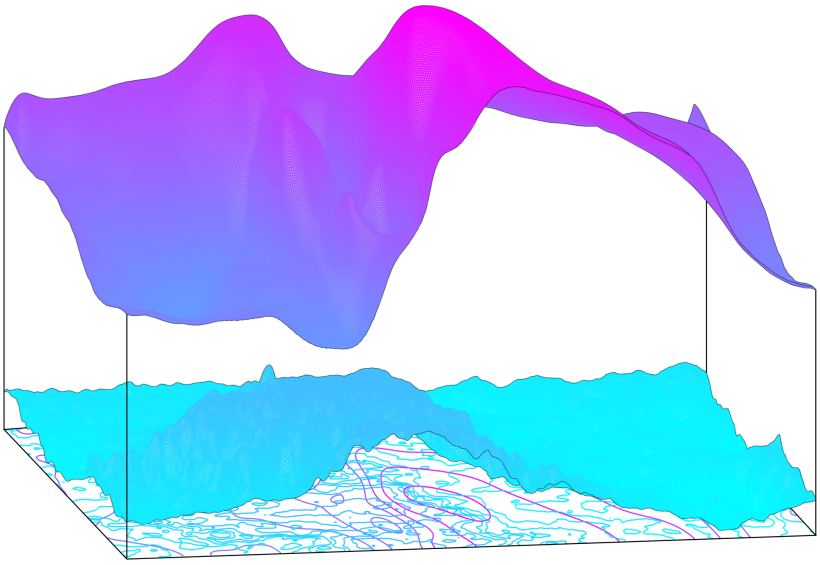

Fig. 4.1 . Surface pressure field (upper plane) that results from geostatistically simulated basal topography (lower plane), using a realisation over flat topography (without BedMachine) that wasn't included in the final paper. Ice motion is left to right through periodic inflow-outflow boundaries.

to enable direct comparison with borehole records, I applied the model to variogram simulated topography overlain on BedMachine topography centred on a central borehole observation record. The results from these runs, which suggest complex patterns of basal slip, internal deformation, and temperate layer variability are an inexorable part of GrIS outlet glacier motion, are presented below.

4.1.2 Contributions

I designed the study with input and support from Poul Christoffersen. Emma 'Mickey' MacKie provided scripts and variograms for the generation of DEMs. Samuel Cook helped me get set up with and troubleshoot Elmer/Ice. Marianne Haseloff gave support on numerical and mathematical implementation. Olivier Gagliardini provided technical Elmer/Ice support, useful discussions on basal motion, and office space for a month at IGE.

4.2 Abstract

Uncertainty associated with ice motion plagues sea-level rise predictions. Much of this uncertainty arises from imperfect representations of physical processes including basal slip and internal ice deformation, with ice-sheet models largely incapable of reproducing

borehole-based observations. To investigate further, we model isolated 3D domains from fast-moving (Sermeq Kujalleq or Store Glacier) and slow-moving (Isunnguata Sermia) ice-sheet settings in Greenland. By incorporating realistic geostatistically simulated topography, we show that a layer of basal temperate ice (much softer ice at the pressure-melting point) with spatially highly variable thickness forms naturally in both settings, alongside ice-motion patterns which are far more complex than previously considered. Temperate ice is vertically extensive in deep troughs, but thins notably over bedrock highs. Basal-slip rates are interconnected with this variability, reaching >90% or <5% of surface velocity dependent on setting. This realistic representation of ice-sheet motion opens new pathways for improving parameterizations in large-scale ice-sheet models.

4.3 Introduction

The Greenland Ice Sheet (GrIS) has transitioned from a state of near zero mass balance in the 1990s to large and sustained (>200 Gt a^{-1}) annual mass losses since the mid-2000s, and is now the largest cryospheric contributor to sea-level rise (Mouginot et al., 2019). While the satellite era has greatly increased the accuracy of mass-balance observations, model predictions for future ice loss remain highly uncertain (Aschwanden et al., 2021;Masson-Delmotte et al., 2021), but indicate substantial and non-linear sea-level rise under future anthropogenic warming (Goelzer et al., 2020; Aschwanden et al., 2019; Hofer et al., 2020; Choi et al., 2021). Ice dynamics, and their parameterization for large ice-sheet models (Durand et al., 2011; Bons et al., 2018; Brondex et al., 2019; Joughin et al., 2019), are crucial components of this uncertainty, being responsible for ice transport to lower and warmer elevations where surface melt rates and runoff increase rapidly, and to the fronts of marine-terminating glaciers where ∼50% of GrIS net annual mass loss occurs through increased calving rates and discharge (13).

Uncertainty related to ice-sheet motion arises from inadequate understanding of its two major components: (i) basal-slip at the ice-sediment or ice-rock interface and (ii) deformation within the ice sheet itself. State-of-the-art GrIS models run with BedMachine, the most advanced gridded data product of GrIS basal topography which is relatively smooth compared to deglaciated terrain (Morlighem et al., 2017; MacKie and Schroeder, 2020), produce basal-slip and ice deformation rates that vary smoothly and are largely independent of one another (e.g. Aschwanden et al., 2016; Cook et al., 2020b; Goelzer et al., 2020). However, GrIS borehole records indicate substantial variation in ice deformation, particularly towards the ice-sheet bed (Lüthi et al., 2002; Ryser et al., 2014b; Maier et al., 2019; Young et al., 2019) and notable catchment-scale variations in the thickness of a much softer,

and relatively poorly understood, basal temperate layer in which ice co-exists with a liquid water phase at the pressure-dependent melting point (Krabbendam, 2016; Law et al., 2021). Here, we advance upon 2D models that begin to unpick this complexity (Ryser et al., 2014b; Maier et al., 2019) by incorporating realistic three-dimensional geostatistically simulated bed topography (Fig. 4.2) and improved temperate ice rheology in a 3D full-Stokes model (Fig. 4.3A). We focus on ice-motion at the previously overlooked intermediate scale ($\leq$25 m, $\lesssim$4 km), bridging recent advances in understanding at small (Zoet and Iverson, 2020; Helanow et al., 2021) and large (Aschwanden et al., 2016) scales. The outcomes explain why field observations can be highly variable over even short distances. This behavior is characterized by spatially complex patterns of modeled ice deformation — focused towards the ice-sheet bed — and basal-slip. The basal temperate layer is an important modulator, extending or compressing in response to topographic perturbations, with vertical gradients in ice velocity notably reduced just above the cold-temperate transition surface (CTS). We suggest that this improved understanding will enable more accurate parameterizations of ice sheet motion at large-scales and hence lead to more accurate predictions of sea-level rise in the coming decades and centuries.

4.4 Results

Our modeling approach explores ice motion in isolated domains across three distinct glaciological settings. Two domains are from the fast-moving ($\sim$500 m a^{-1}) Sermeq Kujalleq (or Store Glacier, Fig. 4.2A), which flows into Uummannaq Fjord in West Greenland. The RESPONDER simulation is centered on the 1,043 m deep RESPONDER project borehole BH19c (Law et al., 2021) drilled at the center of a drained lake above a basal topographic saddle (Figs. 4.2Ei, ii). The SAFIRE simulation is centered on the 611 m deep SAFIRE project borehole BH16c (Doyle et al. 2018), which measures ice motion over a contrasting $\sim$300 m bedrock rise (Fig. 4.2Ev). The third simulation, S5, is centered over the $\sim$818 m S5 borehole site from Harrington et al. (2015) on the slow-moving (<125 m a^{-1}) land-terminating Isunnguata Sermia (Fig. 4.2B, Eiii, Eiv) where there are no substantial large-scale topographic troughs or rises.

All domains are run using geostatistically realistic topography (produced at a horizontal resolution of 20 m) using the sequential Gaussian simulation method. This well-established procedure treats topography as a Gaussian process, thereby matching airborne radar measurements of bed elevation along flight lines exactly, while also reproducing the roughness characteristics observed along flight lines (Materials and methods). The RESPONDER and S5 domains are additionally run using 400 m horizontal resolution BedMachine v3 topog-

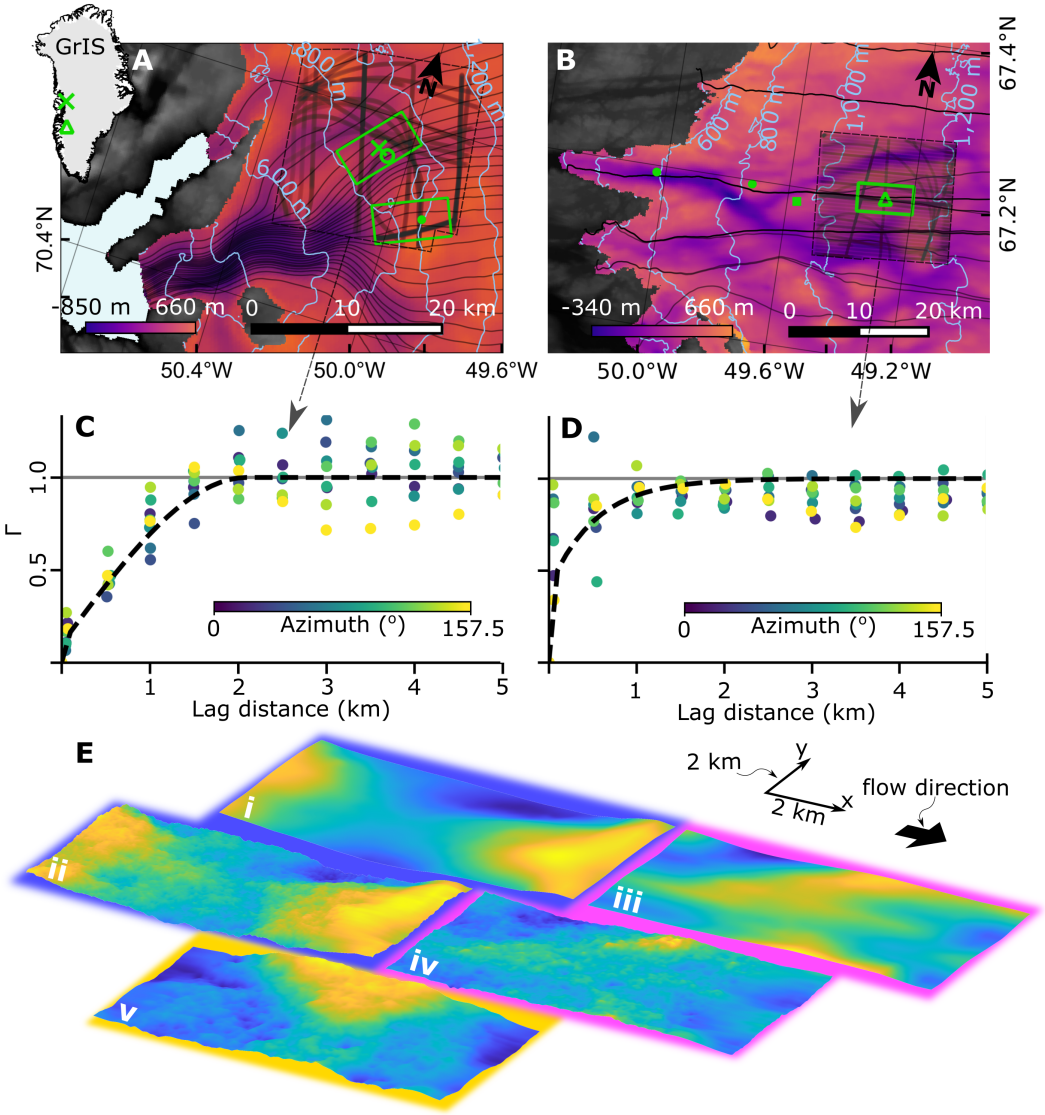

Fig. 4.2 . Location of modeling domains, variograms, and model setup. (A) Sermeq Kujalleq (Store Glacier) showing flowlines in black converging into Uummannaq fjord. BedMachine v3 (Morlighem et al., 2017) basal topography (inferno colormap), land topography (grayscale), and ice surface contours (pale blue). Model domain locations containing RESPONDER (north fluorescent green rectangle), borehole BH19c location (fluorescent green cross, Law et al., 2021), borehole BH18c location (fluorescent circle, Hubbard et al., 2021); SAFIRE domain (south fluorescent green rectangle), borehole BH14b-c location (fluorescent green dot, Doyle et al., 2018) and radar flight lines for RESPONDER domain (bold black strokes within dashed boundary, scatter opacity means darker lines have more measurements, CReSIS, 2021). (B) As for A but Isunnguata Sermia showing the S5 domain (fluorescent green rectangle) and boreholes S5 (fluorescent green triangle), S4 (west fluorescent green dot), S2 (east fluorescent green dot), and IS2015 (fluorescent green square Maier et al., 2019). S2-S5 are from (Harrington et al., 2015). (C) Modeled variogram (dashed line) and empirical variograms for varying azimuths (points) for RESPONDER domain, see Fig. 4.10 for SAFIRE variogram and flight lines. Variograms describe the spatial statistics of measured topography. (D) As for C but for Isunnguata Sermia domain. (E) BedMachine (i and iii) and geostatistically simulated (ii, iv, and v) basal DEMs for RESPONDER (blue outline), Isunnguata Sermia (pink outline), and SAFIRE (yellow outline) domains. Flow direction and x y scale in top right. No vertical exaggeration used.

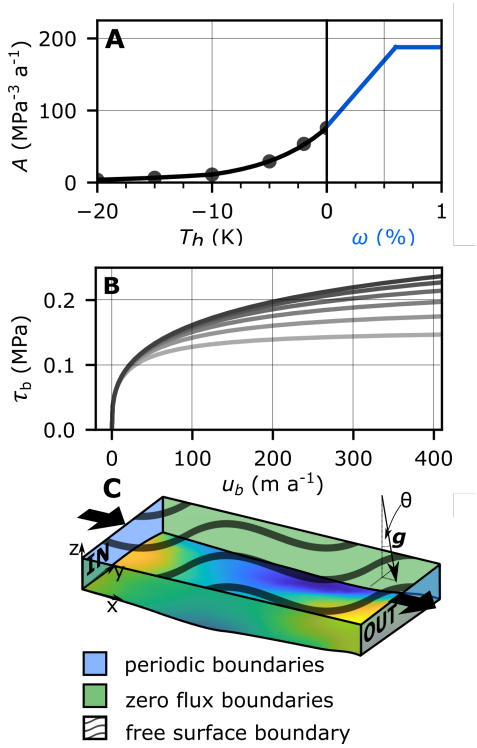

Fig. 4.3 . Ice rheology, basal traction, and periodic setup. (A) Rate parameter, A, as a function of homologous temperature (temperature below, or relative to, the melting point, black line) and water content (blue line). Black dots show values from Cuffey and Paterson (2010). (B) Regularized-Coulomb relationship with F= 1.2, s-b= 1,043 m, C= 0.1617, and θ= 0.8-1.8º in 0.2º increments where θ= 0.8 is light grey and θ= 1.8 is dark grey (see Materials and methods for equation and symbol definitions and data sources). (C) (Periodic) model setup showing inflow and outflow boundaries (labelled IN, OUT) with RESPONDER BedMachine topography (MatLab parula colormap), axis orientation, zero-flux lateral boundaries, free surface, and gravity vector.

raphy to assess the difference in ice-motion behavior resulting from the two topographic approaches. In the areas around our domains, BedMachine is derived from interpolated radar flight lines taking into account mass conservation (Morlighem et al., 2011). While this methodology is a substantial improvement over earlier kriging interpolation, the resulting topography product is still considerably smoother than topography observed along radar flight lines (MacKie et al., 2021). We achieve a close fit between modeled and observed surface velocity in a two-step approach. First, the ice rheology is set from a prescribed vertical temperature profile based on borehole data and the slope of the ice slab is adjusted to match the observed surface velocity (Fig. 4.3C, Table 4.1). Subsequently, we incorporate thermomechanical coupling while keeping the surface and inflow boundary conditions fixed. Basal-slip is calculated using a regularized-Coulomb relationship which parameterizes complex small-scale (<25 m) behavior such as cavitation (Helanow et al., 2021) and sediment ploughing (Zoet and Iverson, 2020). This avoids a basal-traction inversion procedure which masks basal variation at sub ice-thickness scales (Materials and methods).

4.4.1 Ice motion through a topographic saddle (RESPONDER domain)

When forced with geostatistically simulated topography (run Rgb, Figs. 4.4, 4.5, table S14.1), basal-slip rates, internal deformation, and the thickness of the basal temperate layer show great variation across the entire RESPONDER domain, forming a clear contrast to lower variation in the BedMachine topography model output (run Rbm, Fig. 4.5). With geostatistically simulated topography, the basal temperate ice layer is vertically extensive (>90 m) in topographic depressions, with low basal slip rates (<15 m a^{-1}) while fast (∼500 m a^{-1}) surface velocity shows no local variation. However, the basal temperate ice layer thins dramatically (<10 m) over topographic highs, with fast basal-slip rates (>500 m a^{-1}, Figs. 4.4A, B, pink and white rings respectively). To explore the transition from cold to temperate ice we track deformation heat and water content changes in flowlines originating ∼60 m above the bed 3 km along the x axis (Fig. 4.4E). These show transitions from cold ice with no water content to temperate ice with the maximum allowable water content of 2.5% (Materials and methods) over distances as short as ∼0.5-3 km (Fig. 4.4C) due to intense internal heat dissipation caused by the movement of ice over topographic obstacles (Fig. 3C pink and white rings). Deformation heating is notably lower within cold ice regions where ice is stiffer, than in the temperate basal layer where ice is much softer (Fig. 4.3A, Figs. 4.4C, D white line). Large topographic obstacles also divert ice flow horizontally (Fig. 4.4F, white ring) as well as vertically (Fig. 4.4E), thereby influencing the vertical position of the cold-temperate transition surface (CTS) and rheological properties throughout the domain. The ice-sheet (free) surface, with a surface elevation change of 98 m, varies broadly in response to patterns in BedMachine topography, with similar trends across all RESPONDER runs (Fig. 4.11). ParaView output files for all runs across all domains are available in the supplementary material.

Deformation heating profiles for BedMachine (run Rbm) and those from geostatistically simulated topography (run Rgb) are markedly distinct (Fig. 4.5A, B). When forced with geostatistically simulated topography the basal velocity ratio — the basal-slip rate divided by the surface velocity — reaches a maximum of 0.86 on a topographic high (Fig. 4.5C, gray line), where internal deformation drops rapidly above the bed. The basal velocity ratio is smallest within a topographic depression (0.04), where the deformation rate reaches its peak value (5.5 a^{-1}) just below the CTS, 90 m above the bed (Fig. 4.5C, brown line). The CTS velocity ratio — the velocity at the CTS divided by the surface velocity — remains more uniform throughout, peaking over topographic prominences but not dropping below 0.5 (Fig. 4.5E). Profiles also show deformation rates increasing upwards (Fig. 4.5C blue line), downwards (Fig. 4.5C yellow line), or even alternating between both (Fig. 4.5C red line, 1

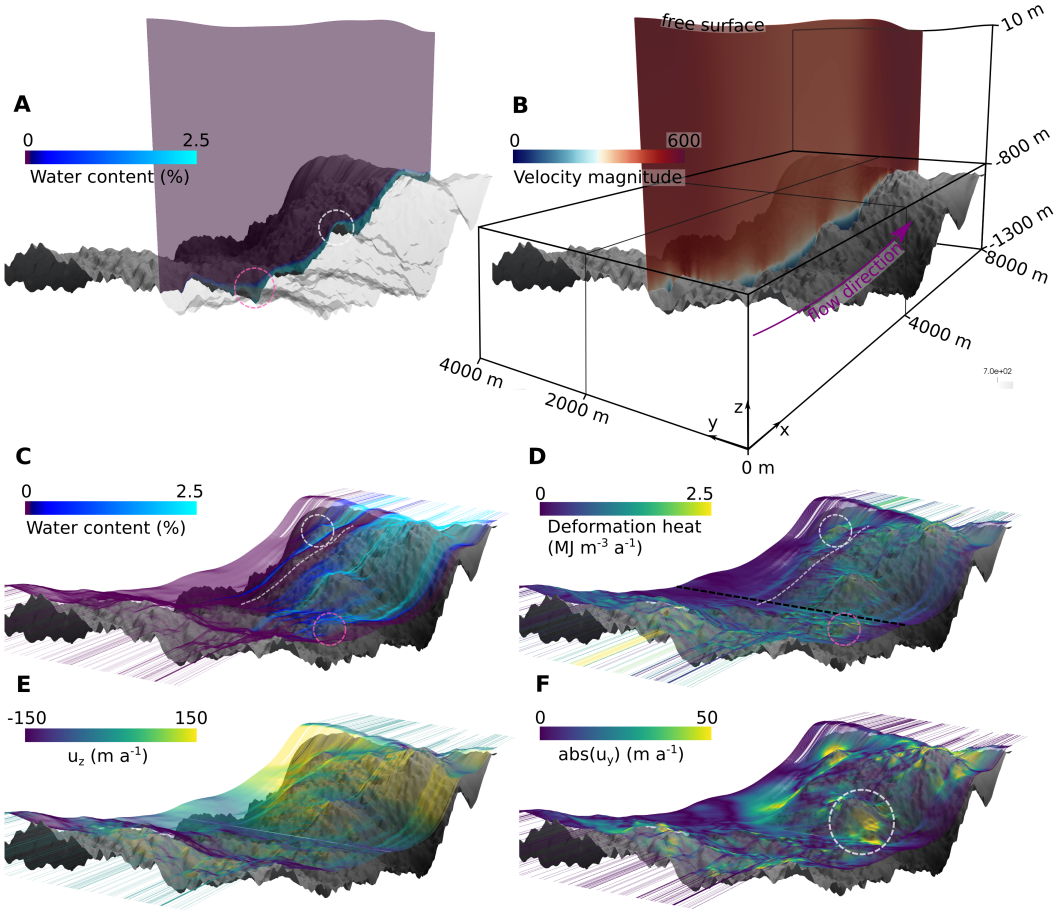

Fig. 4.4 . 3D model output from RESPONDER geostatistical simulation (Rgb). Flow direction is left to right, basal topography is in gray (max and min elevations are -835 and -1349 m respectively). z axis is exaggerated by a factor of 3. (A) shows water content and temperate ice thickness along xz transect intersecting y coordinate 1,300 m (same plane as Fig. 4.5). Transparency applied to topography on the observer's side of the transect. (B) Transect as for A showing velocity magnitude with flow direction in pink, axis orientation and dimensions visible. (C) Water content mapped onto 750 flowlines originating at line with coordinates [(3000, 0, -1083.3), (3000, 4000, -1083.3)] shown as black dashed line in D. (D) As for C but with deformation heat. Pink dashed ring highlights high but variable deformation heating where particles are close to the base over rough topography. White dashed ring highlights high deformation heating over a topographic prominence. White dashed line highlights an area of cold ice with low deformation heating. (E) As for C but z component of velocity vector mapped onto flowlines. (F) As for C but magnitude of y component of velocity vector mapped onto flowlines. White ring highlights region of high abs(u_y) around an area of high topographic prominence.

km). Strain banding towards the top of the temperate zone is evident in several locations, but is not a continuous feature across the entire domain. Distinctive vertical and horizontal banding in deformation heating is seen predominantly within the temperate layer (close-up in Figs. 4.5G-J, expanded upon under Temperate ice deformation-heating behavior). Basal melting varies with basal-sliding (Fig. 4.5F) but removes basal temperate ice at around 1.3 m km^{-1}, making it an important, but not first-order, control on temperate-layer thickness in the RESPONDER domain.

The above behavior contrasts the uniform ice-motion produced when the model is run with BedMachine topography (Fig. 4.5A), which gives deformation profiles that are uniform in shape throughout the model domain (Fig. 4.5B) that broadly conform with deformation profiles obtained from assumptions of plane-strain (e.g. Ryser et al., 2014a). The thin temperate zone, increasing gradually and uniformly along the transect, accommodates the largest rates of internal deformation ($\sim$3 a^{-1}) with a monotonic decrease in the ice above. The basal velocity ratio remains high and relatively uniform across the transect with an average value of 0.72.

4.4.2 Ice motion over a bedrock rise (SAFIRE domain)

At the SAFIRE domain, geostatistically simulated topography (Fig. 4.10) again results in highly variable basal-slip rates, ice deformation, and temperate-layer thickness (Fig. 4.6). The temperate layer thins over the large topographic rise in the domain, with a notable increase in basal velocity ratio (Fig. 4.6A between red and mauve lines). Over the rise, the basal velocity ratio is high (up to 0.98, Fig. 4.6A yellow line), but remains highly variable dropping to a minimum of 0.38 (Fig. 4.6A orange line). The CTS velocity ratio still shows obvious variation, but is much more uniform across the domain than the basal velocity ratio, and only rarely drops below 0.5. Deformation profiles show as much variability as in the RESPONDER simulation, however rates are higher and more spatially concentrated. Basal melt rates are directly correlated with basal slip rates (Fig. 4.6C, D) and drainage from temperate ice is low throughout, increasing on the lee side of the rise to a maximum of 0.22 m a^{-1}.

4.4.3 Ice motion at a land-terminating margin (S5 domain)

Ice motion and temperate ice behavior at the S5 Isunnguata Sermia site with geostatistically simulated topography are once again notably distinct from other domains, forced by increased short wavelength (<500 m, Fig. 4.2D) roughness, reduced topographic perturbations at larger ($\gtrsim$2 km) scales, and lower surface velocity. Along the featured transect (Fig. 4.7C), the basal velocity ratio remains mostly above 0.5 and does not have the same precipitous drops exhibited in the Sermeq Kujalleq domains. High basal velocity ratios (up to 0.83) still occur at topographic prominences, but compared to the Sermeq Kujalleq domains the CTS velocity ratio shows less departure from the basal velocity ratio, particularly in the first half of the transect where the basal temperate ice layer is thinner (<40 m). Deformation heat is less obviously concentrated towards the top of the temperate zone,

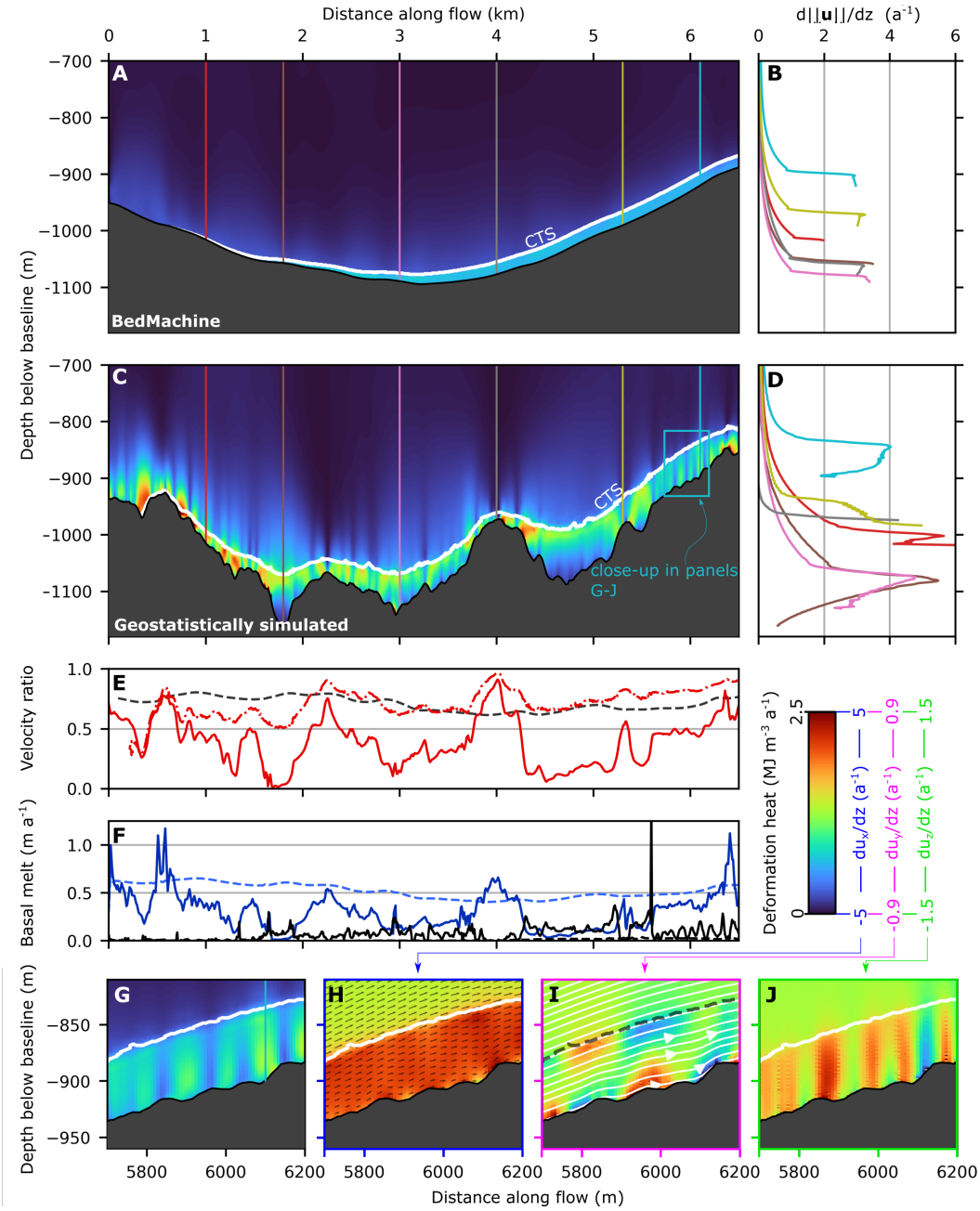

Fig. 4.5 . RESPONDER cross section (Sermeq Kujalleq). Cross section in xz plane showing deformation heat (product of stress and strain matrices) at y = 1,300 m (the same y value as the transects in Fig. 4.4) for (A) BedMachine topography (run Rbm) and (C) geostatistically simulated topography (run Rgb). Panels (B) and (D) show deformation rate profiles (change in velocity magnitude with depth) with colors and depths corresponding to the vertical lines in panels (A) and (C). (E) shows the basal velocity ratio (basal velocity magnitude divided by surface velocity magnitude) for Rbm (dashed line) and Rgb (solid line) along the transect and CTS velocity ratio (velocity magnitude at CTS divided by surface velocity magnitude) for Rgb (dashed black line). (F) shows basal melt rate in blue and drainage from temperate ice in black for Rbm (dashed line) and Rgb (solid line). Lowermost panels are the close up in C for Deformation heat (G), change in x-oriented velocity with depth (H), change in y-oriented velocity with depth (I), and change in z-oriented velocity with depth (J). Colored lines from left to right at 1.0, 1.8, 3, 4, 5.3, and 6.1 km. Colored lines in this figure, and Figs. 4.6 and 4.7, are chosen to highlight interesting deformation behavior.

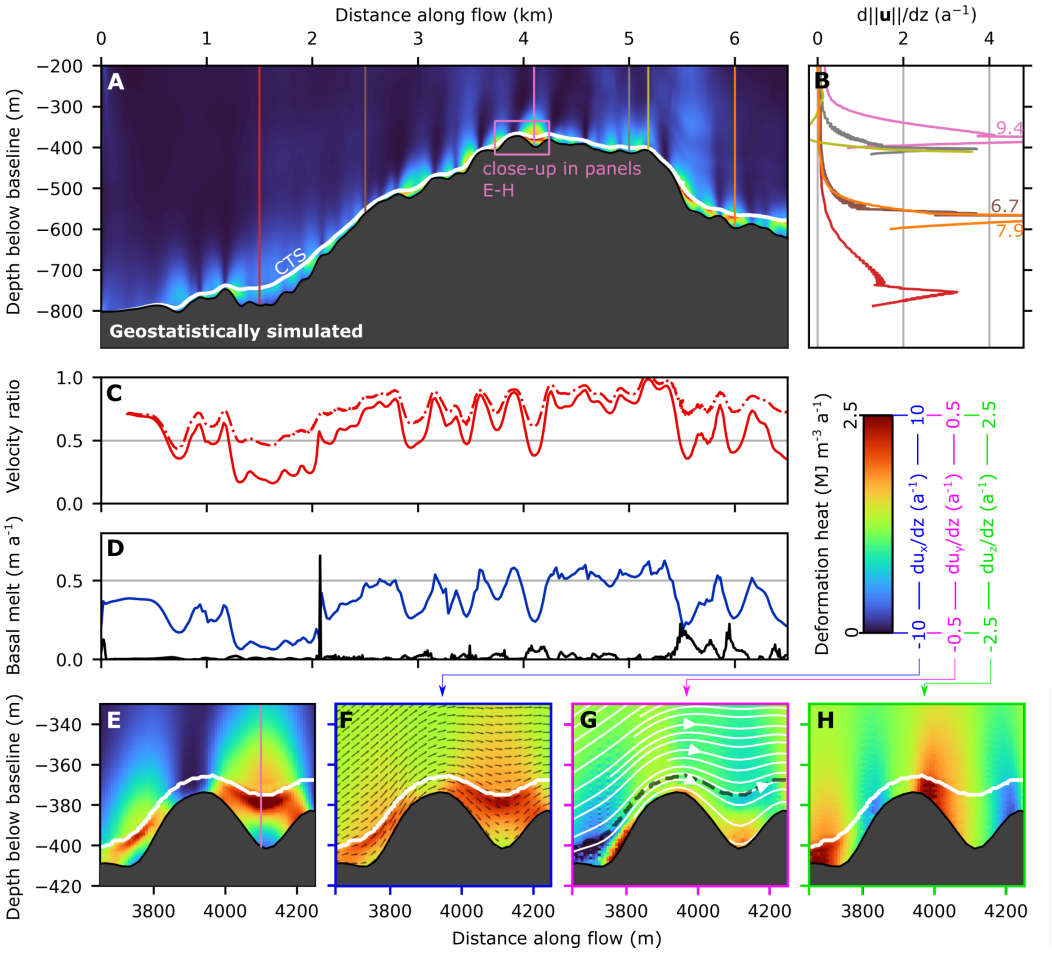

Fig. 4.6 . SAFIRE cross section (Sermeq Kujalleq). Cross section in xz plane at y = 2,850 m for (A) geostatistically simulated topography (run SAFg). The remainder of the figure follows the same layout as Fig. 4.5. Colored lines from left to right at 1.5, 2.5, 4.1, 5, 5.18, and 6 km.

instead projecting upwards through the CTS and well into the cold ice ∼150 m above the bed (close-up in Figs. 4.7G-J). Nevertheless, most deformation profiles for geostatistically simulated topography show deformation rates increasing to a maximum just below the CTS, except over some topographic prominences (e.g. Fig. 4.7D, red line), where deformation decreases monotonically above the bed, as is the case for all deformation profiles for the BedMachine run (Fig. 4.7B). BedMachine topography produces similar features to the Sermeq Kujalleq BedMachine domains: a gradual temperate layer thickness increase and internal deformation concentrated within the temperate layer.

4.4.4 Temperate ice deformation-heating behavior

We observe three characteristic patterns of deformation heating. First 'Truncated spires' (e.g. Figs. 4.5G-J) refers to places where deformation heating is evident in vertically oriented bands (∼50 m across) that terminate abruptly below the CTS. These truncated

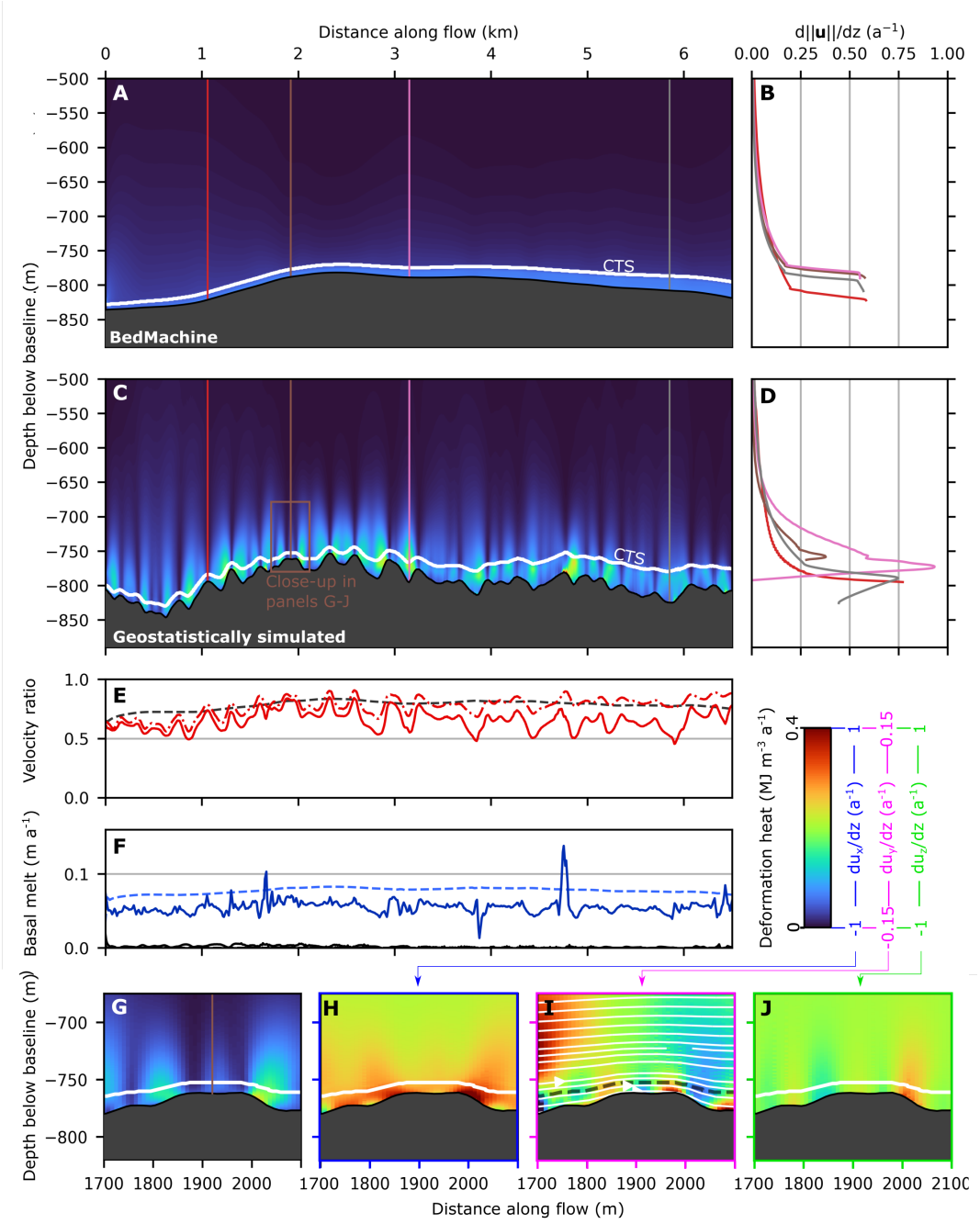

Fig. 4.7 . S5 cross section (Isunnguata Sermia). Cross section in xz plane at y = 2,000 m for (A) BedMachine topography (run S5bm) and (B) geostatistically simulated topography (run S5gb). The remainder of the figure follows the same layout as Fig. 4.5. Colored lines from left to right at 1.06, 1.92, 3.15, and 5.85 km.

spires are connected to changes in x-oriented velocity with depth (Fig. 4.5H) and are more frequent as temperate-layer thickness increases. This pattern of deformation heating is common in both Sermeq Kujalleq domains but is largely absent in the Isunnguata Sermia S5 domain. 'Bridges' (e.g. Figs. 4.6E-H) are another characteristic feature. Here a deformation heating arch below the CTS and above a topographic depression is produced by large changes in x-oriented velocity with depth (Fig. 4.6F). Bridge abutments are produced as

the temperate layer vertically extends and depth-averaged velocity decreases on the lee side of a prominence before vertically compressing with an increase in depth-averaged velocity as the trough is exited. Bridges are also common in both Sermeq Kujalleq domains but are mostly absent in the S5 domain. Last, 'crosscutting spires' or simply 'spires' (e.g. Figs. 4.7G-J) are similar to truncated spires but protrude some distance (∼100 m) above the CTS, gradually reducing in intensity with height. Spires are the most common feature in the Isunnguata Sermia domain but are also common in the two Sermeq Kujalleq domains in locations where the temperate layer is thinner. These features are outlined in further detail in the discussion and used singularly without 'deformation-heating' from here on.

4.4.5 Domain-wide behavior

Domain-wide distributions of basal-velocity ratio and temperate-layer thickness show substantial variation between locations and are further highly dependent upon whether BedMachine or geostatistically simulated topography is used (Fig. 4.8, Fig. 4.12). Runs from Sermeq Kujalleq domains with geostatistically simulated topography exhibit the greatest range in basal velocity ratios, with 1st and 99th percentile values of 0.04 (0.05) to 0.80 (0.92) for RESPONDER and (SAFIRE) respectively. This far exceeds results when BedMachine topography is used (1st and 99th percentile values of 0.43 and 0.86 respectively for the RESPONDER BedMachine run). Modal basal velocity when geostatistically simulated topography is used varies from 0.31 for RESPONDER, to 0.60 at S5 and 0.71 at SAFIRE, with the trend reversed for modal temperate ice thickness (49 m for RESPONDER, 17 m for S5, and 12 m for SAFIRE) and a maximum temperate ice thickness of 189 m modeled in the RESPONDER domain. Each hexbin plot for geostatistically simulated topography has a central 'hotspot' that clearly varies between domains, with the spread around the hot spot showing a broad linear relationship between basal velocity ratio and temperate ice thickness. In contrast to all of the geostatistical runs, the RESPONDER BedMachine hexbin plot (Fig. 4.8D) is much closer to a line. In runs using geostatistically simulated topography, the temperate ice layer thickness only shows a linear increase along flow in the flatter S5 Isunnguata Sermia domain, with average temperate-layer thickness increasing to a maximum that coincides with the topographic minima in the RESPONDER domain, and increasing overall but with no consistent trend in the SAFIRE domain.

Our numerical findings demonstrate that geostatistically realistic topography produces basal-slip and internal deformation rates that conform to a broad uni-modal distribution. Borehole observations will sample the actual distribution of basal velocity ratio and temperate-layer thickness, but are too limited in number to be used to produce a statistically 'correct' distribution. Nonetheless, our model shows good agreement with borehole obser-

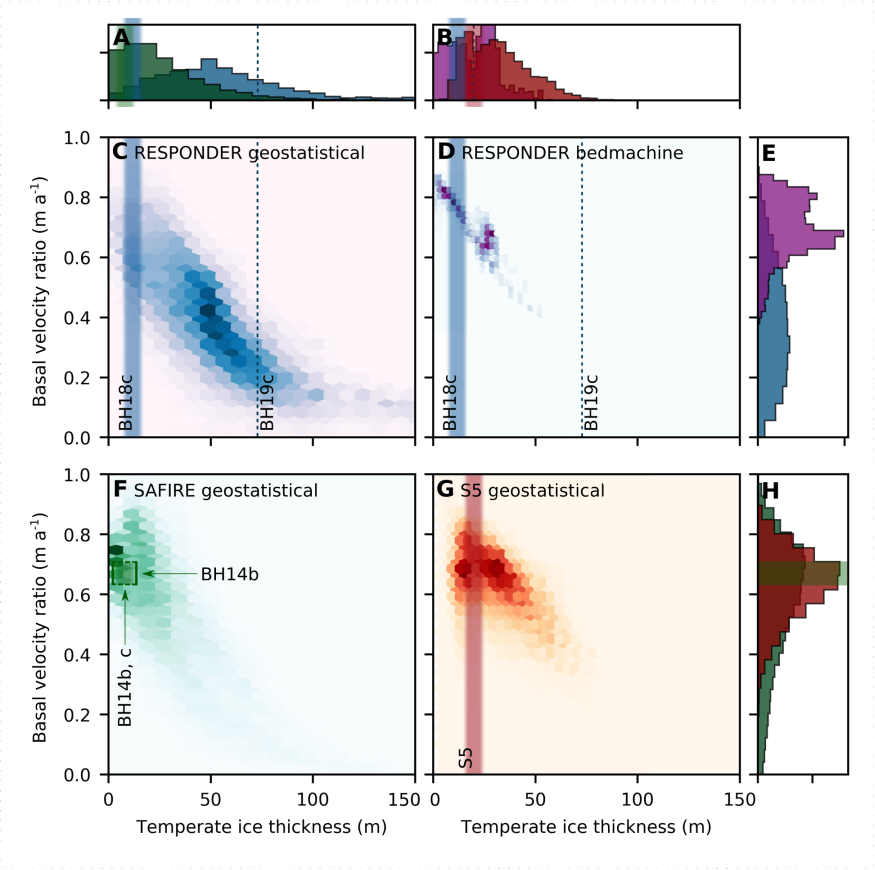

Fig. 4.8 . Domain-wide distributions of basal velocity ratio and temperate ice thickness. (A) Histograms for temperate ice thickness for RESPONDER and SAFIRE geostatistical domains. (B) Histograms for temperate ice thickness for RESPONDER BedMachine and S5 geostatistical domains. (C, D, F, G) Hexbin plots for temperate ice thickness and basal velocity ratios for (C) RESPONDER geostatistical domain (run Rgb, modal bin has 420 counts), (D) RESPONDER BedMachine domain (run Rbm, modal bin has 582 counts), (F) SAFIRE geostatistical domain (run SAFg, modal bin has 755 counts), and (G) S5 geostatistical domain (run S5gb, modal bin has 463 counts). (E, H) Histograms for basal velocity ratio for RESPONDER geostatistical and BedMachine domains (E) and SAFIRE and S5 geostatistical domains (H). Vertical (A, B) and horizontal (E, H) histogram axes are frequency density. A buffer of 500 m, with an additional 1,000 m at the outflow boundary is applied around domain edges to avoid potential boundary effects, giving a total of 34,677 points per domain. Dashed blue line indicates temperate ice thickness recorded at BH19c, the distributed nature of this measurement means there is negligible uncertainty. The vertical green, blue, and red bars for BH14c (Doyle et al., 2018), BH18c (Hubbard et al., 2021), and S5 (Harrington et al., 2015) respectively are blurred to indicate uncertainty due to discrete temperature sensor measurements which may miss the exact location of the CTS. Uncertainty bounds are not provided in the original papers and we do not attempt to create our own. The green horizontal bar (not blurred) spans the uncertainty range of 0.63-0.71 (Doyle et al., 2018). The complex basal motion in our model is supported by borehole observations from within each of the three domains (see main text for details).

vations for all runs with geostatistically simulated topography, matching modal values for temperate ice thickness for SAFIRE and S5. Observed temperate-layer thickness falls either side of the mode for RESPONDER with geostatistically simulated topography, confirming such spread is present in the GrIS. Given that the observed temperate layer thickness of

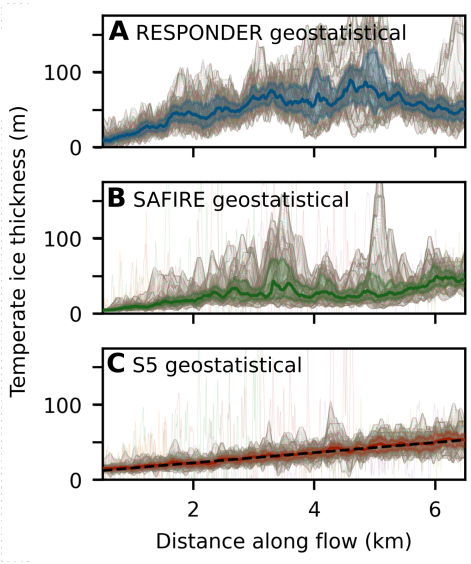

Fig. 4.9 . Temperate ice thickness along flow. Temperate ice thickness interpolated into a 5 m orthogonal grid from output triangular mesh. Gray lines are temperate ice thickness for each y value along x-axis-parallel rows. Highlighted area bounds interquartile range obtained for each y-axis-parallel column, solid colored line is 50% percentile for each y-axis-parallel column. (A) RESPONDER geostatistical domain (run Rgb). (B) SAFIRE geostatistical domain (run SAFg). (C) S5 geostatistical domain (run S5gb) where the black dashed line is the first order polynomial fit of the 50% percentile line.

73 m at BH19c (Law et al., 2021) is entirely outside of the distribution produced with BedMachine topography, we argue that realistic topography is a requirement for realistic temperate-layer thicknesses and therefore also realistic basal motion.

4.5 Discussion

In contrast to the smoothly varying velocity fields produced by most ice-sheet models using BedMachine topography, our simulations indicate that basal-slip and internal deformation are pervasively heterogeneous, with significant variability over sub-kilometer distances, and across disparate catchment settings. In this discussion, we first detail the mechanisms that produce and shape the temperate layer which has a central role in fast ice motion, before outlining the processes behind the complex basal-motion patterns simulated in our model. Both of these aspects are separately compared to borehole observations. Next, while we focus here on descriptions of the complex behavior that emerges from realistic topographic representations, we suggest initial ways to incorporate complex basal motion into numerical parameterizations applicable to large-scale predictive ice-sheet models. Last, we briefly outline directions for future field studies.

4.5.1 Temperate ice: formation and observations

Large regions of the GrIS's bed, including the majority of its margins, are thawed (MacGregor et al., 2016). This facilitates fast ice motion through basal-slip but also creates the conditions required for the development of a basal temperate ice layer as we report here. Such a temperate layer has an important but somewhat mysterious role in ice motion as temperate ice is considerably softer than cold ice (Colbeck and Evans, 1973; Lliboutry, 1976; Duval, 1977; Morgan, 1991; Krabbendam, 2016). This weakness results from liquid water at grain boundaries enhancing diffusion and dislocation creep, dynamic recrystallization, and grain boundary melting (e.g. Duval, 1977; Krabbendam, 2016; Adams et al., 2021) and is particularly important for the basal portions of ice-sheets where the largest deviatoric stresses are focused. Temperate ice can be produced by deformation heating above the CTS, with some studies further suggesting the importance of latent heat transfer across the CTS via water in basal crevasses or ice-grain interfaces (Harper et al., 2010; Harrington et al., 2015; Krabbendam, 2016; Hewitt and Schoof, 2017). Conversely, all basal heat sources will reduce temperate layer thickness through basal melt as the positive upwards temperature gradient defined by the Clausius-Clapeyron slope operates as a thermal barrier. Basal heat sources include viscous heat dissipation in flowing subglacial water (Mankoff and Tulaczyk, 2017), geothermal heat flux, and frictional heat from sliding. While these theoretical underpinnings are well established (Greve and Blatter, 2009; Aschwanden et al., 2012; Harrington et al., 2015; Hewitt and Schoof, 2017; Wang et al., 2020), we show that realistic basal topography is the crucial additional component required to explain borehole observations of complex variation in temperate-layer thickness across the GrIS (Iken et al., 1993; Ryser et al., 2014b; Harrington et al., 2015; Doyle et al., 2018; Maier et al., 2019; Seguinot et al., 2020; (Law et al., 2021)).

At the Isunnguata Sermia S5 domain, the inter-quartile thickness (obtained across width) of the basal temperate layer increases at 5.6-7.9 m km^{-1} when forced with geostatistically simulated topography. While high variability in the spatial rate of change of temperate layer thickness is to be expected (discussed below), our modelled temperate layer growth rate is compatible with Isunnguata Sermia borehole observations where the temperate layer thickness increases at a rate equivalent to $\sim$4.3 m km^{-1} between site S5 and site S4, located 18.4 km downstream in the direction of flow (Fig. 4.2B, Harrington et al., 2015). As we do not include water transport in our model, our results indicate that roughness-controlled deformation heating alone is sufficient to produce temperate ice at observed rates.

The importance of high-resolution realizations of basal topography is further evident when comparing model outputs forced with geostatistically simulated topography and

BedMachine topography, respectively. When topography is smooth (BedMachine run), deformation heat is concentrated within a relatively thin temperate zone and is therefore contributing to internal melt of the temperate layer, not temperate layer growth. A greater basal velocity ratio additionally means basal frictional heating, and therefore basal melt, is increased relative to deformation heat above the CTS. In contrast, perturbations ∼200 m across present in geostatistically simulated topography result in ubiquitous spires protruding through the CTS (Fig. 4.7G-J), which effectively warm cold ice to the point that it becomes temperate. Interestingly, these spires begin to truncate at the CTS as temperate ice thickness increases (Fig. 4.5C) — which can be explained by the temperate layer now being sufficiently thick as to accommodate a greater proportion of internal deformation — indicating that the temperate layer thickness may not continue to increase linearly indefinitely. This non-linearity, and the situation of S3 on a topographic rise, may explain why the observed increase of the temperate layer at Isunnguata Sermia is smaller than predicted in the S5 model domain in isolation. Overall, we view deformation heating above the CTS as a simpler and more general explanation for temperate layer growth than the hydrological mechanism hypothesized by Harrington et al. (2015), which requires pervasive basal crevasses or intergranular water transport, both of which lack a clear observational basis.

Localized shear banding and bridges between topographic prominences are further distinctive features of the temperate layer forming in our model. These features are most easily understood by considering their development as the model approaches steady state (fig. 4.13). As ice slips through a topographic depression it is physically unable to do so without deformation heating increasing the specific enthalpy of the ice locally and downstream and therefore decreasing its viscosity (Fig. 4.3A) — a system which stabilizes at the point where deformation heating balances conductive and advective heat losses (Aschwanden et al., 2012). Bridges thereby connect topographic highs where basal-slip is high sensu stricto with concentrated internal deformation towards the top of the temperate layer which fills the intervening trough, enabling rapid movement of cold ice over comparatively stagnant temperate ice below. These bridges contribute to some heating above the CTS and occur far more frequently in our two fast-moving domains (RESPONDER and SAFIRE, Figs. 4.5C, **??**A), which may be explained by a velocity threshold controlling the transition between these modes.

Bridges, and (truncated) spires help to explain the complicated temperate ice variation modeled and observed at Sermeq Kujalleq. Spires that protrude through the CTS in the RESPONDER domain (Fig. 4.5C) increase the temperate layer thickness to a maximum across-flow average of 100 m after 5 km (Fig. 4.9), beyond which bridges and truncated spires dominate and the rate of temperate layer growth decreases. Convex large-scale ($\gtrsim$2 km) topography further prompts vertical compression and acceleration of the entire ice

column, reducing the absolute thickness of the temperate layer and concentrating more deformation below the CTS. This variation is supported by, and further helps to explain, borehole observations of temperate ice. A 73-m-thick temperate layer observed from borehole BH19c (Law et al., 2021) within the RESPONDER site likely indicates a subglacial topographic depression, while a much smaller temperate-layer thickness (<20 m) only a few kilometers away (but still within the RESPONDER domain, Fig. 4.2A, Doyle et al., 2018) is more likely to sample less temperate ice above a topographic prominence. At SAFIRE, dramatic modeled temperate-zone thinning over a notable bedrock rise is compatible with borehole observations from this site showing either a very thin (<8 m) or absent temperate layer (Doyle et al., 2018). Here, the convex large-scale topography increases basal-slip and hence reduces internal deformation heating. As with RESPONDER, thinning of the entire ice column over a rise will also locally reduce the absolute thickness of the temperate layer.

Our numerical model also aids interpretation of other GrIS borehole observations. At a site 12.75 km from the ∼20 m thick temperate ice layer at S5 (Isunnguata Sermia) and ∼1 km south of the main flow line (hereafter IS2015, Fig. 4.2B), Maier et al. (2019) observe no substantial temperate ice and a high basal-velocity ratio, while a ∼100-m-thick layer of temperate ice was observed just 8 km further along flow at sites S4 and S3 (Harrington et al., 2015). We suggest that this spatial variability is connected to the topographic rise on which IS2015 was located, which can compress and accelerate the overlying ice in a similar manner to modeled ice motion over the SAFIRE rise beneath Sermeq Kujalleq. However, we also emphasize that stochastic spatial variation in temperate-layer thickness, related to local (100s of m) topographic relief, may play an additional role in inter-site variability. This local variation may further explain observations near Swiss Camp, where temperate layer thickness decreased from ∼40 m to ∼20 m over 10 km along flow (Ryser et al., 2014b), which could reflect natural variability as indicated by individual temperate-layer thickness profiles in Fig. 4.9. Last our findings fully support the existence of an inferred extremely thick (>300 m) basal temperate layer in the deeply eroded basal trough of Sermeq Kujalleq in Kangia (Jakobshavn Isbræ) formed largely by vertical ice extension (Lüthi et al., 2002), and offer further avenues to test its importance in fast ice motion. Overall, considerations from our results and from borehole records indicate that large-scale topographic variations (e.g. rises and saddles) control broad patterns of temperate layer thickness, while geostatistically simulated topography is central to the formation of temperate ice and to intermediate-scale ($\geq$25 m, $\lesssim$4 km) variations in its thickness.

These results emphasize the importance of temperate ice, but also the paucity of information regarding temperate ice at micro and macro scales, particularly for the GrIS. Recent laboratory studies on temperate ice are limited (e.g. Adams et al., 2021; Fowler and Iverson, 2022) and the parameter space for temperate ice flow is relatively unconstrained

(e.g. Krabbendam, 2016; Hewitt and Schoof, 2017; Haseloff et al., 2019; Adams et al., 2021), with temperate ice modelling studies mainly directed towards Antarctic shear margins. Although we do not include anisotropy, the rheology of temperate ice in our model is at the most-viscous end of plausible values (Materials and methods), with less-viscous formulations having the potential to further increase the deformation accommodated within the temperate layer. Alternative drainage formulations for temperate ice may also influence rheological properties and therefore temperate layer behavior (Schoof and Hewitt, 2016; Hewitt and Schoof, 2017). While our results reproduce key field observations and provide a framework for understanding temperate ice formation and behavior, further work is urgently required to constrain appropriate parameters and parameterizations for temperate ice.

4.5.2 Complex basal motion: simulations and observations

The model behavior outlined thus far is supported by, and provides an explanation for, the broad spectrum of ice-motion behavior revealed in GrIS borehole records — in addition to the temperate layer thickness variability outlined above. At RESPONDER, damage to a fiber-optic cable at the center of the modeling domain indicated a clear increase in ice deformation towards the top of the temperate ice layer that could not be explained by existing theories (Law et al., 2021). Our model reproduces this strain behavior when a thicker temperate ice layer occupies a local or broad topographic depression (Fig. 4.4C, D brown, pink, and blue lines), showing such deformation heterogeneity is an intrinsic part of GrIS ice motion. As this behavior is reproduced with a near-constant rate factor within the modeled temperate layer — a result of uniform water saturation shortly below the CTS — our results further indicate that varying ice rheology is not a prerequisite for variable temperate-layer deformation, as hypothesized in (Law et al., 2021), but rather, realistic bed topography is. No deformation profile from the BedMachine domain reproduces the fiber-optic cable damage pattern, further indicating that BedMachine topography will not produce realistic ice-motion behavior at intermediate scales ($\lesssim$4 km).

SAFIRE domain model results also show similarly good agreement with observations. Here, Doyle et al. (2018) obtain a basal velocity ratio of 0.63-0.71 and a temperate-layer thickness of up to 8 m, very close to the modal bin of Fig. 4.8F (sliding ratio 0.75, temperate-layer thickness 4 m). Further, the borehole tilt sensor deformation peak of 1.8 a^{-1} 19 m above the ice sheet base (Doyle et al., 2018) is entirely compatible with our modeled deformation rate increases directly (<50 m) above the base (e.g. Fig. 4.6A, B orange, pink lines). Modeled deformation rates change rapidly with distance above the bed, thus Doyle et al.'s 19-m-above-the-bed sensor may not necessarily represent the maximum rate of

deformation within the borehole, which could feasibly continue increasing beyond 1.8 a^{-1} following the gradient between the two lowermost tilt sensors. As our modeling results indicate strain bands are spatially limited yet carry a significant proportion of ice motion, this implies that basal-slip estimates gathered from discrete sensors may be more uncertain and variable than appreciated so far, and — furthermore — be biased towards estimates of greater basal velocity ratio. Another bias comes from the fact that most boreholes in Greenland have been drilled over bedrock highs for practical reasons. Taken together, the SAFIRE and RESPONDER model runs contrast the uniform glacier motion produced in previous Sermeq Kujalleq models forced with smooth BedMachine topography (e.g. Cook et al., 2020b), and suggest that the complex basal motion is the norm rather than the exception in marine-terminating outlet glacier settings.

Complex basal motion also helps to explain observations from the slower-moving land-terminating ice sheet margin at Isunnguata Sermia that may at first appear contradictory. Site IS2015, just 12.75 km from S5 (Fig. 4.2B, outlined under Temperate ice formation, Maier et al., 2019) has a measured basal velocity ratio ranging from 90.6 to 99.7% and no substantial temperate layer. This basal velocity ratio and temperate layer thickness is distinct from (though not completely incompatible with) the distribution modeled at S5. However, we emphasize that the difference between the closely spaced RESPONDER and SAFIRE domains indicates that a high level of variation forced by different long-wavelength topography is not unusual and should in fact be expected. Our analysis of temperate ice formation along the S5 flowline further suggests that if sliding rates are pervasively as high elsewhere in the Isunnguata Sermia catchment as at IS2015, then insufficient deformation heat will occur to prompt the very large observed temperate layers at S1-S4 (Harrington et al., 2015). Therefore, while it has been hypothesized that sliding is the most important component of ice-motion in land-terminating sectors of the GrIS (Maier et al., 2019), our model shows that sliding dominance is confined to topographic high points and is not a general condition of motion across the GrIS.

4.5.3 Complex basal motion: application to large-scale models

Our process-based understanding of basal motion at small (<25 m) scales has progressed significantly in recent years. Laboratory work for ice overlying deformable sediments (Zoet and Iverson, 2020) and 3D numerical-modeling of glacier slip over hard beds with water-filled cavities (Helanow et al., 2021) both suggest that basal traction conforms to a regularized-Coulomb relationship: slip resistance first increases with slip velocity before reaching a threshold velocity where till shears at its rate-independent yield strength or cavity dimensions stabilize (Fig. 4.3B). However, while some large-scale studies support

the above experiments (e.g. Tsai et al., 2015; Joughin et al., 2019), this is not universal, with other studies suggesting a Weertman-type slip relationship of ice motion, where basal-traction increases indefinitely with increasing basal velocity (Gimbert et al., 2021; Maier et al., 2021). The selected basal-slip relationship is then used in an inversion procedure over smooth BedMachine topography for basal-traction parameters that are typically assumed to be time-invariant.

The above contention surrounding appropriate parameterizations has significant ramifications. The choice of basal-slip relationship significantly alters ice-sheet model predictions (e.g. Parizek et al., 2013; Gillet-Chaulet et al., 2016; Kyrke-Smith et al., 2018; Brondex et al., 2019) and 'deep' process uncertainty in ice-sheet models is a key concern in the most recent IPCC report (Masson-Delmotte et al., 2021). We propose that expanding our conception of ice-sheet motion to include intermediate-scale flow variability ($\geq$25 m, $\lesssim$4 km), and the complexity in topography and basal conditions clearly evident from observations beneath past (e.g. Roberts and Long, 2005; Krabbendam et al., 2016) and present (e.g. Dow et al., 2013; Bingham et al., 2017; Harper et al., 2017; Holschuh et al., 2020) ice sheets, offers a route forward. Parameters derived from inverse methods for heuristically-applied basal-slip relationships (including Weertman or regularized-Coulomb) over smooth BedMachine topography can implicitly account for the complex ice-motion described here. However, while parameters from inversions may reproduce observed velocities well, divergence between predicted and actual ice-sheet behavior is likely to increase over model time if the form of the basal-motion relationship is an incorrect representation of intermediate-scale basal motion processes and does not account for temporal changes in motion conditions (Goelzer et al., 2017) such as a local change in temperate layer thickness influencing the basal velocity ratio.

Incorporating the process-based understanding we have generated here into a parameterization that explicitly accounts for basal-motion over realistic topography, in addition to basal-slip, provides a potential solution. This is achievable by treating basal temperate ice as a distinct layer that includes both internal deformation and basal-slip. This approach would yield a high CTS velocity ratio akin to the one produced for basal slip using BedMachine topography. Application of geostatistically generated topography to BedMachine in full ice-sheet models is not a requirement. If the developed basal-motion relationship can account for spatial variations in geostatistical parameters, then coarse-resolution grid cells can still be effectively used, with the knowledge that complex basal topography and processes are still parametrically incorporated. Further geological considerations are outlined in the supplementary text. Development and implementation of such a basal-motion relationship will increase confidence that predictive ice-sheet models are accurately representing the

complex reality of ice-sheet motion and may therefore improve the accuracy of sea-level rise predictions.

4.5.4 Outlook

Our results show that while the basal velocity ratio and temperate layer thickness can vary across a small region ($\sim$0.25 km^2) and may mimic catchment-scale results, most small regions in isolation will not be representative of basal-motion at larger scales. A focus in field studies on coarser ($\geq$1 km) borehole arrays covering a wider range of topographic features may therefore enable more accurate characterization of ice-motion variability. Separately, as temperate layer thickness variation is directly influenced by deformation heating within the ice and hence the basal velocity ratio, intensive borehole- and radar-based investigation across a domain similar in size to the ones used here would allow improved estimates of parameters by fitting model data to observations.

Overall, our results indicate unavoidable complexity in descriptions of ice-sheet motion. We provide a unified explanation for borehole observations of spatial variability in basal temperate ice thickness and basal velocity ratio, and for down-borehole variability in deformation rates. In sum, we hope that these advances in understanding will facilitate the development of improved representations of ice-sheet motion and hence more accurate predictions of sea level rise.

4.6 Materials and methods

4.6.1 Numerical modelling

We model ice flow in rectangular 8 km (along flow) by 4 km (across flow) domains oriented along flow where the x y z axes define length, width, and depth, respectively (Fig. 4.2f). This allows a high mesh resolution and a focus on basal-motion processes, without requiring modeling of an entire glacier catchment. To obtain realistic boundary conditions for our model domains we first use time-evolving runs with periodic inflow-outflow conditions and a free surface (FS runs) to determine the gravity vector orientation (or slope) needed to approximate satellite-derived glacier velocities characterizing each domain. We then obtain a free-surface DEM, surface pressure field, and inflow boundary conditions for the velocity vector components and pressure. We use these derived boundary conditions and

gravity-vector orientation on the same domain for the final thermomechanically coupled runs (TC runs) in which the enthalpy and velocity fields are allowed to evolve until steady-state convergence is reached. TC runs are not compatible with periodic domains as it is unphysical for the enthalpy field and hence rheological characteristics at the outflow boundary to match the inflow boundary.

We use the Elmer/Ice (version 9.0) finite element modeling package (Gagliardini et al., 2013) on GNU/Linux with 191.9 GB total memory and 18 @2.20 GHz processor partitions for all runs. FS runs take ∼5 days, TC runs take ∼12 hr. A triangular mesh with representative edge length of 25 m and ∼124,119 triangular elements is made with Gmsh and vertically extruded using the Elmer/Ice StructuredMeshMapper, with vertical layer spacing decreasing towards the base. Further increasing the spatial resolution does not meaningfully alter model output (fig. 4.14). FS runs use 25 vertical layers to reduce computation time, increased to 42 for TC runs, giving a lowermost cell thickness of 1.6 m for an ice column of 1 km (fig. 4.15). Domains are centered about a borehole location, with the basal topography normalized such that the average DEM value is equivalent to the negative of the thickness obtained by the central borehole(s), giving an initially flat surface with z coordinate 0 m. To maintain inflow outflow boundaries at the same z coordinates, the SAFIRE domain is additionally detrended to remove an average slope of 2.7o. Table 1 provides details on specific run setups. Table S2 provides parameter and constant values.

We solve the standard Stokes equations governing ice flow,

$$\nabla \cdot \boldsymbol{u} = 0 \text{ (conservation of mass)}, \tag{4.1}$$

$$\nabla \cdot \boldsymbol{\tau} - \nabla \cdot p = -\rho \boldsymbol{g} \text{ (balance of momentum)}, \tag{4.2}$$

where $\boldsymbol{u} = u_i$ (m a^{-1}) is the ice velocity, $\boldsymbol{\tau} = \tau_{ij}$ (MPa) is the deviatoric stress tensor, p (MPa) is the ice pressure, ρ (MPa m^{-2} a^{-2}) is the ice density (assumed constant, with no adjustment for water content) and $\boldsymbol{g} = g_i$ (m a^{2}) is the gravitational acceleration vector. The slope, θ (°), is set by assigning $\boldsymbol{g} = [g\text{sin}(\theta), 0, -g\text{cos}(\theta)]$, where g= 9.81 m a^{-2} , to remove the requirement for vertical displacement of periodic inflow-outflow boundaries. Stress is related to strain using the Nye-Glen isotropic flow law (Nye, 1953; Glen, 1955),

$$\dot{\boldsymbol{\epsilon}} = A\tau_e^{n-1}\boldsymbol{\tau} \tag{4.3}$$

where $\dot{\boldsymbol{\epsilon}} = \dot{\epsilon}_{ij} = \frac{1}{2}\left(\frac{\partial u_i}{\partial x_j} + \frac{\partial u_j}{\partial x_i}\right)$ (a^{-1}) is the strain rate tensor, $\tau_e^2 = \frac{1}{2}\text{tr}\left(\boldsymbol{\tau}^2\right)$ (MPa) is the effective stress in the ice, n is the flow exponent assumed to equal 3, and A is the creep parameter (MPa^{-3} a^{-1}). A is calculated from the homologous temperature, T_h (K), if below the pressure-dependent melting point, T_m, or water content, ω (proportion), if above as

$$A = \begin{cases} A_1 \text{exp}\left(\frac{Q_1}{RT_h}\right), & T_h \leq T_{lim} \\ A_2 \text{exp}\left(\frac{Q_2}{RT_h}\right), & T_{lim} < T_h < T_m \\ (W_1 + W_2 \times 100)W_3, & T_h \geq T_m, \omega < \omega_{lim} \\ A_{max}, & \omega \geq \omega_{lim} \end{cases} \tag{4.4}$$

where $T_m(p) = T_{tr} - \gamma\left(p - p_{tr}\right)$ where γ ($K\ MPa^{-1}$) is the Clausius-Clapeyron constant, T_{tr} is the triple point water temperature, and p_{tr} is the triple point water pressure. A_1 and A_2 are rate factors (MPa a^{-1}) and Q_1 and Q_2 are activation energies (J mol-1) for $T \leq T_{lim}$ and $T_{lim} < T < T_m$ respectively where T_{lim} = 263.2 K is the limit temperature. R is the gas constant (J mol-1 K-1) and W_1, W_2, and W_3 (all in MPa a^{-1}) are water viscosity factors, with default values taken from the linear fit of Duval (1977) adapted by Haseloff et al. (2019) for water contents up to 0.7±0.1% under tertiary creep. We hold W_1, W_2, and W_3 constant for all model runs and set a conservative limit for ω_{lim} of 0.6% as Adams et al. (2021) propose A does not increase between water contents of 0.6-2% following experiments conducted under secondary creep. Once ω_{lim} is exceeded $A = A_{max}$, limiting the rate factor of temperate ice. Fig. 4.3a shows the increase of A with temperature and then water content as used in our model.

Specific enthalpy, H (J kg-1), is used as the state variable with the Elmer/Ice Enthalpy-Solver (Gilbert et al., 2014) and is related to T and ω as

$$H(T, \omega) = \begin{cases} \frac{1}{2}C_a\left(T^2 - T_{ref}^2\right) + C_b\left(T - T_{ref}\right), & H < H_m(p) \\ \omega L + H_m, & H \geq H_m(p) \end{cases} \tag{4.5}$$

where C_a (J kg-1 K-2) and C_b (J kg-1 K-1) are enthalpy heat capacity constants, L (J kg-1), is the latent heat capacity of ice, $H_m(p) = \frac{1}{2}C_a\left(T_m(p)^2 - T_{ref}^2\right) + C_b\left(T_m(p) - T_{ref}\right)$ is the specific enthalpy at the pressure-dependent melting point, and T_{ref} = 200 K is the reference temperature.

Our mesh representative edge length of 25 m makes the use of a physically-derived small-scale sliding relationship most appropriate and so we follow the regularized-Coulomb relationship of (30) and (29). Basal traction, τ_b (MPa), is given as

$$\tau_b = CN_e \left(\frac{u_b^{-n+1}}{u_b + A_s C^n N_e^n} \right)^{\frac{1}{n}} u_b \tag{4.6}$$

where C (dimensionless) is a parameter that depends on basal morphology and cannot be readily estimated from irregular topographies but must be less than the maximum up-slope gradient of the bed (Helanow et al., 2021), u_b, is the basal velocity (m a^{-1}) tangential to the ice-bed interface, n=3 is the same exponent used in the flow relationship. A_s (m a^{-1} MPa^{-3}) depends on ice rheology and morphology of the bed and is used in the case of hard-bed sliding with no cavitation (Weertman, 1957), and N_e (MPa) is the effective pressure at the bed. Helanow et al. (2021) provide six values for A_s and C based on representative element-area DEMs obtained from un-crewed aerial-vehicle surveys on bedrock surfaces recently exposed by glacier recession. We take the average of these six values for each of A_s and C as constant for all runs rather than apply a basal-traction inversion procedure that would require inherent assumptions about ice deformation. N_e is then varied as the only free parameter controlling basal traction though we note this has a similar effect to varying C.

We make the simplifying assumption that N_e is related to the overburden pressure alone via a proportionality parameter, O (dimensionless), as $N_e = -\rho g_z O(Z_s - Z_b)$ where Z_b (m) is the elevation of the glacier base and Z_s (m) is the surface elevation. However, basal traction has an upper limit under Eq. 6 of $\tau_{b_{max}} = N_e C$ which can lead to instability when the average driving stress, $\tau_d = \rho g h \sin(\theta)$, cannot be supported within the modeling domain, leading to the inequality

$$O \geq \frac{F \tan(\theta)}{C} \tag{4.7}$$

where F is a parameter that would equal 1 if $\tau_{b_{max}} \approx \tau_d$. In practice, the model ceases to converge to reasonable values for RESPONDER BedMachine runs if $F \lesssim 1.15$ and for RESPONDER geostatistical runs if $F \lesssim 0.85$ due to the additional support from the stoss side of basal obstacles. To ensure we are sufficiently within the convergence space of the system we set F= 1.2 for all BedMachine runs, and run geostatistical runs with F= 1.2 and F= 0.9. We note that we are therefore close to maximum possible sliding rates given our domain geometries where force balance is met locally (which is similar to the

assumptions of the shallow-ice approximation). Fig. 4.3B illustrates the range of behavior for τ_b with F= 1.2 and $s - b$= 1,043 m. For the range of slopes and F values covered and C= 0.1617, this gives a range in O from 0.0.0874 to 0.240, comparable to values in other studies (Mankoff and Tulaczyk, 2017; Cook et al., 2021a). Increasing the proportion of driving stress supported by the maximum basal traction value slightly shifts the basal-velocity-ratio distribution towards lower values, with a new mode of 0.28 (fig. 4.12). θ is then altered in 0.05° increments (with concomitant change in O) to obtain the best match between modeled surface velocity and satellite measurements. Surface slopes in the regions studied are 1-2° with variation in $\boldsymbol{g}$ away from the long-wavelength borehole site value expected as $\boldsymbol{g}$ in our model will also be accounting for longitudinal and transverse stresses in the ice.

4.6.2 Free-surface runs

In FS runs enthalpy and hence A is calculated as a function of normalized depth, $D = \frac{d}{Z_b + Z_s}$, where d (m) is depth, as $H = E_a D^2 + E_b D + E_c$ where E_a, E_b, and E_c are quadratic curve parameters. E_a, E_b, and E_c are obtained via a second-order polynomial fitting procedure (Matlab polyfit) of borehole data with minor adjustments to only just remove the temperate ice layer (fig. 4.16). This approach ensures consistent rheology at the periodic inflow-outflow boundaries. These profiles are also used for the input enthalpy field in TC runs.

The free surface is computed with the Elmer/Ice FreeSurfaceSolver as

$$\frac{\partial Z_s}{\partial t} + u_x \frac{\partial Z_s}{\partial x} + u_y \frac{\partial Z_s}{\partial y} = u_z \tag{4.8}$$

where u_x, u_y, u_z are components of the surface velocity vector $\boldsymbol{u}$. No accumulation or ablation is accounted for as this would require a corresponding removal of mass from elsewhere in the model hence $u_z = 0$. The timestep is set to 0.015 a and the simulation is stopped when the maximum and minimum surface show only minor variation (fig. 4.17). The free surface DEM, surface pressure field, and inflow pressure and velocity fields are then extracted and reprojected as boundary conditions onto the TC mesh.

4.6.3 Thermomechanically coupled runs

The specific enthalpy field is allowed to freely evolve until a steady-state is reached and is calculated as

$$\rho\left(\frac{\partial H}{\partial t}+\boldsymbol{u}\cdot\nabla H\right)=\nabla(\kappa\nabla H)+\mathrm{tr}\,(\boldsymbol{\tau}\dot{\boldsymbol{\epsilon}}) \tag{4.9}$$

where tr $(\boldsymbol{\tau}\dot{\boldsymbol{\epsilon}})$ is the strain heating term. κ (kg m^{-1} s^{-1}) is the enthalpy diffusivity defined as

$$\kappa=\begin{cases}\kappa_c, & H<H_m(p)\\ \kappa_t, & H\geq H_m(p)\end{cases} \tag{4.10}$$

where κ_c and κ_t are enthalpy diffusivities for cold and temperate ice respectively, meaning water movement within the temperate ice is assumed to be a diffusive process. H is limited by ω_{max} set at 2.5%, around the level of field observations of water content (Pettersson et al., 2004 and references therein). However, as we limit increases in A to water contents of 0.6% we note that a greater maximum water content value only acts to increase water-content gradient and hence enthalpy transfers within the temperate zone and across the cold-temperate transition zone, though κ_t is an order of magnitude lower than κ_c.

Drainage is treated simply by setting an upper specific enthalpy limit equivalent to ω_{max} with drainage assumed to occur instantaneously above this threshold. Vertically integrated drainage volumes, D_v (m^3 a^{-1}), are then obtained from specific enthalpy loads, H_{loads}, and element weighting, $H_{weights}$, as

$$D_v=\int_{Z_b}^{CTS}\frac{H_{loads}}{H_{weights}}dz \tag{4.11}$$

where CTS is the z coordinate of the cold-temperate transition surface. More advanced drainage formulations exist (Schoof and Hewitt, 2016; Hewitt and Schoof, 2017) but their implementation is beyond the scope of this paper.

For the purposes of basal sliding, we make no adjustment for the small sections where basal temperatures are below the pressure melting point, effectively assuming that the bed is sufficiently-well hydrologically connected to provide water to these regions for freeze-on. Considerations for basal freeze-on rates required to pin the basal temperature at the pressure melting point are presented in the Supplementary material, showing the water required is negligible in context. The basal mass balance, M_b (kg m^{-2} a^{-1}), is calculated as

$$M_b = \frac{1}{H}\left(F_b + Q_b + \boldsymbol{G}_b \cdot \boldsymbol{n}_b - \boldsymbol{q} \cdot \boldsymbol{n}_b\right) \tag{4.12}$$

where $F_b = u_b \tau_b$ is the frictional heating at the bed, $\boldsymbol{G}_b$ is the geothermal heat flux, $\boldsymbol{n}_b$ is the basal normal vector, $q = -\kappa \nabla T$ is the energy flux into the ice where k is the thermal conductivity of the ice, and Q_b is the rate at which hydrological storage and transport mechanisms deliver latent heat to the base of the ice which we set as 0 across all of our model domains. When a temperate layer is present q is a small negative value (flux directed towards the base) determined by the local pressure gradient. If no temperate layer is present q is a small positive value (directed away from the base). Comparisons of inflowing and outflowing ice volumes for the RESPONDER BedMachine run, where mass loss is greatest, shows basal melting has a negligible effect on overall ice flow volumes (0.3%). Elmer/Ice solver input files and post-processing scripts are available in the Supplementary material.

4.6.4 Geostatistical DEM simulations

We use conditional geostatistical simulations Deutsch and Journel, 1998 to produce DEMs for each site that (a) match basal topography from radar flight lines that cross each domain, (b) reproduce the roughness exhibited in radar flight line profiles (Fig. 4.2), and (c) retain the long-wavelength ($\gtrsim$2 km) features of BedMachine. In order to create the most direct comparison with BedMachine topography (Morlighem et al., 2017) we simulate topography by adding roughness to BedMachine based on the characteristics of the residual between BedMachine and radar measurements. It is customary to simulate multiple realizations in order to quantify uncertainty (e.g. MacKie et al., 2021); however, no great variation in the form of the hexbin cloud for the RESPONDER domain is produced when the model is forced with topography from the second topographic realizations of this region (fig. 4.12, Materials and methods), so only one realization is used for the SAFIRE and S5 domains. Two realizations are used for the RESPONDER domain for a sensitivity analysis.

The simulation is carried out in the following steps. First, the residuals between BedMachine v3 and CReSIS radar measurements (from 1993 to 2017, CReSIS, 2021) are calculated. We included all data within a 5 km buffer around each study area so that these observations can serve as outside constraints on the simulations. Residual data is used rather than raw radar measurements to ensure the simulated topography retains long-wavelength BedMachine features. A normal score transformation is then performed on the residuals so that the data conforms to standard Gaussian assumptions required by the simulation algorithm. An empirical variogram $\check{\Gamma}(h)$, is produced for each site to quantify spatial covariance, or

topographic roughness (Fig. 4.2C, D). The variogram relates the variance of each pair of residual bed measurements to their separation (lag) distance. The variance increases with lag distance. For example, two bed measurements that are close together typically have a low variance because nearby points often have similar values. However, at large lag distances, the variance is much greater because bed measurements that are far apart are not strongly correlated. The empirical variogram is calculated as

$$\check{\Gamma}(h) = \frac{1}{2N(h)} \sum_{\alpha=1}^{N} \left(Z_b\left(x_\alpha\right) - Z_b\left(x_\alpha + h\right) \right)^2 \tag{4.13}$$

where $Z_b\left(x_\alpha\right)$ is measured bed topography, x_α is a spatial location, and N is the number of point pairs for a given lag distance, h (m). Each empirical variogram was calculated with different azimuthal directions in order to capture any roughness anisotropy. A variogram model is manually fitted to the empirical variogram. For S5 the modeled variogram is

$$\Gamma(h) = 0.4 + 0.6 \times \exp(h, 1600) \tag{4.14}$$

where $\exp(h, c)$ is the exponential variogram function with a range c (m) (Deutsch and Journel, 1998). The S5 model variogram has a nugget of 0.4 which represents the short-range variability. No significant topographic anisotropy was found. The RESPONDER model variogram is fitted as

$$\Gamma = 0.1 + 0.9 \times \mathrm{sph}(h, 2100) \tag{4.15}$$

where $\mathrm{sph}(h, \alpha)$ is the spherical variogram function (Chiles and Delfiner, 2012). The RESPONDER model variogram has a smaller nugget and larger range than the S5 model variogram, indicating smoother residual roughness at RESPONDER. The RESPONDER model variogram is also isotropic.

The modeled variograms are then used to perform a sequential Gaussian simulation which produces random realizations of phenomena such that the output realization has the same spatial covariance as the input data (e.g. Deutsch and Journel, 1998). The sequential Gaussian simulation uses a random path to visit each grid cell and simulate a value. At each grid cell, the variogram is used to estimate the mean and variance of bed, which defines a Gaussian probability distribution. While kriging interpolation will select the mean of the distribution, sequential Gaussian simulation randomly draws from the distribution to

Run (abbreviation)	Location*	Depth (m)	Slope (°)	F	Seed †
S5 BedMachine (S5bm)	49.2889 W, 67.2014 N (S5)	818‡	0.8	1.2	NA
S5 geostat a (S5ga)	-	-	1.05	1.2	i
S5 geostat b (S5gb)	-	-	0.9	0.9	i
RESPONDER BedMachine (Rbm)	-50.0875 W, 70.5683 N (BH19c)	1,043	1.4	1.2	NA
RESPONDER geostat a (Rga)	-	-	1.85	1.2	i
RESPONDER geostat b (Rgb)	-	-	1.775	0.9	i
RESPONDER geostat c (RGc)	-	-	1.85	1.2	ii
SAFIRE geostat (SAFg)	-49.92 W, 70.52 N (S30)	611	3.0	0.9	i
Resolution tests	§	1,043	1.775	0.9	i

Table 4.1 . Details for model runs. * Domain center (longitude, latitude in decimal degrees). † Seed used to simulate topography from model variogram, i = 10007, ii = 10009. ‡ From the average of two boreholes drilled at S5 detailed in (Harrington, Humphrey, and Harper 2015). § northeast quarter of RESPONDER domain.

generate a simulated value. To ensure a seamless interpolation, each simulated value is constrained by previously simulated grid cells. This process is repeated until every grid cell is populated. This technique has previously been used to simulate the basal topography of Sermeq Kujalleq in Kangia (also known as Jakobshavn Isbræ) in west Greenland (MacKie et al., 2021).

The simulated residual roughness is then back-transformed to recover the original data distribution and added to BedMachine data to produce output DEMs. A Gaussian filter with standard deviation 1.5 is applied to remove very short wavelength ($\lesssim$50 m) topographic features which can cause unrealistic model behavior. The simulation was implemented using the GeostatsPy software package (Pyrcz et al., 2021). For a detailed description of the methodology, see Deutsch and Journel (1998) and Pyrcz and Deutsh (2014) and workflow scripts in the Supplementary material. Last, a tapering algorithm detailed in (Helanow et al. 2021) is applied to the final 1.6 km of the DEMs to ensure periodic boundaries have equal elevations and minimize topographic modification.

Symbol	Units	Variable	Value	Citation
A_1	MPa a^{-1}	Rate factor 1	9.133e12	
A_2	MPa a^{-1}	Rate factor 2	7.477e23	
A_s	m a^{-1} MPa^{-n}	Sliding coefficient	2.13e4	Average of Helanow et al. (2021) values
C		Maximum slope value	0.16167	Average of Helanow et al. (2021) values
C_a	J kg^{-1} K^{-2}	Enthalpy heat capacity A	7.253	Gilbert et al. (2014)
C_b	J kg^{-1} K^{-1}	Enthalpy heat capacity B	146.3	Gilbert et al. (2014)
E_a	J kg^{-1}	Enthalpy curve parameter a*	1.6155e5 7.5645e4	
E_b	J kg^{-1}	Enthalpy curve parameter b*	-1.5091e5 -5.8647e4	
E_c	J kg^{-1}	Enthalpy curve parameter c*	1.2341e5 1.189e5	
G_b	W m^{-2}	Geothermal heat flux	55e-3	Cook et al. (2020b)
L	J kg^{-1}	Latent heat of fusion of ice	3.34e4	
κ_c	kg m^{-1} a^{-1}	Cold ice enthalpy diffusivity	1.024e-3	Gilbert et al. (2014)
κ_t	kg m^{-1} a^{-1}	Temperate ice enthalpy diffusivity	1.045e-4	Gilbert et al. (2014)
P_{tr}	MPa	Triple-point pressure of water	0.612	
Q_1	J mol^{-1}	Activation energy 1	60e3	
Q_2	J mol^{-1}	Activation energy 2	115e3	
ρ_i	kg m^{-3}	Ice density	910	
T_{lim}	K	Limit temperature	263.2	Cuffey and Paterson (2010)
T_{ref}	K	Reference temperature	200	
T_{tr}	K	Triple-point temperature of water	273.2	
W_1	MPa a^{-1}	Water viscosity factor 1	1.0	
W_2	MPa a^{-1}	Water viscosity factor 2	2.35	
W_3	MPa a^{-1}	Water viscosity factor 3	77.945	
ω		Upper water limit	0.025	

Table 4.2 . Model parameters. * Value for Sermeq Kujalleq then Isunnguata Sermia.

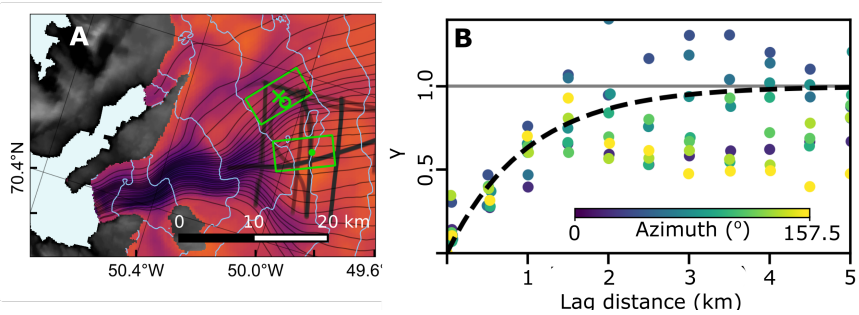

Fig. 4.10 . (A) Sermeq Kujalleq showing flowlines in black converging into fjord (pale blue). BedMachine v3 (Morlighem et al., 2017) basal topography (inferno), land topography (grayscale), and ice surface contours (pale blue). Model domain locations (fluorescent green rectangles) containing RESPONDER BH19c location (fluorescent green cross Law et al., 2021), RESPONDER BH18c location (fluorescent circle Hubbard et al., 2021), SAFIRE BH14b and BH14c locations (fluorescent green dot Doyle et al., 2018) and radar flight lines for SAFIRE domain (black strokes within dashed boundary, scatter opacity means darker lines have more measurements, CReSIS, 2021). (B) modeled variogram (dashed line) and empirical variograms for varying azimuths (scatter points) for SAFIRE domain.

4.7 Supplementary material

4.7.1 Supplementary text, geological considerations

Individual GrIS glacier catchments are often assumed to be underlain by either hard crystalline bedrock or soft sediments. However, this assumption rests on a paucity of data constraining the physical characteristics of the ice-bed interface. Collection of new GrIS field data over the last decade suggests a more complicated situation, with no clear consensus for blanket hard- or soft-bed settings. At Isunnguata Sermia, borehole data mostly from topographic highs (sites S1-S5) suggests hard-bed conditions (Harper et al., 2017), while seismic surveys from topographic depressions indicate deformable sediment (Dow et al., 2013; Kulessa et al., 2017), and ice-marginal studies for the nearby Russell Glacier indicate basal ice with a high debris content (Baltrūnas et al., 2009). At Sermeq Kujalleq, distributed acoustic sensing data from BH19c and seismic surveys across the SAFIRE domain both suggest a layer of sediment (Hofstede et al., 2018; Booth et al., 2020), yet ice-marginal glacial geology is dominated by areal scour with limited and isolated zones of sediment deposition (Lane et al., 2016). Furthermore, the crystalline Precambrian rock over which both our domains probably lie (Dawes, 2009) typically exhibits a 'cnoc-and-lochan' landscape in deglaciated areas — characterized by overdeepened glacier-eroded rock basins and knolls with amplitudes up to 100 m (Roberts and Long, 2005; Krabbendam and Bradwell, 2014) — as broadly recreated in our geostatistical simulations (Fig. 4.2).

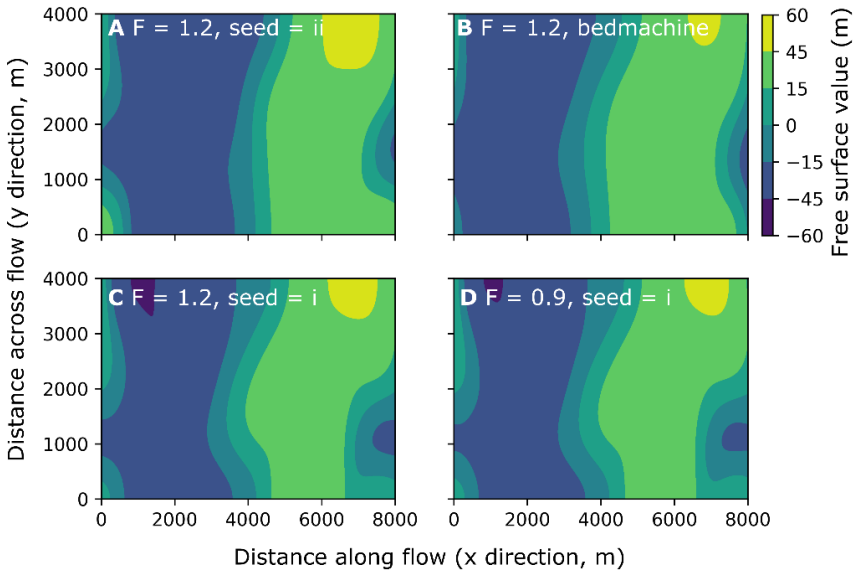

Fig. 4.11 . Free surface variation for RESPONDER runs (A) Rgc, (B) Rbm, (C) Rga, and (D) Rgb.

Our understanding of subglacial transport processes remains poorly quantified (Alley et al., 2019), but we suggest that realistically rough topography, and a variable basal stress/velocity field as produced in our model, are likely to result in heterogeneous sediment distribution and hence heterogeneous basal traction characteristics. High slip rates and basal traction over topographic highs are likely to lead to high rates of erosion, meaning these regions are most likely composed of hard bedrock. Conversely, topographic lows may act as sites of sediment accumulation through basal melt-out, lower bed-normal pressure (Alley et al., 2021) and slower glacier motion. This has important implications for basal motion. Although topographic prominences occupy a small overall area they are sites of high basal-slip and the traction at these locations will exert a disproportionate control on basal motion. This variation may explain the success of hard-bed Weertman-style basal-slip relationships across the GrIS when viewed at >1 km scales (Maier et al., 2021) even when more recent studies suggest a regularized-Coulomb approach is more applicable (Helanow et al., 2021), particularly if the viscous flow of temperate ice is contributing a considerable proportion of overall motion. Models investigating spatial variation in basal-traction relationships, similar to (Koellner et al., 2019) but also incorporating realistic topography, will shed further light on these processes.

4.7.2 Basal freeze on

In order to hold the basal temperature constant at the melting point the following energy consideration must be met

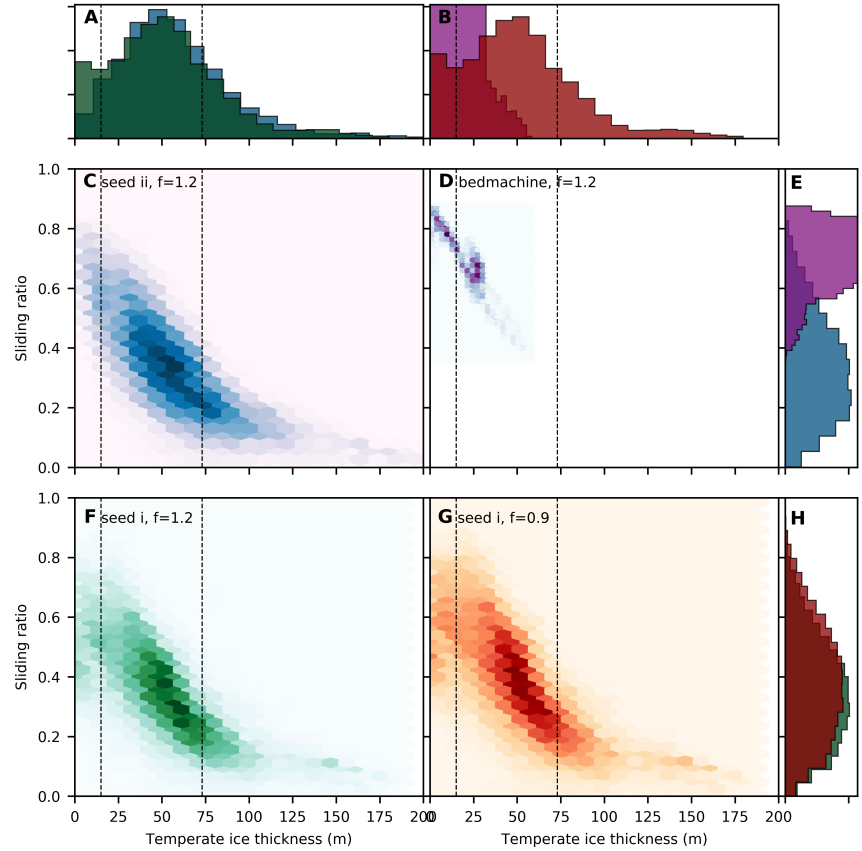

Fig. 4.12 . Hexbins and histograms for four RESPONDER domain runs. Panel details refer to run details. (C) = Rgc, (D) = Rbm, (F) = Rga, (G) = Rgb.

$$\rho \frac{\partial H}{\partial t} = -\frac{\partial q}{\partial z} + \gamma = \kappa_c \frac{\partial^2 H}{\partial z^2} + \gamma = 0 \tag{4.16}$$

where q is vertically directed energy flux into the ice and γ accounts for other sources of energy supplied to the bed

$$\gamma = F_b + \boldsymbol{G}_b + Q_b + VHD + \rho V_b L \tag{4.17}$$

where VHD is viscous heat dissipation (Mankoff and Tulaczyk, 2017) and V_b is the basal freeze on rate of liquid water. Neglecting terms other than $\rho V_b L$ then gives

$$\rho V_b L = \kappa_c \frac{\partial^2 H}{\partial z^2} \tag{4.18}$$

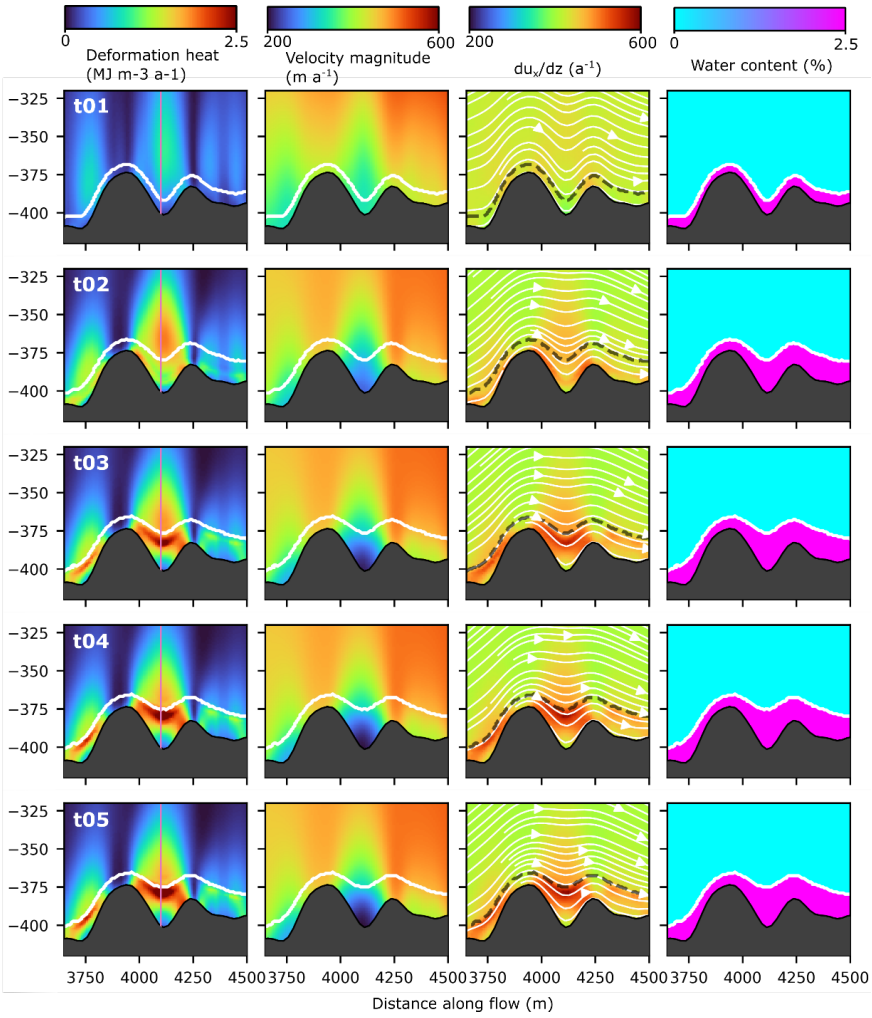

Fig. 4.13 . Evolution towards steady state for deformation heat (column 1), velocity magnitude (column 2), change in x velocity component with height (column 3), and water content (column 4) for the five iterations (rows) required for steady state for the close-up in Fig. 4.6.

and, setting the right hand side to 2.7e-4 (the largest value from the borehole profile of Law et al. (2021) gives V_b = 2.8e-5 m a^{-1}, negligible in the context of high basal melt rates modeled across the domain.

4.8 Postface

Variation in subglacial water pressure is not included in the submitted paper (though it is dealt with for Thwaites Glacier, Antarctica, in chapter 5). A simulation to quickly test the influence of variable subglacial water pressure shows however that if subglacial water pressure is increased from 82.76% of overburden (Fig. 4.19A) where F= 0.9 to 95% of

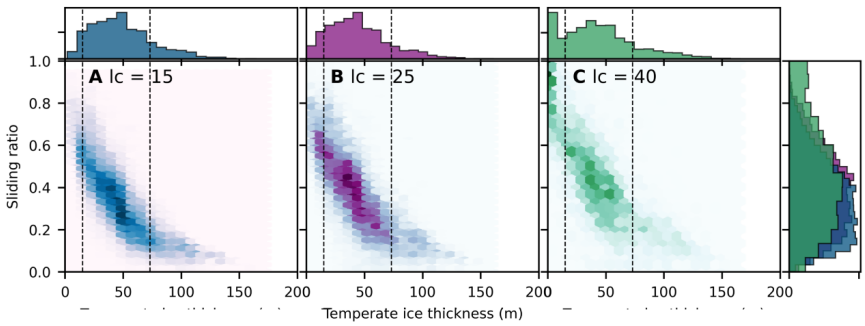

Fig. 4.14 . Hexbins and histograms for representative element length (lc) of 15, 25, and 40 m (A, B, and C respectively). These show minor difference between lc = 15 m and lc = 25 m, with notable increases in temperate ice in the lowest-thickness bin, and high basal velocity ratios for lc = 40 m.

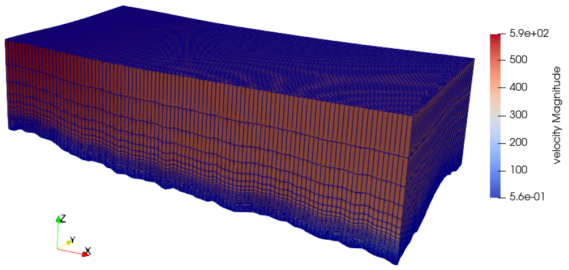

Fig. 4.15 . Domain used in resolution tests, here with lc = 40. Dimensions are 2 km across flow, 4 km along flow, depth ~1,043 m. This is the bottom left corner of the full RESPONDER seed i domain as viewed from above.

overburden (Fig. 4.19B) where $F = 0.26$ (meaning that the domain is quite far from local force balance) the trend of basal slip along the transect is very similar, but shifted upwards by around 150 m a^{-1}. The surface velocity actually decreases by around 5 m a^{-1} as a result of lower internal deformation rates (Ryser et al., 2014a). The thickness of the temperate layer also decreases slightly. This reaffirms the important influence of subglacial water pressure on basal velocity rates, but suggests that their broad pattern at intermediate-scales is largely controlled by topography.

It is further interesting that as driving stress increases, and assuming no variation in bed conditions, which is reasonable for hard beds which are unlikely to be transiently reshaped (chapter 5), subglacial water pressure must decrease in order for local force balance to be met. A relationship between bed shear stress and effective pressure does have observational support from Argentière Glacier in the French Alps (Gimbert et al., 2021), however further work is required to thoroughly understand the processes controlling this relationship.

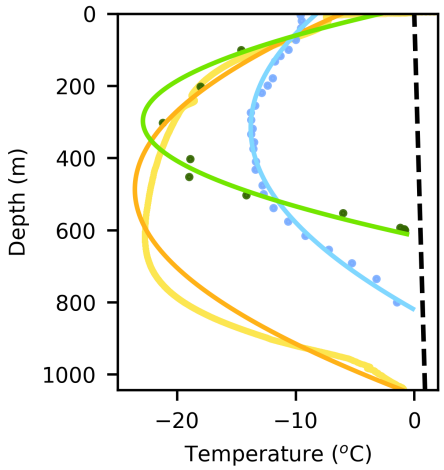

Fig. 4.16 . Temperature profiles with fitted curves for Sermeq Kujalleq (orange) and Isunnguata Sermia (sky blue). Yellow line is from BH19c (Law et al., 2021), blue scatter is from S5 (Harrington et al., 2015). Black dashed line is the pressure melting point using a Clausius-Clapeyron slope of 0.0974 K MPa^{-1}.

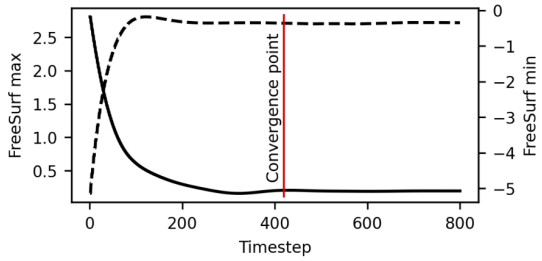

Fig. 4.17 . Change in free surface max (dashed line) and min (solid line) values with time including point where the model is deemed to have converged.

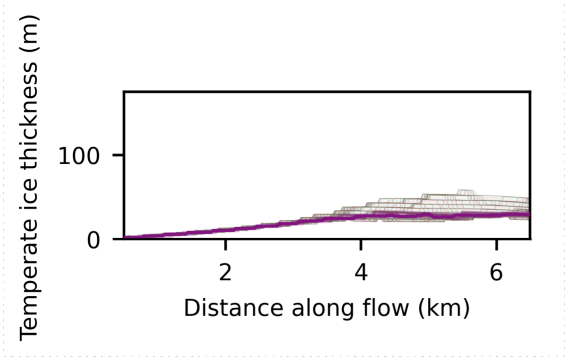

Fig. 4.18 . Basal temperate layer ice thickness averaged across flow for the RESPONDER domain forced with BedMachine topography (Run Rbm).

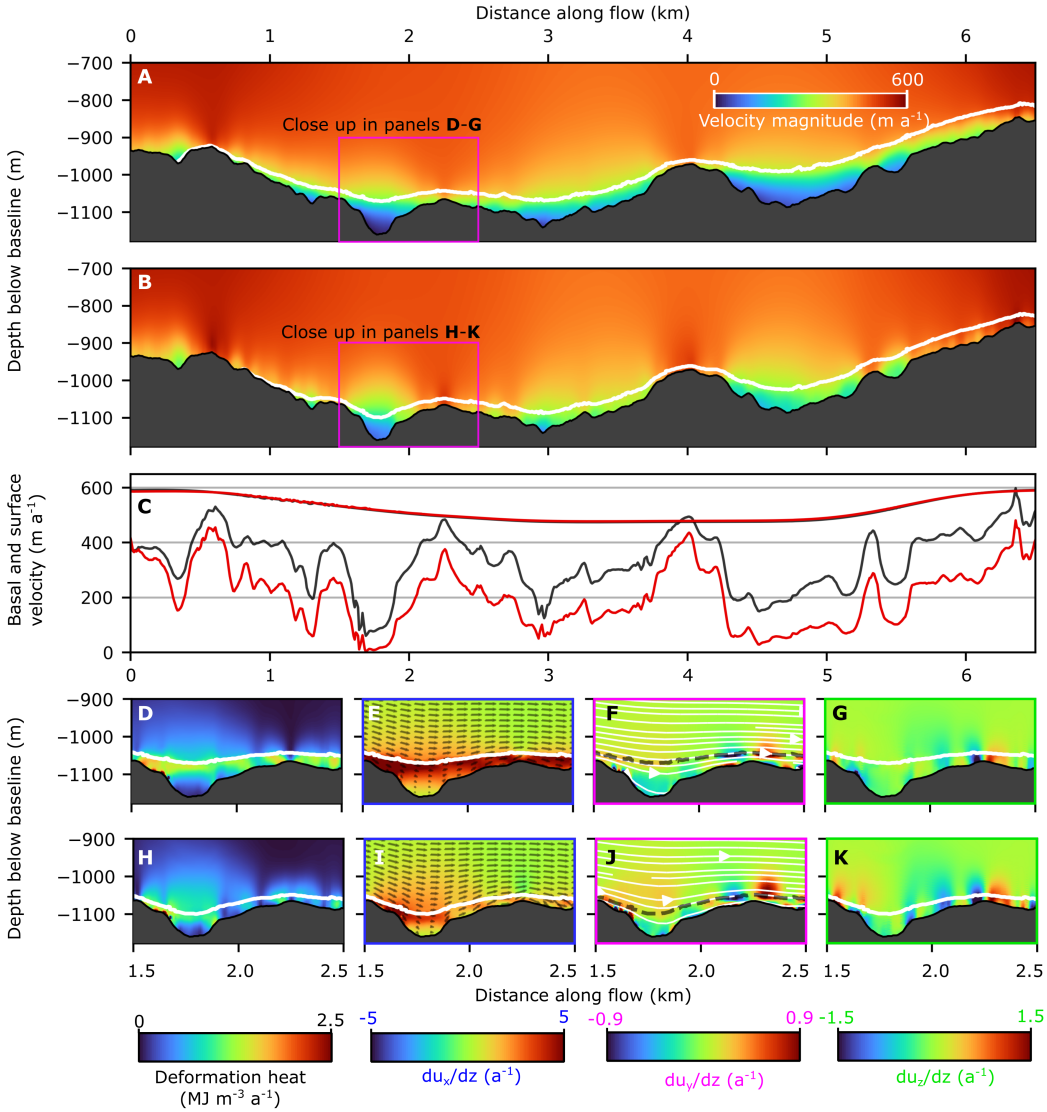

Fig. 4.19 . Cross section in xz plane showing velocity magnitude at y = 1,300 m for RESPONDER at Sermeq Kujalleq for (A) a subglacial water pressure at 82.76% of overburden and (B) a subglacial water pressure at 95% of overburden. (C) shows basal and surface velocity magnitude with red for subglacial water pressure at 82.76% of overburden and black for subglacial water pressure at 95% of overburden. (D)-(G) and (H)-(K) show deformation heat, change in x-oriented velocity with depth, change in y-oriented velocity with depth, and change in z-oriented velocity with depth for subglacial water pressure at 82.76% and 95% of overburden respectively.

Chapter 5

Results III: Complex motion and landscape formation of Thwaites Glacier

5.1 Preface

5.1.1 Setting

This study grew as an extension of the modelling and observation work for the GrIS. The unique geology of Thwaites Glacier and the availability of high-resolution bed topography data made it a useful test case for mechanics towards the streaming side of the ice-sheet motion spectrum (Truffer and Echelmeyer, 2003). The crucial importance of Thwaites Glacier in WAIS mass loss over the coming decades to centuries, and lack of borehole observations, also made it an ideal site to use a model previously shown to be effective in reproducing borehole records. I intend to submit an edited version of this study to the Journal of Glaciology or The Cryosphere in the near future.

5.1.2 Contributions

Nick Holschuh provided the swath radar data necessary for this study from his Holschuh et al. (2020) paper, suggested initial sites that may be interesting for modelling, and got me up to speed with landform formation literature. Ian Joughin provided basal traction inversion data for Thwaites Glacier from his Joughin et al. (2014) paper. I designed the study and wrote the manuscript with support from Poul Christoffersen.

5.2 Abstract

Thwaites Glacier is a crucial contributor to observed and predicted WAIS mass loss. However, with no direct borehole observations, our understanding of ice-motion beneath the

surface of Thwaites Glacier remains enigmatic, with the interaction of ice-motion patterns with the subglacial landscape also unclear. Here I use a 3D thermomechanically coupled periodic model shown to be effective in reproducing borehole observations from the GrIS with recently acquired high resolution swath radar DEMs to investigate ice motion and landscape formation. I show that basal slip rates are highly variable at rough topographic highs where inferred basal traction is high and landforms are interpreted to be predominantly erosive, but that basal slip rates are high and uniform in topographic basins where inferred basal traction is low and landforms are interpreted to be predominantly depositional. Temperate ice is likely to be at least locally present at rough topographic highs, where it may sensitively influence their resistance to flow. Preexisting geology is found to be a crucial decider of landform morphology, particularly in the predominantly erosive settings. The longevity of these landforms over millennia suggests that patterns of basal traction beneath Thwaites Glacier are largely controlled by subglacial topography, not subglacial drainage.

5.3 Introduction

Thwaites Glacier (Fig. 5.1) has undergone the largest change of any Antarctic ice-ocean system since the dawn of the satellite era (Paolo et al., 2015) with large ($\sim$ 50 Gt a^{-1}) and sustained mass loss over the last several decades (Mouginot et al., 2014; Rignot et al., 2014; Medley et al., 2014). A complete retreat of Thwaites Glacier would shift ice divides, entraining ice from adjacent catchments, and raise global sea level by in excess of three metres (Scambos et al., 2017). With a further increase in ice discharge possible within decades (Joughin et al., 2014; DeConto and Pollard, 2016) mass loss from Thwaites Glacier is of significance to coastal communities over the 21st century and beyond.

Thwaites Glacier's particular vulnerability is largely a result of its unique bathymetry and subglacial topography. Thwaites Glacier has an ice-ocean front spanning $\sim$120 km and the greatest width-depth ratio of any Antarctic ice stream (Hunter et al., 2021), with a bathymetric profile that facilitates a direct connection between the relatively warm and dense mid-depth ocean water (Circumpolar Deep Water) surrounding the Antarctic continental shelf and the deep WAIS interior (Holt et al., 2006). Meanwhile, the neighbouring Pine Island Glacier has a topographically-constrained terminus, inhibiting the incursion of warm ocean currents more effectively (Vaughan et al., 2006; Fretwell et al., 2013) though it is still far from immune to a warming climate (Smith et al., 2016). In addition, while the Siple Coast ice streams flowing into the Ross Sea Embayment are directed along the tectonic fabric formed by extension between the Transantarctic Mountains and the Amundsen

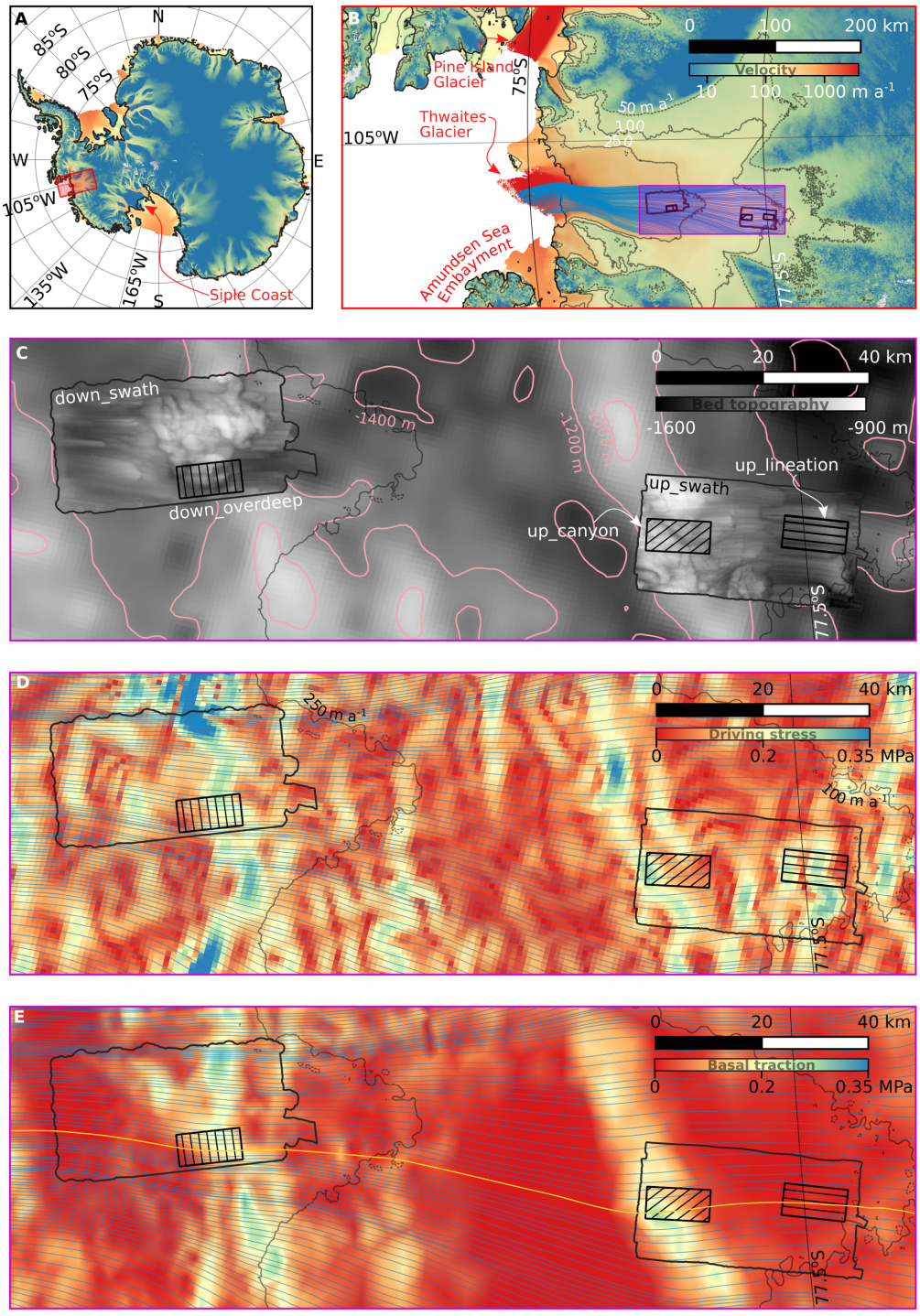

Fig. 5.1 . Location of Thwaites Glacier in Antarctica (A, B) showing surface velocity (log scale) from MEaSUREs data (Rignot et al., 2011) with contours at 50, 100, and 250 m a^{-1}. Thick black line indicates the grounding line from (Rignot et al., 2013). Purple shaded box contains outlines of up_swath, down_swath (from Holschuh et al., 2020), and modelled settings, enlarged in (C)-(E). Flow lines (in blue) are spaced at 2 km on he upstream boundary and 4 km at inflow portions of lateral boundaries and also shown in (D) and (E). (C) Bed elevation from Bedmap2 (Fretwell et al., 2013) with swath radar topography within outlines from Holschuh et al. (2020). (D) Driving stress derived from Bedmap2 surface and bed topography. (E) Basal traction inferred from the inversion of Joughin et al. (2014).

Coast, Thwaites Glacier is driven across this tectonic fabric and through high-level gaps at the Pacific rift margin (Alley et al., 2021). The outcome of this unique geological setting is (1) significant topographic deepening to a basin ∼1200 m below sea level inland from the glacier terminus (currently ∼600 m below sea level) with very little topographic confinement and (2) bands of prominent topography ∼20 km across, inferred to be topographic rift blocks (Muto et al., 2019a; Alley et al., 2021), cross-cutting the direction of ice surface motion.

Aspect (1) makes Thwaites Glacier a classic example of vulnerability to marine ice sheet instability (Hughes, 1981), suggested by some to already be underway (Joughin et al., 2014), and likely to have occurred during the last interglacial when atmospheric CO_2 concentrations were lower than present (though temperature was 1-2°C higher, Dutton et al., 2015; Steig et al., 2015). The unconfined nature of Thwaites Glacier additionally means that more resistance to driving stress comes from the basal traction than at narrower ice streams where transverse stresses are more important (Sergienko and Hindmarsh, 2013). Aspect (2) means Thwaites Glacier bed characteristics are distinct in West Antarctica, with recent geophysical observations (Muto et al., 2019a; Muto et al., 2019b; Clyne et al., 2020; Holschuh et al., 2020) indicating alternating basins and crests oriented roughly perpendicular to flow at a scale of ∼40 km (Fig. 5.1C), which, where observations are available, coincide with inferred bands of alternating bed strength (Fig. 5.1, Joughin et al., 2014). How these bed conditions are implemented in numerical models has a significant control on predictions of the future of Thwaites Glacier (Tsai et al., 2015).

However, despite Thwaites Glacier's vulnerability to climate change, ice motion beneath the surface and its interaction with the subglacial environment is still very poorly constrained. There are no borehole observations that enable estimation of the basal velocity ratio (basal velocity divided by surface velocity) or constraint of basal conditions at any point, and, while seismic- and radar-derived ice-fabric studies indicate increased deformation rates towards the ice-sheet bed these methods cannot at present provide a quantitative measure of this deformation (Horgan et al., 2011). Here, I use the model developed in chapter 4, which was shown to be effective in reproducing borehole observations across the GrIS, to investigate ice motion over high-resolution bed topography from recently obtained swath radar data (Holschuh et al., 2020). Comparison of modeled patterns of ice motion with landscape characteristics and an inferred basal traction field (Fig. 5.1, Joughin et al., 2014) allows the importance of the subglacial landscape on Thwaites Glacier motion to be assessed in detail for the first time. Model results also enable theories of subglacial landscape formation to be tested in the context of realistic ice-motion and glaciostatic pressure fields. I focus on three 6 by 12 km settings (Fig. 5.1), proceeding downflow these are:

up_lineation (in up_swath area from Holschuh et al., 2020, Fig. 5.2E)**.** This setting is characterized by lineations oriented parallel to surface velocity direction, extending across the entire domain, with a vertical amplitude of up to ∼100 m. Across flow variation in topography is comparatively low.

up_canyon (in up_swath area, Fig. 5.5E)**.** A canyon, up to ∼175 m deep and oriented at ∼ 45° to surface velocity direction is the dominant feature of this setting. The higher elevation areas up and downflow of the canyon are characterized by obvious topographic undulations. The end sections of lineations similar to those in up_lineation are featured in the first 2.5 km of up_canyon, terminating in places with a trough up to ∼100 m deep.

down_overdeep (in down_swath area, Fig. 5.7E)**.** Here, a large streamlined feature >2 km in length rises ∼ 200 m above a broad plane, with a further area of high bed topography featuring a steep stoss side slope to the right of the domain (when looking along the direction of flow). A moat, up to ∼50 m deep is positioned in front of the central streamlined feature, and proceeds to curve around its left flank.

Along-flow seismic data lines from up_swath and down_swath areas (Muto et al., 2019a; Muto et al., 2019b; Clyne et al., 2020) measure high acoustic impedance and normal-incidence reflectance coefficients at topographic highs — which include the downflow portion of up_canyon and the higher elevation areas of down_overdeep — suggesting harder-bed, if not definitively hard-bed, conditions. Conversely, low acoustic impedance and normal-incidence reflectance coefficients in topographic basins — which include all of up_lineation, the inflow portion of up_canyon, and lower elevation areas of down_overdeep — suggest soft-bed conditions. This evidence is not equivocal, and is limited to observation lines but is further supported by a coincident basal traction inversion (Muto et al., 2019a), consideration of the morphology of deglaciated 'hard' and 'soft' landforms, and the interpretation that this region of the Thwaites Glacier bed is well-represented as a tectonic rift fault-block landscape (Muto et al., 2019a; Alley et al., 2021).

5.4 Methods

The main model methodology is outlined in section 4.6. Three model alterations are made here. First, swath radar output is used for the DEM, meaning no geostatistical simulations required. This radar data is supplied at 25 m spatial resolution, with full details available in Holschuh et al. (2020). The topography is still smoothed using a Gaussian filter with standard deviation 1 to soften occasional sharp-point radar artefacts

that result in unrealistically high basal velocity values. Second, the representative edge length for model elements is increased to 37.5 m (from 25 m) and the model domain is increased to 12 km by 6 km (from 8 km by 4 km) resulting in the same overall number of model elements. A taper is still applied to match inflow and outflow boundary elevations. Third, temperature is assumed to follow a linear interpolation between the year-averaged 2020 surface temperature obtained from RACMO2.3p1 (van den Broeke, 2019) and the pressure melting point at the ice-sheet base, rather than the quadratic profile used for the GrIS. This is in broad agreement with available borehole data from elsewhere in the WAIS (Fisher et al., 2015; Engelhardt et al., 1990). The temperature is calculated as a function of depth for the free surface runs and applied as a fixed inflow boundary condition for the thermomechanically coupled runs.

In addition, once the free surface and pressure and velocity boundary conditions are obtained in the free surface run, the value of O — the effective stress as proportion of overburden — is varied in order to test the influence of varying subglacial water pressure upon the average basal velocity ratio and temperate layer thickness. This means that the free surface and boundary conditions will not be quite as well adjusted as in chapter 4, but does allow the first-order nature of this relationship to be evaluated. The O values used are displayed in Fig. 5.15. Two different rheologies are applied for these tests in the up_canyon setting. Full temperate, as used in all simulations in chapter 4 (Fig. 4.3A), and simple temperate where the rate factor, A, is capped at a homologous temperature of 0°C or water content, ω, of 0. All settings required a surface slope of 0.25°. The F value used for up_lineation was 1 to prevent unstable velocity behaviour, however this was reduced to 0.9 for up_canyon and down_overdeep due to the additional support from stoss-side obstacle. As the F value decreases below the value used for free surface runs (0.9 or 1) this means increasingly more support comes from far-field stresses. In the case of this model this means longitudinal stresses as the lateral boundaries have zero-flux and zero-friction conditions while the inlfow boundary has a prescribed 2D velocity field. If the F value increases above the value used for free surface runs this means the local traction supplied by the bed can exceed the local driving stress, mimicking support of compressive far-field stresses.

Using outputs from the numerical simulations, stress normal to the ice bed surface (analogous to pressure in Alley et al., 2021) is calculated as

$$\sigma_n = \text{sgn}\left(\sigma_{ii} n_i\right) \sqrt{\sigma_{ii} n_i} \tag{5.1}$$

where σ_{ii} are stress tensor components, and n_i are components of the ice-bed interface normal vector. Glaciostatic pressure, ξ (MPa), is calculated as

$$\xi = (\rho_i g Z_s + (\rho_w - \rho_i) g Z_b) \times 10^{-6} \tag{5.2}$$

where ρ_i and ρ_w are the densities of ice and water respectively, g is gravitational acceleration, and Z_s and Z_b are the positions of the ice surface and base respectively. Last, to enter the ice surface position into Paraview, Z_s is approximated as a function of x and y coordinates using a 3D polynomial using least squares of the form

$$Z_s = \nu_{00} + \nu_{10}x + \nu_{01}y + \nu_{20}x^2 + \nu_{11}xy + \nu_{02}y^2 + \nu_{30}x^3 + \nu_{21}x^2y + \nu_{12}xy^2 \tag{5.3}$$

where ν values are fitting coefficients for each term. This approach results in only minor (at the very most 5 m, and usually much less) deviation away from the measured ice surface (Fretwell et al., 2013) — natural surface elevation variation over timescales considered important for landscape development is likely to be far greater.

5.5 Results

My results demonstrate that patterns of ice motion are considerably more complex in settings characterized by heterogeneous bed topography (up_canyon and down_overdeep) than in settings where bed topography is more uniform (up_lineation), with implications for large-scale ice-motion interactions between settings and for how subglacial landscapes are shaped by overriding ice. Here, for each setting in turn, I detail basal velocity, normal stress, and glaciostatic pressure at the ice-bed interface and present 2D transects of deformation heating to allow comparison with results from chapter 4. Normal stress at the ice-bed interface, which is lower than glaciostatic pressure due to the influence of high subglacial water pressure, allows comparison with the landscape formation hypothesis of Alley et al. (2021) where it is suggested to be the primary driver of overdeepened moat formation. Glaciostatic pressure allows approximate determination of subglacial water pathways, with water expected to flow perpendicular to contours from regions of high

to low glaciostatic pressure. Following these descriptions, I illustrate plan-view fields of basal velocity orientation for down_overdeep and up_canyon to asses the importance of basal-topographic features in directing basal ice motion. For all settings I present 3D views of the interaction between basal slip and internal deformation and diagrams of changes in basal-ice water content and temperate layer thickness. Unless otherwise stated, figures describing the above features are thermomechanical runs using the same F value as used to obtain the free surface position (see sections 4.6, 5.4). Last, I cover setting-wide averages of basal velocity ratios and temperate layer thickness and show the influence that variations in subglacial water pressure can have upon these.

5.5.1 up_lineation: ice motion over streamlined lineations

The up_lineation setting (Fig. 5.2) results in the most uniform ice motion behaviour. Basal velocity reaches a high of just over 100 m a^{-1} (surface velocity, $v_s \approx 130$ m a^{-1}) ~4 km along flow, where basal topography is also at a maximum, and gradually decreases from there. In the lineations proceeding downflow of the main topographic high, basal velocity is greater on the lineation crests and lower within the lineation troughs (reaching a minimum of 70 m a^{-1}). Notably, this difference diminishes gradually but does not disappear entirely as subglacial water pressure is increased from 97.03% ($F = 1$) to 99.5% ($F = 0.19$, Fig. 5.3). Modeled normal stress magnitudes are lower at up_lineation than the other settings. The stoss side of the topographic high supports the largest normal stresses (up to 0.2 MPa), with some negative values behind local small-scale (<200 m across, <40 m high) topographic perturbations which are possibly swath-radar artefacts. Where the lineations become more pronounced downflow of the topographic high point, absolute normal stress values are very low, both at lineation crests and troughs. Ice surface topography increases to a maximum above the stoss side of the broad topographic peak and drops to a low where bed elevation is lower towards the end of the domain (range 9 m) — note though that in no cases does the ice surface displayed in figures reflect the rotation in the xz plane of the applied gravity vector (here 0.25°). Last, glaciostatic pressure has a broad maximum on the stoss side of the broad topographic high, decreasing thereafter to the downflow edge of the domain. Glaciostatic pressure is greater on lineation crests than troughs when distance along flow is equivalent.

At the up_lineation 2D transect, 3000 m across flow (Fig. 5.4), a basal temperate layer only develops beyond 5 km along flow and proceeds to gradually increase in thickness from there. The basal velocity ratio is relatively uniform and high throughout (average of 0.72), increasing from a low of 0.52 at the inflow boundary to a peak of 0.84 at the crest of the broad topograhic high before gradually decreasing again towards the end of the domain.

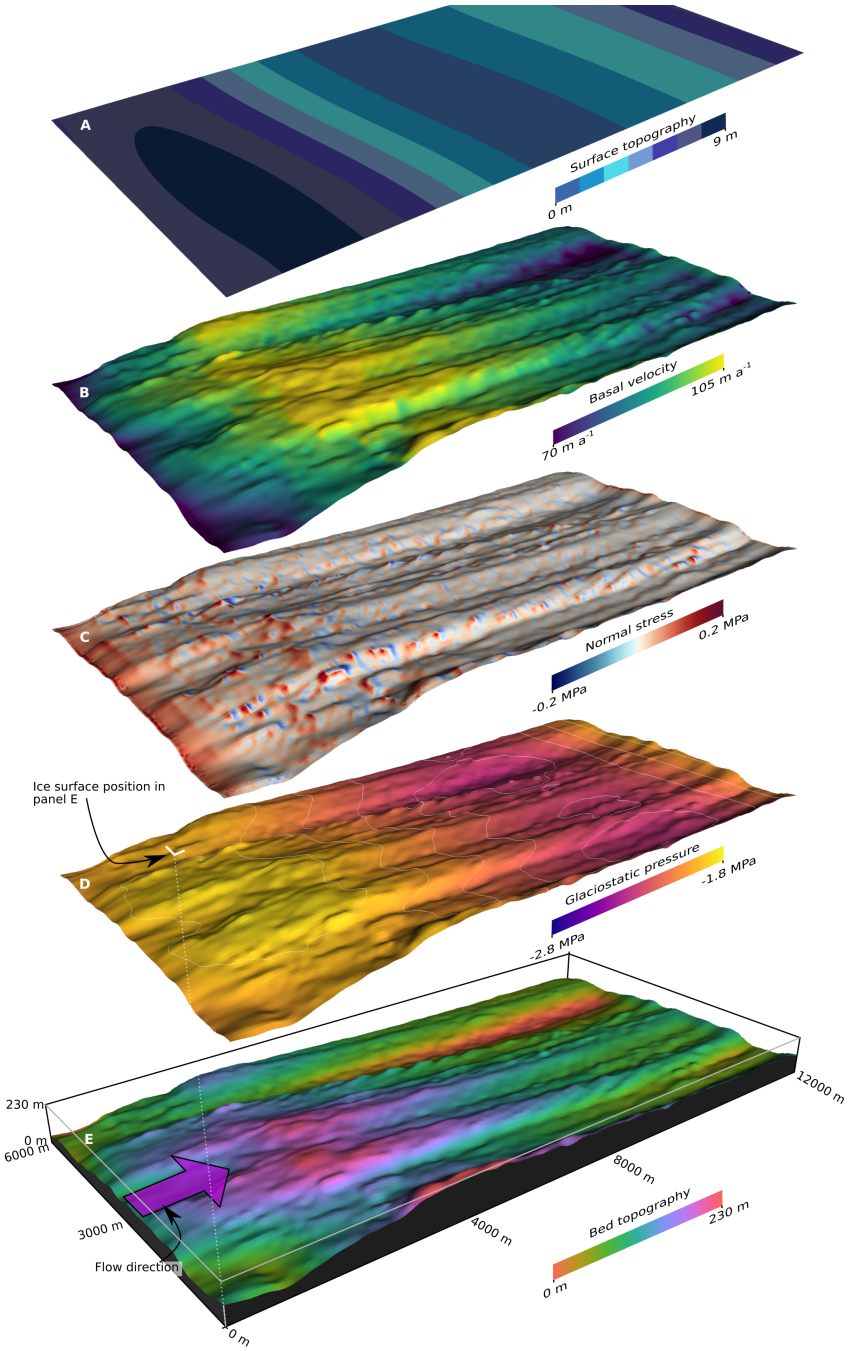

Fig. 5.2 . Topography planes with the vertical (z) axis exaggerated by a factor of three for (A) modeled ice surface topography, (B) modeled basal velocity, (C) modeled normal stress, (D) glaciostatic pressure calculated from surface and bed position, and (E) bed topography from swath radar data Holschuh et al. (2020)). Contours in (D) are at a spacing of 0.1 MPa. Basal velocity is defined as the velocity magnitude tangential to the ice-bed interface. Basal and surface topographies are normalised to have minimum values of 0. Note that the surface topography does not account for the slope applied to the gravity vector. Dashed line extending from (E) indicates total thickness of domain from bed to surface.

Where present, the CTS velocity ratio (velocity magnitude at the CTS divided by surface velocity magnitude) is only marginally higher than the basal velocity ratio and even more uniform. Deformation profiles (Fig. 5.4B) are relatively conventional, with monotonic

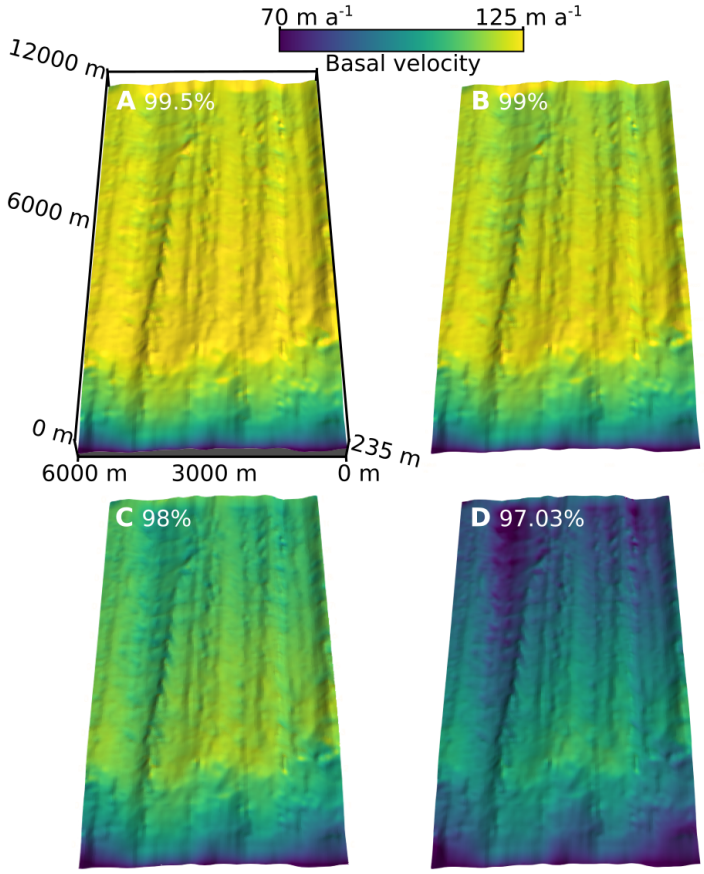

Fig. 5.3 . Alternative view of up_lineation showing basal velocity for subglacial water pressure as a proportion of overburden at (A), 99.5%, (B), 99%, (C), 98%, and (D), 97.03%. Ice motion up/into page.

increases with depth throughout, albeit with deformation increasingly concentrated within the temperate layer as the temperate layer develops. This transect has the most similarities with the BedMachine transects in chapter 4.

5.5.2 up_canyon: ice motion over an obliquely oriented canyon

In contrast to up_lineation, the up_canyon setting (Fig. 5.5) has notably more variation in basal velocity and normal stress fields. Basal velocity is greatest at topographic high points (>280 m) reaching up to 85 m a^{-1} and at its lowest in topographic depressions where it falls below 40 m a^{-1} ($v_s \approx 100$ m a^{-1}), both in the central canyon that runs obliquely through the setting and in local topographic lows both down and upflow of the central canyon. Normal stress magnitudes are higher throughout than in the up_lineation setting (up to 0.35 MPa), with alternating bands of positive and negative values corresponding to the stoss and lee sides of obstacles. The canyon, and the lineation features at the upflow end of the domain have the lowest absolute normal stress values. Ice surface topography variation

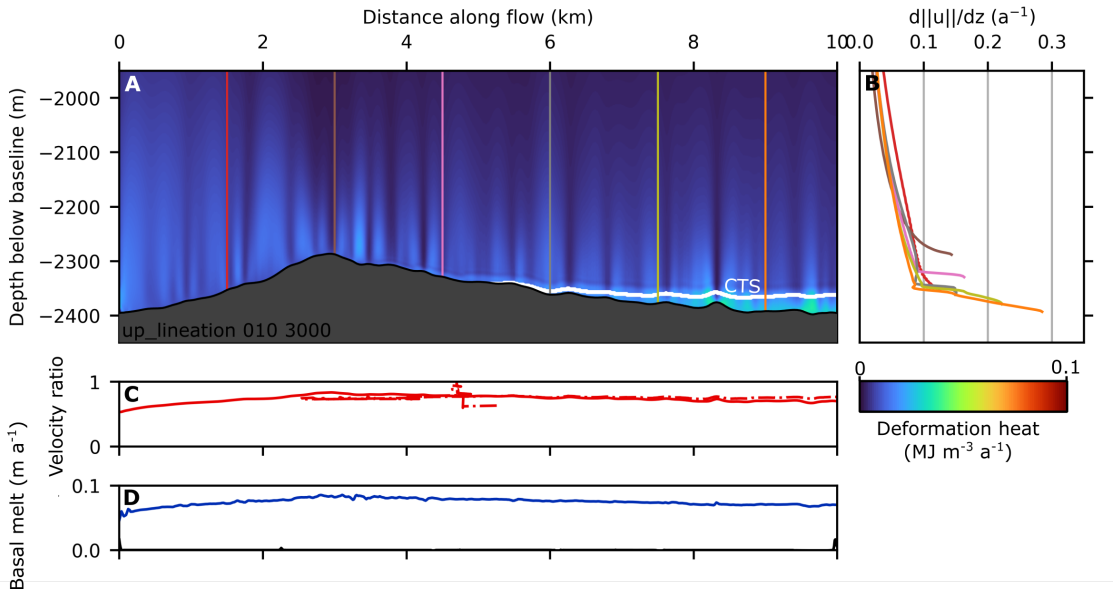

Fig. 5.4 . (A) Cross section in xz plane showing deformation heat (product of stress and strain matrices) at y = 3000 m for up_lineation. CTS position shown with white line, ice-bed interface shown with black line. (B) deformation rate profiles (change in velocity magnitude with depth) with colors and depths corresponding to the vertical lines in (A). (C) shows the basal velocity ratio (basal velocity magnitude divided by surface velocity magnitude, solid red line) and CTS velocity ratio (velocity magnitude at the CTS divided by the surface velocity magnitude, dashed red line). (D) shows basal melt rate (blue line) and drainage from temperate ice (black line).

here is greater than at up_lineation in the across flow direction, though the range is only slightly greater (10 m). The deepest part of the canyon (on the left looking along flow) has the lowest elevation ice surface above it. Glaciostatic pressure clearly decreases in the downflow direction along the canyon, with local topographic highs and lows substantial enough to be the main local control elsewhere, rather than the ice-surface slope.

Deformation profiles and basal velocity ratios from an up_canyon transect 4150 m across flow (Fig. 5.6) are less straightforward than at the up_lineation setting. The basal velocity ratio is smoothly varying in comparison to results produced with geostatistically simulated topography in chapter 4 but does become notably more variable over the rough and relatively high topography towards the end of the domain. The basal topographic depression between ∼4-6 km results in a moderately decreased basal velocity ratio as the thickness of temperate layer locally increases. The largest deformation heating value is found within the temperate layer on the stoss side of a ∼30 m obstacle in the undulating topography downflow of the canyon.

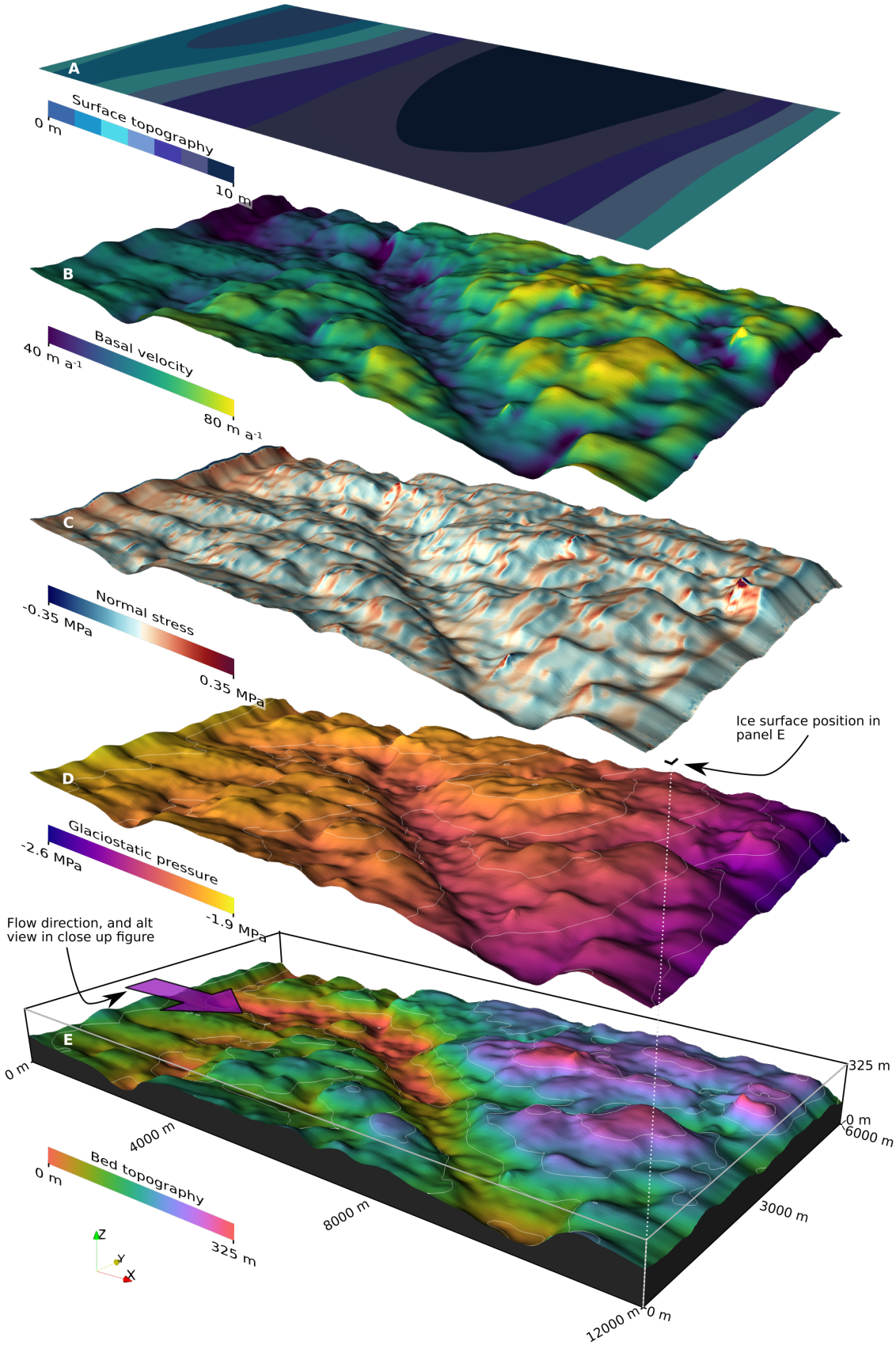

Fig. 5.5 . As for Fig. 5.2 but for up_canyon with contours in (E) at 35 m intervals.

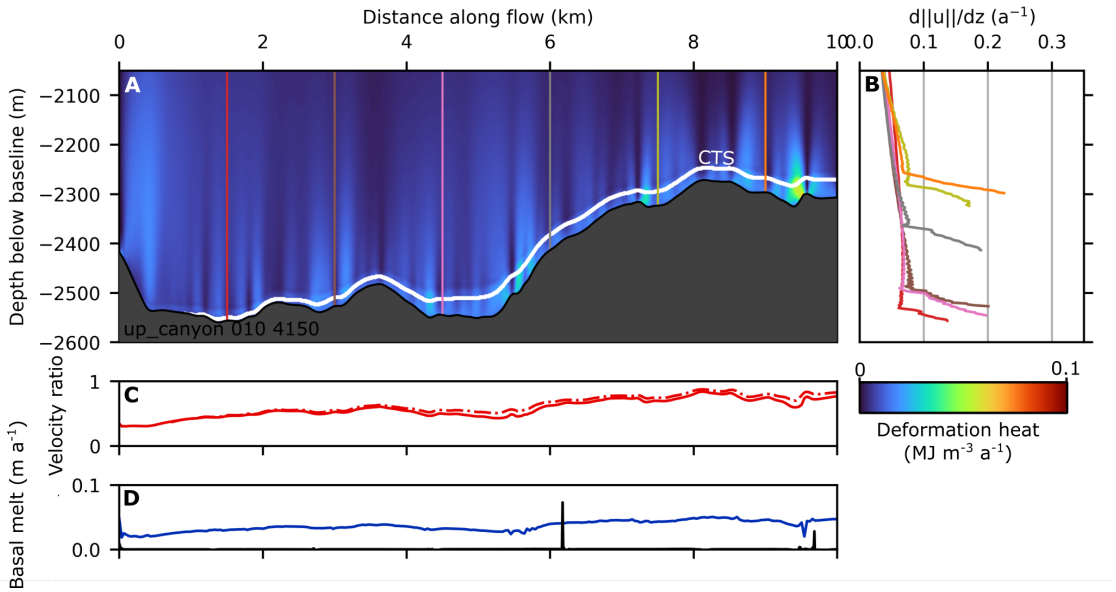

Fig. 5.6 . As for Fig. 5.4 but for up_canyon setting at y = 4150 m.

5.5.3 down_overdeep: ice motion over a large streamlined topographic obstacle with a moat

Last, ice-motion and normal stress fields at the down_overdeep setting (Fig. 5.7) are predominantly controlled by the two largest topographic features, the central streamlined feature, and the topographic highlands to the right of the setting (looking downflow). Velocity reaches a maximum on the stoss side slopes of these features (>250 m a^{-1}) but is more uniform elsewhere (∼200 m a^{-1}) and at a minimum (<120 m a^{-1}) in the overdeepened moat ($v_s \approx 300$ m a^{-1}). Large positive normal stress values (up to 0.45 MPa) are found on obstacle stoss slopes, grading into alternating positive-negative banding at obstacle crests and around the edge of the central streamlined feature, with large and sustained negative normal stresses on the lee side of obstacles. Glaciostatic pressure is at its highest atop the large obstacles, but decreases in a uniform manner across the flatter plains between these features towards the downflow end of the model domain. This domain has the greatest range in ice surface topography values, with a difference of 20 m between the high over the central streamlined feature and the low towards the downflow end of the domain. Further detail reveals the normal stress, velocity, and glaciostatic pressure fields in the down_overdeep overdeepened moat (Fig. 5.8). Normal stress is negative on the lee side of the moat, and near zero within the depression of the moat itself. Alongside basal velocity, glaciostatic pressure is also at local minima in the moat, with contours suggesting substantial routing of upstream water through the moat.

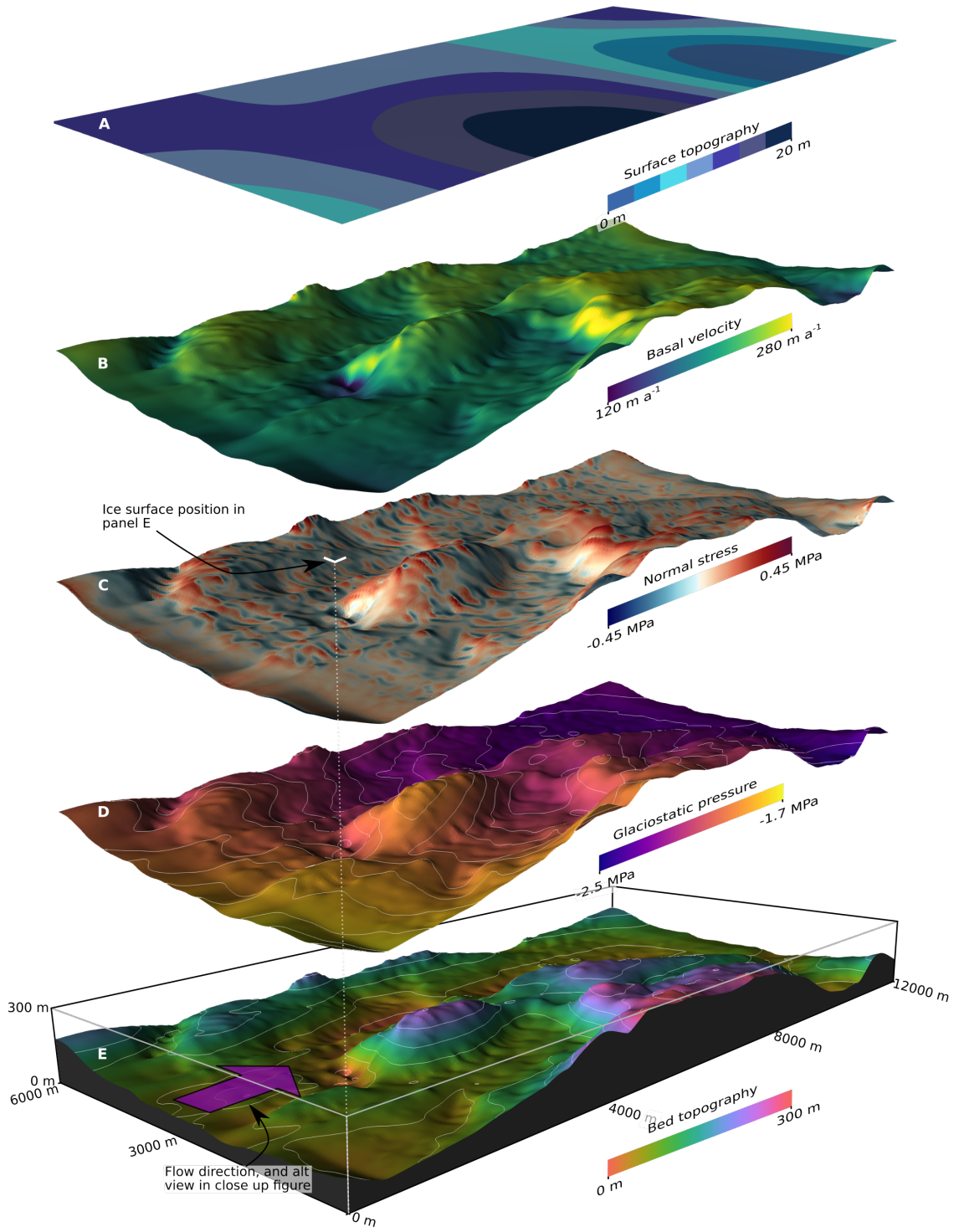

Fig. 5.7 . As for Fig. 5.2 but for down_overdeep setting with contours in (E) at 50 m intervals an contours in (D) at 0.05 MPa intervals

A transect at down_overdeep at 3260 m along flow shows that clear deformation bridges (see chapter 4 for full description) form over the overdeepened moat, and in a secondary depression immediately downflow of it. These two bridges notably increase the thickness of the temperate layer downflow, which remains much thicker (up to 100 m) beyond the

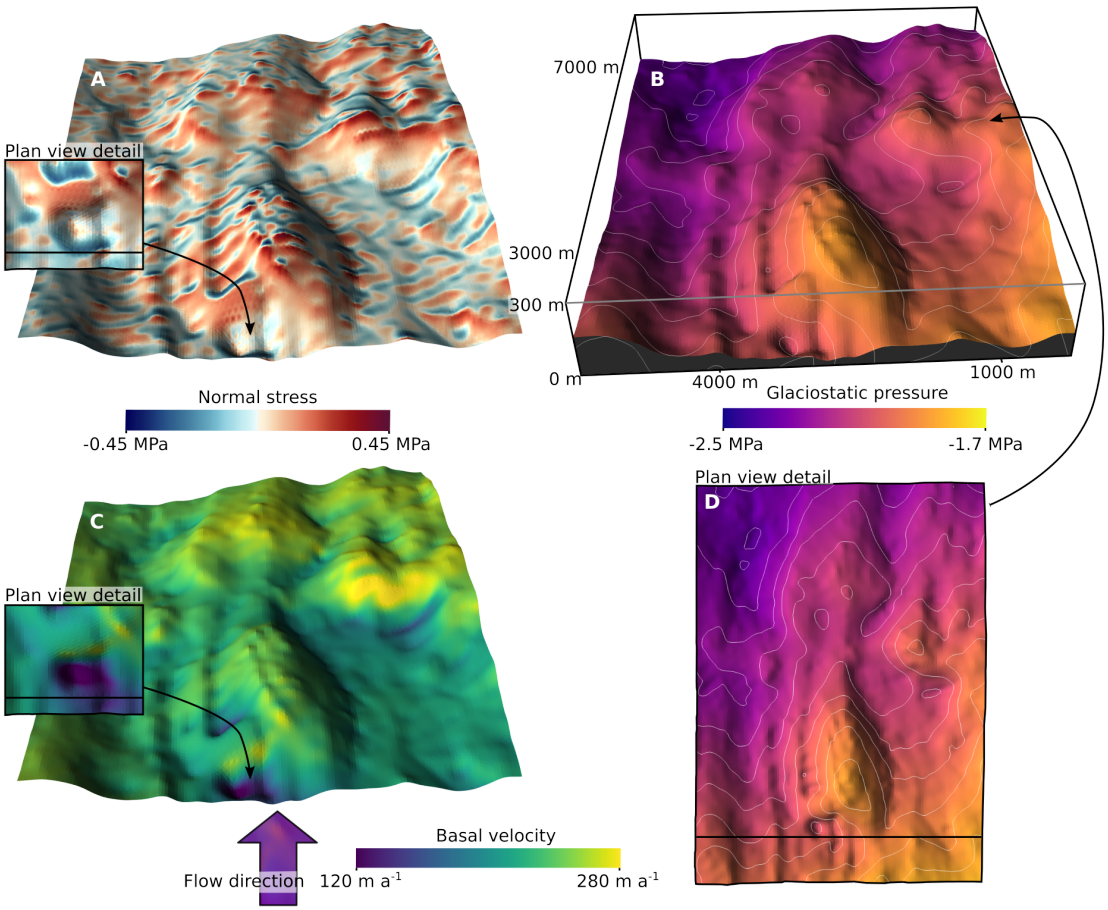

Fig. 5.8 . Close up of the bed for the streamlined feature and moat in down_overdeep showing (A) modeled normal stress, (B) glaciostatic pressure calculated from surface and bed position, and (C) modeled basal velocity with contour spacing at 0.05 MPa. (D) is the plan view of (B).

central streamlined feature. The two topographic depressions also notably locally lower the basal velocity ratio (to a minimum of 0.40) before the basal velocity ratio gradually reaches a high of 0.94 over the topograhic rise at around 7.5 km downflow. In this transect, similar to transects from the GrIS (Figs. 4.5-4.7), deformation rates both increase and decrease with height above the bed in the same profile. The CTS velocity ratio departs from the basal velocity ratio over the overdeepenings, but not as notably as with transects from the GrIS (maximum of 0.1 here compared to >0.5 at the RESPONDER site). In transects from all settings (Figs. 5.4-5.9) basal melt rates (section 4.6.3 for calculation) follow basal velocity rates and drainage from the temperate layer is negligible as the temperate layer does not reach the saturation water content of 2.5% at any point. A further down_overdeep transect at 1450 m is available in the supplementary material for this chapter.

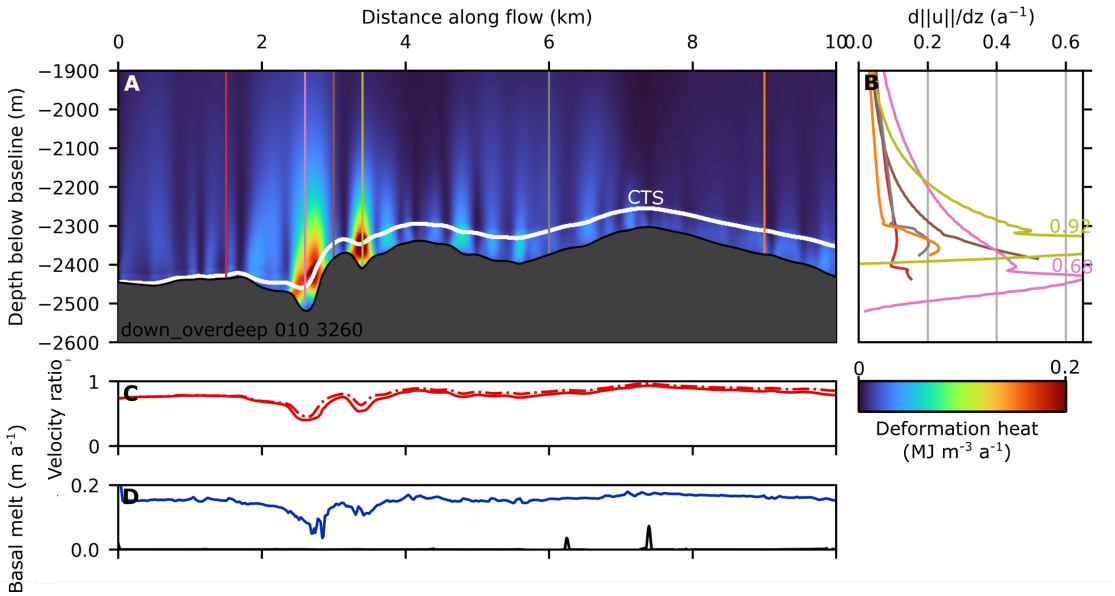

Fig. 5.9 . As for Fig. 5.4 but for down_overdeep setting at y = 3260 m.

5.5.4 Topography influence on basal velocity direction

The central diagonally cross-cutting canyon in the up_canyon setting does not exert a strong control on basal velocity direction (Fig. 5.10). Some diversion is visible towards the downflow end of the canyon, but this is not pervasive across the entire length of the canyon. No major difference in vector orientation is apparent when (1) the zero-flux condition normal to the domain sides is dropped (Fig. 5.10B) or (2) the effective pressure is reduced from 2.43% of overburden to 1% of overburden. The central topographic rise in the down_overdeep setting (Fig. 5.11) produces a more notable effect, diverting ice around the central streamlined feature, particularly proximal to the overdeepening. This suggests topographic rises have a greater influence on patterns of basal ice velocity orientation than topographic depressions.

5.5.5 Velocity magnitude variation

Ice velocity magnitude varies not only at the ice-sheet base, but also within the overlying ice column. This is most apparent in the down_overdeep setting. Here (Figs. 5.12A, B), basal velocity magnitude is at its greatest on the stoss side of large obstacles and at its lowest in the adjacent upflow troughs, establishing a large velocity magnitude gradient which is mirrored in the overlying ice. Contours are grouped closest together towards the base, with more gradual velocity magnitude variation above ∼-1900 m. Velocity magnitude variability above this point is more gradual, with some further variability noted in the

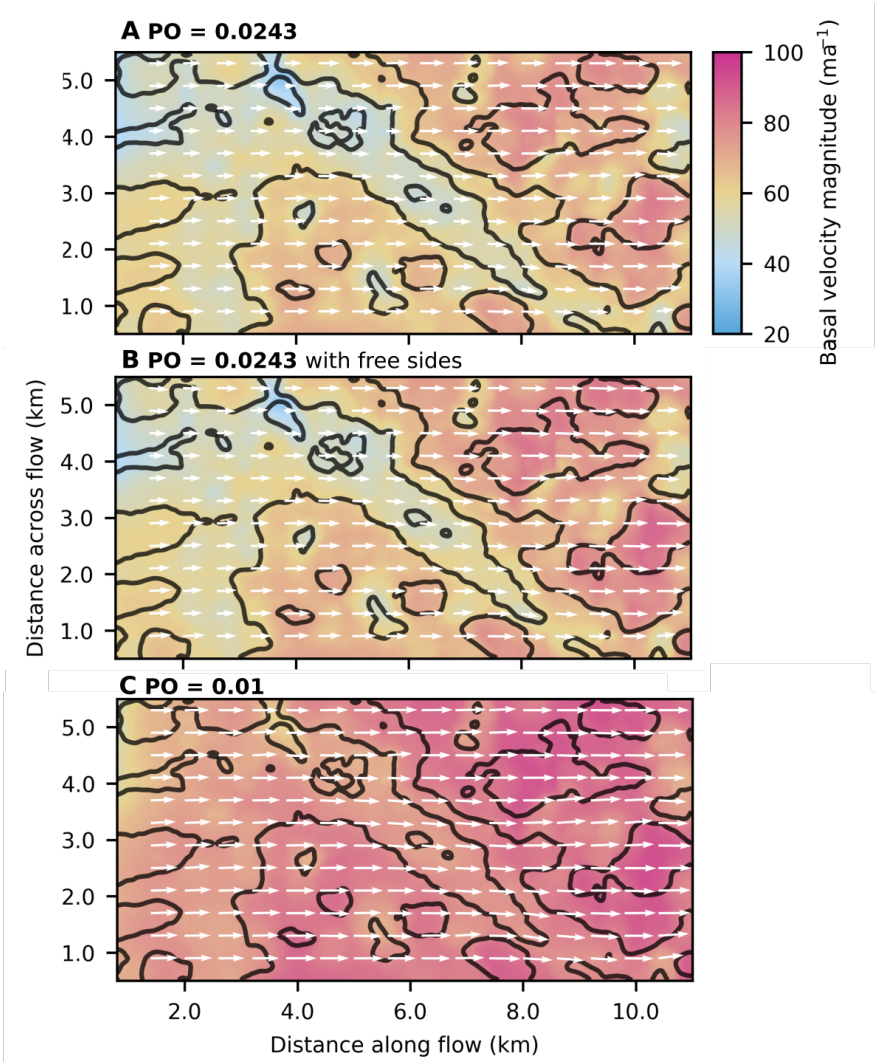

Fig. 5.10 . 2D plan view of up_canyon setting showing basal velocity magnitude (basal velocity tangential to ice-bed normal) in blue-yellow-red colourmap with vectors of x and y velocity components as white arrows. Bed topography contours between 2550 and 2250 m below baseline with 75 m spacing in black. Subglacial water pressure at 97.57% of overburden in (A) and (B) and 99% in (C). In (B) there is no zero-flux condition on the lateral boundaries with ice having the same enthalpy profile as at the inflow boundary.

shallower depression behind the central streamlined feature. The velocity-field effect of the other large stoss side feature (Fig. 5.12B) extends further both vertically and along flow, although the velocity gradient is similar in the immediate vicinity of the obstacle. Last, for down_overdeep note that directly above the stoss-side slope the velocity magnitude at first decreases vertically upwards before increasing again beyond ∼-1800 m. At up_canyon, velocity magnitude contours increase more uniformly above the bed. The slope of these contours is relatively level above the canyon itself, but they slope gently downwards along flow to meet the topographic high point beyond the canyon. up_lineation has the most uniform contours, which remain sub-parallel throughout, gradually departing in turn from the ice-bed interface at the gentle bed slope downflow of the broad topographic high point. The exception to this is the 130 m a^{-1} contour, which rises near vertically to meet the surface.

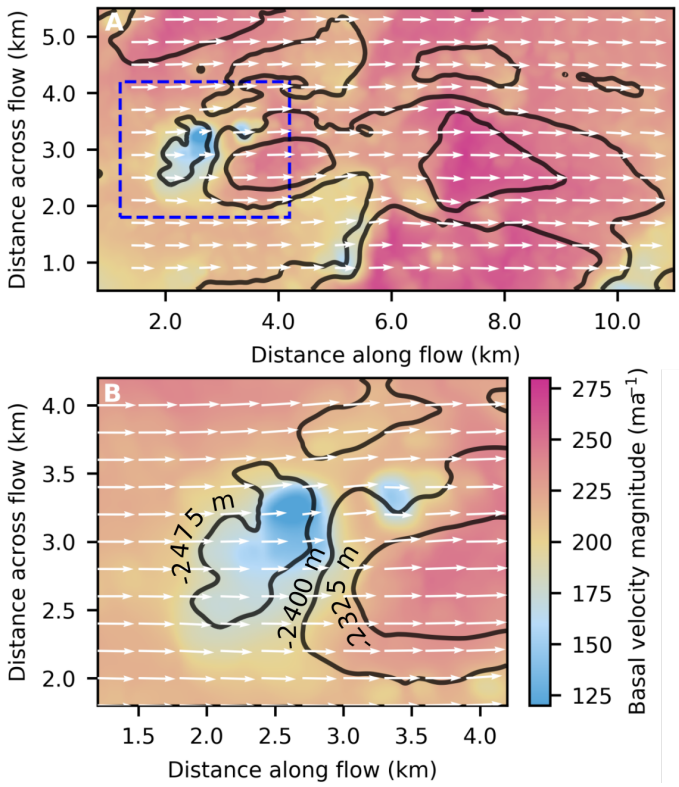

Fig. 5.11 . As for Fig. 5.10 but showing down_overdeep setting. Contours still at 75 m spacing. Both panels are for effective pressure of 2.43% with zero-flux boundary conditions for lateral boundaries, and with the area covered in (B) shown by the blue dashed line in (A).

Fig. 5.12 illustrates in sum that complex patterns of velocity magnitude at the ice-sheet base are connected to complex patterns of velocity magnitude within the ice itself.

5.5.6 Temperate ice and basal specific enthalpy

Basal homologous specific enthalpy (the phase change specific enthalpy subtracted from the specific enthalpy), H_h, shows distinct patterns within and across settings. At up_lineation (Fig. 5.13D) contours spaced at 750 J kg^{-1} intervals show similar patterns — lineation troughs are the first to reach a given homologous specific enthalpy while lineation crests are the last. Contour spacing decreases towards the downflow end of the domain, indicating the rate of change of basal homologous specific enthalpy is increasing. At the up_canyon setting (Figs. 5.13A, C) the canyon broadly demarcates lower H_h from higher H_h, coincident with increased deformation heating through the canyon. Basal temperate layer thickness (Fig. 5.13C) shows further variation across this setting, increasing in thickness in topographic troughs and decreasing over topographic highs. Water contents are much lower than in domains from the GrIS (chapter 4), only reaching values of 1% (much below the limit of 2.5%) towards the end of the domain. Last, at the down_overdeep setting basal homologous

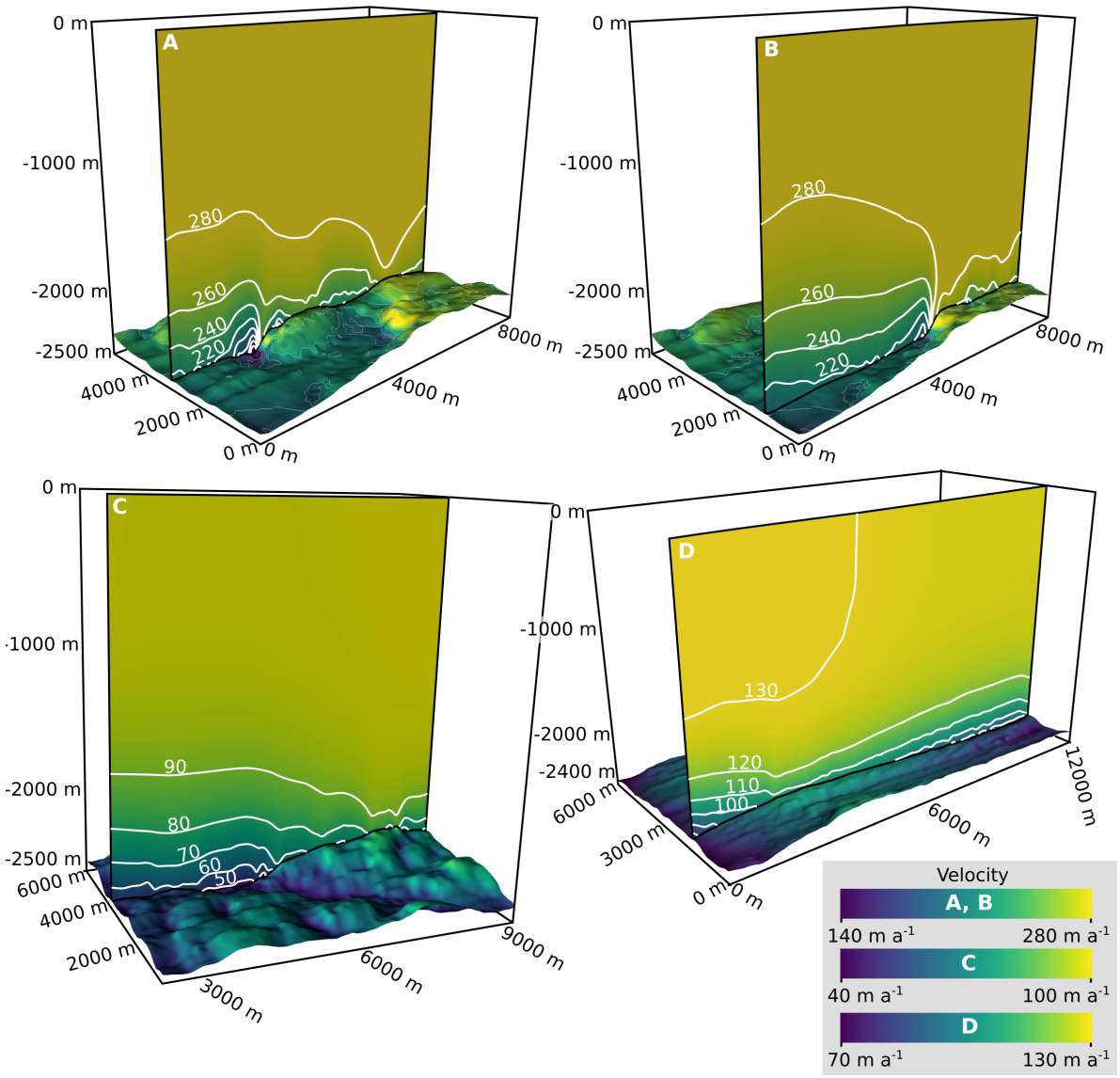

Fig. 5.12 . 2D transects and ice-bed showing ice velocity magnitude (viridis) and contours. down_overdeep in (A) and (B), up_canyon in (C), and up_lineation in (D). Ice motion is from left to right in all panels.

specific enthalpy is very clearly controlled by the moat and topographic highs. The moat prompts a sharp transition to above 750 J kg^{-1} with the only basal ice to surpass the 1500 J kg^{-1} contour directly downflow of this point. Topographic highs result in isolated regions of locally decreased homologous specific enthalpy, with may be related to the phase change enthalpy increasing at topographic highs as the pressure decreases.

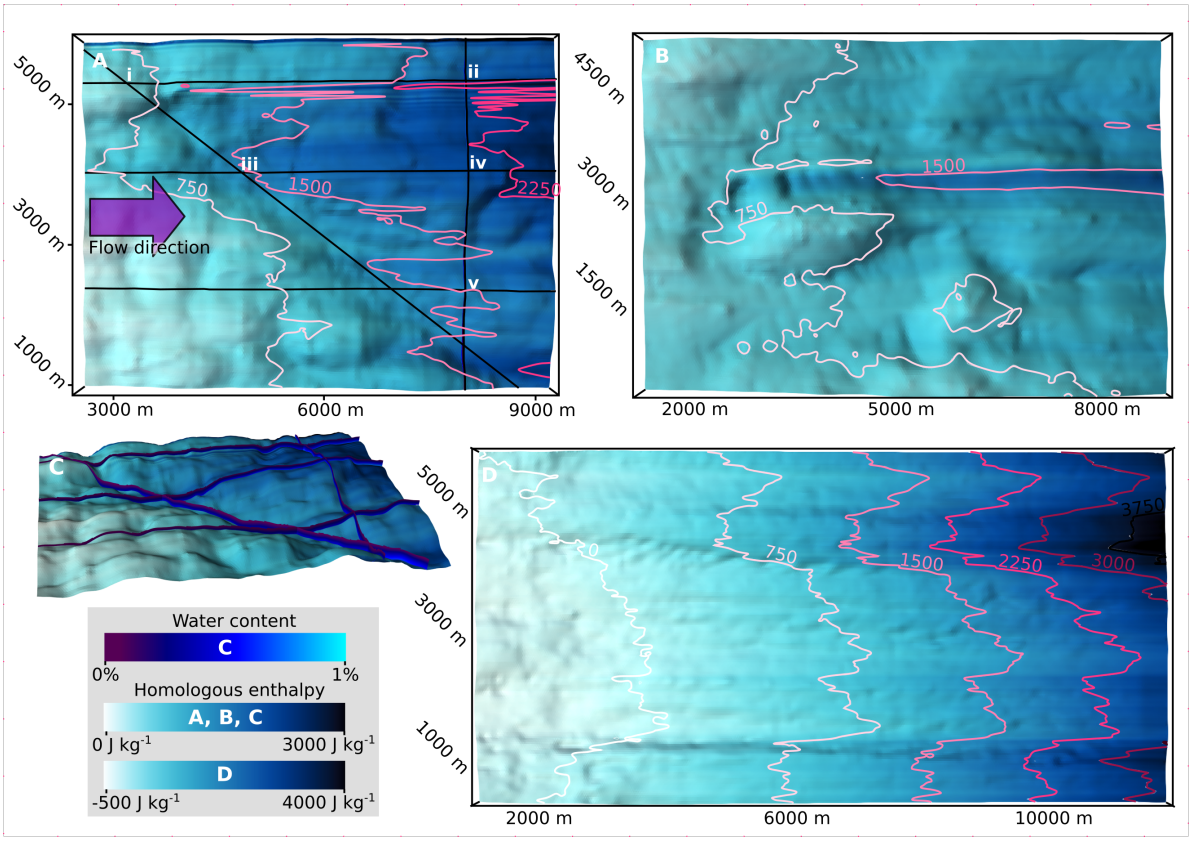

Fig. 5.13 . Temperate ice and homologous specific enthalpy (difference between specific enthalpy and phase change specific enthalpy) for up_canyon (A and C), down_overdeep (B), and up_lineation (D). (A), (B), and (D) Plan view with contours at 750 J kg^{-1} intervals in increasing shades of pink. Black lines in (A) show position of temperate ice transects in (C) with colour indicating water content up to 1%. Vertical point where transect terminates is where water content is 0. Numerals marked on (A) are for transect intersections where temperate layer thickness is: i 9.4 m, ii 45.8 m, iii 42.2, iv 27.0 m, v 39.6. Along flow slices are at y = 5380 m, y = 4062 m, and y = 2320 m.

5.5.7 Setting-wide characteristics

Each setting has a notably different hexbin distribution of basal velocity ratio and temperate layer thickness (Fig. 5.14). The two settings with greater topographic variation (up_canyon and down_overdeep) both have cloud-like appearances with no distinct central cluster, and no obvious basal velocity ratio-temperate layer thickness correlation (both of which are features of the geostatistical domains modelled in chapter 4). The up_lineation setting has an almost linear link between basal velocity ratio and temperate layer thickness, similar to BedMachine runs in chapter 4, which is related to the steady increase in temperate layer thickness across the transect as basal topography and basal velocity both decrease (Fig. 5.4). The up_canyon setting has both the lowest modal basal velocity ratio, and the broadest basal velocity ratio distribution. up_lineation, despite having a nearly linear relationship between basal velocity ratio and temperate layer thickness, still has an approximately normal distribution of basal velocity ratio. Last, down_overdeep has the greatest mode

of any basal velocity ratio distribution but a spread between that of up_lineation and up_canyon.

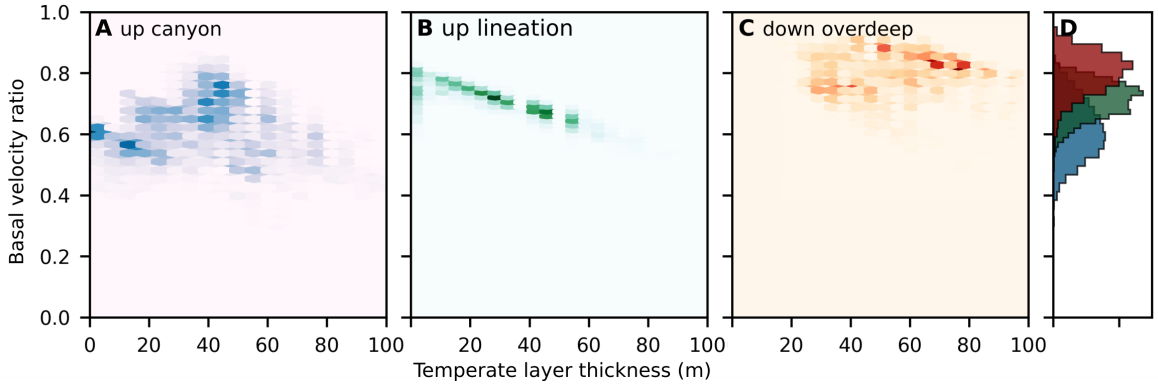

Fig. 5.14 . Hexbins of temperate layer thickness and basal velocity ratio for (A) up_canyon setting, (B) up_lineation setting, and (C) down_overdeep setting. (D) Histograms for basal velocity ratio for up_canyon (blue), up_lineation (green), and down_overdeep (red).

5.5.8 Model sensitivity to subglacial water pressure

Fig. 5.15 indicates that both average basal velocity ratio and average temperate layer thickness are sensitive to variations in F (and therefore, in linear proportion, to subglacial water pressure) with a similar trend modelled in each setting. This sensitivity is greatest for subglacial water pressures between 99 and 95% of ice overburden pressure, with the average basal velocity ratio roughly halving, and the average temperate layer thickness roughly tripling between these values. Above a subglacial water pressure of 99% of overburden the average thickness of the temperate layer decreases less rapidly, and the rate of change of the average basal velocity decreases. Below a pressure of 95% of overburden, changes in both average basal velocity ratio and average temperate layer thickness are much lower and stabilise towards subglacial water pressures of about 85% of overburden. When simple temperate rheology is implemented for up_canyon, the trend is similar, but the average temperate layer is consistently thicker and the average basal velocity ratio is consistently greater. Hexbin plots for selected subglacial water pressures for up_canyon are available in the supplementary material (Fig. 5.16).

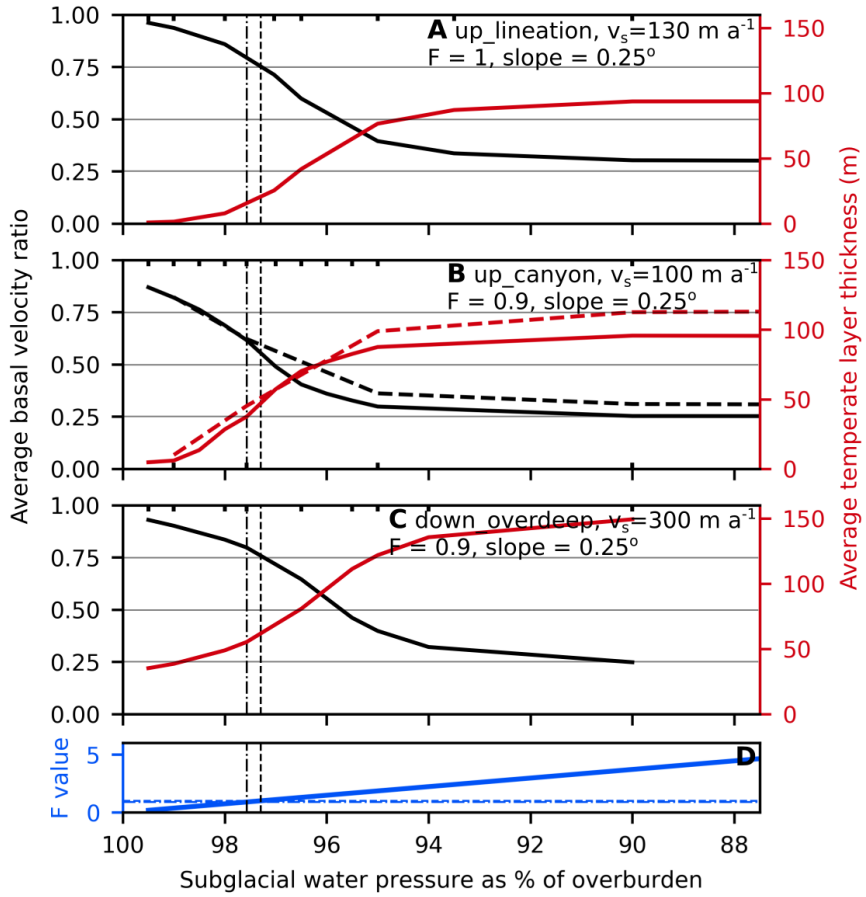

Fig. 5.15 . Average basal velocity ratio (black solid lines) and average temperate layer thickness (red solid lines) for full temperate rheology across settings for each of up_lineation (A), up_canyon (B), and down_overdeep (C). (B) additionally has simple temperate rheology in dashed line. See Methods for more information on rheologies. Black ticks on upper horizontal axis indicate input pressure values used in simulations. (D) F value related to subglacial water pressure as % of overburden. Blue dot-dash line is for an F value of 0.9, black dash line is for and F value of 1, with corresponding values of subglacial water pressure as % of overburden in black.

5.6 Discussion

5.6.1 Intermediate-scale characteristics of ice motion at Thwaites Glacier

At present, basal-slip and sediment deformation are viewed as the primary processes for Thwaites Glacier motion, drawing largely from borehole observations of the Siple Coast ice streams and from outputs of models using the shallow ice approximation (Engelhardt et al., 1990; Scambos et al., 2017). More recent work at high resolution (up to 500 m horizontally, 10 vertical layers) and with an anisotropic flow relationship does however suggest greater regional variability, separating ice motion at Thwaites Glacier into three distinct regions (McCormack et al., 2022, their fig. 1). First, the BDZ (bed-parallel vertical

simple shear deformation zone) upflow of the 50 m a^{-1} surface velocity contour where the basal velocity ratio is modelled to be an average of 0.24. Second, the SLZ (sliding zone) downflow of the 50 m a^{-1} surface velocity contour but further than 80 km upflow of the glacier terminus where the basal velocity ratio is modelled to be an average of 0.95. Third, the DSZ (deformation-sliding zone) within 80 km upflow of the glacier terminus where bed elevation is greater and the average modeled basal velocity ratio is 0.8 (with basal velocity ratios in each zone varying when McCormack et al., 2022 instead use a standard isotropic Glen's flow relationship). All three settings modelled here are within the SLZ. McCormack et al. (2022) indicates substantial variability in Thwaites Glacier motion at a scale of tens of kilometres and provides an impressive framework with which to asses the results presented here. However, the resolution McCormack et al. (2022) use is still coarser than the dimensions of the topographic obstacles I model here and the application of relatively smooth Bedmap2 topography means that McCormack et al. (2022) cannot provide details about the intermediate-scale influence of realistic topography upon ice motion in the SLZ.

My results demonstrate that consideration of real high-resolution topography within the SLZ significantly complicates patterns of ice motion, thus suggesting ice-motion heterogeneity at a far more local scale than modelled in McCormack et al. (2022). Ice motion is modelled to be relatively uniform over streamlined lineations (Figs. 5.2, 5.4, 5.12, 5.14) observed to be widespread in topographic basins with very low (<0.01 MPa) inferred basal traction (Fig. 5.1). In contrast, ice-motion is modelled to be considerably more complex, with highly variable basal velocity ratios, at topographic highs (Figs. 5.5, 5.7, 5.8, 5.6, 5.12, 5.14, 5.9) where observed topography is rough and basal traction is inferred to be much greater than over smoother lineations (Fig. 5.1). I therefore suggest that overall ice motion in the SLZ is controlled by the interaction between these two morphologically distinct settings. In the up_swath area (Fig. 5.1), effective pressure was required to be 22% higher at up_lineation than at up_canyon for periodic numerical simulations to be stable despite equal slope values. Given the very low inferred basal traction at up_lineation (Fig. 5.1), local force balance is unlikely to be met at up_lineation and my modeled effective pressure difference at $F = 1$ is unlikely to be indicative of real variation in the subglacial hydrology system. Instead, ice in up_swath is likely to be largely supported by the stoss-slopes of the rougher terrain in the downflow half of up_swath where inferred basal traction is greater. Considering the relationship between subglacial water pressure and basal velocity ratio at up_lineation (Fig. 5.15A) further suggests that if local force balance is not met at up_lineation (i.e. $F < 1$) then the basal velocity ratio will be considerably higher (up to 0.96 at a subglacial water pressure of 99.5%), just exceeding the values obtained by McCormack et al. (2022) and likely to also extend across other areas of observed streamlined lineations. In contrast, spatially less extensive rough topographic highs that are closer to

local force balance will have an F value closer to or above 1, with locally greatly increased basal velocity ratios (Figs. 5.15B, C). This implies that the SLZ region of Thwaites Glacier is characterized by narrow crests of complex ice motion, where ice motion is similar to the GrIS domains modelled in chapter 4, amongst broad basins of relatively uniform ice motion where basal slip is much higher.

Considering up_lineation in isolation further suggests that the influence of typical depositional subglacial landforms oriented in the direction of flow on internal ice deformation is low, with the hexbin for up_lineation (Fig. 5.14B) very similar in appearance to the hexbins for the transversely smoother BedMachine topography in chapter 4. This is supported by Ockenden et al. (2021) who also suggest that flow-parallel features do not have a large influence on ice motion as they are unable to resolve flow-parallel topography features from inversions of surface velocity and elevation. The outlook of this is that subglacial areas understood to be characterised by extensive regions of soft sediment with no notable rough topographic obstacles (for example the Siple Coast ice streams, Engelhardt et al., 1990; Fisher et al., 2015, or marine sections of the British-Irish Ice Sheet, Ó Cofaigh et al., 2013a) are likely well captured with existing slip relationships tailored to soft-bedded sediment deformation. It is when regions of rough topography are considered, even if isolated and sporadic, that the situation becomes more complicated and complex internal deformation patterns and support from the stoss-side slopes of obstacles becomes more important.

In contrast to smooth lineations, the significant influence stoss-side slopes can have on ice motion is most impressively illustrated by the down_overdeep setting (Figs. 5.7, 5.8, 5.12A, B). This clearly demonstrates the large normal stress provided by the two large stoss-side slopes (Figs. 5.7C, 5.8A) as well their effect in inducing complex patterns of internal deformation. However, the same surface slope (and therefore average driving stress) required to match faster surface velocity at down_overdeep with slower surface velocity at up_canyon, suggests that pervasively rough topography (i.e. up_canyon) has a greater cumulative effect on resisting ice motion than large but isolated features when the surrounding topography is relatively smooth (i.e. down_overdeep). This resistance to motion from topography is commonly termed 'form drag', in contrast to 'skin drag', or resistance at the ice-sheet bed due to bed material properties, with enhanced resolution of rough topographic obstacles previously demonstrated to increase form drag (e.g. Kyrke-Smith et al., 2018). My results imply that increased form drag in a setting directly relates to a decreased basal velocity ratio (Fig. 5.14) and further suggest that, even without the extensive temperate-ice shear-banding features modelled in GrIS domains (chapter 4), ice motion over rough features is not adequately captured by a basal-slip relationship

concentrating exclusively on small-scale processes, as form drag can not be adequately represented without considering ice motion at intermediate scales (Fig. 5.12).

Last, while up_swath and down_swath are presently the only high-resolution bed-topography available for Thwaites Glacier, the most reasonable extrapolation of the good local alignment between higher inferred basal traction and higher observed topographic roughness (Figs. 5.1C, E) is that the regional banding in Thwaites Glacier basal traction (Joughin et al., 2009) is connected to variations in basal roughness, which may in turn be connected to more-resistant, topographically prominent rift blocks eroding in a more heterogeneous manner (further covered in landscape discussion below). A topographic roughness control on basal traction at Thwaites Glacier, rather than pattern-forming instabilities in the subglacial drainage system (Sergienko and Hindmarsh, 2013), would indicate that the basal traction field is less sensitive to variations in ice thickness and subglacial water supply than previously assumed.

5.6.2 Temperate ice in Antarctica

My results suggest that a basal temperate ice layer exists at the rough topographic highs beneath Thwaites Glacier, with the further possibility that this temperate layer extends into the soft-bed regions characterized by mega-scale glacial lineations (MSGLs, see landscape discussion below). As outlined in section 5.6.1, the requirement for local force balance may overestimate the importance of local basal traction at up_lineation and therefore unrealistically enhance internal ice deformation and temperate layer formation when $F = 1$. However, consideration of the driving stress and inferred basal traction fields at up_canyon and down_overdeep (Fig. 5.1) suggests that force balance is approximately met at these locations, which will additionally be providing support to upflow ice resting on a very weak bed. Then, given the considerable topographic obstacles present in up_canyon and down_overdeep result in temperate ice formation even at high subglacial water pressures (Figs. 5.16), it seems unfeasible that a basal temperate ice layer is not at least locally present, even if it is gradually eroded downflow where basal traction and hence deformation heating decrease and frictional basal heating increases.

This finding is contrary to numerical modelling of Antarctic ice streams where it is implicit that basal temperate ice is limited to narrow zones located beneath the shear margins (Haseloff et al., 2019; Hunter et al., 2021) and to borehole observations from Siple Coast ice streams (Engelhardt et al., 1990; Fisher et al., 2015) where the base is thawed but no temperate layer is present. Notably however, existing models of temperate ice assume a flat bed beneath ice streams and the Siple Coast ice streams flow parallel to the regional

tectonic fabric meaning far fewer flow-transverse obstacles are present (Alley et al., 2021). Two further factors actually make Antarctic ice streams more conducive to temperate ice formation than the GrIS outlet glaciers covered in chapter 4. (1) basal melting will be reduced if there is no annual input of surface melt water with coincident viscous heat dissipation (Mankoff and Tulaczyk, 2017) and (2) the basal ice temperature gradient at Thwaites Glacier is expected to be lower than sites in chapter 4 due to thicker ice and the absence of a central concave cold section, meaning conductive heat losses from the ice-sheet base will be lower. The latter factor may also partly explain why temperate layer thicknesses are relatively high — less deformation heating is required to bring Thwaites Glacier ice which is warmer than ice from the GrIS at an equivalent position above the bed to the melting point — and why water contents are generally lower — a lower temperature gradient above the CTS at Thwaites Glacier means conductive heat losses are also lower.

The existence of temperate ice at rough topographic highs has important implications for overall ice motion as these features exert an oversized influence on the regional force balance of this section of Thwaites Glacier and the resistance they provide will be diminished if they are overlain by temperate ice. Further, if temperate ice exists at these locations >100 km upflow of the terminus, then it seems likely that temperate ice also develops at the region within 80 km of the terminus modelled by McCormack et al. (2022) to have a lower basal velocity ratio (0.8 rather than 0.95) and where surface velocities also increase substantially. Borehole observations are the key way to confirm or rebut these suggestions and, in addition to direct measurements of ice deformation profiles, observation of a temperate layer would enable indirect constraint of the regional basal velocity ratio through its relationship to average temperate layer thickness (Fig. 5.15).

Last, the minor difference between the CTS and basal velocity ratios across all settings (Figs. 5.4-5.9) when compared with results from chapter 4 suggests that a basal motion relationship explicitly incorporating temperate ice deformation is less essential in a WAIS setting, though this may not be the case closer to the terminus where inferred basal traction is greater (McCormack et al., 2022). Inclusion of rougher topography at a finer resolution than the swath radar (25 m) may also complicate the situation by prompting an increased number and intensity of deformation spires and bridges (described in section 4.4.4) and increased variability in basal slip rates. This study outlines the initial possibility of temperate ice beneath the trunks of WAIS ice streams. Further modelling and observation work is required to fully asses its importance in basal ice motion across the Antarctic continent.

5.6.3 Basal motion in West Antarctica and Greenland

The transects produced using swath radar data produce notably fewer deformation heating patterns (spires, truncates spires, and bridges, Figs. 5.4-5.9) than modelled in chapter 4. This remains the case between down_overdeep (Thwaites Glacier) and S5 (Isunnguata Sermia), despite the surface velocity at the former being roughly three times greater than the latter suggesting surface velocity is not the primary cause. The principle reason for this difference appears to be the less rough DEMs used for Thwaites Glacier simulations. In the case of up_lineation this lack of roughness is warranted and radar artefacts may in fact artificially enhance the roughness of these lineations. At up_canyon and down_overdeep however, the 25 m swath radar resolution will not capture smaller scale details. Comparison of swath radar data with individual radar flight lines would allow the magnitude of this difference to be determined.

5.6.4 Landscape formation at Thwaites Glacier

My results provide the first 3D model simulations of ice-motion over real subglacial landforms beneath ice sheets. This detail allows existing hypothesis on landscape formation to be tested in the context of realistic, rather than idealized, velocity and stress fields. It is first helpful however to go beyond the hard or soft bed characterisation in the introduction of this chapter and separate modelled landforms into predominantly erosive and predominantly depositional. Direct subglacial access is not available for this purpose, but consideration of seismic data (Muto et al., 2019a; Muto et al., 2019b; Clyne et al., 2020) and comparison to inventories of landforms in deglaciated areas (e.g. Margold et al., 2015) allows reasonable distinction. up_lineation is covered by streamlined lineations that match well with terrestrial observations of MSGLs which are predominantly depositional features, though with local erosional reshaping (see Ó Cofaigh et al., 2013b; Stokes et al., 2013; Holschuh et al., 2020). Excepting lineations in the first few km along flow, up_canyon is interpreted as mostly erosive — a conclusion drawn from increased seismic reflectance indicative of greater bed strength (Muto et al., 2019a) and the fact that the bed topography undulations around the canyon feature do not match commonly used classifications of depositional landforms (Barchyn et al., 2016). down_overdeep is interpreted as undergoing a combination of erosion and deposition. The lower elevation plane has some streamlined features typical of deposition (for example, fringing the left of the central topographic obstacle when viewed downflow) but the high elevation region to the right of the domain (viewed downflow) has more similarities with the downflow region of the up_canyon domain, interpreted to be primarily erosive in nature. The central streamlined feature,

showing some resemblance to Suilven in the Scottish Highlands, may be a combination of both, with erosion on the stoss-side where normal stresses and basal velocities are very high, and deposition on the lee. The above interpretations are not definitive, but are reasonably based, and are important to allow distinction between leading theories of landscape formation.

Mega-scale glacial lineations

Streamlined lineations, interpreted to be MSGLs, are the only very clear predominantly depositional features modelled here, present across the up_lineation setting, and at the start of the up_canyon setting. MSGLs are highly elongate (elongation ratio up to 150:1) bedforms with lengths <1-180 km, widths 40-5000 m, heights 1-100 m, and across flow spacings between corrugations of 50-5000 m (Spagnolo et al., 2014), that were first documented following the advent of Landsat imagery which made them more accessible to study (Clark, 1993). MSGLs are comprised of subglacial till and glacitectonite (Ó Cofaigh et al., 2013b; Stokes et al., 2013) and are frequently used to determine paleo-ice stream locations (e.g. Stokes and Clark, 1999; Spagnolo et al., 2014), supported by their existence beneath present day Antarctic ice streams (King et al., 2009; Holschuh et al., 2020; Schlegel et al., 2022). Improved understanding of MSGLs may improve understanding of glacier motion over soft beds, yet while much progress has been made there is still not a definitive consensus behind MSGL formation. Nonetheless, recent observational studies do enable some theories to be ruled out. Stokes et al. (2013), Ó Cofaigh et al. (2013b), and Holschuh et al. (2020) exclude the helicoidal flow hypothesis of Schoof and Clarke (2008), where a transverse secondary flow gradually deforms ice, as the required formation timescale of 1000s of years does not agree with sedimentary evidence suggesting formation over a period of decades. Catastrophic subglacial floods (Shaw et al., 2008) and sediment ploughing (Clark et al., 2003) are further excluded on the basis of sedimentary evidence (Ó Cofaigh et al., 2013b; Stokes et al., 2013).

Two theories do have observational support. Clark (1993) suggest that MSGLs form from the incremental action of fast ice motion streamlining pre-existing till heterogeneities, with some support from sedimentary evidence (Ó Cofaigh et al., 2013b) and contemporary radar evidence beneath Rutford Ice Stream, West Antarctica, (King et al., 2009), but with no direct relationship apparent between surface ice velocity and lineation length beneath Thwaites Glacier (Holschuh et al., 2020). The rilling instability theory of Fowler (2010a) — an extension of the instability theory for drumlin formation — where subglacial streams with intervening ridges form in a similar manner to subaerially, also has some support from remote sensing (Stokes et al., 2013) and sedimentary evidence (Ó Cofaigh et al.,

2013b), but again has no clear correlation with water transport directions in the analysis of Holschuh et al. (2020). It is important to note however that the baseline assumptions when questioning the theories outlined above are uniform material properties and relatively uniform topography, with the degree of heterogeneity introduced by these factors very difficult to quantify. These studies therefore suggest overall a partial control from each of (1) differential supply/removal of subglacial sediment as a result of basal ice velocity, (2) channel erosion directed by subglacial drainage, and (3) the influence of pre-exiting geological heterogeneity.

What my results contribute to this conception of MSGL formation is that modelled basal velocity is greater on lineation crests than in lineation troughs (Figs. 5.2, 5.3). This finding has implications for all three controls outlined above. Faster motion at crests presents a mechanism for preferential sediment delivery along crests, which may be self-sustaining provided there is a sufficient upflow sediment supply. However, if net sediment transport at crests is negative then greater velocity at crests may reduce their prominence, which could be important in regularizing the elevation differential between crests and troughs as formulated by Fowler (2010b). Last, greater velocity at (presumably mechanically stronger) preexisting topographic perturbations may precondition MSGL formation downflow (Holschuh et al., 2020). Note that borehole observations from Ice Stream B suggested a subglacial water pressure at 98.3% of overburden. At this pressure, the modelled difference in basal velocity between crests and troughs is still high (Fig. 5.3) but already less than at 97.03%. Variable subglacial water pressure between crests and troughs, and hence variable basal traction and enhanced difference in basal velocities, may further be influential in the formation of MSGLs. Further work is required to fully understand the influence of greater crest velocity on lineation formation and preservation, and whether variable subglacial pressure across lineations may be important, but this work provides the first demonstration of this process in action.

Predominantly erosional features

Hallet (1981) (hereafter Hallet_1981) suggest that propensity for subglacial erosion scales in proportion with basal velocity magnitude (confirmed experimentally, Hansen and Zoet, 2022) and the quantity and size of entrained basal debris. This theory is effective at describing the evolution of glacial U-shaped valleys (Harbor et al., 1988; MacGregor et al., 2000) but studies examining subglacial erosion in Antarctica are few, and limited to large scales without explicit modelling of erosion processes (e.g. Smith et al., 2012; Thomson et al., 2013). Subglacial quarrying was also suggested by Hallet (1996) where variability in subglacial water pressure controls erosion rate. This theory is effective at

explaining small-scale quarrying features (Alley et al., 2019) but was originally formulated with reference to valley glacier settings where annual and diurnal variability in surface water input is high, which is not the case at Thwaites Glacier where there are no surface-bed hydrological connections and its relatively uniform motion (annual velocity variation at the front of ∼10%, Rabus et al., 2003) implies temporal variation in frictional-heating-forced basal melt rates is also likely to be low. I therefore view subglacial quarrying as unlikely to be of first-order importance when considering erosion beneath Thwaites Glacier and focus here on the Hallet_1981 theory.

In my results, basal velocity magnitude is greatest at topographic highs and lowest at topographic lows (Figs. 5.2-5.7), which is accentuated further when along-flow bed slope gradients are high. Under the Hallet_1981 hypothesis, the ice-motion patterns I model would then result in topography becoming more subdued over time if all other factors were constant. An expected longevity of topographic obstacles beneath Thwaites Glacier of multiple millennia therefore suggests that basal velocity magnitude cannot be the first order driver of erosional feature morphology beneath Thwaites Glacier. The discrepancy between my results and the effectiveness of Hallet_1981 in describing U-shaped valley formation may be accounted for by the erosion feedback in the latter process. Ice basal slip magnitude in an initially small depression where ice does not extend beyond the depression sides is approximately U-shaped across flow, and becomes more so as the canyon becomes more pronounced, creating a self-reinforcing erosion pattern. In contrast, the considerable pre-existing thickness of Thwaites Glacier swamps any such nascent canyon. This removes the initial step of this feedback mechanism and actually works to prevent formation of deep localised canyons. It is clear from consideration of basal ice velocity orientation (Fig. 5.10) and basal-slip rates (Fig. 5.5) for example, that the canyon in up_canyon is not a result of concentrated ice-motion through this feature. Preexisting geological weakness must then dictate local rates of ice-motion erosion resulting in the heterogeneity observed at up_canyon and in highland sections of down_overdeep. Erosion controlled by temporally-uniform subglacial drainage, so far seldom quantitatively explored, may also be important, and could exploit pre-existing geological weaknesses, particularly when the glaciostatic pressure field encourages water movement along the feature, as with the canyon in up_canyon (Fig. 5.5).

Erosion and deposition features

Alley et al. (2021) (hereafter Alley_2021) propose that patterns of erosion and deposition are controlled by pressure (here referred to as normal stress) at the ice-bed interface in agreement with some theory and modelling (Rempel, 2008; Zoet and Iverson, 2020). With

particular reference to overdeepened moats, Alley_2021 suggest that higher subglacial pressure excludes much of the ice-contact basal water, resulting in greater ice-sediment coupling and sediment transfer rates. Alley_2021 apply this theoretical landscape formation framework to a numerical 2D model of a curved moat and use this to argue for the development of the distinctive moat as a result of elevated pressure within the moat, and reduced pressure behind the obstacle (their fig. 4). This idealized feature is constructed to be broadly similar to the moat features found in up_swath and down_swath areas, including the moat and rise in my down_overdeep setting. However, here my model produces negative, or near-zero normal stress within the depression, with the largest normal stresses focused instead on the high-angle stoss side of the obstacle (Fig. 5.8) which, despite millennia of overriding ice flow, has remained prominent. Basal velocity magnitude is further at an absolute minimum within the topographic depression, suggesting that both Hallet_1981 and Alley_2021 hypotheses cannot explain the existence of the subglacial moat. The model of Alley_2021 is complicated further by more recent laboratory evidence from Hansen and Zoet (2022) which indicates that the relationship between sediment flux and effective stress (not normal stress) is non-monotonic, also depends upon the thickness of the deforming shear band, and that in any case sediment flux variability is not greater than 20%.

Subglacial water flow may be a more reasonable contender to describe the formation of the moat in down_overdeep. Glaciostatic pressure is at a minima within the moat (Fig. 5.8B, D), meaning it would therefore route a considerable proportion of water from the upflow region. Considering the wider topographic setting also suggests the moat may be first possible passing point for water coming from the lineations upflow and to east of down_overdeep within down_swath, an area of many square kilometres. However, while patterns of glaciostatic pressure may be able to describe the formation of the moat they cannot explain the initial formation of the topographically prominent streamlined feature. I suggest that the only reasonable genesis of the streamlined feature is as a pre-existing region of particularly resistant geology, with ice motion subsequently acting to streamline it in the direction of flow. Deposition and reworking of subglacial sediment may additionally attenuate its lee side, in a similar manner to the MSGLs outlined above.

Landscape outlook: are unifying descriptors possible?

The above discussion suggests that an extremely diverse range of mechanisms are important when considering landscape evolution beneath Thwaites Glacier, including subglacial water routing, basal velocity, and ice-bed normal stress. Preexisting geology however appears to be the key decider of morphology type, with interpreted fault-block highs

having rough predominantly erosive topography and interpreted fault-block basins having smooth predominantly depositional landforms. Preexisting geology also appears to dictate the overall form of predominantly erosive landscapes. The outlook of this is that a unifying description of landscape formation still seems intractable at present. However, this may actually simplify the problem of including subglacial topography in ice-sheet models. That the features beneath Thwaites Glacier have withstood or been continuously shaped by ongoing ice motion at least since the last interglacial (∼125 ka, MIS5e), and possibly since MIS11 (∼400 ka, e.g. Hay et al., 2014; Sutter et al., 2016) indicates that they are unlikely to change at timescales important for predictive ice-sheet models (decades to centuries, or even millennia), suggesting that the use of invariant roughness beneath ice-sheets is acceptable.

5.7 Conclusions

This study has demonstrated the crucial role that rough topographic highs oriented perpendicular to flow have upon ice motion in the central subglacial basin (the SLZ) of Thwaites Glacier. Basal slip is expected to be high with plug-like flow in topographic basins characterized by predominantly depositional streamlined lineations and low inferred basal traction. In contrast, ice motion is expected to be complex with highly variable basal velocity ratio at rough highs where the landscape is predominantly erosive. Basal temperate ice at these topographic highs may further influence their resistance to ice-motion.

The landscape formation and ice motion aspects of this study have important interactions. The easily deformable nature of MSGLs makes it more likely that these are subject to change over timescales important for predictive ice-sheet models (100s of years) given reorganisations of flow patterns and/or subglacial hydrology. However, I have shown that flow-parallel streamlined features do not have an important bearing on overall patterns of ice motion when compared to relatively uniform beds. In contrast, the predominantly erosive features that do have a large influence on ice motion are likely (1) very long lasting given the duration of ice coverage at Thwaites Glacier and (2) predominantly controlled by pre-existing geological heterogeneity rather than ice motion characteristics. Last, in agreement with Kyrke-Smith et al. (2018) but extending to much higher resolution, my results suggest that the processes controlling form drag extend beyond the small-scale processes currently explicitly incorporated into basal-motion relationships. Given the important role of form drag in resisting ice motion at Thwaites Glacier at topographic highs, it seems important to focus future work on better understanding how roughness-controlled form drag interacts with overall ice motion.

5.8 Supplementary material

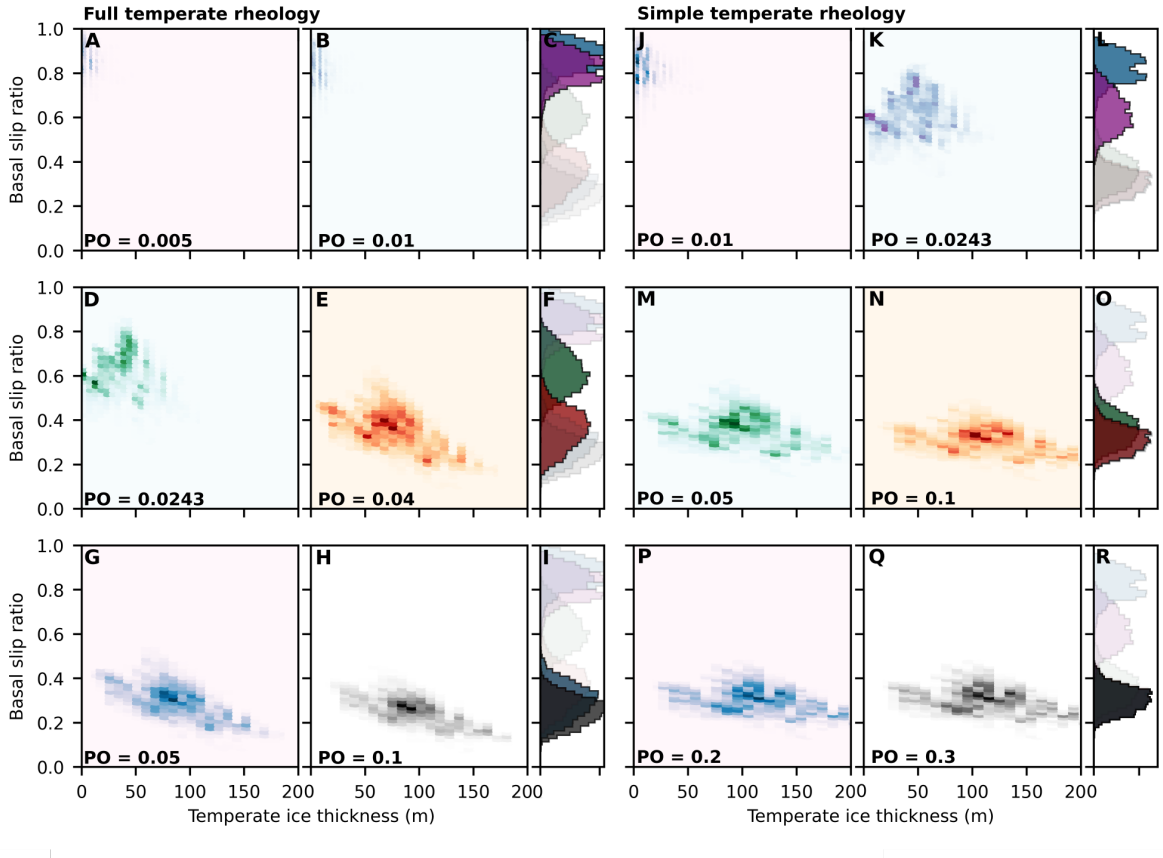

Fig. 5.16 . Hexbins for full and simple temperate rheologies (see Methods for description) for temperate layer thickness and basal velocity ratio when varying the effective pressure as a proportion of overburden (indicated by PO value in bottom left of panels). Colours in histograms correspond to colours in hexbin plots, with runs from other simulations using that rheology faded but included to allow comparison.

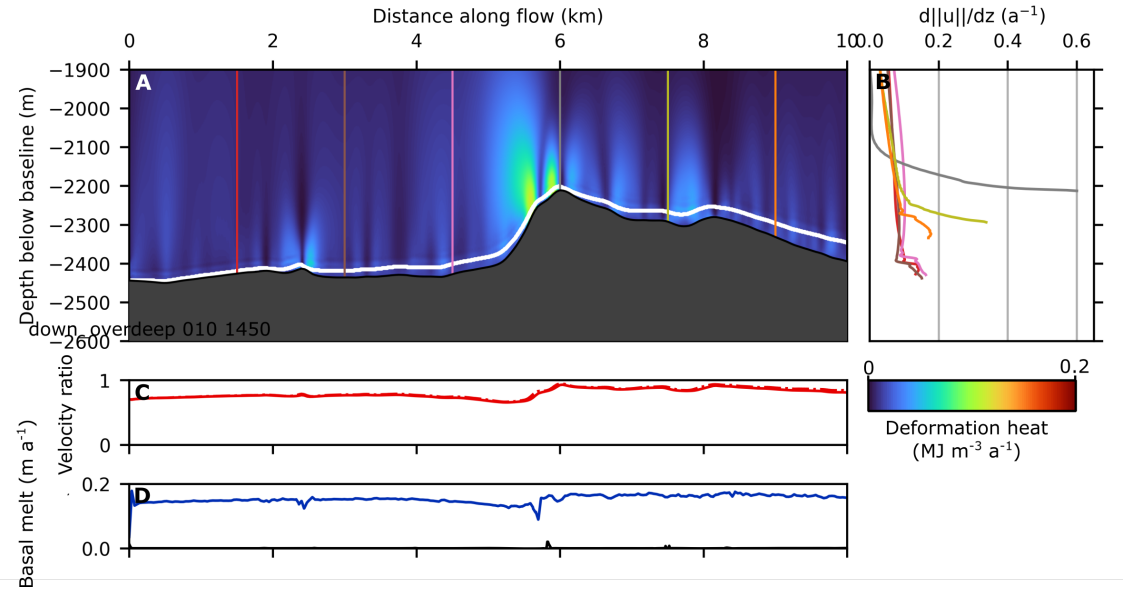

Fig. 5.17 . As for Fig. 5.4 but for down_overdeep setting at y = 1450 m.

Chapter 6

Synthesis and conclusion

'Well the universe is shaped exactly like the earth,
if you go straight long enough you'll end up where you were.' — **The Moon & Antarctica**

In this thesis I first used novel fibre-optic temperature sensing down a 1,043 m hot-water drilled borehole to reveal the thermodynamic conditions facilitating the fast motion of the marine-terminating Sermeq Kujalleq, Greenland. These observations included previously unrecorded strain banding in Holocene ice, substantial heterogeneity in deformation at the sub-metre scale in pre-Holocene ice, and deformation increasing upwards towards the top of a 73-m-thick temperate ice layer. My observations also demonstrated a high degree of spatial variability in the thickness of this temperate layer across the Sermeq Kujalleq catchment, with a thickness of <14 m recorded just 1 km away (Doyle et al., 2018). Given the much lower viscosity of temperate ice, this layer (and its spatial variability) was inferred to be significant for the fast motion of Sermeq Kujalleq.

Next, I showed that including geostatistically realistic topography in 3D model domains of isolated glacier subsections from Sermeq Kujalleq and the land-terminating Isunnguata Sermia could account for borehole observations of both ice deformation and temperate layer thickness variability. Temperate ice was modelled to be vertically extensive in deep troughs — where basal-slip rates could drop to <5% of surface velocity — but to thin notably over topographic highs — where basal-slip rates could reach >90% of surface velocity. These simulations, alongside the observations that support them, demonstrated that ice-motion patterns at intermediate scales (<25 m, $\lesssim$2 km) are far more complex than previously considered, where complexity here refers to a departure from the uniform partitioning between basal slip and internal deformation produced by most ice-sheet models. This work suggested overall that parameterisations of basal-slip are omitting important ice-motion processes crucial to explaining GrIS borehole observations.

Last, I used the model I developed to demonstrate that complex basal motion is also important at Thwaites Glacier, Antarctica. Rough topographic highs inferred to be hard-bedded have high variability in basal-slip rates and likely produce at least locally-extensive temperate ice. Meanwhile, broader topographic basins inferred to be soft-bedded have much more uniform ice motion with consistently high basal-slip rates. I further showed that the main control on the morphology of the rough erosional features is likely to be preexisting geological heterogeneity, suggesting longevity in inferred patterns of basal

traction that are detached from abrupt changes in the subglacial drainage system and that time-invariant roughness characteristics are a reasonable assumption.

When combined, the observations and numerical modelling presented in this thesis show that, despite the relatively simple composition of glacier ice, ice-sheet motion is an inescapably complex and highly heterogeneous process. Fibre-optic borehole observations (chapter 3) show that as measurement resolution increases, so to does the complexity of the process in question. Where previously interpolation between discrete sensors smoothed over unknown temperature and deformation fields, my high-resolution fibre-optic record shows that both of these can change abruptly, even down to a sub-metre scale. Chapters 4 and 5) show that consideration of realistic or real (and therefore necessarily not neat and not periodic) basal topography in numerical models can account well for some of this complexity and offer insights into subglacial landform formation. Nonetheless, no (earth science) model will ever be an ideal reflection of reality. However, as computational capabilities and process-based understanding advance, so to can our numerical treatment of physical processes. Below, I detail ways to (1) further investigate the complexity in ice-sheet motion established here before (2) using this understanding to build improved process-based parameterisations of ice-sheet motion applicable to predictive ice-sheet models.

6.1 Comparing basal motion across ice sheets

My work has covered two distinct settings in terms of regional subglacial topography but my model domains have been limited to no more than 12 km along flow. Can these results be generalised to different settings or to entire ice-sheets? Considering the GrIS first, the majority of this ice sheet is thought to be underlain by old crystalline rock (Dawes, 2009) that is relatively typical of the continental shield that also comprises large parts of North America and Scandinavia (though with some discussion over the predominance of hard or soft bed settings, see section 4.7.1). This geological uniformity suggests relative uniformity in the morphology of subglacial landscapes. Further, as my approach here involved regional statistics, it should then be possible to simply broaden the area considered when generating these statistics to provide a more regionally representative idea of roughness. Such statistics may offer an effective way to reduce the complexity inherent in ice motion when incorporated into a basal motion relationship.

The WAIS and its rift-basin structure presents more challenges, with the clear contrast between inferred hard- and soft-bedded catchments meaning regionally averaged statistics

will be less representative. The morphology of Pine Island Glacier and Thwaites Glacier are also clearly differentiable from one another and from the ice streams draining into the Ross and Filchner–Ronne ice shelves (Alley et al., 2021). Additionally, even within Thwaites it is possible that the regions defined by McCormack et al. (2022) (the BDZ, SLZ, and DSZ) have distinct regional morphological characteristics. Depending on the outcome of assessments determining the importance of spatially variable basal traction regimes (sections 6.2.1, 6.2.2), this may indicate that each catchment requires individual treatment. Nonetheless, the framework presented here provides an effective method to begin this work. Separately, it seems sensible that presently offshore regions of pervasive soft bed where good geophysical and sediment core records are available, and where there is an absence of sizeable topographic obstacles – such as the North Sea (e.g. Kirkham et al., 2022) – a soft-bed regularized-Coulomb relationship can be used without the assumptions behind it being questionable.

Next, the EAIS, which was not covered in this thesis, covers a high-grade shield terrane similar to the GrIS (Harley and Kelly, 2007) with rough bedrock characteristics[1] (Eisen et al., 2020). Combined, these geological and roughness characteristics suggest that ice-motion patterns in East Antarctica are broadly likely to be closer to those modelled for the GrIS rather than those modelled for Thwaites Glacier. Note that the absence of an active surface to bed hydrological system in East Antarctica should not be expected to interfere with this suggestion as uniform basal water pressure over a range of values produces the complex basal motion observed for both the GrIS and Thwaites Glacier.

Comparing results from chapters 4 and 5, the variable nature of complex basal motion across the domains modelled in this thesis can be at least partly accounted for by marked variation in topographic profiles and the disparate range of scales over which these variations occur (Fig. 6.1). All GrIS profiles exhibit greater topographic variation than the WAIS profiles (Fig. 6.1), which, alongside increased ice velocity in GrIS model settings prompts more internal strain heating and hence a more rapidly increasing temperate layer thickness. The heightened basal temperature gradient in comparison to models of Thwaites Glacier (see also section 5.6.2) also prompts a shorter transition between high water contents (up to the maximum allowable 2.5%) and cold overlying ice. In comparison, Thwaites Glacier transects are typically less rough with concomitantly lower absolute temperate layer thicknesses and lower temperate layer variations. As discussed in chapters 4 and 5, this temperate layer variability is intertwined with variability in basal velocity ratio meaning lower variation in basal velocity in the Thwaites Glacier domains is to be expected. Future work will allow ice motion across a continuum of landscapes, beyond those covered in this thesis, to be comprehensively explored.

[1] though there is not yet a universally defined roughness measure to allow direct intercomparison

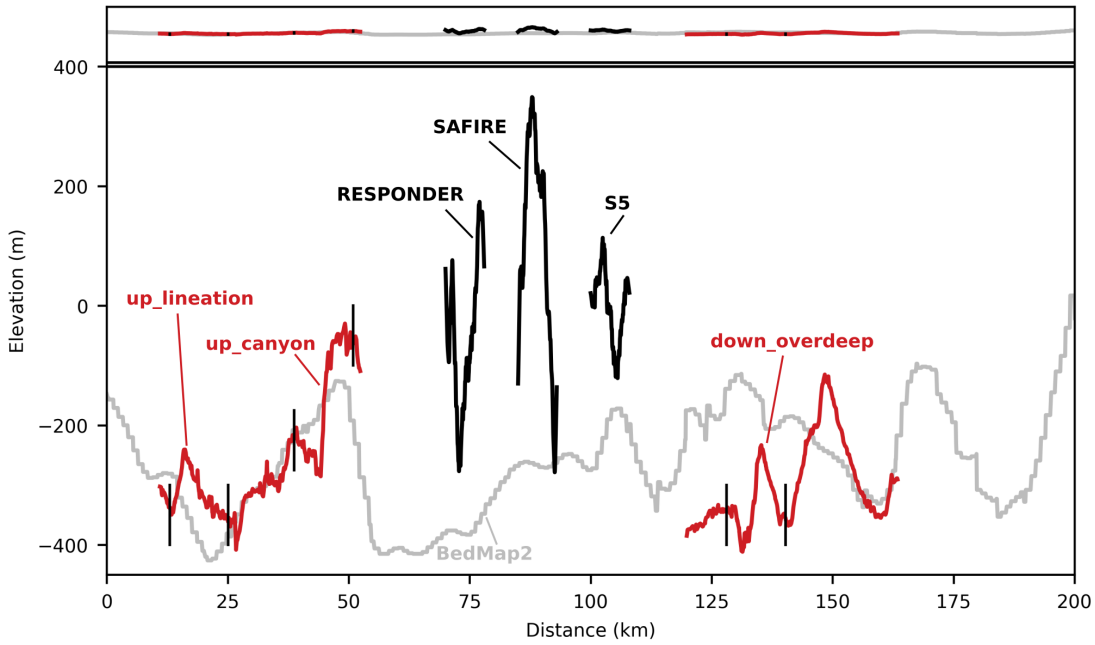

Fig. 6.1 . Comparison of bed topography transects featured throughout this thesis. Grey line is BedMap2 following the yellow flow line in Fig. 5.1E (Fretwell et al., 2013). Red lines are transects through swath radar data from Holschuh et al. (2020) where vertical black lines isolate labelled model domains, again following the yellow flow line in Fig. 5.1E. Black lines are transects cutting through the middle of model domains along flow in chapter 4. Colour indication remains the same above the double black line but aspect ratio is reduced from 1:133 to 1:2.

Finally, lower basal velocity ratios in topographic troughs within GrIS and WAIS domains (troughs of at most a $\sim$2 km across, within a domain of at most 12 km long), but increased basal velocity ratio in the broader topographic trough containing up_lineation ($\gtrsim$30 km across) can be accounted for by considering the scale of the respective features. A distance of $\gtrsim$30 km is much greater than the local ice thickness ($\sim$2 km) meaning far-field large-scale topographic protuberances, such as the broad $\gtrsim$15 km rise on which up_canyon is located on, do not have a direct effect on more local patterns of basal motion. Future work can elucidate the exact range of scales over which these transitions occur, alongside their dependence on ice velocity and more local roughness characteristics. In sum, I expect that the complex basal-motion patterns described in this thesis characterize most ice-sheet settings, including paleo ice sheets, and become increasingly prevalent as the degree of heterogeneity in the subglacial landscape increases.

6.2 Future work

6.2.1 Expanding complexity

The rheological realism of the model I presented here could be developed further. First, the rheology of softer pre-Holocene ice could be included. This may lead to a decreased basal velocity ratio if increased ice deformation is then accommodated within the pre-Holocene ice occupying the lower portion of the modelled ice column. The temperate layer may also grow more rapidly downflow to the point that all pre-Holocene ice becomes temperate if strain heating is preferentially concentrated within the pre-Holocene layer. Use of the age solver in Elmer/Ice and age-dependent rheology would make this a relatively simple alteration to the existing model. A very-high-resolution vertical mesh at the Last Glacial-Interglacial Transition may even enable a first constraint on the stresses responsible for possible fault-like behaviour at this boundary (Lüthi et al., 2003; chapter 3). To my knowledge no studies include explicit treatment of softer pre-Holocene ice and this seems like an important process to consider. Further, evolutive anisotropic rheology could also be incorporated using existing Elmer/Ice solvers (Gagliardini et al., 2013) with the cuboid model developed in this thesis providing the perfect sandbox in which to test the effect of various anisotropic formulations. As the rheology of temperate ice is directly linked to water content, alternative models for water flux within temperate ice (Hewitt and Schoof, 2017; Schoof and Hewitt, 2016) may also influence overall ice motion. The non-linear dependence of water flux upon water content in some of these models means that finite-element implementation is not straightforward, but comparison of these approaches, and of their presently uncertain parameter space, would allow quantification of their respective influence upon ice motion and would help determine the most urgent directions for future research into temperate ice water flux.

The influence of spatially varying basal-traction parameters and/or parameterisations on ice motion could also be further investigated. Consideration of both presently glaciated and deglaciated landscapes suggests a spatially diverse range of hard-bed settings (e.g. Helanow et al., 2021; Woodard et al., 2021), soft-bed settings (Clark et al., 2018), and combinations thereof (e.g. Muto et al., 2019a). However, studies examining the influence of spatially varying basal-traction[2] are few, and are limited to idealised 2D geometries (Ryser et al., 2014a; Koellner et al., 2019; Alley et al., 2021). Moderate modification of the model developed in this thesis would allow the influence of variable basal traction parameters/parameterisations to be investigated in 3D over real or realistic basal topography. Interpretation of the appropriate basal traction relationship and parameters to

[2] At an intermediate scale, so excluding basal traction fields derived from inversions.

use in a given setting is subjective, but this approach would enable a far more realistic understanding of the influence of this heterogeneity than is available at present.

Variability in basal traction also extends to consideration of spatial and temporal variation in the subglacial hydrological system. My work begins to analyse this (Figs. 4.19, 5.15), but it would be interesting to investigate the annually averaged influence of variable subglacial water pressure in the ablation zone of the GrIS on temperate ice formation and basal velocity ratios. Comparison with available borehole data suggests that my model performs well, but understanding could be advanced further by using a time-dependent simulation where basal traction is temporarily lowered, and inflow velocity increased, to emulate summer speed ups of the GrIS. Given a moderate increase in model resolution, the influence of individual subglacial channels or variable subglacial drainage configurations could also be probed. Last, while the domains I study in this thesis are relatively fast moving, the heterogeneous topography used here may be able to elucidate processes responsible for transitions from frozen to thawed bed conditions (Mantelli and Schoof, 2019), observed to be heterogeneous over 10-20 km at Petermann Glacier, northwest Greenland (Chu et al., 2018).

Considering the factors outlined above in turn will enable the most significant drivers of complex ice-sheet motion (beyond real or realistic bed topography) to be determined. This complexity can then be simplified into more accurate parameterisations for possible inclusion in large-scale (catchment or entire ice-sheet) ice-sheet models.

6.2.2 Collapsing complexity

The resolution required to capture the topographic interactions modelled in chapters 4 and 5 is too high for whole ice-sheet, or even whole catchment, applications. This means that for my findings to be of direct use in these applications some adaption to coarser-resolution meshes is required. This can be achieved using a similar approach to Helanow et al. (2021) who also use a periodic cuboid domain but at a much smaller scale (<25 m) to derive the basal-traction relationship that is used in my model. Area-averaged basal traction (including the support of stoss-side obstacles) as a function of surface slope and therefore driving stress could be compared to area-averaged basal velocities. Exploring the dependency of this relationship on the size of the chosen area would provide extremely useful information about the point at which the intermediate-scale processes revealed in this thesis grade into the large-scale processes central to ice-sheet modelling. Large-scale parameterisations of basal roughness would further enable explicit rather than implicit incorporation of form-drag processes into basal-motion relationships. This approach,

rather than focusing on the CTS velocity ratio alone as suggested in chapter 4, also allows for a more comprehensive and regionally-averaged assessment of form drag, whether the temperate layer is (chapter 4) or is not (chapter 5) central to describing ice-motion patterns. As briefly outlined in chapter 4 this approach may also explain the continued utility of Weertman-type sliding (e.g. Gimbert et al., 2021; Maier et al., 2021) even when process-based theory and experiments indicate a regularised-Coulomb relationship is more appropriate at small scales. This is perhaps the most pressing research priority to arise from this thesis.

Next, as covered in chapter 5, predominantly erosive and predominantly depositional landforms have distinct along- and across-flow characteristics, with depositional features generally not having the large stoss-side slopes that produce complex patterns of basal-slip rates and internal deformation (Fig. 5.12). Exactly how variation in depositional features influences flow could be examined by creating synthetic but representative fields of drumlins, mega-scale glacial lineations, mega-ribs, ribbed domains, and quasi-circular forms (Ely et al., 2016) and using these as inputs for the model developed here.

On heuristics

Do parameterisations of basal motion, whether process-based or applied heuristically, actually meaningfully capture the processes at work in nature? I think that for process-based formulations this is presently unclear. My results indicate that basal-slip rates can vary considerably over distances much shorter than the size of individual mesh elements or cells used in typical ice-sheet model applications. If, for example, a regularised-Coulomb relationship was directly scaled from experiments and theory of sediment deformation based on a 2 m shear-ring apparatus, this would implicate a uniform bed (i.e. flat and materially homogeneous) and uniform basal-slip rates across a considerably broader area (kilometres), which may only be met on particularly uniform continental shelves and is clearly not the case for Thwaites Glacier or the western margin of the GrIS. Could, for example, one section of hard-bedded topographic roughness amidst a soft-bedded region fundamentally alter the nature of the basal traction relationship that should most accurately be applied to that model cell/mesh element? The ideas presented above offer a way to test this problem across different settings and quantitatively determine its significance.

As for the heuristic application of basal-motion relationships to a setting to best account for a limited time series of observational data (e.g. Joughin et al., 2009; Maier et al., 2021; Minchew et al., 2016), functionally, it should not matter if the underlying reasons why such a relationship works are not fully understood (as would inherently be the case in

machine-learning applications). However, I do not think that this would be particularly satisfying. Given the global importance of ice-sheet mass loss I think it is important to have a firm understanding of the processes behind the parameterisation, particularly as this allows outlying eventualities to be tested in a sandbox setting (for example feedbacks between temperate-layer development and ice motion). In addition, as it stands process-based models are probably a more direct approach to a 'correct' basal-motion relationship when there are still great challenges in inferring basal-traction relationships from remotely sensed data (e.g. Aschwanden et al., 2021).

On a 'unifying' basal-slip relationship

As a last comment on basal slip, the two recently proposed regularised-Coulomb basal-slip relationships (Zoet and Iverson, 2020; Helanow et al., 2021), suggested to unify hard and soft beds (Minchew and Joughin, 2020), do actually have notable differences at high subglacial water pressures (Fig. 6.2). It is further quite difficult to reconcile the two without applying an unrealistically low friction angle to the Zoet and Iverson (2020) relationship (Fig. 6.2), with the Zoet and Iverson (2020) relationship actually suggesting largely greater basal-traction values than its hard-bed equivalent. This discrepancy, and the general conception that soft beds are weaker than their hard-bed equivalents (e.g. Koellner et al., 2019; Joughin et al., 2009), has three possible explanations. (1) The nature of hard beds often means intermediate-scale topographic variation is greater than for soft-bed regions (compare e.g. Roberts and Long, 2005; Kirkham et al., 2019). This intermediate-scale topographic roughness would be manifest as form drag in large-scale basal-traction inversions but is not incorporated into the experiments of Helanow et al. (2021). (2) Hard beds may typically have lower subglacial water pressure (required to be about 4% lower) than soft beds, which does seem to be supported by available evidence (e.g. Sokołowski and Wysota, 2020 Wright et al., 2016; Engelhardt et al., 1990; Doyle et al., 2018) though further observations would be useful. The difference between bed strength is then a simple function of the subglacial water pressure each setting can sustain. (3) There are some processes not included in one or other formulation which reduces their realism. There is some important future work to be done testing these hypothesis to determine how accurately the slip formulations of (Zoet and Iverson, 2020) and (Helanow et al., 2021) can be directly compared. The model setup I developed in this thesis would be a useful starting point.

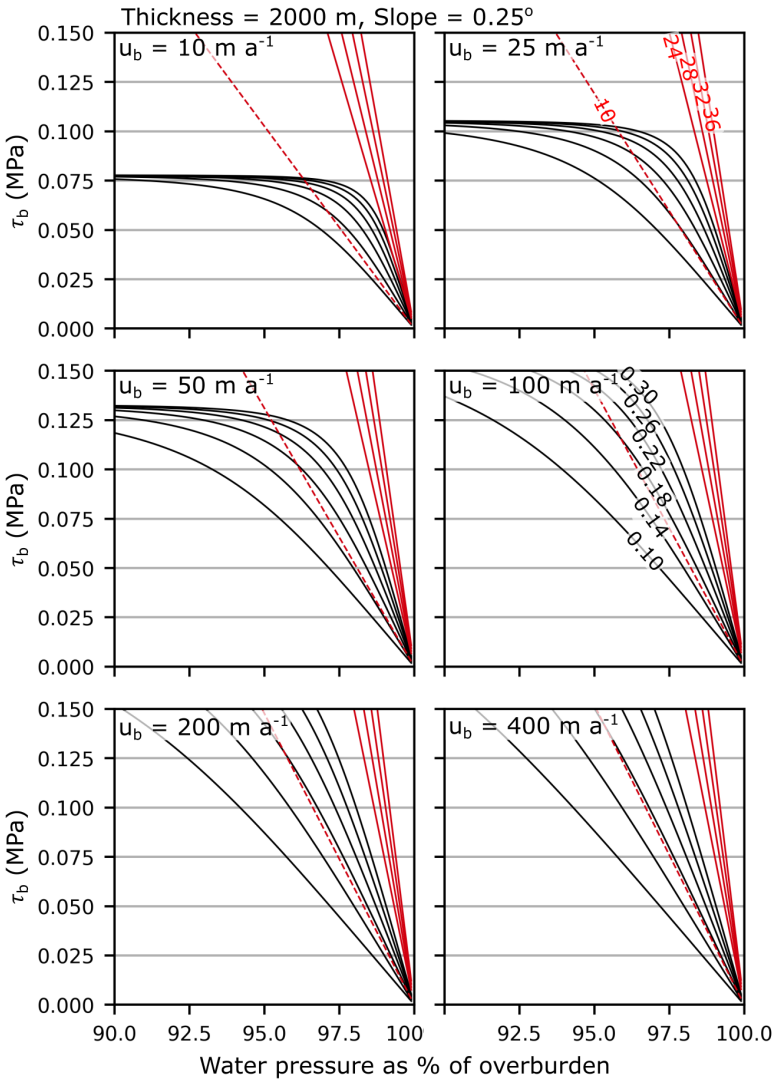

Fig. 6.2 . Difference between Zoet and Iverson (2020) (red) and Helanow et al. (2021) (black) slip relationships at high subglacial water pressures for different basal velocity values. Values in red on Zoet and Iverson (2020) refer to friction angle. Values in black on Helanow et al. (2021) refer to C value (my model used a value of 0.1617).

6.2.3 Fieldwork

Some suggestions for future fieldwork are already outlined in chapters 4 and 5. Boreholes from diverse topographic settings, or in an array around the size of the domains used in chapter 4, would help advance our understanding of fast ice-motion processes in the GrIS. Any borehole at all from Thwaites, and in particular information on temperate layer thickness at topographic obstacles, would help constrain ice-motion processes there. Looking at an ideal set-up however, combining swath radar with an array of borehole data would offer unparalleled capability to calibrate ice motion parameters that could then be applied across a wider area, whether in Greenland or Antarctica. It would also be of great value to see the fibre-optic possibilities discussed in chapter 2.4 applied in the future. DSS

in particular has the potential to revolutionise our understanding of internal deformation processes.

6.3 Conclusion

In this thesis I have (1) presented a fibre-optic borehole temperature record from Sermeq Kujalleq, a marine-terminating GrIS outlet glacier, which revealed that highly variable internal deformation and temperate-layer thickness are important aspects of fast ice motion, (2) modeled isolated 3D outlet-glacier subsections from the GrIS over geostatistically simulated topography to demonstrate the importance of the intermediate scale in reconciling borehole observations and advancing our conception of ice-sheet motion, and (3) used swath radar bed-topography data to show that ice-motion patterns at Thwaites Glacier, Antarctica, are also highly heterogeneous, particularly at the rough topographic highs that exert a major control on the regional force balance. These findings demonstrate that, in most settings, a neat partitioning between basal slip and internal deformation is not an effective descriptor of ice-sheet motion but also offer meaningful pathways to improve the accuracy and realism of parameterisations used in predictive ice-sheet models. Given several of the papers crucial to the development of this thesis were not even published when I began (incl. Muto et al., 2019a; Holschuh et al., 2020; des Tombe et al., 2020; Zoet and Iverson, 2020; Helanow et al., 2021; MacKie et al., 2021), I have no doubt that these challenges can be overcome by the time all trace of R29 has vanished from the surface of Sermeq Kujalleq.

References

Adalgeirsdóttir, G., Aschwanden, A., Khroulev, C., Boberg, F., Mottram, R., Lucas-Picher, P., and Christensen, J. H. (2014). Role of model initialization for projections of 21st-century Greenland ice sheet mass loss. *Journal of Glaciology*, 60(222):782–794.

Adams, C. J., Iverson, N. R., Helanow, C., Zoet, L. K., and Bate, C. E. (2021). Softening of Temperate Ice by Interstitial Water. *Frontiers in Earth Science*, 9:702761.

Agassiz, L. (1840). *Études sur les glaciers*. Cambridge University Press, Cambridge.

Ajo-Franklin, J. B., Dou, S., Lindsey, N. J., Monga, I., Tracy, C., Robertson, M., Rodriguez Tribaldos, V., Ulrich, C., Freifeld, B., Daley, T., and Li, X. (2019). Distributed Acoustic Sensing Using Dark Fiber for Near-Surface Characterization and Broadband Seismic Event Detection. *Scientific Reports*, 9(1):1328.

Alley, R. B. (1990). West Antarctic collapse -How likely? *Episodes Journal of International Geoscience*, 13(4):231–238.

Alley, R. B., Cuffey, K. M., and Zoet, L. K. (2019). Glacial erosion: Status and outlook. *Annals of Glaciology*, 60(80):1–13.

Alley, R. B., Holschuh, N., MacAyeal, D. R., Parizek, B. R., Zoet, L., Riverman, K., Muto, A., Christianson, K., Clyne, E., Anandakrishnan, S., Stevens, N., Smith, A., Arthern, R., and others (2021). Bedforms of Thwaites Glacier, West Antarctica: Character and Origin. *Journal of Geophysical Research: Earth Surface*, 126(12):e2021JF006339.

Alley, R. B. and MacAyeal, D. R. (1994). Ice-rafted debris associated with binge/purge oscillations of the Laurentide Ice Sheet. *Paleoceanography*, 9(4):503–511.

Alley, R. B. and Whillans, I. M. (1984). Response of the East Antarctica ice sheet to sea-level rise. *Journal of Geophysical Research*, 89(C4):6487.

Arrhenius, S. (1896). On the influence of carbonic acid in the air upon the temperature of the ground. *The London, Edinburgh, and Dublin Philosophical Magazine and Journal of Science*, 41(251):237–276.

Aschwanden, A., Bartholomaus, T. C., Brinkerhoff, D. J., and Truffer, M. (2021). Brief communication: A roadmap towards credible projections of ice sheet contribution to sea level. *Cryosphere*, 15(12):5705–5715.

Aschwanden, A., Bueler, E., Khroulev, C., and Blatter, H. (2012). An enthalpy formulation for glaciers and ice sheets. *Journal of Glaciology*, 58(209):441–457.

Aschwanden, A., Fahnestock, M. A., and Truffer, M. (2016). Complex Greenland outlet glacier flow captured. *Nature Communications*, 7:10524.

Aschwanden, A., Fahnestock, M. A., Truffer, M., Brinkerhoff, D. J., Hock, R., Khroulev, C., Mottram, R., and Abbas Khan, S. (2019). Contribution of the Greenland Ice Sheet to sea level over the next millennium. *Science Advances*, 5(6):eaav9396.

Babaniyi, O., Nicholson, R., Villa, U., and Petra, N. (2021). Inferring the basal sliding coefficient field for the Stokes ice sheet model under rheological uncertainty. *Cryosphere*, 15(4):1731–1750.

Bagshaw, E. A., Wadham, J. L., Mowlem, M., Tranter, M., Eveness, J., Fountain, A. G., and Telling, J. (2011). Determination of Dissolved Oxygen in the Cryosphere: A Comprehensive Laboratory and Field Evaluation of Fiber Optic Sensors. *Environmental Science & Technology*, 45(2):700–705.

Baltrūnas, V., Šinkūnas, P., Karmaza, B., Česnulevičius, A., and Šinkūnė, E. (2009). The sedimentology of debris within basal ice, the source of material for the formation of lodgement till: an example from the Russell Glacier, West Greenland. *Geologija*, 51(1):12–22.

Bamber, J. L., Oppenheimer, M., Kopp, R. E., Aspinall, W. P., and Cooke, R. M. (2019). Ice sheet contributions to future sea-level rise from structured expert judgment. *Proceedings of the National Academy of Sciences of the United States of America*, 166(23):11195–11200.

Bamber, J. L., Riva, R. E., Vermeersen, B. L., and Lebrocq, A. M. (2009). Reassessment of the potential sea-level rise from a collapse of the west antarctic ice sheet. *Science*, 324(5929):901–903.

Bamber, J. L., Westaway, R. M., Marzeion, B., and Wouters, B. (2018). The land ice contribution to sea level during the satellite era. *Environmental Research Letters*, 13(6):063008.

Barchyn, T. E., Dowling, T. P., Stokes, C. R., and Hugenholtz, C. H. (2016). Subglacial bed form morphology controlled by ice speed and sediment thickness. *Geophysical Research Letters*, 43(14):7572–7580.

Barnes, J. M., Dias Dos Santos, T., Goldberg, D., Hilmar Gudmundsson, G., Morlighem, M., and De Rydt, J. (2021). The transferability of adjoint inversion products between different ice flow models. *Cryosphere*, 15(4):1975–2000.

Benn, D. I. and Evans, D. J. A. (2010). Glaciers and glaciation. *London: Hodder Education*.

Benn, D. I., Hulton, N. R., and Mottram, R. H. (2007). 'Calving laws', 'sliding laws' and the stability of tidewater glaciers. *Annals of Glaciology*, 46:123–130.

Berg, B. and Bassis, J. (2022). Crevasse advection increases glacier calving. *Journal of Glaciology*, pages 1–10.

Bevis, M., Harig, C., Khan, S. A., Brown, A., Simons, F. J., Willis, M., Fettweis, X., Van Den Broeke, M. R., and others (2019). Accelerating changes in ice mass within Greenland, and the ice sheet's sensitivity to atmospheric forcing. *Proceedings of the National Academy of Sciences of the United States of America*, 116(6):1934–1939.

Bindschadler, R. A., Nowicki, S., Abe-Ouchi, A., Aschwanden, A., Choi, H., Fastook, J., Granzow, G., Greve, R., Gutowski, G., and others (2013). Ice-sheet model sensitivities to environmental forcing and their use in projecting future sea level (the SeaRISE project). *Journal of Glaciology*, 59(214):195–224.

Bingham, R. G., Vaughan, D. G., King, E. C., Davies, D., Cornford, S. L., Smith, A. M., Arthern, R. J., Brisbourne, A. M., De Rydt, J., Graham, A. G., Spagnolo, M., Marsh, O. J., and Shean, D. E. (2017). Diverse landscapes beneath Pine Island Glacier influence ice flow. *Nature Communications*, 8:1618.

Björnsson, H. and Pálsson, F. (2020). Radio-echo soundings on Icelandic temperate glaciers: history of techniques and findings. *Annals of Glaciology*, 61(81):25–34.

Blankenship, D. D., Bentley, C. R., Rooney, S. T., Alley, R. B., Blankenship, D. D., Bentley, C. R., Rooney, S. T., and Alley, R. B. (1986). Seismic measurements reveal a saturated porous layer beneath an active Antarctic ice stream. *Natur*, 322(6074):54–57.

Boers, N. and Rypdal, M. (2021). Critical slowing down suggests that the western Greenland Ice Sheet is close to a tipping point. *Proceedings of the National Academy of Sciences*, 118(21).

Bons, P. D., Jansen, D., Mundel, F., Bauer, C. C., Binder, T., Eisen, O., Jessell, M. W., Llorens, M.-G., Steinbach, F., Steinhage, D., and Weikusat, I. (2016). Converging flow and anisotropy cause large-scale folding in Greenland's ice sheet. *Nature Communications*, 7:11427.

Bons, P. D., Kleiner, T., Llorens, M.-G., Prior, D. J., Sachau, T., Weikusat, I., and Jansen, D. (2018). Greenland Ice Sheet: Higher Nonlinearity of Ice Flow Significantly Reduces Estimated Basal Motion. *Geophysical Research Letters*, 45(13):6542–6548.

Booth, A. D., Christoffersen, P., Schoonman, C., Clarke, A., Hubbard, B., Law, R., Doyle, S. H., Chudley, T. R., and Chalari, A. (2020). Distributed Acoustic Sensing of Seismic Properties in a Borehole Drilled on a Fast-Flowing Greenlandic Outlet Glacier. *Geophysical Research Letters*, 47(13):e2020GL088148.

Born, A. and Robinson, A. (2021). Modeling the Greenland englacial stratigraphy. *Cryosphere*, 15(9):4539–4556.

Bougamont, M., Christoffersen, P., Hubbard, A. L., Fitzpatrick, A. A., Doyle, S. H., and Carter, S. P. (2014). Sensitive response of the Greenland Ice Sheet to surface melt drainage over a soft bed. *Nature Communications*, 5:5052.

Bougamont, M., Price, S., Christoffersen, P., and Payne, A. J. (2011). Dynamic patterns of ice stream flow in a 3-D higher-order ice sheet model with plastic bed and simplified hydrology. *Journal of Geophysical Research: Earth Surface*, 116(F4):4018.

Boulton, G. S. and Hindmarsh, R. C. (1987). Sediment deformation beneath glaciers: Rheology and geological consequences. *Journal of Geophysical Research: Solid Earth*, 92(B9):9059–9082.

Brondex, J., Gagliardini, O., Gillet-Chaulet, F., and Durand, G. (2017). Sensitivity of grounding line dynamics to the choice of the friction law. *Journal of Glaciology*, 63(241):854–866.

Brondex, J., Gillet-Chaulet, F., and Gagliardini, O. (2019). Sensitivity of centennial mass loss projections of the Amundsen basin to the friction law. *Cryosphere*, 13:177–195.

Budd, W. F. and Jacka, T. H. (1989). A review of ice rheology for ice sheet modelling. *Cold Regions Science and Technology*, 16(2):107–144.

Budd, W. F., Keage, P. L., and Blundy, N. A. (1979). Empirical Studies of Ice Sliding. *Journal of Glaciology*, 23(89):157–170.

Bueler, E. and Brown, J. (2009). Shallow shelf approximation as a "sliding law" in a thermomechanically coupled ice sheet model. *Journal of Geophysical Research*, 114(F3):F03008.

Caissie, D. and Luce, C. H. (2017). Quantifying streambed advection and conduction heat fluxes. *Water Resources Research*, 53(2):1595–1624.

Campanella, C., Cuccovillo, A., Campanella, C., Yurt, A., Passaro, V., Campanella, C. E., Cuccovillo, A., Campanella, C., Yurt, A., and Passaro, V. M. N. (2018). Fibre Bragg Grating Based Strain Sensors: Review of Technology and Applications. *Sensors*, 18(9):3115.

Cazenave, A., Meyssignac, B., Ablain, M., Balmaseda, M., Bamber, J., Barletta, V., Beckley, B., Benveniste, J., Berthier, E., Blazquez, A., Boyer, T., Caceres, D., and others (2018). Global sea-level budget 1993-present. *Earth System Science Data*, 10(3):1551–1590.

Chamberlin, R. T. (1928). Instrumental Work on the Nature of Glacier Motion. *The Journal of Geology*, 36(1):1–30.

Chandler, D., Hubbard, B., Hubbard, A., Murray, T., and Rippin, D. (2008). Optimising ice flow law parameters using borehole deformation measurements and numerical modelling. *Geophysical Research Letters*, 35(12):L12502.

Cheng, G., Kirchner, N., and Lötstedt, P. (2021). Sensitivity of ice sheet surface velocity and elevation to variations in basal friction and topography in the full Stokes and shallow-shelf approximation frameworks using adjoint equations. *The Cryosphere*, 15(2):715–742.

Chiles, J.-P. and Delfiner, P. (2012). *Geostatistics : modeling spatial uncertainty*. Wiley, Hoboken, 2nd edition.

Choi, Y., Morlighem, M., Rignot, E., and Wood, M. (2021). Ice dynamics will remain a primary driver of Greenland ice sheet mass loss over the next century. *Communications Earth & Environment*, 2:26.

Christie, F. D., Bingham, R. G., Gourmelen, N., Steig, E. J., Bisset, R. R., Pritchard, H. D., Snow, K., and Tett, S. F. (2018). Glacier change along West Antarctica's Marie Byrd Land Sector and links to inter-decadal atmosphere-ocean variability. *Cryosphere*, 12(7):2461–2479.

Chu, V. W. (2014). Greenland ice sheet hydrology. *Progress in Physical Geography*, 38(1):19–54.

Chu, W., Schroeder, D. M., Seroussi, H., Creyts, T. T., and Bell, R. E. (2018). Complex Basal Thermal Transition Near the Onset of Petermann Glacier, Greenland. *Journal of Geophysical Research: Earth Surface*, 123(5):985–995.

Chudley, Christoffersen, P., Doyle, S., Bougamont, M., Schoonman, C., Hubbard, B., and James, M. (2019). Supraglacial lake drainage at a fast-flowing Greenlandic outlet glacier. *Proceedings of the National Academy of Sciences of the United States of America*, 116(51):25468–25477.

Chudley, T. R., Christoffersen, P., Doyle, S. H., Abellan, A., and Snooke, N. (2019). High-accuracy UAV photogrammetry of ice sheet dynamics with no ground control. *The Cryosphere*, 13(3):955–968.

Chudley, T. R., Christoffersen, P., Doyle, S. H., Dowling, T. P., Law, R., Schoonman, C. M., Bougamont, M., and Hubbard, B. (2021). Controls on Water Storage and Drainage in Crevasses on the Greenland Ice Sheet. *Journal of Geophysical Research: Earth Surface*, 126(9):e2021JF006287.

Clark, C. D. (1993). Mega-scale glacial lineations and cross-cutting ice-flow landforms. *Earth Surface Processes and Landforms*, 18(1):1–29.

Clark, C. D., Ely, J. C., Greenwood, S. L., Hughes, A. L., Meehan, R., Barr, I. D., Bateman, M. D., Bradwell, T., Doole, J., Evans, D. J., Jordan, C. J., Monteys, X., Pellicer, X. M., and Sheehy, M. (2018). BRITICE Glacial Map, version 2: a map and GIS database of glacial landforms of the last British–Irish Ice Sheet. *Boreas*, 47(1):11–e8.

Clark, C. D., Tulaczyk, S. M., Stokes, C. R., and Canals, M. (2003). A groove-ploughing theory for the production of mega-scale glacial lineations, and implications for ice-stream mechanics. *Journal of Glaciology*, 49(165):240–256.

Clarke, G. K. (1987). A short history of scientific investigations on glaciers. *Journal of Glaciology*, 33(S1):4–24.

Clarke, G. K. (2005). Subglacial processes. *Annual Review of Earth and Planetary Sciences*, 33(1):247–276.

Clow, G. D., Saltus, R. W., and Waddington, E. D. (1996). A new high-precision borehole-temperature logging system used at GISP2, Greenland, and Taylor Dome, Antarctica. *Journal of Glaciology*, 42(142):576–584.

Clyne, E. R., Anandakrishnan, S., Muto, A., Alley, R. B., and Voigt, D. E. (2020). Interpretation of topography and bed properties beneath Thwaites Glacier, West Antarctica using seismic reflection methods. *Earth and Planetary Science Letters*, 550:116543.

Cohen, D. (1998). *Rheology of basal ice at Engabreen, Norway*. PhD thesis, University of Minnesota, Minnesota.

Colbeck, S. C. and Evans, R. J. (1973). A Flow Law for Temperate Glacier Ice. *Journal of Glaciology*, 12(64):71–86.

Colgan, W., Rajaram, H., Abdalati, W., McCutchan, C., Mottram, R., Moussavi, M. S., and Grigsby, S. (2016). Glacier crevasses: Observations, models, and mass balance implications. *Reviews of Geophysics*, 54(1):119–161.

Cook, J. M., Tedstone, A. J., Williamson, C., McCutcheon, J., Hodson, A. J., Dayal, A., Skiles, M., Hofer, S., Bryant, R., McAree, O., McGonigle, A., and others (2020a). Glacier algae accelerate melt rates on the south-western Greenland Ice Sheet. *The Cryosphere*, 14:309–330.

Cook, S. J., Christoffersen, P., and Todd, J. (2021a). A fully-coupled 3D model of a large Greenlandic outlet glacier with evolving subglacial hydrology, frontal plume melting and calving. *Journal of Glaciology*, pages 1–17.

Cook, S. J., Christoffersen, P., Todd, J., Slater, D., and Chauché, N. (2020b). Coupled modelling of subglacial hydrology and calving-front melting at Store Glacier, West Greenland. *Cryosphere*, 14(3):905–924.

Cook, S. J., Christoffersen, P., Truffer, M., Chudley, T. R., and Abellán, A. (2021b). Calving of a Large Greenlandic Tidewater Glacier has Complex Links to Meltwater Plumes and Mélange. *Journal of Geophysical Research: Earth Surface*, 126(4):e2020JF006051.

Coulon, V., Bulthuis, K., Whitehouse, P. L., Sun, S., Haubner, K., Zipf, L., and Pattyn, F. (2021). Contrasting Response of West and East Antarctic Ice Sheets to Glacial Isostatic Adjustment. *Journal of Geophysical Research: Earth Surface*, 126(7):e2020JF006003.

Crawford, A. J., Benn, D. I., Todd, J., Åström, J. A., Bassis, J. N., and Zwinger, T. (2021). Marine ice-cliff instability modeling shows mixed-mode ice-cliff failure and yields calving rate parameterization. *Nature Communications 2021 12:1*, 12(1):1–9.

CReSIS (2021). CReSIS radar depth sounder data. *Center for Remote Sensing of Ice Sheets, Lawrence, Kansas, USA.*

Cuffey, K. and Kavanaugh, J. (2011). How nonlinear is the creep deformation of polar ice? A new field assessment. *Geology*, 39(11):1027–1030.

Cuffey, K. M. and Paterson, W. S. B. (2010). *The Physics of Glaciers*. Elsevier Science & Technology Books, Amsterdam, 4 edition.

Dahl-Jensen, D. (1989). Steady thermomechanical flow along two-dimensional flow lines in large grounded ice sheets. *Journal of Geophysical Research*, 94(B8):355–362.

Dahl-Jensen, D. and Gundestrup, N. S. (1987). Constitutive properties of ice at Dye 3, Greenland. *International Association of Hydrological Sciences Publication*, (170):31–43.

Dahl-Jensen, D., Mosegaard, K., Gundestrup, N., Clow, G. D., Johnsen, S. J., Hansen, A. W., and Balling, N. (1998). Past temperatures directly from the greenland ice sheet. *Science*, 282(5387):268–271.

Dakin, J. P., Pratt, D. J., Bibby, G. W., and Ross, J. N. (1986). Temperature Distribution Measurement Using Raman Ratio Thermometry. In *Proc. SPIE 0566, Fiber Optic and Laser Sensors III*, volume 0566, page 249. International Society for Optics and Photonics.

Dash, J. G., Rempel, A. W., and Wettlaufer, J. S. (2006). The physics of premelted ice and its geophysical consequences. *Reviews of Modern Physics*, 78(3):695–741.

Dawes, P. R. (2009). The bedrock geology under the Inland Ice: the next major challenge for Greenland mapping. *GEUS Bulletin*, 17(17):57–60.

de Fleurian, B., Gagliardini, O., Zwinger, T., Durand, G., Le Meur, E., Mair, D., and Råback, P. (2014). A double continuum hydrological model for glacier applications. *The Cryosphere*, 8(1):137–153.

DeConto, R. M. and Pollard, D. (2016). Contribution of Antarctica to past and future sea-level rise. *Nature 2016 531:7596*, 531(7596):591–597.

Derkacheva, A., Gillet-Chaulet, F., Mouginot, J., Jager, E., Maier, N., and Cook, S. (2021). Seasonal evolution of basal environment conditions of Russell sector, West Greenland, inverted from satellite observation of surface flow. *The Cryosphere*, 15(12):5675–5704.

des Tombe, B., Schilperoort, B., and Bakker, M. (2020). Estimation of Temperature and Associated Uncertainty from Fiber-Optic Raman-Spectrum Distributed Temperature Sensing. *Sensors*, 20(8):2235.

Deutsch, C. V. and Journel, A. G. (1998). *GSLIB : geostatistical software library and user's guide*. Oxford University Press, Oxford.

Dow, C. F., Hubbard, A., Booth, A. D., Doyle, S. H., Gusmeroli, A., and Kulessa, B. (2013). Seismic evidence of mechanically weak sediments underlying Russell Glacier, West Greenland. *Annals of Glaciology*, 54(64):135–141.

Dow, C. F., Karlsson, N. B., and Werder, M. A. (2018). Limited Impact of Subglacial Supercooling Freeze-on for Greenland Ice Sheet Stratigraphy. *Geophysical Research Letters*, 45(3):1481–1489.

Dowdeswell, J. A., Ottesen, D., and Rise, L. (2010). Rates of sediment delivery from the Fennoscandian Ice Sheet through an ice age. *Geology*, 38(1):3–6.

Doyle, S. (2020). RESPONDER borehole instrumentation report. Technical report, Prifysgol Aberystwyth University, Aberystwyth.

Doyle, S. H., Hubbard, B., Christoffersen, P., Law, R., Hewitt, D. R., Neufeld, J. A., Schoonman, C. M., Chudley, T. R., and Bougamont, M. (2021). Water flow through sediments and at the ice-sediment interface beneath Sermeq Kujalleq (Store Glacier), Greenland. *Journal of Glaciology*, pages 1–20.

Doyle, S. H., Hubbard, B., Christoffersen, P., Young, T. J., Hofstede, C., Bougamont, M., Box, J. E., and Hubbard, A. (2018). Physical Conditions of Fast Glacier Flow: 1. Measurements From Boreholes Drilled to the Bed of Store Glacier, West Greenland. *Journal of Geophysical Research: Earth Surface*, 123(2):324–348.

Durand, G., Gagliardini, O., Favier, L., Zwinger, T., and Le Meur, E. (2011). Impact of bedrock description on modeling ice sheet dynamics. *Geophysical Research Letters*, 38:L20501.

Dutton, A., Carlson, A. E., Long, A. J., Milne, G. A., Clark, P. U., DeConto, R., Horton, B. P., Rahmstorf, S., and Raymo, M. E. (2015). Sea-level rise due to polar ice-sheet mass loss during past warm periods. *Science*, 349(6244).

Dutton, A. and Lambeck, K. (2012). Ice volume and sea level during the last interglacial. *Science*, 337(6091):216–219.

Duval, P. (1977). The role of the water content on the creep rate of poly-crystalline ice. *International Association of Hydrological Sciences Publication*, 118:29–33.

Duval, P., Ashby, M. F., and Anderman, I. (1983). Rate-controlling processes in the creep of polycrystalline ice. *Journal of Physical Chemistry*, 87(21):4066–4074.

Edwards, T. L., Brandon, M. A., Durand, G., Edwards, N. R., Golledge, N. R., Holden, P. B., Nias, I. J., Payne, A. J., Ritz, C., and Wernecke, A. (2019). Revisiting Antarctic ice loss due to marine ice-cliff instability. *Nature 2019 566:7742*, 566(7742):58–64.

Eisen, O., Winter, A., Steinhage, D., Kleiner, T., and Humbert, A. (2020). Basal roughness of the East Antarctic Ice Sheet in relation to flow speed and basal thermal state. *Annals of Glaciology*, 61(81):162–175.

Ely, J. C., Clark, C. D., Spagnolo, M., Stokes, C. R., Greenwood, S. L., Hughes, A. L., Dunlop, P., and Hess, D. (2016). Do subglacial bedforms comprise a size and shape continuum? *Geomorphology*, 257:108–119.

Enderlin, E. M., Howat, I. M., Jeong, S., Noh, M. J., Van Angelen, J. H., and Van Den Broeke, M. R. (2014). An improved mass budget for the Greenland ice sheet. *Geophysical Research Letters*.

Engelhardt, H. and Determann, J. (1987). Borehole evidence for a thick layer of basal ice in the central Ronne Ice Shelf. *Nature 1987 327:6120*, 327(6120):318–319.

Engelhardt, H., Humphrey, N., Kamb, B., and Fahnestock, M. (1990). Physical conditions at the base of a fast moving Antarctic ice stream. *Science*, 248(4951):57–59.

Evans, D. J., Clark, C. D., and Mitchell, W. A. (2005). The last British Ice Sheet: A review of the evidence utilised in the compilation of the Glacial Map of Britain. *Earth-Science Reviews*, 70(3-4):253–312.

Favier, L., Durand, G., Cornford, S. L., Gudmundsson, G. H., Gagliardini, O., Gillet-Chaulet, F., Zwinger, T., Payne, A. J., and Le Brocq, A. M. (2014). Retreat of Pine Island Glacier controlled by marine ice-sheet instability. *Nature Climate Change*, 4(2):117–121.

Fisher, A. T., Mankoff, K. D., Tulaczyk, S. M., Tyler, S. W., Foley, N., and WISSARD Science Team (2015). High geothermal heat flux measured below the West Antarctic Ice Sheet. *Science Advances*, 1(6):e1500093.

Flowers, G. E. (2018). Hydrology and the future of the Greenland Ice Sheet. *Nature Communications 2018 9:1*, 9(1):1–4.

Forbes, J. D. (1842). On a Remarkable Structure Observed by the Author in the Ice of Glaciers. *Edinburgh Natural Philosophy Journal*, 32(63):84–91.

Fountain, A. G. and Walder, J. S. (1998). Water flow through temperate glaciers. *Reviews of Geophysics*, 36(3):299–328.

Fowler, A. C. (1987). Sliding with Cavity Formation. *Journal of Glaciology*, 33(115):255–267.

Fowler, A. C. (2010a). The formation of subglacial streams and mega-scale glacial lineations. *Proceedings of the Royal Society A: Mathematical, Physical and Engineering Sciences*, 466(2123):3181–3201.

Fowler, A. C. (2010b). Weertman, Lliboutry and the development of sliding theory. *Journal of Glaciology*, 56(200):965–972.

Fowler, J. R. and Iverson, N. R. (2022). A permeameter for temperate ice: first results on permeability sensitivity to grain size. *Journal of Glaciology*, pages 1–11.

Fox-Kemper, B., Hewitt, H., Xiao, C., Aðalgeirsdóttir, G., Drijfhout, S., Edwards, T., Golledge, M., Hemer, R., Kopp, G., Krinner, A., and others (2021). Ocean, Cryosphere and Sea Level Change. Climate Change 2021: The Physical Science Basis. *Contribution of Working Group I to the Sixth Assessment Report of the Intergovernmental Panel on Climate Change*.

Freifeld, B. M., Finsterle, S., Onstott, T. C., Toole, P., and Pratt, L. M. (2008). Ground surface temperature reconstructions: Using in situ estimates for thermal conductivity acquired with a fiber-optic distributed thermal perturbation sensor. *Geophysical Research Letters*, 35(14):L14309.

Fretwell, P., Pritchard, H. D., Vaughan, D. G., Bamber, J. L., Barrand, N. E., Bell, R., Bianchi, C., Bingham, R. G., Blankenship, D. D., Casassa, G., Catania, G., Callens, D., Conway, H., and others (2013). Bedmap2: Improved ice bed, surface and thickness datasets for Antarctica. *Cryosphere*, 7(1):375–393.

Fricker, H. A., Arndt, P., Brunt, K. M., Datta, R. T., Fair, Z., Jasinski, M. F., Kingslake, J., Magruder, L. A., Moussavi, M., Pope, A., Spergel, J. J., Stoll, J. D., and Wouters, B. (2021). ICESat-2 Meltwater Depth Estimates: Application to Surface Melt on Amery Ice Shelf, East Antarctica. *Geophysical Research Letters*, 48(8):e2020GL090550.

Funk, M., Echelmeyer, K., and Iken, A. (1994). Mechanisms of fast flow in Jakobshavns Isbrae, West Greenland: Part II. Modeling of englacial temperatures. *Journal of Glaciology*, 40(136):569–585.

Gagliardini, O., Cohen, D., Råback, P., and Zwinger, T. (2007). Finite-element modeling of subglacial cavities and related friction law. *Journal of Geophysical Research: Earth Surface*, 112(F2):2027.

Gagliardini, O., Gillet-Chaulet, F., and Montagnat, M. (2009). A Review of Anisotropic Polar Ice Models : from Crystal to Ice-Sheet Flow Models. In *Physics of Ice Core Records II : Papers collected after the 2nd International Workshop on Physics of Ice Core Records*, Hokkaido. Institute of Low Temperature Science, Hokkaido University.

Gagliardini, O., Zwinger, T., Gillet-Chaulet, F., Durand, G., Favier, L., De Fleurian, B., Greve, R., Malinen, M., Martín, C., Räback, P., Ruokolainen, J., Sacchettini, M., Schäfer, M., Seddik, H., and Thies, J. (2013). Capabilities and performance of Elmer/Ice, a new-generation ice sheet model. *Geoscientific Model Development*, 6(4):1299–1318.

Garbe, J., Albrecht, T., Levermann, A., Donges, J. F., and Winkelmann, R. (2020). The hysteresis of the Antarctic Ice Sheet. *Nature*, 585(7826):538–544.

Gerrard, J. A. F., Perutz, M. F., Roch, A., and Taylor, G. I. (1952). Measurement of the velocity distribution along a vertical line through a glacier. *Proceedings of the Royal Society of London. Series A. Mathematical and Physical Sciences*, 213(1115):546–558.

Gilbert, A., Flowers, G. E., Miller, G. H., Rabus, B. T., Van Wychen, W., Gardner, A. S., and Copland, L. (2016). Sensitivity of Barnes Ice Cap, Baffin Island, Canada, to climate state and internal dynamics. *Journal of Geophysical Research: Earth Surface*, 121(8):1516–1539.

Gilbert, A., Gagliardini, O., Vincent, C., and Wagnon, P. (2014). A 3-D thermal regime model suitable for cold accumulation zones of polythermal mountain glaciers. *Journal of Geophysical Research: Earth Surface*, 119(9):1876–1893.

Gilbert, A., Sinisalo, A., R. Gurung, T., Fujita, K., B. Maharjan, S., C. Sherpa, T., and Fukuda, T. (2020). The influence of water percolation through crevasses on the thermal regime of a Himalayan mountain glacier. *Cryosphere*, 14(4):1273–1288.

Gillet-Chaulet, F., Durand, G., Gagliardini, O., Mosbeux, C., Mouginot, J., Rémy, F., and Ritz, C. (2016). Assimilation of surface velocities acquired between 1996 and 2010 to constrain the form of the basal friction law under Pine Island Glacier. *Geophysical Research Letters*, 43(19):311–10.

Gillet-Chaulet, F., Gagliardini, O., Seddik, H., Nodet, M., Durand, G., Ritz, C., Zwinger, T., Greve, R., and Vaughan, D. G. (2012). Greenland ice sheet contribution to sea-level rise from a new-generation ice-sheet model. *Cryosphere*, 6(6):1561–1576.

Gillet-Chaulet, F., Hindmarsh, R. C. A., Corr, H. F. J., King, E. C., and Jenkins, A. (2011). In-situ quantification of ice rheology and direct measurement of the Raymond Effect at Summit, Greenland using a phase-sensitive radar. *Geophysical Research Letters*, 38(24):L24503.

Gimbert, F., Gilbert, A., Gagliardini, O., Vincent, C., and Moreau, L. (2021). Do Existing Theories Explain Seasonal to Multi-Decadal Changes in Glacier Basal Sliding Speed? *Geophysical Research Letters*, 48(15):e2021GL092858.

Glen, J. W. (1952). Experiments on the Deformation of Ice. *Journal of Glaciology*, 2(12):111–114.

Glen, J. W. (1955). The creep of polycrystalline ice. *Proceedings of the Royal Society of London. Series A. Mathematical and Physical Sciences*, 228(1175):519–538.

Goelzer, H., Nowicki, S., Edwards, T., Beckley, M., Abe-Ouchi, A., Aschwanden, A., Calov, R., Gagliardini, O., Gillet-Chaulet, F., and others (2018). Design and results of the ice sheet model initialisation experiments initMIP-Greenland: an ISMIP6 intercomparison. *The Cryosphere*, 125194:1433–1460.

Goelzer, H., Nowicki, S., Payne, A., Larour, E., Seroussi, H., Lipscomb, W. H., Gregory, J., Abe-Ouchi, A., Shepherd, A., Simon, E., Agosta, C., Alexander, P., and Aschwanden, A. (2020). The future sea-level contribution of the Greenland ice sheet: A multi-model ensemble study of ISMIP6. *The Cryosphere*, 14(9):3071–3096.

Goelzer, H., Robinson, A., Seroussi, H., and van de Wal, R. S. (2017). Recent Progress in Greenland Ice Sheet Modelling. *Current Climate Change Reports*, 3(4):291–302.

Goldsby, D. L. and Kohlstedt, D. L. (2001). Superplastic deformation of ice: Experimental observations. *Journal of Geophysical Research: Solid Earth*, 106(B6):11017–11030.

Goodman, D. J., King, G. C. P., Millar, D. H. M., and Robin, G. d. Q. (1979). Pressure-Melting Effects in Basal Ice of Temperate Glaciers: Laboratory Studies and Field Observations Under Glacier D'Argentière. *Journal of Glaciology*, 23(89):259–271.

Graham, F. S., Morlighem, M., Warner, R. C., and Treverrow, A. (2018). Implementing an empirical scalar constitutive relation for ice with flow-induced polycrystalline anisotropy in large-scale ice sheet models. *The Cryosphere*, 12:1047–1067.

Greenler, L., Benson, T., Cherwinka, J., Elcheikh, A., Feyzi, F., Karle, A., and Paulos, R. (2014). Modeling hole size, lifetime and fuel consumption in hot-water ice drilling. *Annals of Glaciology*, 55(68):115–123.

Gregory, J. M., George, S. E., and Smith, R. S. (2020). Large and irreversible future decline of the Greenland ice sheet. *The Cryosphere*, 14(12):4299–4322.

Greve, R. (1997). A continuum–mechanical formulation for shallow polythermal ice sheets. *Philosophical Transactions of the Royal Society of London. Series A: Mathematical, Physical and Engineering Sciences*, 355(1726):921–974.

Greve, R. and Blatter, H. (2009). *Dynamics of Ice Sheets and Glaciers*. Springer, Berlin.

Großwig, S., Hurtig, E., and Kühn, K. (1996). Fibre optic temperature sensing: A new tool for temperature measurements in boreholes. *GEOPHYSICS*, 61(4):1065–1067.

Gudmundsson, G. H. (1997). Basal-flow characteristics of a linear medium sliding frictionless over small bedrock undulations. *Journal of Glaciology*, 43(143):71–79.

Gustafson, C. D., Key, K., Siegfried, M. R., Winberry, J. P., Fricker, H. A., Venturelli, R. A., and Michaud, A. B. (2022). A dynamic saline groundwater system mapped beneath an Antarctic ice stream. *Science*, 376(6593):640–644.

Hallet, B. (1981). Glacial Abrasion and Sliding: their Dependence on the Debris Concentration in Basal Ice. *Annals of Glaciology*, 2:23–28.

Hallet, B. (1996). Glacial quarrying: a simple theoretical model. *Annals of Glaciology*, 22:1–8.

Hansen, D. D. and Zoet, L. K. (2022). Characterizing Sediment Flux of Deforming Glacier Beds. *Journal of Geophysical Research: Earth Surface*, 127(4):e2021JF006544.

Hansen, J., Johnson, D., Lacis, A., Lebedeff, S., Lee, P., Rind, D., and Russell, G. (1981). Climate Impact of Increasing Atmospheric Carbon Dioxide. *Science*, 213(4511):957–966.

Harbor, J. M., Hallet, B., and Raymond, C. F. (1988). A numerical model of landform development by glacial erosion. *Nature 1988 333:6171*, 333(6171):347–349.

Harley, S. L. and Kelly, N. M. (2007). Chapter 3.2 Ancient Antarctica: The Archaean of the East Antarctic Shield. In *Developments in Precambrian Geology, Earth's Oldest Rocks*, volume 15, pages 149–186. Elsevier.

Harper, J. T., Bradford, J. H., Humphrey, N. F., and Meierbachtol, T. W. (2010). Vertical extension of the subglacial drainage system into basal crevasses. *Nature*, 467(7315):579–582.

Harper, J. T., Humphrey, N. F., Meierbachtol, T. W., Graly, J. A., and Fischer, U. H. (2017). Borehole measurements indicate hard bed conditions, Kangerlussuaq sector, western Greenland Ice Sheet. *Journal of Geophysical Research: Earth Surface*, 122(9):1605–1618.

Harrington, J. A., Humphrey, N. F., and Harper, J. T. (2015). Temperature distribution and thermal anomalies along a flowline of the Greenland ice sheet. *Annals of Glaciology*, 56(70):98–104.

Harrison, W. D. (1972). Temperature of a Temperate Glacier. *Journal of Glaciology*, 11(61):15–29.

Haseloff, M., Hewitt, I. J., and Katz, R. F. (2019). Englacial Pore Water Localizes Shear in Temperate Ice Stream Margins. *Journal of Geophysical Research: Earth Surface*, 124(11):2019JF005399.

Hausner, M. B., Suárez, F., Glander, K. E., Giesen, N. v. d., Selker, J. S., Tyler, S. W., Hausner, M. B., Suárez, F., Glander, K. E., Giesen, N. v. d., Selker, J. S., and Tyler, S. W. (2011). Calibrating Single-Ended Fiber-Optic Raman Spectra Distributed Temperature Sensing Data. *Sensors*, 11(11):10859–10879.

Hay, C., Mitrovica, J. X., Gomez, N., Creveling, J. R., Austermann, J., and Kopp, R. R. (2014). The sea-level fingerprints of ice-sheet collapse during interglacial periods. *Quaternary Science Reviews*, 87:60–69.

Hayes, J. (2010). *Fiber optics technician's manual*. Cengage Delmar Learning, 4 edition.

Hecht, J. (1999). *City of light : the story of fiber optics*. Oxford University Press.

Helanow, C., Iverson, N. R., Woodard, J. B., and Zoet, L. K. (2021). A slip law for hard-bedded glaciers derived from observed bed topography. *Science Advances*, 7(20):eabe7798.

Helanow, C., Iverson, N. R., Zoet, L. K., and Gagliardini, O. (2020). Sliding Relations for Glacier Slip With Cavities Over Three-Dimensional Beds. *Geophysical Research Letters*, 47(3):e2019GL084924.

Herron, S. L., Langway, C. C., and Brugger, K. A. (1985). Ultrasonic velocities and crystalline anisotropy in the ice core from Dye 3, Greenland. *Geophysical Monograph Series*, 33:23–31.

Hewitt, I. J. and Schoof, C. (2017). Models for polythermal ice sheets and glaciers. *The Cryosphere*, 11(1):541–551.

Hills, B. H., Harper, J. T., Humphrey, N. F., and Meierbachtol, T. W. (2017). Measured Horizontal Temperature Gradients Constrain Heat Transfer Mechanisms in Greenland Ice. *Geophysical Research Letters*, 44(19):9778–9785.

Hofer, S., Lang, C., Amory, C., Kittel, C., Delhasse, A., Tedstone, A., and Fettweis, X. (2020). Greater Greenland Ice Sheet contribution to global sea level rise in CMIP6. *Nature Communications*, 11:6289.

Hofstede, C., Christoffersen, P., Hubbard, B., Doyle, S. H., Young, T. J., Diez, A., Eisen, O., and Hubbard, A. (2018). Physical Conditions of Fast Glacier Flow: 2. Variable Extent of Anisotropic Ice and Soft Basal Sediment From Seismic Reflection Data Acquired on Store Glacier, West Greenland. *Journal of Geophysical Research: Earth Surface*, 123(2):349–362.

Holschuh, N., Christianson, K., Paden, J., Alley, R. B., and Anandakrishnan, S. (2020). Linking postglacial landscapes to glacier dynamics using swath radar at Thwaites Glacier, Antarctica. *Geology*, 48(3):268–272.

Holt, J. W., Blankenship, D. D., Morse, D. L., Young, D. A., Peters, M. E., Kempf, S. D., Richter, T. G., Vaughan, D. G., and Corr, H. F. (2006). New boundary conditions for the West Antarctic Ice Sheet: Subglacial topography of the Thwaites and Smith glacier catchments. *Geophysical Research Letters*, 33(9):L09502.

Hooke, R. L. B. (2005). *Principles of glacier mechanics, Second edition*. Cambridge University Press, 2 edition.

Hopkins, H. H. and Kapany, N. S. (1954). A Flexible Fibrescope, using Static Scanning. *Nature*, 173(4392):39–41.

Horgan, H. J., Anandakrishnan, S., Alley, R. B., Burkett, P. G., and Peters, L. E. (2011). Englacial seismic reflectivity: imaging crystal-orientation fabric in West Antarctica. *Journal of Glaciology*, 57(204):639–650.

Hu, Z., Kuipers Munneke, P., Lhermitte, S., Izeboud, M., and Van Den Broeke, M. (2021). Improving surface melt estimation over the Antarctic Ice Sheet using deep learning: A proof of concept over the Larsen Ice Shelf. *Cryosphere*, 15(12):5639–5658.

Hubbard, A. L., Hubbard, B., Christoffersen, P., Doyle, S. H., Chudley, T. R., Schoonman, C. M., Law, R., and Bougamont, M. (2021). Borehole-Based Characterization of Deep Mixed-Mode Crevasses at a Greenlandic Outlet Glacier. *AGU Advances*, 2(2):e2020AV000291.

Hubbard, B., Christoffersen, P., Doyle, S. H., Chudley, T. R., Bougamont, M. H., Law, R., and Schoonman, C. (2020). Borehole-based characterization of deep crevasses at a Greenlandic outlet glacier [v2]. *Earth and Space Science Open Archive*.

Hubbard, B. P., Sharp, M. J., Willis, I. C., Nielsen, M. K., and Smart, C. C. (1995). Borehole water-level variations and the structure of the subglacial hydrological system of Haut Glacier d'Arolla, Valais, Switzerland. *Journal of Glaciology*, 41(139):572–583.

Hughes, T. J. (1981). The weak underbelly of the West Antarctic ice sheet. *Journal of Glaciology*, 27(97):518–525.

Hugi, F. J. (1842). *Ueber das Wesen der Gletscher und Winterreise in das Eismeer*. J G Cotta, Stuttgart.

Humphrey, N. (1991). Estimating ice temperature from short records in thermally disturbed boreholes. *Journal of Glaciology*, 37(127):414–419.

Hunter, P., Meyer, C., Minchew, B., Haseloff, M., and Rempel, A. (2021). Thermal controls on ice stream shear margins. *Journal of Glaciology*, 67(263):435–449.

Hurtig, E., Kühn, S., and Grosswig, K. (1997). Distributed Fibre Optic Temperature Sensing: A New Tool for Long-Term and Short-Term Temperature Monitoring in Boreholes. *Energy Sources*, 19(1):55–62.

Hutter, K. (1982). A Mathematical Model of Polythermal Glaciers and Ice Sheets. *Geophysical & Astrophysical Fluid Dynamics*, 21(3-4):201–224.

Hutter, K. (1983). Theoretical Glaciology. *Mathematical Approaches to Geophysics, Springer*, 1.

Iken, A. (1981). The effect of the subglacial water pressure on the sliding velocity of a glacier in an idealized numerical model. *Journal of Glaciology*, 27(97):407–421.

Iken, A., Echelmeyer, K., Harrison, W., and Funk, M. (1993). Mechanisms of fast flow in Jakobshavns Isbrae, West Greenland: Part I. Measurements of temperature and water level in deep boreholes. *Journal of Glaciology*, 39(131):15–25.

Iverson, N. R. (2010). Shear resistance and continuity of subglacial till: hydrology rules. *Journal of Glaciology*, 56(200):1104–1114.

Jamieson, S. S., Sugden, D. E., and Hulton, N. R. (2010). The evolution of the subglacial landscape of Antarctica. *Earth and Planetary Science Letters*, 293(1-2):1–27.

Jones, R. S., Mackintosh, A. N., Norton, K. P., Golledge, N. R., Fogwill, C. J., Kubik, P. W., Christl, M., and Greenwood, S. L. (2015). Rapid Holocene thinning of an East Antarctic outlet glacier driven by marine ice sheet instability. *Nature Communications*, 6:8910.

Joughin, I., Smith, B., Howat, I., and Scambos, T. (2015). MEaSUREs Greenland Ice Sheet Velocity Map from InSAR Data, Version 2.

Joughin, I., Smith, B. E., Howat, I. M., Scambos, T., and Moon, T. (2010). Greenland flow variability from ice-sheet-wide velocity mapping. *Journal of Glaciology*, 56(197):415–430.

Joughin, I., Smith, B. E., and Medley, B. (2014). Marine Ice Sheet Collapse Potentially Under Way for the Thwaites Glacier Basin, West Antarctica. *Science*, 344(6185):735–738.

Joughin, I., Smith, B. E., and Schoof, C. G. (2019). Regularized Coulomb Friction Laws for Ice Sheet Sliding: Application to Pine Island Glacier, Antarctica. *Geophysical Research Letters*, 46(9):4764–4771.

Joughin, I., Tulaczyk, S., Bamber, J. L., Blankenship, D., Holt, J. W., Scambos, T., and Vaughan, D. G. (2009). Basal conditions for Pine Island and Thwaites Glaciers, West Antarctica, determined using satellite and airborne data. *Journal of Glaciology*, 55(190):245–257.

Jousset, P., Reinsch, T., Ryberg, T., Blanck, H., Clarke, A., Aghayev, R., Hersir, G. P., Henninges, J., Weber, M., and Krawczyk, C. M. (2018). Dynamic strain determination using fibre-optic cables allows imaging of seismological and structural features. *Nature Communications*, 9(1):2509.

Kääb, A., Winsvold, S. H., Altena, B., Nuth, C., Nagler, T., and Wuite, J. (2016). Glacier Remote Sensing Using Sentinel-2. Part I: Radiometric and Geometric Performance, and Application to Ice Velocity. *Remote Sensing*, 8(7):598.

Kamb, B. (1970). Sliding motion of glaciers: Theory and observation. *Reviews of Geophysics*, 8(4):673–728.

Kamb, B. (1991). Rheological nonlinearity and flow instability in the deforming bed mechanism of ice stream motion. *Journal of Geophysical Research: Solid Earth*, 96(B10):16585–16595.

Karlsson, N. B., Dahl-Jensen, D., Gogineni, S. P., and Paden, J. D. (2013). Tracing the depth of the Holocene ice in North Greenland from radio-echo sounding data. *Annals of Glaciology*, 54(64):44–50.

Keller, C. A., Huwald, H., Vollmer, M. K., Wenger, A., Hill, M., Parlange, M. B., and Reimann, S. (2011). Fiber optic distributed temperature sensing for the determination of the nocturnal atmospheric boundary layer height. *Atmospheric Measurement Techniques*, 4(2):143–149.

Kendrick, A. K., Schroeder, D. M., Chu, W., Young, T. J., Christoffersen, P., Todd, J., Doyle, S. H., Box, J. E., Hubbard, A., Hubbard, B., Brennan, P. V., Nicholls, K. W., and Lok, L. B. (2018). Surface Meltwater Impounded by Seasonal Englacial Storage in West Greenland. *Geophysical Research Letters*, 45(19):474–10.

King, E. C., Hindmarsh, R. C., and Stokes, C. R. (2009). Formation of mega-scale glacial lineations observed beneath a West Antarctic ice stream. *Nature Geoscience 2009 2:8*, 2(8):585–588.

Kirchner, N., Ahlkrona, J., Gowan, E. J., Lötstedt, P., Lea, J. M., Noormets, R., von Sydow, L., Dowdeswell, J. A., and Benham, T. (2016). Shallow ice approximation, second order shallow ice approximation, and full Stokes models: A discussion of their roles in palaeo-ice sheet modelling and development. *Quaternary Science Reviews*, 147:136–147.

Kirkham, J. D., Hogan, K. A., Larter, R. D., Arnold, N. S., Ely, J. C., Clark, C. D., Self, E., Games, K., Huuse, M., Stewart, M. A., Ottesen, D., and Dowdeswell, J. A. (2022). Tunnel valley formation beneath deglaciating mid-latitude ice sheets: Observations and modelling. *Quaternary Science Reviews*, page 107680.

Kirkham, J. D., Hogan, K. A., Larter, R. D., Arnold, N. S., Nitsche, F. O., Golledge, N. R., and Dowdeswell, J. A. (2019). Past water flow beneath Pine Island and Thwaites glaciers, West Antarctica. *Cryosphere*, 13(7):1959–1981.

Koellner, S., Parizek, B. R., Alley, R. B., Muto, A., and Holschuh, N. (2019). The impact of spatially-variable basal properties on outlet glacier flow. *Earth and Planetary Science Letters*, 515:200–208.

Krabbendam, M. (2016). Sliding of temperate basal ice on a rough, hard bed: creep mechanisms, pressure melting, and implications for ice streaming. *The Cryosphere*, 10(5):1915–1932.

Krabbendam, M. and Bradwell, T. (2014). Quaternary evolution of glaciated gneiss terrains: pre-glacial weathering vs. glacial erosion. *Quaternary Science Reviews*, 95:20–42.

Krabbendam, M., Dioguardi, F., Arnhardt, C., Roberson, S., and Hall, A. M. (2022). Drag forces at the ice-sheet bed and resistance of hard-rock obstacles: the physics of glacial ripping. *Journal of Glaciology*, pages 1–17.

Krabbendam, M., Eyles, N., Putkinen, N., Bradwell, T., and Arbelaez-Moreno, L. (2016). Streamlined hard beds formed by palaeo-ice streams: A review. *Sedimentary Geology*, 338:24–50.

Krohn, D. A., MacDougall, T. W., and Mendez, A. (2014). *Fiber Optic Sensors: Fundamentals and Applications*. Society of Photo-Optical Instrumentation Engineers (SPIE).

Kuiper, E. J. N., De Bresser, J. H., Drury, M. R., Eichler, J., Pennock, G. M., and Weikusat, I. (2020a). Using a composite flow law to model deformation in the NEEM deep ice core, Greenland-Part 2: The role of grain size and premelting on ice deformation at high homologous temperature. *Cryosphere*, 14(7):2449–2467.

Kuiper, E. J. N., Weikusat, I., De Bresser, J. H., Jansen, D., Pennock, G. M., and Drury, M. R. (2020b). Using a composite flow law to model deformation in the NEEM deep ice core, Greenland-Part 1: The role of grain size and grain size distribution on deformation of the upper 2207 m. *Cryosphere*, 14(7):2429–2448.

Kulessa, B., Hubbard, A. L., Booth, A. D., Bougamont, M., Dow, C. F., Doyle, S. H., Christoffersen, P., Lindbäck, K., Pettersson, R., Fitzpatrick, A. A., and Jones, G. A. (2017). Seismic evidence for complex sedimentary control of Greenland Ice Sheet flow. *Science Advances*, 3(8):e1603071.

Kulp, S. A. and Strauss, B. H. (2019). New elevation data triple estimates of global vulnerability to sea-level rise and coastal flooding. *Nature Communications*, 10(1):1–12.

Kyrke-Smith, T. M., Gudmundsson, G. H., and Farrell, P. E. (2018). Relevance of detail in basal topography for basal slipperiness inversions: A case study on Pine Island Glacier, Antarctica. *Frontiers in Earth Science*, 11:33.

Lai, C. Y., Kingslake, J., Wearing, M. G., Chen, P. H. C., Gentine, P., Li, H., Spergel, J. J., and van Wessem, J. M. (2020). Vulnerability of Antarctica's ice shelves to meltwater-driven fracture. *Nature 2020 584:7822*, 584(7822):574–578.

Lane, T. P., Roberts, D. H., Ó Cofaigh, C., Rea, B. R., and Vieli, A. (2016). Glacial landscape evolution in the Uummannaq region, West Greenland. *Boreas*, 45(2):220–234.

Law, R., Arnold, N., Benedek, C., Tedesco, M., Banwell, A., and Willis, I. (2020). Overwinter persistence of supraglacial lakes on the Greenland Ice Sheet: results and insights from a new model. *Journal of Glaciology*, 66(257):362–372.

Law, R., Christoffersen, P., Hubbard, B., Doyle, S. H., Chudley, T. R., Schoonman, C., Bougamont, M., des Tombe, B., Schilperoort, B., Kechavarzi, C., Booth, A., and Young, T. J. (2021). Thermodynamics of a fast-moving Greenlandic outlet glacier revealed by fiber-optic distributed temperature sensing. *Science Advances*, 7(20):eabe7136.

Law, R., Christoffersen, P., MacKie, E., Cook, S., Haseloff, M., and Gagliardini, O. (2022). Complex motion of Greenland Ice Sheet outlet glaciers with basal temperate ice. *EarthArXiv*, (3331).

Le Bars, D., Drijfhout, S., and De Vries, H. (2017). A high-end sea level rise probabilistic projection including rapid Antarctic ice sheet mass loss. *Environmental Research Letters*, 12(4):044013.

Liehr, S. (2018). Polymer Fiber Sensors for Structural and Civil Engineering Applications. In *Handbook of Optical Fibers*, pages 1–36. Springer, Singapore.

Liehr, S., Lenke, P., Wendt, M., and Krebber, K. (2008). Perfluorinated graded-index polymer optical fibers for distributed measurement of strain. In *17th International Conference on Plastic Optical Fibers*, pages 1–5.

Liehr, S., Münzenberger, S., and Krebber, K. (2018). Wavelength-scanning coherent OTDR for dynamic high strain resolution sensing. *Optics Express*, 26:10573–10588.

Liehr, S., Wendt, M., and Krebber, K. (2009). Distributed perfluorinated POF strain sensor using OTDR and OFDR techniques. In *Proc. SPIE 7503, 20th International Conference on Optical Fibre Sensors*.

Liehr, S., Wendt, M., and Krebber, K. (2010). Distributed strain measurement in perfluorinated polymer optical fibres using optical frequency domain reflectometry. *Measurement Science and Technology*, 21(9):094023.

Lliboutry, L. (1968). General Theory of Subglacial Cavitation and Sliding of Temperate Glaciers. *Journal of Glaciology*, 7(49):21–58.

Lliboutry, L. (1971). Permeability, Brine Content and Temperature of Temperate Ice. *Journal of Glaciology*, 10(58):15–29.

Lliboutry, L. (1976). Physical Processes in Temperate Glaciers. *Journal of Glaciology*, 16(74):151–158.

Lliboutry, L. (1993). Internal melting and ice accretion at the bottom of temperate glaciers. *Journal of Glaciology*, 39(131):50–64.

Lliboutry, L. and Duval, P. (1985). Various isotropic and anisotropic ices found in glaciers and polar ice caps and their corresponding rheologies. *Annales Geophysicae*, 3(2):207–224.

Llorens, M. G., Griera, A., Bons, P. D., Gomez-Rivas, E., Weikusat, I., Prior, D. J., Kerch, J., and Lebensohn, R. A. (2020). Seismic Anisotropy of Temperate Ice in Polar Ice Sheets. *Journal of Geophysical Research: Earth Surface*, 125(11):e2020JF005714.

Llubes, M., Lanseau, C., and Rémy, F. (2006). Relations between basal condition, subglacial hydrological networks and geothermal flux in Antarctica. *Earth and Planetary Science Letters*, 241(3-4):655–662.

Lowry, C. S., Walker, J. F., Hunt, R. J., and Anderson, M. P. (2007). Identifying spatial variability of groundwater discharge in a wetland stream using a distributed temperature sensor. *Water Resources Research*, 43(10).

Lüthi, Funk, M., Iken, A., Gogineni, S., and Truffer, M. (2002). Mechanisms of fast flow in Jakobshavn Isbræ, West Greenland: Part III. Measurements of ice deformation, temperature and cross-borehole conductivity in boreholes to the bedrock. *Journal of Glaciology*, 48(162):369–385.

Lüthi, M., Fahnestock, M., and Glaciology, M. T. (2009). Calving icebergs indicate a thick layer of temperate ice at the base of Jakobshavn Isbræ, Greenland. *Journal of Glaciology*, 55(191):563–566.

Lüthi, M. P. and Funk, M. (2001). Modelling heat flow in a cold, high-altitude glacier: interpretation of measurements from Colle Gnifetti, Swiss Alps. *Journal of Glaciology*, 47(157):314–324.

Lüthi, M. P., Funk, M., and Iken, A. (2003). Indication of active overthrust faulting along the Holocene-Wisconsin transition in the marginal zone of Jakobshavn Isbræ. *Journal of Geophysical Research*, 108(B11):2543.

Lüthi, M. P., Ryser, C., Andrews, L. C., Catania, G. A., Funk, M., Hawley, R. L., Hoffman, M. J., and Neumann, T. A. (2015). Heat sources within the Greenland Ice Sheet: dissipation, temperate paleo-firn and cryo-hydrologic warming. *The Cryosphere*, 9:245–253.

MacGregor, J. A., Boisvert, L. N., Medley, B., Petty, A. A., Harbeck, J. P., Bell, R. E., Blair, J. B., Blanchard-Wrigglesworth, E., Buckley, E. M., Christoffersen, M. S., Cochran, J. R., and Csathó, B. M. (2021). The Scientific Legacy of NASA's Operation IceBridge. *Reviews of Geophysics*, 59(2):e2020RG000712.

MacGregor, J. A., Fahnestock, M. A., Catania, G. A., Aschwanden, A., Clow, G. D., Colgan, W. T., Gogineni, S. P., Morlighem, M., Nowicki, S. M. J., Paden, J. D., Price, S. F., and Seroussi, H. (2016). A synthesis of the basal thermal state of the Greenland Ice Sheet. *Journal of Geophysical Research: Earth Surface*, 121(7):1328–1350.

Macgregor, J. A., Fahnestock, M. A., Catania, G. A., Paden, J. D., Prasad Gogineni, S., Young, S. K., Rybarski, S. C., Mabrey, A. N., Wagman, B. M., and Morlighem, M. (2015). Radiostratigraphy and age structure of the Greenland Ice Sheet. *Journal of Geophysical Research: Earth Surface*, 120(2):212–241.

MacGregor, K. R., Anderson, R. S., Anderson, S. P., and Waddington, E. D. (2000). Numerical simulations of glacial-valley longitudinal profile evolution. *Geology*, 28(11):1031–1034.

MacKie, E. J. and Schroeder, D. M. (2020). Geostatistically Simulating Subglacial Topography with Synthetic Training Data. *International Geoscience and Remote Sensing Symposium (IGARSS)*, pages 2991–2994.

MacKie, E. J., Schroeder, D. M., Zuo, C., Yin, Z., and Caers, J. (2021). Stochastic modeling of subglacial topography exposes uncertainty in water routing at Jakobshavn Glacier. *Journal of Glaciology*, 67(261):75–83.

Maier, N., Gimbert, F., Gillet-Chaulet, F., and Gilbert, A. (2021). Basal traction mainly dictated by hard-bed physics over grounded regions of Greenland. *Cryosphere*, 15(3):1435–1451.

Maier, N., Humphrey, N., Harper, J., and Meierbachtol, T. (2019). Sliding dominates slow-flowing margin regions, Greenland Ice Sheet. *Science Advances*, 5(7):eaaw5406.

Mankoff, K. D. and Tulaczyk, S. M. (2017). The past, present, and future viscous heat dissipation available for Greenland subglacial conduit formation. *The Cryosphere*, 11(1):303–317.

Mantelli, E. and Schoof, C. (2019). Ice sheet flow with thermally activated sliding. Part 2: the stability of subtemperate regions. *Proceedings of the Royal Society A*, 475(2231):20190411.

Margold, M., Stokes, C. R., Clark, C. D., and Kleman, J. (2015). Ice streams in the Laurentide Ice Sheet: a new mapping inventory. *Journal of Maps*, 11(3):380–395.

Marshall, H. P., Harper, J. T., Pfeffer, W. T., and Humphrey, N. F. (2002). Depth-varying constitutive properties observed in an isothermal glacier. *Geophysical Research Letters*, 29(23):61–1.

Martin-Español, A., Bamber, J. L., and Zammit-Mangion, A. (2017). Constraining the mass balance of East Antarctica. *Geophysical Research Letters*.

Masson-Delmotte, V., Zhai, P., Pirani, A., Connors, S. L., Péan, C., Berger, S., Caud, N., and others (2021). Summary for Policymakers. In: Climate Change 2021: The Physical Science Basis. Contribution of Working Group I to the Sixth Assessment Report of the Intergovernmental Panel on Climate Change. Technical report, IPCC.

Mastrandrea, M. D., Field, C. B., Stocker, T. F., Ebi, K. L., Frame, D. J., Held, H., Kriegler, E., and others (2010). Guidance Note for Lead Authors of the IPCC Fifth Assessment Report on Consistent Treatment of Uncertainties IPCC Cross-Working Group Meeting on Consistent Treatment of Uncertainties Core Writing Team. Technical report, Intergovernmental Panel on Climate Change.

McCormack, F. S., Warner, R. C., Seroussi, H., Dow, C. F., Roberts, J. L., and Treverrow, A. (2022). Modeling the Deformation Regime of Thwaites Glacier, West Antarctica, Using a Simple Flow Relation for Ice Anisotropy (ESTAR). *Journal of Geophysical Research: Earth Surface*, 127(3):e2021JF006332.

Medley, B., Joughin, I., Smith, B. E., Das, S. B., Steig, E. J., Conway, H., Gogineni, S., Lewis, C., Criscitiello, A. S., and others (2014). Constraining the recent mass balance of pine island and thwaites glaciers, west antarctica, with airborne observations of snow accumulation. *The Cryosphere*, 8(4):1375–1392.

Mercer, J. (1968). Antarctic ice and Sangamon sea level. *International Association of Scientific Hydrology*, 79:217–225.

Mercer, J. H. (1978). West Antarctic ice sheet and CO2 greenhouse effect: a threat of disaster. *Nature*, 271(5643):321–325.

Meyer, C. R. and Minchew, B. M. (2018). Temperate ice in the shear margins of the Antarctic Ice Sheet: Controlling processes and preliminary locations. *Earth and Planetary Science Letters*, 498:17–26.

Meyer, C. R., Yehya, A., Minchew, B., and Rice, J. R. (2018). A Model for the Downstream Evolution of Temperate Ice and Subglacial Hydrology Along Ice Stream Shear Margins. *Journal of Geophysical Research: Earth Surface*, 123(8):1682–1698.

Miles, K. E., Hubbard, B., Quincey, D. J., Miles, E. S., Sherpa, T. C., Rowan, A. V., and Doyle, S. H. (2018). Polythermal structure of a Himalayan debris-covered glacier revealed by borehole thermometry. *Scientific Reports*, 8(1):16825.

Millstein, J. D., Minchew, B. M., and Pegler, S. S. (2022). Ice viscosity is more sensitive to stress than commonly assumed. *Communications Earth & Environment 2022 3:1*, 3(1):1–7.

Mims III, F. M. (1982). The First Century of Lightwave Communications. *Fiber Optics Weekly Update*, pages 6–23.

Minchew, B. and Joughin, I. (2020). Toward a universal glacier slip law: A new friction rule may describe ice flow over rigid or deformable surfaces. *Science*, 368(6486):29–30.

Minchew, B., Simons, M., Björnsson, H., Pálsson, F., Morlighem, M., Seroussi, H., Larour, E., and Hensley, S. (2016). Plastic bed beneath Hofsjökull Ice Cap, central Iceland, and the sensitivity of ice flow to surface meltwater flux. *Journal of Glaciology*, 62(231):147–158.

Minchew, B. M., Meyer, C. R., Pegler, S. S., Lipovsky, B. P., Rempel, A. W., Hilmar Gudmundsson, G., and Iverson, N. R. (2019). Comment on "Friction at the bed does not control fast glacier flow".

Minchew, B. M., Meyer, C. R., Robel, A. A., Gudmundsson, G. H., and Simons, M. (2018). Processes controlling the downstream evolution of ice rheology in glacier shear margins: Case study on Rutford Ice Stream, West Antarctica. *Journal of Glaciology*, 64(246):583–594.

Moffett, K. B., Tyler, S. W., Torgersen, T., Menon, M., Selker, J. S., and Gorelick, S. M. (2008). Processes Controlling the Thermal Regime of Saltmarsh Channel Beds. *Environmental Science & Technology*, 42(3):671–676.

Morgan, V. I. (1991). High-temperature ice creep tests. *Cold Regions Science and Technology*, 19(3):295–300.

Morlighem, M., Rignot, E., Seroussi, H., Larour, E., Ben Dhia, H., and Aubry, D. (2011). A mass conservation approach for mapping glacier ice thickness. *Geophysical Research Letters*, 38(19):L19503.

Morlighem, M., Williams, C. N., Rignot, E., An, L., Arndt, J. E., Bamber, J. L., Catania, G., Chauché, N., Dowdeswell, J. A., Dorschel, B., Fenty, I., Hogan, K., Howat, I., and others (2017). BedMachine v3: Complete Bed Topography and Ocean Bathymetry Mapping of Greenland From Multibeam Echo Sounding Combined With Mass Conservation. *Geophysical Research Letters*, 44(21):11051–11061.

Mouginot, J., Rignot, E., Bjørk, A. A., van den Broeke, M., Millan, R., Morlighem, M., Noël, B., Scheuchl, B., and Wood, M. (2019). Forty-six years of Greenland Ice Sheet mass balance from 1972 to 2018. *Proceedings of the National Academy of Sciences of the United States of America*, 116(19):9239–9244.

Mouginot, J., Rignot, E., and Scheuchl, B. (2014). Sustained increase in ice discharge from the Amundsen Sea Embayment, West Antarctica, from 1973 to 2013. *Geophysical Research Letters*, 41(5):1576–1584.

Muanenda, Y. (2018). Recent Advances in Distributed Acoustic Sensing Based on Phase-Sensitive Optical Time Domain Reflectometry. *Journal of Sensors*, 2018:3897873.

Muanenda, Y., Oton, C. J., and Di Pasquale, F. (2019). Application of Raman and Brillouin Scattering Phenomena in Distributed Optical Fiber Sensing. *Frontiers in Physics*, 0:155.

Muto, A., Alley, R. B., Parizek, B. R., and Anandakrishnan, S. (2019a). Bed-type variability and till (dis)continuity beneath Thwaites Glacier, West Antarctica. *Annals of Glaciology*, 60(80):82–90.

Muto, A., Anandakrishnan, S., Alley, R. B., Horgan, H. J., Parizek, B. R., Koellner, S., Christianson, K., and Holschuh, N. (2019b). Relating bed character and subglacial morphology using seismic data from Thwaites Glacier, West Antarctica. *Earth and Planetary Science Letters*, 507:199–206.

Ng, W. P. and Lalam, N. (2017). Future of distributed fiber sensors. *15th International Conference on Optical Communications and Networks*, pages 1–3.

NKT (2019). Distributed Temperature Sensing - LIOS SENSING.

Nye, J. F. (1952a). Reply to Mr. Joel E. Fisher's Comments. *Journal of Glaciology*, 2(11):52–53.

Nye, J. F. (1952b). The Mechanics of Glacier Flow. *Journal of Glaciology*, 2(12):82–93.

Nye, J. F. (1953). The flow law of ice from measurements in glacier tunnels, laboratory experiments and the Jungfraufirn borehole experiment. *Proceedings of the Royal Society A*, 219(1139):477–489.

Nye, J. F. (1969). A calculation on the sliding of ice over a wavy surface using a Newtonian viscous approximation. *Proceedings of the Royal Society of London. A. Mathematical and Physical Sciences*, 311(1506):445–467.

Nye, J. F. (1970). Glacier sliding without cavitation in a linear viscous approximation. *Proceedings of the Royal Society of London. A. Mathematical and Physical Sciences*, 315(1522):381–403.

Ó Cofaigh, C., Andrews, J. T., Jennings, A. E., Dowdeswell, J. A., Hogan, K. A., Kilfeather, A. A., and Sheldon, C. (2013a). Glacimarine lithofacies, provenance and depositional processes on a West Greenland trough-mouth fan. *Journal of Quaternary Science*, 28(1):13–26.

Ó Cofaigh, C., Stokes, C. R., Lian, O. B., Clark, C. D., and Tulacyzk, S. (2013b). Formation of mega-scale glacial lineations on the Dubawnt Lake Ice Stream bed: 2. Sedimentology and stratigraphy. *Quaternary Science Reviews*, 77:210–227.

Ockenden, H., Bingham, R., Curtis, A., and Goldberg, D. (2021). Inverting ice surface elevation and velocity for bed topography and slipperiness beneath Thwaites Glacier. *The Cryosphere Discussions*.

Overeem, I., Hudson, B. D., Syvitski, J. P., Mikkelsen, A. B., Hasholt, B., Van Den Broeke, M. R., Noel, B. P., and Morlighem, M. (2017). Substantial export of suspended sediment to the global oceans from glacial erosion in Greenland. *Nature Geoscience*, 10(11):859–863.

Pales, J. C. and Keeling, C. D. (1965). The concentration of atmospheric carbon dioxide in Hawaii. *Journal of Geophysical Research*, 70(24):6053–6076.

Paolo, F. S., Fricker, H. A., and Padman, L. (2015). Volume loss from Antarctic ice shelves is accelerating. *Science*, 348(6232):327–331.

Parizek, B. R., Christianson, K., Anandakrishnan, S., Alley, R. B., Walker, R. T., Edwards, R. A., Wolfe, D. S., Bertini, G. T., Rinehart, S. K., Bindschadler, R. A., and Nowicki, S. M. (2013). Dynamic (in)stability of Thwaites Glacier, West Antarctica. *Journal of Geophysical Research: Earth Surface*, 118(2):638–655.

Parker, T., Shatalin, S., and Farhadiroushan, M. (2014). Distributed Acoustic Sensing – a new tool for seismic applications. *First Break*, 32(2010):61–69.

Paschotta, R. (2008a). Effective Mode Area.

Paschotta, R. (2008b). fiber Bragg gratings.

Paterson, W. S. (1991). Why ice-age ice is sometimes "soft". *Cold Regions Science and Technology*, 20(1):75–98.

Pattyn, F. (2017). Sea-level response to melting of Antarctic ice shelves on multi-centennial timescales with the fast Elementary Thermomechanical Ice Sheet model (f.ETISh v1.0). *Cryosphere*, 11(4):1851–1878.

Pattyn, F. (2018). The paradigm shift in Antarctic ice sheet modelling. *Nature Communications 2018 9:1*, 9(1):1–3.

Pegler, S. S. (2018). Suppression of marine ice sheet instability. *Journal of Fluid Mechanics*, 857:648–680.

Peltier, R., Goldsby, D. L., Kohlstedt, D. L., and Tarasov, L. (2000). Ice-age ice-sheet rheology: Constraints from the Last Glacial Maximum form of the Laurentide ice sheet. *Annals of Glaciology*, 30:163–176.

Peng, W., Pickrell, G. R., Huang, Z., Xu, J., Kim, W., Qi, B., and Wang, A. (2004). Self compensating fiber optic flow sensor system and its field applications. *Applied optics*, 43(8):1752–1760.

Perutz, M. F. (1950). Direct Measurement of the Velocity Distribution in a Vertical Profile Through a Glacier. *Journal of Glaciology*, 1(7):382–383.

Peters, S. T., Schroeder, D. M., Chu, W., Castelletti, D., Haynes, M. S., Christoffersen, P., and Romero-Wolf, A. (2021). Glaciological Monitoring Using the Sun as a Radio Source for Echo Detection. *Geophysical Research Letters*, 48(14):e2021GL092450.

Pettersson, R., Jansson, P., and Blatter, H. (2004). Spatial variability in water content at the cold-temperate transition surface of the polythermal Storglaciären, Sweden. *Journal of Geophysical Research: Earth Surface*, 109:F02009.

Porter, C., Morin, P., Howat, I., Noh, M.-J., Bates, B., Peterman, K., Keesey, S., Schlenk, M., Gardiner, J., Tomko, K., Willis, M., Kelleher, C., Cloutier, M., Husby, E., Foga, S., Nakamura, H., Platson, M., Wethington Jr., M., Williamson, C., Bauer, G., Enos, J., Arnold, G., Kramer, W., Becker, P., Doshi, A., D'Souza, C., Cummens, P., Laurier, F., and Bojesen, M. (2018). ArcticDEM. *Polar Geospatial Center, University of Minnesota*.

Prior-Jones, M. R., Bagshaw, E. A., Lees, J., Clare, L., Burrow, S., Werder, M. A., Karlsson, N. B., Dahl-Jensen, D., Chudley, T. R., Christoffersen, P., Wadham, J. L., Doyle, S. H., and Hubbard, B. (2021). Cryoegg: development and field trials of a wireless subglacial probe for deep, fast-moving ice. *Journal of Glaciology*, 67(264):627–640.

Pyrcz, M. and Deutsh, C. (2014). *Geostatistical Reservoir Modeling*. Number 2. Oxford University Press, Oxford, 2nd edition.

Pyrcz, M., Jo, J., Kupenko, H., Liu, A., Gigliotti, A. E., Salomaki, T., and Santos, J. E. (2021). GeostatsPy.

Rabus, B. T., Lang, O., and Adolphs, U. (2003). Interannual velocity variations and recent calving of Thwaites Glacier Tongue, West Antarctica. *Annals of Glaciology*, 36:215–224.

Rada, C. and Schoof, C. (2018). Channelized, distributed, and disconnected: Subglacial drainage under a valley glacier in the Yukon. *Cryosphere*, 12(8):2609–2636.

Reid, H. (1896). The Mechanics of Glaciers. I. *The Journal of Geology*, 4(8):912–928.

Rempel, A. W. (2008). A theory for ice-till interactions and sediment entrainment beneath glaciers. *Journal of Geophysical Research: Earth Surface*, 113(F1):1013.

Reusch (1864). Beitrage zur Lehre vom Eis. *Annalen der Physik und Chemie*, 121(1):573–578.

Riel, B., Minchew, B., and Bischoff, T. (2021). Data-Driven Inference of the Mechanics of Slip Along Glacier Beds Using Physics-Informed Neural Networks: Case study on Rutford Ice Stream, Antarctica. *Journal of Advances in Modeling Earth Systems*, 13(11):e2021MS002621.

Rignot, E., Box, J. E., Burgess, E., and Hanna, E. (2008). Mass balance of the Greenland ice sheet from 1958 to 2007. *Geophysical Research Letters*, 35(20):L20502.

Rignot, E., Casassa, G., Gogineni, P., Krabill, W., Rivera, A., and Thomas, R. (2004). Accelerated ice discharge from the Antarctic Peninsula following the collapse of Larsen B ice shelf. *Geophysical Research Letters*, 31(18):9310.

Rignot, E., Jacobs, S., Mouginot, J., and Scheuchl, B. (2013). Ice-Shelf Melting Around Antarctica. *Science*, 341(6143):266–270.

Rignot, E. and Mouginot, J. (2012). Ice flow in Greenland for the International Polar Year 2008-2009. *Geophysical Research Letters*, 39:L11501.

Rignot, E., Mouginot, J., Morlighem, M., Seroussi, H., and Scheuchl, B. (2014). Widespread, rapid grounding line retreat of Pine Island, Thwaites, Smith, and Kohler glaciers, West Antarctica, from 1992 to 2011. *Geophysical Research Letters*, 41(10):3502–3509.

Rignot, E., Mouginot, J., and Scheuchl, B. (2011). Ice Flow of the Antarctic Ice Sheet. *Science*, 333(6048):1427–1430.

Rignot, E., Mouginot, J., Scheuchl, B., Van Den Broeke, M., Van Wessem, M. J., and Morlighem, M. (2019). Four decades of Antarctic ice sheet mass balance from 1979–2017. *Proceedings of the National Academy of Sciences of the United States of America*, 116(4):1095–1103.

Ritz, C., Edwards, T. L., Durand, G., Payne, A. J., Peyaud, V., and Hindmarsh, R. C. (2015). Potential sea-level rise from Antarctic ice-sheet instability constrained by observations. *Nature 2015 528:7580*, 528(7580):115–118.

Ritz, C., Fabre, A., and Letréguilly, A. (1996). Sensitivity of a Greenland ice sheet model to ice flow and ablation parameters: consequences for the evolution through the last climatic cycle. *Climate Dynamics*, 13(1):11–23.

Robel, A. A., Seroussi, H., and Roe, G. H. (2019). Marine ice sheet instability amplifies and skews uncertainty in projections of future sea-level rise. *Proceedings of the National Academy of Sciences of the United States of America*, 116(30):14887–14892.

Roberts, D. H. and Long, A. J. (2005). Streamlined bedrock terrain and fast ice flow, Jakobshavns Isbrae, West Greenland : implications for ice stream and ice sheet dynamics. *Boreas*, 34(1):25–42.

Robinson, A., Calov, R., and Ganopolski, A. (2012). Multistability and critical thresholds of the Greenland ice sheet. *Nature Climate Change*, 2(6):429–432.

Roth, T. R., Westhoff, M. C., Huwald, H., Huff, J. A., Rubin, J. F., Barrenetxea, G., Vetterli, M., Parriaux, A., Selker, J. S., and Parlange, M. B. (2010). Stream Temperature Response to Three Riparian Vegetation Scenarios by Use of a Distributed Temperature Validated Model. *Environmental Science & Technology*, 44(6):2072–2078.

Rott, H., Wuite, J., De Rydt, J., Gudmundsson, G. H., Floricioiu, D., and Rack, W. (2020). Impact of marine processes on flow dynamics of northern Antarctic Peninsula outlet glaciers. *Nature Communications 2020 11:1*, 11(1):1–3.

Ryser, C., Lüthi, M., Blindow, N., Suckro, S., Funk, M., and Bauder, A. (2013). Cold ice in the ablation zone: Its relation to glacier hydrology and ice water content. *Journal of Geophysical Research: Earth Surface*, 118(2):693–705.

Ryser, C., Lüthi, M. P., Andrews, L. C., Catania, G. A., Funk, M., Hawley, R., Hoffman, M., and Neumann, T. A. (2014a). Caterpillar-like ice motion in the ablation zone of the Greenland ice sheet. *Journal of Geophysical Research: Earth Surface*, 119(10):2258–2271.

Ryser, C., Lüthi, M. P., Andrews, L. C., Hoffman, M. J., Catania, G. A., Hawley, R. L., Neumann, T. A., and Kristensen, S. S. (2014b). Sustained high basal motion of the Greenland ice sheet revealed by borehole deformation. *Journal of Glaciology*, 60(222):647–660.

Scambos, T. A., Bell, R. E., Alley, R. B., Anandakrishnan, S., Bromwich, D. H., Brunt, K., Christianson, K., and others (2017). How much, how fast?: A science review and outlook for research on the instability of Antarctica's Thwaites Glacier in the 21st century. *Global and Planetary Change*, 153:16–34.

Schilperoort, B., Coenders-Gerrits, M., Luxemburg, W., Rodríguez, C. J., Cisneros Vaca, C., and Savenije, H. (2018). Technical note: Using distributed temperature sensing for Bowen ratio evaporation measurements. *Hydrology and Earth System Sciences*, 22(1):819–830.

Schlegel, R., Murray, T., Smith, A. M., Brisbourne, A. M., Booth, A. D., King, E. C., and Clark, R. A. (2022). Radar Derived Subglacial Properties and Landforms Beneath Rutford Ice Stream, West Antarctica. *Journal of Geophysical Research: Earth Surface*, 127(1):e2021JF006349.

Schoof, C. (2005). The effect of cavitation on glacier sliding. *Proceedings of the Royal Society A: Mathematical, Physical and Engineering Sciences*, 461(2055):609–627.

Schoof, C. (2007). Ice sheet grounding line dynamics: Steady states, stability, and hysteresis. *Journal of Geophysical Research: Earth Surface*, 112(F3).

Schoof, C. and Hewitt, I. J. (2016). A model for polythermal ice incorporating gravity-driven moisture transport. *Journal of Fluid Mechanics*, 797:504–535.

Schoof, C. G. and Clarke, G. K. (2008). A model for spiral flows in basal ice and the formation of subglacial flutes based on a Reiner-Rivlin rheology for glacial ice. *Journal of Geophysical Research: Solid Earth*, 113(B5).

Schroeder, D. M., Seroussi, H., Chu, W., and Young, D. A. (2016). Adaptively constraining radar attenuation and temperature across the Thwaites Glacier catchment using bed echoes. *Journal of Glaciology*, 62(236):1075–1082.

Seguinot, J., Funk, M., Bauder, A., Wyder, T., Senn, C., and Sugiyama, S. (2020). Englacial Warming Indicates Deep Crevassing in Bowdoin Glacier, Greenland. *Frontiers in Earth Science*, 8:65.

Selker, J. S., Thévenaz, L., Huwald, H., Mallet, A., Luxemburg, W., van de Giesen, N., Stejskal, M., Zeman, J., Westhoff, M., and Parlange, M. B. (2006). Distributed fiber-optic temperature sensing for hydrologic systems. *Water Resources Research*, 42(12).

Sergienko, O. V. and Hindmarsh, R. C. (2013). Regular patterns in frictional resistance of ice-stream beds seen by surface data inversion. *Science*, 342(6162):1086–1089.

Seroussi, H., Morlighem, M., Rignot, E., Larour, E., Aubry, D., Dhia, H. B., and Kristensen, S. S. (2011). Ice flux divergence anomalies on 79north Glacier, Greenland. *Geophysical Research Letters*, 38:L09501.

Seroussi, H., Nowicki, S., Payne, A. J., Goelzer, H., Lipscomb, W. H., Abe-Ouchi, A., Agosta, C., Albrecht, T., Asay-Davis, X., Barthel, A., Calov, R., Cullather, R., Dumas, C., Galton-Fenzi, B. K., and others (2020). ISMIP6 Antarctica: A multi-model ensemble of the Antarctic ice sheet evolution over the 21st century. *The Cryosphere*, 14(9):3033–3070.

Shaw, J., Pugin, A., and Young, R. R. (2008). A meltwater origin for Antarctic shelf bedforms with special attention to megalineations. *Geomorphology*, 102(3-4):364–375.

Shepherd, A., Ivins, E. R., A, G., Barletta, V. R., Bentley, M. J., Bettadpur, S., Birggs, K. H., Bromwich, D. H., Forsberg, R., and Galin, N. (2012). A Reconciled Estimate of Ice-Sheet Mass Balance. *Science*, 338(6111):1183–1189.

Siegert, M., Atkinson, A., Banwell, A., Brandon, M., Convey, P., Davies, B., Downie, R., Edwards, T., Hubbard, B., Marshall, G., Rogelj, J., Rumble, J., Stroeve, J., and Vaughan, D. (2019). The Antarctic Peninsula under a 1.5°C global warming scenario. *Frontiers in Environmental Science*, 7(JUN):102.

Sigl, M., Winstrup, M., McConnell, J. R., Welten, K. C., Plunkett, G., Ludlow, F., Büntgen, U., Caffee, M., Chellman, N., Dahl-Jensen, D., and other (2015). Timing and climate forcing of volcanic eruptions for the past 2,500 years. *Nature*, 523(7562):543–549.

Silixa (2018). XT-DTS Datasheet. Technical report, Elstree.

Smith, A. M., Bentley, C. R., Bingham, R. G., and Jordan, T. A. (2012). Rapid subglacial erosion beneath Pine Island Glacier, West Antarctica. *Geophysical Research Letters*, 39(12):12501.

Smith, A. M., Murray, T., Nicholls, K. W., Makinson, K., Adalgeirsdóttir, G., Behar, A. E., and Vaughan, D. G. (2007). Rapid erosion, drumlin formation, and changing hydrology beneath an Antarctic ice stream. *Geology*, 35(2):127–130.

Smith, J. A., Andersen, T. J., Shortt, M., Gaffney, A. M., Truffer, M., Stanton, T. P., Bindschadler, R., Dutrieux, P., Jenkins, A., Hillenbrand, C. D., Ehrmann, W., Corr, H. F., Farley, N., Crowhurst, S., and Vaughan, D. G. (2016). Sub-ice-shelf sediments record history of twentieth-century retreat of Pine Island Glacier. *Nature 2016 541:7635*, 541(7635):77–80.

Sokołowski, R. J. and Wysota, W. (2020). Differentiation of subglacial conditions on soft and hard bed settings and implications for ice sheet dynamics: a case study from north-central Poland. *International Journal of Earth Sciences*, 109(8):2699–2717.

Spagnolo, M., Clark, C. D., Ely, J. C., Stokes, C. R., Anderson, J. B., Andreassen, K., Graham, A. G., and King, E. C. (2014). Size, shape and spatial arrangement of mega-scale glacial lineations from a large and diverse dataset. *Earth Surface Processes and Landforms*, 39(11):1432–1448.

Stearns, L. A. and Van Der Veen, C. J. (2018). Friction at the bed does not control fast glacier flow. *Science*, 361(6399):273–277.

Steig, E. J., Huybers, K., Singh, H. A., Steiger, N. J., Ding, Q., Frierson, D. M. W., Popp, T., and White, J. W. C. (2015). Influence of West Antarctic Ice Sheet collapse on Antarctic surface climate. *Geophysical Research Letters*, 42(12):4862–4868.

Stern, A. A., Dinniman, M. S., Zagorodnov, V., Tyler, S. W., and Holland, D. M. (2013). Intrusion of warm surface water beneath the McMurdo Ice Shelf, Antarctica. *Journal of Geophysical Research: Oceans*, 118(12):7036–7048.

Stokes, C. R. and Clark, C. D. (1999). Geomorphological criteria for identifying Pleistocene ice streams. *Annals of Glaciology*, 28:67–74.

Stokes, C. R., Spagnolo, M., Clark, C. D., Ó Cofaigh, C., Lian, O. B., and Dunstone, R. B. (2013). Formation of mega-scale glacial lineations on the Dubawnt Lake Ice Stream

bed: 1. size, shape and spacing from a large remote sensing dataset. *Quaternary Science Reviews*, 77:190–209.

Suckale, J., Platt, J. D., Perol, T., and Rice, J. R. (2014). Deformation-induced melting in the margins of the West Antarctic ice streams. *Journal of Geophysical Research: Earth Surface*, 119(5):1004–1025.

Sutter, J., Gierz, P., Grosfeld, K., Thoma, M., and Lohmann, G. (2016). Ocean temperature thresholds for Last Interglacial West Antarctic Ice Sheet collapse. *Geophysical Research Letters*, 43(6):2675–2682.

The IMBIE Team (2019). Mass balance of the Greenland Ice Sheet from 1992 to 2018. *Nature*, 579:233–239.

The IMBIE Team (2021). Antarctic and Greenland Ice Sheet mass balance 1992-2020 for IPCC AR6.

The Nobel Prize (2019). The Nobel Prize in Physics 1930.

Thomson, S. N., Reiners, P. W., Hemming, S. R., and Gehrels, G. E. (2013). The contribution of glacial erosion to shaping the hidden landscape of East Antarctica. *Nature Geoscience 2013 6:3*, 6(3):203–207.

Thorsteinsson, T., Waddington, E. D., Taylor, K. C., Alley, R. B., and Blankenship, D. D. (1999). Strain-rate enhancement at Dye 3, Greenland. *Journal of Glaciology*, 45(150):338–345.

Todd, J., Christoffersen, P., Zwinger, T., Råback, P., Chauché, N., Benn, D., Luckman, A., Ryan, J., Toberg, N., Slater, D., and Hubbard, A. (2018). A full-Stokes 3-D calving model applied to a large Greenlandic glacier. *Journal of Geophysical Research: Earth Surface*, 123(3):410–432.

Truffer, M. and Echelmeyer, K. A. (2003). Of isbræ and ice streams. *Annals of Glaciology*, 36:66–72.

Trusel, L. D., Frey, K. E., Das, S. B., Munneke, P. K., and Van Den Broeke, M. R. (2013). Satellite-based estimates of Antarctic surface meltwater fluxes. *Geophysical Research Letters*, 40(23):6148–6153.

Tsai, V. C., Smith, L. C., Gardner, A. S., and Seroussi, H. (2021). A unified model for transient subglacial water pressure and basal sliding. *Journal of Glaciology*, 68(268):390–400.

Tsai, V. C., Stewart, A. L., and Thompson, A. F. (2015). Marine ice-sheet profiles and stability under Coulomb basal conditions. *Journal of Glaciology*, 61(226):205–215.

Tuckett, P. A., Ely, J. C., Sole, A. J., Livingstone, S. J., Davison, B. J., and van Wessem, J. M. (2020). Reply to: "Impact of marine processes on flow dynamics of northern Antarctic Peninsula outlet glaciers" by Rott et al. *Nature Communications 2020 11:1*, 11(1):1–4.

Tulaczyk, S., Kamb, W. B., and Engelhardt, H. F. (2000). Basal mechanics of Ice Stream B, west Antarctica: 1. Till mechanics. *Journal of Geophysical Research: Solid Earth*, 105(B1):463–481.

Tulaczyk, S., Mikucki, J. A., Siegfried, M. R., Priscu, J. C., Barcheck, C. G., Beem, L. H., Behar, A., Burnett, J., Christner, B. C., and Fisher, A. T. (2014). WISSARD at Subglacial Lake Whillans, West Antarctica: scientific operations and initial observations. *Annals of Glaciology*, 55(65):51–58.

Tyler, S., Holland, D., Zagorodnov, V., Stern, A., Sladek, C., Kobs, S., White, S., Suárez, F., and Bryenton, J. (2013). Using distributed temperature sensors to monitor an Antarctic ice shelf and sub-ice-shelf cavity. *Journal of Glaciology*, 59(215):583–591.

Tyler, S., Selker, J. S., Hausner, M. B., Hatch, C. E., Torgersen, T., Thodal, C. E., and Schladow, S. G. (2009). Environmental temperature sensing using Raman spectra DTS fiber-optic methods. *Water Resources Research*, 45(4).

Vallon, M., Petit, J., and B Fabre (1976). Study of an ice core to the bedrock in the accumulation zone of an alpine glacier. *Journal of Glaciology*.

van de Giesen, N., Steele-Dunne, S. C., Jansen, J., Hoes, O., Hausner, M. B., Tyler, S., and Selker, J. (2012). Double-ended calibration of fiber-optic raman spectra distributed temperature sensing data. *Sensors*, 12(5):5471–5485.

van den Broeke, M. (2019). RACMO2.3p1 annual surface mass balance Antarctica (1979-2014). *PANGAEA*.

Van Den Broeke, M. R., Enderlin, E. M., Howat, I. M., Munneke, P. K., Noël, B. P. Y., Van De Berg, W. J., Van Meijgaard, E., and Wouters, B. (2016). On the recent contribution of the Greenland ice sheet to sea level change. *The Cryosphere*, 10:1933–1946.

Van Heel, A. C. S. (1954). A New Method of transporting Optical Images without Aberrations. *Nature*, 173(4392):39–39.

Vaughan, D. G. and Arthern, R. (2007). Why is it hard to predict the future of ice sheets? *Science*, 315(5818):1503–1504.

Vaughan, D. G., Corr, H. F., Ferraccioli, F., Frearson, N., O'Hare, A., Mach, D., Holt, J. W., Blankenship, D. D., Morse, D. L., and Young, D. A. (2006). New boundary conditions for the West Antarctic ice sheet: Subglacial topography beneath Pine Island Glacier. *Geophysical Research Letters*, 33(9).

Walder, J. and Hallet, B. (1979). Geometry of Former Subglacial Water Channels and Cavities. *Journal of Glaciology*, 23(89):335–346.

Wang, W. L. and Warner, R. C. (1999). Modelling of anisotropic ice flow in Law Dome, East Antarctica. *Annals of Glaciology*, 29:184–190.

Wang, Y., Zhang, T., Xiao, C., Ren, J., and Wang, Y. (2020). A two-dimensional, higher-order, enthalpy-based thermomechanical ice flow model for mountain glaciers and its benchmark experiments. *Computers and Geosciences*, 141:104526.

Webb, D. J. (2015). Fibre Bragg grating sensors in polymer optical fibres. *Measurement Science and Technology*, 26(9):092004.

Weertman, J. (1957). On the sliding of glaciers. *Journal of Glaciology*, 3(21):33–38.

Weertman, J. (1964). The Theory of Glacier Sliding. *Journal of Glaciology*, 5(39):287–303.

Werner, C., Bedford, T., Cooke, R. M., Hanea, A. M., and Morales-Nápoles, O. (2017). Expert judgement for dependence in probabilistic modelling: A systematic literature review and future research directions. *European Journal of Operational Research*, 258(3):801–819.

Whitehouse, P. L., Gomez, N., King, M. A., and Wiens, D. A. (2019). Solid Earth change and the evolution of the Antarctic Ice Sheet. *Nature Communications 2019 10:1*, 10(1):1–14.

Willis, I., Mair, D., Hubbard, B., Nienow, P., Fischer, U. H., and Hubbard, A. (2003). Seasonal variations in ice deformation and basal motion across the tongue of Haut Glacier d'Arolla, Switzerland. *Annals of Glaciology*, 36:157–167.

Wilson, C. J. L. (1986). Deformation induced recrystallization of ice: The application of in situ experiments. In *Mineral and Rock Deformation: Laboratory Studies*, volume 36, pages 213–232. American Geophysical Union.

Wise, M. G., Dowdeswell, J. A., Jakobsson, M., and Larter, R. D. (2017). Evidence of marine ice-cliff instability in Pine Island Bay from iceberg-keel plough marks. *Nature*, 550(7677):506–510.

Wolff, E. W., Chappellaz, J., Blunier, T., Rasmussen, S. O., and Svensson, A. (2010). Millennial-scale variability during the last glacial: The ice core record. *Quaternary Science Reviews*, 29(21-22):2828–2838.

Woodard, J. B., Zoet, L. K., Iverson, N. R., and Helanow, C. (2021). Variations in Hard-Bedded Topography Beneath Glaciers. *Journal of Geophysical Research: Earth Surface*, 126(9):e2021JF006326.

Wright, P. J., Harper, J. T., Humphrey, N. F., and Meierbachtol, T. W. (2016). Measured basal water pressure variability of the western Greenland Ice Sheet: Implications for hydraulic potential. *Journal of Geophysical Research: Earth Surface*, 121(6):1134–1147.

Young, T. J., Christoffersen, P., Bougamont, M., Tulaczyk, S. M., Hubbard, B., Mankoff, K. D., Nicholls, K. W., and Stewart, C. L. (2022). Rapid basal melting of the Greenland Ice Sheet from surface meltwater drainage. *Proceedings of the National Academy of Sciences*, 119(10).

Young, T. J., Christoffersen, P., Doyle, S. H., Nicholls, K. W., Stewart, C. L., Hubbard, B., Hubbard, A., Lok, L. B., and others (2019). Physical Conditions of Fast Glacier Flow: 3. Seasonally-Evolving Ice Deformation on Store Glacier, West Greenland. *Journal of Geophysical Research: Earth Surface*, 124(1):245–267.

Young, T. J., Schroeder, D. M., Christoffersen, P., Lok, L. B., Nicholls, K. W., Brennan, P. V., Doyle, S. H., Hubbard, B., and Hubbard, A. (2018). Resolving the internal and basal geometry of ice masses using imaging phase-sensitive radar. *Journal of Glaciology*, 64(246):649–660.

Young, T. J., Schroeder, D. M., Jordan, T. M., Christoffersen, P., Tulaczyk, S. M., Culberg, R., and Bienert, N. L. (2021). Inferring Ice Fabric From Birefringence Loss in Airborne Radargrams: Application to the Eastern Shear Margin of Thwaites Glacier, West Antarctica. *Journal of Geophysical Research: Earth Surface*, 126(5):e2020JF006023.

Yuan, W., Stefani, A., Bache, M., Jacobsen, T., Rose, B., Herholdt-Rasmussen, N., Nielsen, F. K., Andresen, S., Sørensen, O. B., Hansen, K. S., and Bang, O. (2011). Improved thermal and strain performance of annealed polymer optical fiber Bragg gratings. *Optics Communications*, 284(1):176–182.

Zeitz, M., Levermann, A., and Winkelmann, R. (2020). Sensitivity of ice loss to uncertainty in flow law parameters in an idealized one-dimensional geometry. *Cryosphere*, 14(10):3537–3550.

Zhang, H., Davis, T., Katz, R. F., Stevens, L. A., and May, D. A. (2022). Basal hydrofractures near sticky patches. *ArXiv*, page 11697.

Zoet, L. K. and Iverson, N. R. (2015). Experimental determination of a double-valued drag relationship for glacier sliding. *Journal of Glaciology*, 61(225):1–7.

Zoet, L. K. and Iverson, N. R. (2020). A slip law for glaciers on deformable beds. *Science*, 368(6486):76–78.

Zoet, L. K., Iverson, N. R., Andrews, L., and Helanow, C. (2021). Transient evolution of basal drag during glacier slip. *Journal of Glaciology*, pages 1–10.